Modelling of the freshwater flux over the Vietnamese Mekong Delta

Zur Erlangung des akademischen Grades eines
DOKTORS DER NATURWISSENSCHAFTEN
von der KIT-Fakultät für Physik des
Karlsruher Instituts für Technologie (KIT)

angenommene

DISSERTATION

von

M.Sc. Anh Duc Tran
aus Ninh Binh

Tag der mündlichen Prüfung:	13.02.2026
Referent:	Prof. Dr. Andreas H. Fink
Korreferent:	Prof. Dr. Harald Kunstmann

Abstract

Freshwater flux is a critical controlling factor for food production, ecosystem functioning, and socio-economic stability in the Vietnamese Mekong Delta, particularly over the Ca Mau Peninsula, which represents the country's most important aquaculture region. Rapid land-use and land-cover change (LULCC) over recent decades has substantially altered land-atmosphere interactions, increasing uncertainty in regional freshwater flux estimates. This dissertation aims to improve the simulation of freshwater fluxes over the Ca Mau Peninsula by applying the Advanced Research Weather Research and Forecasting (WRF-ARW) model at a 5-km gray-zone resolution for the period 2007–2016, explicitly accounting for physical parameterization choices and LULCC effects.

Freshwater flux is assessed as the difference between precipitation and evapotranspiration, using both potential evapotranspiration (PET) and actual evapotranspiration (AET) concepts. The study pursues three main objectives: (i) identifying an optimal configuration of WRF-ARW physical parameterizations for freshwater flux simulation, (ii) evaluating the long-term performance of the optimized configuration in reproducing daily precipitation, its diurnal cycle, and daily PET, and (iii) quantifying the response of freshwater flux components to updated/more realistic LULC datasets and hypothetical LULC scenarios.

Sensitivity experiments indicate that, at a 5-km resolution, the most reliable physical parameterization combines explicit convection (without cumulus parameterization), activation of sst_skin option, the Mellor-Yamada-Nakanishi-Niino Level 2.5 (MYNN2.5) planetary boundary layer (PBL) scheme, and the dynamic vegetation option within the Noah Land Surface Model with Multiparameterization options (Noah-MP). This experiment consistently yields the best overall performance across daily and diurnal cycles of precipitation and daily PET, outperforming alternative schemes. Enabling the sst_skin option reduces precipitation biases and improves the representation of coastal diurnal rainfall peaks, while the MYNN2.5 PBL scheme provides the most balanced performance across precipitation and PET.

Long-term simulations demonstrate that WRF-ARW accurately captures the spatial distribution and seasonal contrast in daily precipitation, with higher rainfall during the rainy season and significantly lower rainfall during the dry season. The dominant early-afternoon rainfall peak is well-reproduced, although rainfall frequency and nighttime precipitation are generally underestimated, resulting in a persistent dry bias relative to Climate Hazard Infrared Precipitation with Stations (CHIRPS), Tropical Rainfall Measuring Mission (TRMM) Multisatellite Precipitation Analysis (TMPA), and station observations. Despite these limitations, the model reliably captures the phase and structure of the diurnal precipitation cycle. WRF-ARW also demonstrates strong capability for simulating daily PET, with good agreement

with Daily Potential Evapotranspiration (DPET) data, the ECMWF fifth-generation reanalysis (ERA5), and station-based references. PET exhibits a systematic negative bias, primarily driven by uncertainties in the 10-m wind speed simulation, but the model successfully reproduces the seasonal evolution and spatial homogeneity of PET, supporting its use for freshwater flux assessment.

Analysis of LULCC impacts reveals that updated/more realistic LULC datasets exert only minor effects on domain-scale precipitation and PET, whereas extreme hypothetical scenarios induce substantial changes, particularly in precipitation timing and PET magnitude. In contrast, AET is highly sensitive to LULCC, with differences primarily controlled by changes in transpiration associated with altered vegetation cover. Representing aquaculture areas as permanent wetlands is found to be more physically defensible than treating them as open water bodies, although current wetland parameterizations in Noah-MP remain simplified.

Using the most realistic observed LULC scenario, the model produces a physically consistent seasonal freshwater flux cycle, closely matching estimates from TMPA and DPET. While LULCC effects on freshwater flux, defined as precipitation minus PET, are negligible at the regional scale, they become critical when freshwater flux is defined as precipitation minus AET, highlighting the dominant role of transpiration.

Overall, this dissertation demonstrates that WRF-ARW, when properly configured, provides a robust tool for assessing long-term freshwater fluxes over the Ca Mau Peninsula under LULCC, offering valuable insights for water resource management and climate impact studies in the Vietnamese Mekong Delta.

Zusammenfassung

Der Süßwasserfluss stellt einen zentralen Steuerungsfaktor für die Nahrungsmittelproduktion, die Funktionsfähigkeit von Ökosystemen sowie die sozioökonomische Stabilität im vietnamesischen Mekongdelta dar, insbesondere auf der Ca-Mau-Halbinsel, die als wichtigste Aquakulturregion Vietnams gilt. In den vergangenen Jahrzehnten haben rasche Landnutzungs- und Landbedeckungsänderungen (Land Use and Land Cover Change, LULCC) die Wechselwirkungen zwischen Landoberfläche und Atmosphäre erheblich verändert und damit die Unsicherheiten bei der regionalen Abschätzung des Süßwasserflusses deutlich erhöht. Ziel dieser Dissertation ist es, die Simulation von Süßwasserflüssen über der Ca-Mau-Halbinsel zu verbessern, indem das Advanced Research Weather Research and Forecasting-Modell (WRF-ARW) mit einer grauzonenspezifischen horizontalen Auflösung von 5 km für den Zeitraum 2007–2016 eingesetzt wird, unter expliziter Berücksichtigung physikalischer Parametrisierungsentscheidungen sowie der Effekte von LULCC.

Der Süßwasserfluss wird als Differenz zwischen Niederschlag und Evapotranspiration quantifiziert, wobei sowohl das Konzept der potenziellen Evapotranspiration (PET) als auch der tatsächlichen Evapotranspiration (AET) herangezogen wird. Die Arbeit verfolgt drei zentrale Zielsetzungen: (i) die Identifikation einer optimalen Konfiguration physikalischer Parametrisierungen im WRF-ARW-Modell für die Simulation von Süßwasserflüssen, (ii) die Bewertung der langfristigen Leistungsfähigkeit dieser optimierten Konfiguration hinsichtlich der Reproduktion des täglichen Niederschlags, seines diurnalen Zyklus sowie der täglichen PET und (iii) die Quantifizierung der Reaktion der einzelnen Komponenten des Süßwasserflusses auf aktualisierte, realistischere Landnutzungsdatensätze sowie auf hypothetische LULC-Szenarien.

Sensitivitätsexperimente zeigen, dass bei einer horizontalen Auflösung von 5 km die zuverlässigste Modellkonfiguration durch eine explizite Darstellung der Konvektion (ohne Kumulusparametrisierung), die Aktivierung der sst_skin-Option, die Verwendung des planetaren Grenzschichtschemas Mellor-Yamada-Nakanishi-Niino der Stufe 2.5 (MYNN2.5) sowie die dynamische Vegetationsdarstellung im Noah-Landoberflächenmodell mit Mehrfachparametrisierung (Noah-MP) erreicht wird. Diese Konfiguration liefert über verschiedene Zeitskalen hinweg – insbesondere für tägliche und tageszeitliche Zyklen von Niederschlag und täglicher PET – die insgesamt beste Modellleistung und übertrifft alternative Parametrisierungsansätze. Die Aktivierung der sst_skin-Option reduziert systematische Niederschlagsabweichungen und verbessert die Darstellung küstennaher diurnaler Niederschlagsmaxima, während das MYNN2.5-Grenzschichtschema eine ausgewogene Simulation sowohl des Niederschlags als auch der PET ermöglicht.

Langzeitsimulationen belegen, dass WRF-ARW die räumliche Verteilung sowie den saisonalen Kontrast des täglichen Niederschlags realistisch erfasst, mit erhöhten Niederschlagsmengen während der Regenzeit und deutlich geringeren Werten in der Trockenzeit. Das dominante Niederschlagsmaximum am frühen Nachmittag wird gut reproduziert, während die Niederschlagshäufigkeit sowie nächtliche Niederschläge tendenziell unterschätzt werden, was zu einem persistierenden Trockenbias im Vergleich zu CHIRPS-, TRMM-TMPA- und stationsbasierten Beobachtungen führt. Trotz dieser Einschränkungen bildet das Modell die Phasenlage und Struktur des diurnalen Niederschlagszyklus zuverlässig ab. Darüber hinaus zeigt WRF-ARW eine hohe Leistungsfähigkeit bei der Simulation der täglichen PET, mit guter Übereinstimmung zu DPET-Datensätzen, der ERA5-Reanalyse sowie stationsbasierten Referenzen. Ein systematischer negativer Bias der PET ist überwiegend auf Unsicherheiten in der Simulation der 10-m-Windgeschwindigkeit zurückzuführen, während die saisonale Entwicklung und die räumliche Homogenität der PET insgesamt gut reproduziert werden.

Die Analyse der Auswirkungen von LULCC zeigt, dass realistische, beobachtungsbasierte Landnutzungsdatensätze nur geringe Effekte auf domänenweite Niederschläge und PET aufweisen, wohingegen hypothetische Extremszenarien substanzielle Veränderungen hervorrufen, insbesondere hinsichtlich des zeitlichen Auftretens des Niederschlags sowie der Größenordnung der PET. Im Gegensatz dazu reagiert die AET äußerst sensitiv auf LULCC, wobei die Unterschiede primär durch Änderungen der Transpiration infolge variierender Vegetationsbedeckung bestimmt werden. Die Darstellung von Aquakulturflächen als permanente Feuchtgebiete erweist sich dabei als physikalisch konsistenter als ihre Behandlung als offene Wasserflächen, wenngleich die derzeitigen Feuchtgebietparametrisierungen im Noah-MP-Modell weiterhin vereinfacht sind.

Unter Verwendung des realistischsten beobachtungsbasierten LULC-Szenarios reproduziert das Modell einen physikalisch konsistenten saisonalen Zyklus des Süßwasserflusses, der eng mit Schätzungen aus TMPA- und DPET-Datensätzen übereinstimmt. Während die Effekte von LULCC auf den Süßwasserfluss, definiert als Niederschlag minus PET, auf regionaler Skala vernachlässigbar sind, gewinnen sie erheblich an Bedeutung, wenn der Süßwasserfluss als Niederschlag minus AET definiert wird, was die dominante Rolle der Transpiration unterstreicht.

Insgesamt zeigt diese Dissertation, dass WRF-ARW bei geeigneter Konfiguration ein robustes Instrument zur Analyse langfristiger Süßwasserflüsse über der Ca-Mau-Halbinsel unter Berücksichtigung von LULCC darstellt und damit eine fundierte Grundlage für wasserwirtschaftliche Anwendungen sowie für Klimafolgenstudien im vietnamesischen Mekongdelta liefert.

Preface

The PhD candidate confirms that the research presented in this thesis contains significant scientific contributions by himself. This thesis reuses material from the following publications:

1. Tran-Anh, D., Fink, A. H., Laux, P., Arnault, J., van der Linden, R., Phan-Van, T., Kunstmann, H. (2025). WRF Gray-Zone Simulations of the Freshwater flux over the Ca Mau Peninsula, Southern Vietnam: Impacts of Planetary Boundary Layer Parameterizations. Atmospheric Research. Submitted December 2025.

The abstract and Chapters 1, 3, 4, 5, and the appendix reuse material from Tran-Anh et al. (2025), which was submitted to the Elsevier journal Atmospheric Research. Copyright in this work may be transferred without further notice.

The research leading to these results was supported by a KAAD PhD Fellowship. The research proposal for this project was written by Andreas H. Fink and Roderick van der Linden. The analyses and result interpretation by Tran-Anh et al. (2025) were solely performed by the candidate, who also wrote the text with advice from Andreas H. Fink and comments from all co-authors during manuscript preparation. The candidate confirms that appropriate credit has been given within the thesis, where references to the publications of others have been made.

Contents

Acronyms

ACM2 Asymmetric Convective Model version 2

AET Actual Evapotranspiration

Boulac Bougeault–Lacarrère

CCAM Conformal Cubic Atmospheric Model

CCI Climate Change Initiative

CHIRPS Climate Hazard Infrared Precipitation with Stations

CPC Climate Prediction Center

DPET Daily Potential Evapotranspiration

ENSO El Niño-Southern Oscillation

ERA5 ECMWF fifth-generation reanalysis

ET_0 Reference Evapotranspiration

FVEG Vegetation Fraction

GEO European Geoland

GPM IMERG The Integrated Multi-satellite Retrievals for Global Precipitation Measurement

GLEAM Global Land Evaporation: Amsterdam Methodology

IGBP International Geosphere-Biosphere Program

JRA-55 Japanese 55-year Reanalysis Project

LAI Leaf area index

LULC Land-use/Land-cover

LULCC Land-use and Land-cover Change

MCD12Q1 MODIS Collection 6 Land Cover Type Product

MERRA-2 Modern-Era Retrospective Analysis for Research and Application 2

MODIS Moderate Resolution Imaging Spectroradiometer

MYJ Mellor–Yamada–Janjic

MYNN2.5 Mellor-Yamada-Nakanishi-Niino Level 2.5

NCHMF National Center for Hydro-Meteorological Forecasting of Vietnam

NOAA National Oceanic and Atmospheric Administration

Noah-MP Noah Land Surface Model with Multiparameterization options

PBIAS Percent Bias

PBL Planetary Boundary Layer

PET Potential Evapotranspiration

PR Public rain gauge

RCM Regional Climate Model

REA Reliability Ensemble Averaging

RMSE Root Mean Square Error

RRTM Rapid Radiative Transfer Model

SST Sea Surface Temperature

SSKT Sea Surface Skin temperature

TMPA TRMM Multisatellite Precipitation Analysis

USGS United States Geological Survey

WMO World Meteorological Organization

WRF Weather Research and Forecasting

WRF-ARW Advanced Research WRF

WSM6 WRF Double Moment 6-class

YSU Yonsei University

1. Introduction

The Mekong Delta is one of the world's three largest deltas (Coleman et al., 2003). The Vietnamese part of the Mekong Delta was home to 17 million people in 2020. It plays a crucial role in Vietnam's socioeconomic development, supplying 55% of the country's rice and other agricultural products (General Statistics Office of Vietnam, 2023). While playing a central role in the national economy, the delta is particularly exposed to relative sea-level rise owing to its exceptionally low elevation, which averages around 0.8 m above mean sea level (Minderhoud et al., 2019). This vulnerability is further exacerbated by land subsidence, a widespread process affecting more than half of the world's major deltas, where subsidence rates often surpass the magnitude of global mean sea-level rise (Syvitski et al., 2009). From a global perspective, the Vietnamese Mekong Delta is identified as one of the regions experiencing the greatest impacts. Recent observational analyses and modelling investigations consistently indicate pronounced rates of land subsidence across the Vietnamese Mekong Delta (e.g., Erban et al., 2014; Minh et al., 2015; Minderhoud et al., 2017). Notably, reported subsidence rates in this region exceed global mean sea-level rise by approximately an order of magnitude (Erban et al., 2014). A major problem is the land subsidence mentioned, which has been affecting the Vietnamese Mekong Delta for more than 15 years. It has been mainly attributed to the excessive extraction of groundwater (e.g., Minderhoud et al., 2017; Erban et al., 2014), which might be accelerated by additional loading due to the recent intensive construction activity (Minderhoud et al., 2018). Results from a coupled hydrogeological and geomechanical modelling approach indicate that the Vietnamese Mekong Delta underwent mean land subsidence of roughly 1.1 cm yr^{-1} during 1990–2015, largely driven by intensive groundwater extraction (Minderhoud et al., 2017). In heavily exploited zones, subsidence rates were substantially higher, locally exceeding 2.5 cm yr^{-1}. Over this period, demand for groundwater, the primary source of freshwater in the Vietnamese Mekong Delta (Wagner et al., 2012), intensified due to Vietnam's robust economic growth. Land subsidence poses several bioenvironmental challenges, including saltwater intrusion into surface and groundwater, a lack of clean drinking water during dry periods, and increased vulnerability to storm-surge-related flooding.

Because of these anthropogenic threats, solutions need to be explored to at least reduce the amount of groundwater being abstracted in order to reduce or even stop the high rates of subsidence. One solution to reduce pressure on groundwater resources is to utilize rainwater for irrigation and potentially as a source of drinking water, as outlined in the ViWAT Engineering proposal. This requires collecting, storing, and possibly treating rainwater. Additionally, its availability during the dry season and periods of drought must be ensured. The scientific challenge is to quantitatively assess the spatiotemporal

variability of the difference between precipitation and evapotranspiration or the freshwater flux over the Vietnamese Mekong Delta.

To address this issue, we first need to determine the precipitation over the Vietnamese Mekong Delta. The regional rainfall regime exhibits a pronounced seasonal contrast, characterized by a dry period extending from November to April and a rainy season occurring between May and October (Nguyen et al., 2014a). This results in a surplus of available water during the rainy season, but a deficit during the dry season. Additionally, rainfall during the rainy season is often convective, meaning that very high amounts of precipitation occur over a short period rather than a large area. The El Niño-Southern Oscillation (ENSO) exerts a significant control on interannual rainfall variability across the Vietnamese Mekong Delta. While excess rainfall occurs during La Niña events (Gobin et al., 2016), dry season droughts are associated with El Niño events; a recent example with strong impacts is the 2015/2016 Mekong Delta drought (Nations, 2016). To evaluate precipitation, this study utilizes observation data from fairly dense ground-based rain gauge networks, along with several satellite-derived rainfall datasets.

A significant challenge is determining actual evapotranspiration (AET), i.e., the sum of evaporation from soil and leaves and transpiration from plants. Although the Vietnamese Mekong Delta hosts a relatively dense network of precipitation gauges, no station directly measures AET. Approximately six stations in the Vietnamese Mekong Delta measure potential evaporation using World Meteorological Organization Class A pans; however, these measurements are based on evaporation over a ventilated water surface, and it is not possible to infer AET. To overcome this observational limitation, the present study focuses on the other concept of evapotranspiration, specifically potential evapotranspiration (PET), which is defined as the maximum rate of evaporation under given climatic conditions with an excess of soil moisture (Allen et al., 1994). PET has become increasingly prominent in freshwater flux research across Asia (e.g., Ta et al., 2018; Chen et al., 2020; Das et al., 2022). The use of PET over the Vietnamese Mekong Delta is supported by the availability of several PET observational products, including in-situ estimates, satellite-derived datasets, and model-derived datasets suitable for validation. First, PET measurements derived from the GGI-3000 evaporimeter, an instrument formerly standard across the Soviet Union, measure daily open-water evaporation and are still maintained at two stations in the Mekong Delta. Second, PET can be estimated empirically using the Penman–Monteith method (Allen et al., 1998), which requires station-based measurements of air temperature, humidity, sunshine duration, and 10-m wind speed at three sites. Third, satellite- and model-derived PET products provide spatially continuous fields that complement sparse ground observations. These include the Moderate Resolution Imaging Spectroradiometer MOD16 product (MODIS; Mu et al., 2011), ECMWF fifth-generation reanalysis (ERA5; Hersbach et al., 2020), the daily aggregation PET dataset, which is computed using meteorological variables output from the ERA-Land dataset (DPET; Singer et al., 2021), and the Global Land Evaporation Amsterdam Methodology dataset (GLEAM; Martens et al., 2017). While uncertainties inherent to each dataset remain unavoidable, their combination enables narrowing down the range of PET values, forming a robust basis for PET validation and subsequent freshwater flux analysis in the

Vietnamese Mekong Delta.

Numerical atmospheric models provide potential alternatives to assess both components of the freshwater flux over the Vietnamese Mekong Delta, which consist of precipitation and PET. As computing power develops, kilometre-scale simulations of regional climate models, namely convection-permitting models, are increasingly prevalent. Convection-permitting models eliminate the need to parameterize atmospheric deep convection, thereby mitigating a significant source of uncertainty and error in conventional regional climate models (Prein et al., 2015; Schär et al., 2020). However, conducting such simulations remains computationally challenging due to the limitations of our current resources. Despite these constraints, high-resolution simulations (finer than 25 km) are essential for producing more accurate assessments of freshwater flux across the Vietnamese Mekong Delta. To balance computational efficiency and model performance, gray-zone resolutions (approximately 4–10 km) are widely employed for long-term regional climate simulations over Asia (e.g., Chen et al., 2018; Taraphdar and Pauluis, 2021; Hoang-Cong et al., 2022; Zhou et al., 2023). It is noteworthy that these resolutions are insufficient to explicitly resolve individual convective clouds yet too fine to fully rely on convective parameterization (Taraphdar and Pauluis, 2021; Taraphdar et al., 2021). As highlighted by Taraphdar et al. (2021), gray-zone simulations can perform as well as convection-permitting simulations when appropriate physical parameterizations are employed to capture synoptic and mesoscale processes. This insight suggests that conducting freshwater flux simulations for the Vietnamese Mekong Delta at gray-zone resolution, with appropriately chosen physics schemes, constitutes a scientifically robust and computationally feasible strategy for this study. Additionally, land surface models, which are essential components of climate models, have been developed to capture the exchanges of water, energy, and momentum between the atmosphere and the land surface, thereby providing more precisely simulated PET (Pal and Sharma, 2021). From a regional perspective, the Vietnamese Mekong Delta constitutes a key hotspot of anthropogenic land-use and land-cover change (LULCC) in Southeast Asia. (Giri et al., 2003). By incorporating updated land-use and land-cover (LULC) datasets derived from remote-sensing products into land surface models, regional climate models (RCMs) can therefore more accurately represent land–atmosphere interactions, ultimately enhancing the reliability of simulated freshwater flux components across the region.

My study contributes to improving the assessment of freshwater flux over the Vietnamese Mekong Delta, particularly under the constraints of limited PET observations and the absence of AET measurements. To address this objective, simulations are performed using the Advanced Research Weather Research and Forecasting model (WRF-ARW) at gray-zone resolution, complemented by a series of sensitivity experiments designed to identify optimal physical parameterization schemes and an appropriate land-use and land-cover (LULC) dataset for accurately representing freshwater flux components over the Vietnamese Mekong Delta. The thesis is structured as follows: Section 2 presents the State of the Art and Literature Review; Section 3 outlines the Objectives and Structure of the Work; Section 4 describes the Data and Methods; Sections 5–7 provide the Results; and Section 8 concludes with a summary and outlook.

2. State of the art / Literature review

This section provides an overview of the climatic characteristics and land-use/land-cover conditions of the Vietnamese Mekong Delta, along with recent trends in the two components of the freshwater flux: precipitation and evapotranspiration.

2.1. Climate over the Vietnamese Mekong Delta

The Vietnamese Mekong Delta, characterized by the populous floodplains of the Mekong River, offers the most favorable environmental (edaphic, climatic) conditions for aquaculture and rice cropping in Vietnam (Wilder and Phuong, 2002; Ha et al., 2013). The region's agricultural productivity is heavily dependent on water resources, which are influenced by climate variability at various temporal scales, most notably the seasonal scale, as well as by interannual and multiannual variations.

Due to its geographic location, Vietnam's seasonal climate is largely influenced by the Indo-Asian monsoon system (Wang, 2006). The rainy season in Vietnam typically runs from May to October, coinciding with seasonal shifts in the Intertropical Convergence Zone and the subtropical ridge from north to south (Nguyen et al., 2014a). In southern Vietnam, including the Vietnamese Mekong Delta and the Central Highlands, the peak rainy months occur between August and October, attributed to warm, humid marine airflow blowing from the Bay of Bengal (Nguyen et al., 2014b). Based on the observational data for the period 1979–2019, Pham-Thanh et al. (2020) showed that the mean annual precipitation over the Vietnamese Mekong Delta ranges from approximately 1300 to 2400 mm, with the highest totals observed along the western coastal zones (Fig. 2.1a). The rainy season in the Vietnamese Mekong Delta is well-defined, occurring from May to October, with a peak in August (Nguyen et al., 2014a), and contributes more than 90% of the annual rainfall total (Lee and Dang, 2019; Nguyen et al., 2022). This pronounced seasonality in precipitation results in a marked contrast between water abundance during the rainy season and water scarcity during the dry season. Such an imbalance poses significant challenges for water resources management, particularly for irrigation and agricultural production, as prolonged dry season water deficits can adversely affect crop yields and food security in the region (Kontgis et al., 2019; Dang et al., 2020a). Beyond the pronounced seasonal cycle, the rainfall regime of the Vietnamese Mekong Delta is also strongly characterized by a distinct diurnal cycle, with precipitation consistently peaking during the afternoon hours across all seasons (Huang et al., 2025).

The seasonal climate of Vietnam is heavily influenced by changing sea surface temperature (SST)

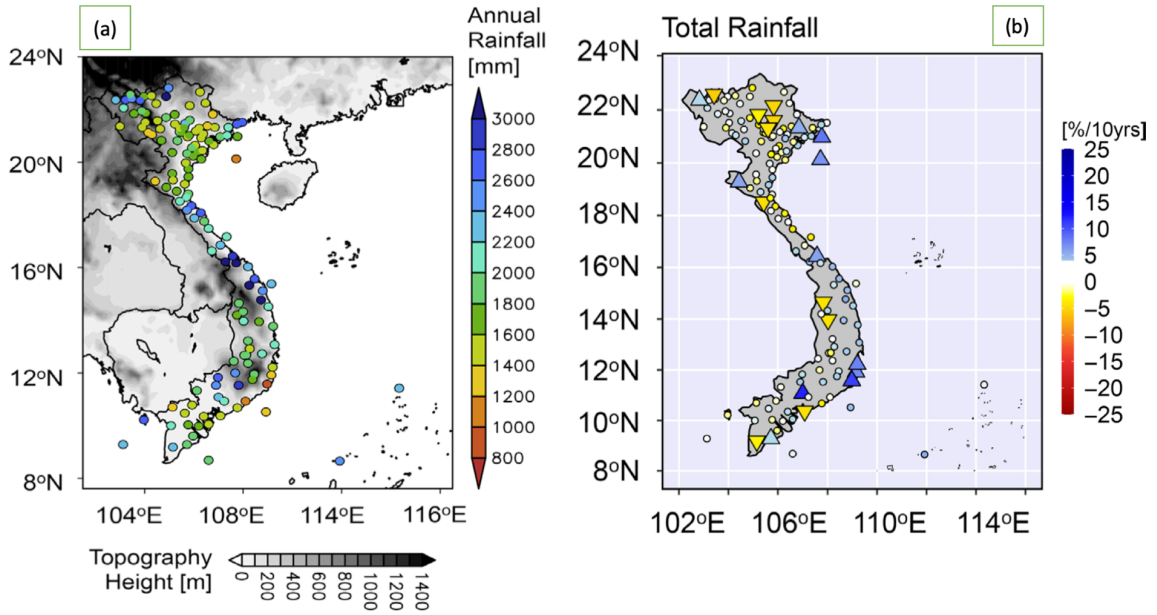

Figure 2.1.: Spatial distribution of (a) climatological mean annual rainfall and (b) Sen's slope–based trends in total annual precipitation derived from observations at 138 meteorological stations across Vietnam for the period 1979–2019, adapted from Pham-Thanh et al. (2020). Trend magnitudes are reported as percentage changes per decade relative to the 1979–2019 climatological mean. Circular markers indicate trends that are not statistically significant, whereas triangular markers denote statistically significant trends at the 5% confidence level based on the Mann–Kendall test.

patterns in the Pacific Ocean, modulated by the ENSO, Pacific Decadal Oscillation, and Interdecadal Pacific Oscillation phenomena (Nguyen et al., 2014a; Gobin et al., 2016; Duc et al., 2018). Among these climate drivers, ENSO and the Interdecadal Pacific Oscillation are most dominant in the southern part, while the Pacific Decadal Oscillation shows the largest influence on rainfall in the central part of Vietnam. Duc et al. (2018) utilized monthly rainfall data from 172 weather stations across Vietnam during 1975–2006 to examine the teleconnection between ENSO and regional rainfall variability. This relationship was found to be more pronounced in the central and southern regions rather than in the northern regions, and it is particularly more significant during the boreal spring and weaker in winter. More recently, focusing specifically on the Vietnamese Mekong Delta, Dang et al. (2020b) analyzed rainfall data from 102 stations (1989–2017) across coastal provinces in the Mekong Delta, showing how ENSO affects the onset/cessation dates of the rainy season, as well as rainfall amounts during the dry season. They indicated that La Niña years are generally associated with earlier rainy season onset, later rainy season cessation, and higher rainfall totals, including dry season amounts that often exceed 100 mm. In contrast, El Niño years tend to produce reduced rainfall and shorter rainy seasons, with dry-season totals typically below 100 mm.

Intraseasonal oscillation also has a significant role in modulating rainfall in Southern Vietnam (Van der Linden et al., 2016; Truong and Tuan, 2018, 2019), characterized by two predominant oscillation modes: 10–20 days and 20–60 days. This modulation is associated with tropical climate drivers,

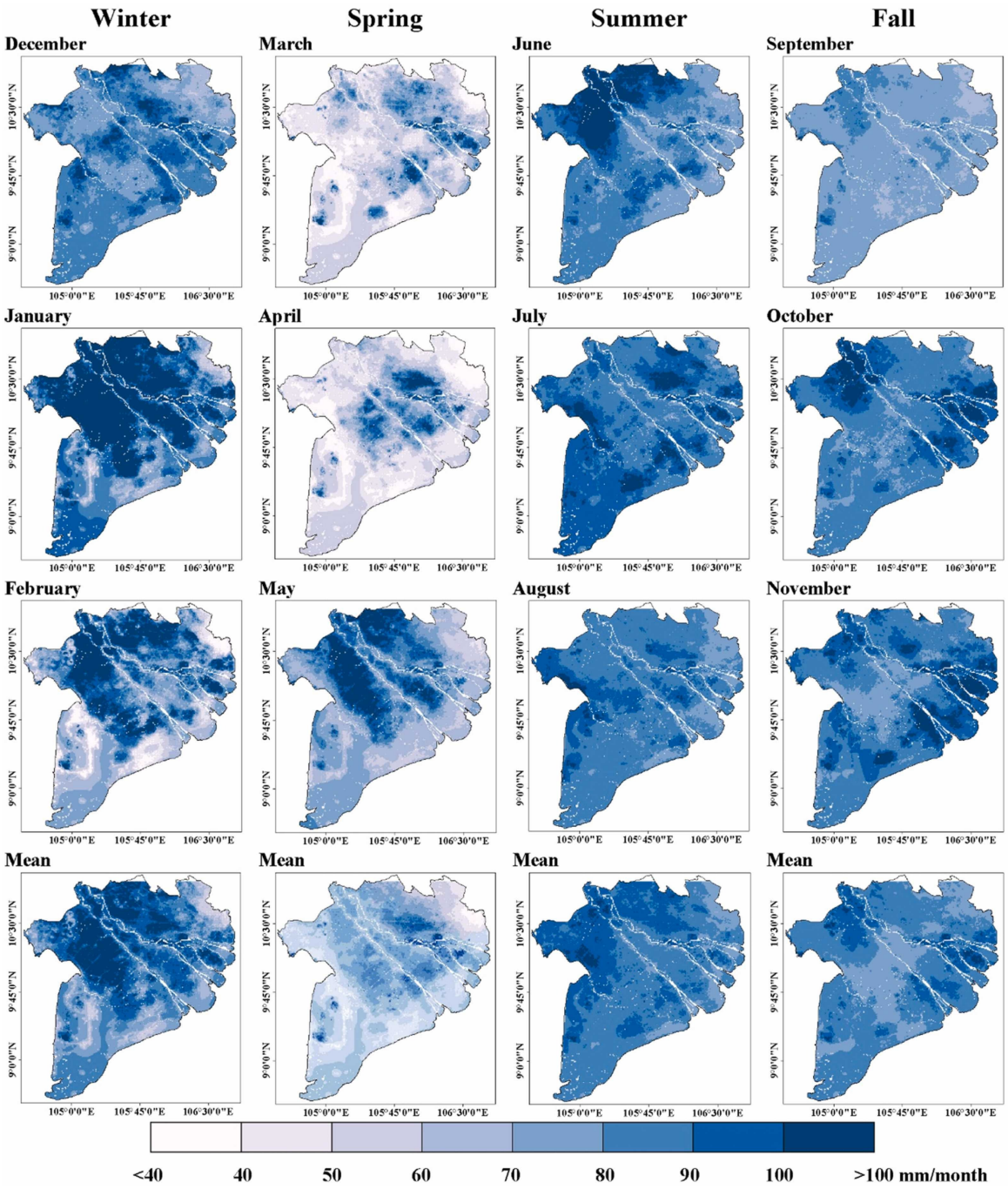

Figure 2.2.: Mean AET climatology at monthly and seasonal scales based on MODIS products covering 2001–2018 over the Vietnamese Mekong Delta (Mondal et al., 2022). Monthly AET distributions are displayed in the top rows, whereas seasonal means are provided in the bottom row. Columns correspond to individual seasons, ordered from winter (left) to fall (right).

including the Madden–Julian Oscillation (Madden and Julian, 1972) and convectively equatorial waves, such as Kelvin and Rossby waves. The variability of daily precipitation is closely linked to the evolving phases of the MJO and equatorial wave activity, with increased frequencies of intense rainfall events during their active (wet) phases (Van der Linden et al., 2016). Moreover, interactions among different wave modes can further amplify regional rainfall anomalies, leading to pronounced wet or dry conditions depending on the phases of these modes. In alignment with these findings, Truong and Tuan (2018, 2019) demonstrated that rainfall variability in southern Vietnam is influenced by distinct intraseasonal modes, with variability on the 10–20 days timescale is closely associated with a tropical Indian Ocean mode expressed as equatorial Rossby waves (Truong and Tuan, 2018), while variability on the 20–60 days timescale is predominantly driven by MJO activity (Truong and Tuan, 2019).

Regarding evapotranspiration, the limited availability of reliable in situ observations over the Vietnamese Mekong Delta has constrained comprehensive assessments. Consequently, existing studies have predominantly relied on satellite-derived and model-derived products of AET or PET (e.g., Hu and Mo, 2021; Chen et al., 2022; Mondal et al., 2022; Pan et al., 2022). In this context, Mondal et al. (2022) provided the first regional-scale characterization of AET over the Vietnamese Mekong Delta using the MODIS MOD16 product (Mu et al., 2011) for the period 2001–2018. Their analysis presented the spatial distribution of mean AET across the delta (Fig. 2.2), revealing distinct features compared to precipitation patterns. In contrast to the pronounced seasonal asymmetry observed in rainfall, AET exhibits a relatively weak seasonal contrast between the dry and rainy seasons. The lowest AET values occur during March and April, when most areas of the Vietnamese Mekong Delta have less than 60 mm of AET. Conversely, the highest AET values are observed in January, with the centre portion almost entirely covered by approximately 100 mm. Furthermore, evapotranspiration displays greater spatial homogeneity in summer and autumn than in spring and winter.

Overall, the rainfall regime of the Vietnamese Mekong Delta is characterized by a pronounced seasonal contrast between the dry and rainy seasons, strongly modulated by ENSO and intraseasonal oscillations. In contrast, AET displays a comparatively weak seasonal contrast, with maximum values typically occurring in January and minimum values in March and April.

2.2. Land-use/Land-cover over the Vietnamese Mekong Delta

The increasing availability of long-term remote sensing data, enhanced computational resources, and advances in machine–learning–based classification techniques have enabled a new generation of cost-effective LULC mapping. Using multi-source satellite imagery in combination with a random forest classification framework, Phan et al. (2021) provided the first comprehensive national-scale assessment of annual LULC dynamics across mainland Vietnam over the period 1990–2020. Their results reveal substantial LULCC across the country over the past three decades, largely driven by socio-economic

development policies and accelerated economic growth. Spatially, the most pronounced transformations occurred in northern and southern Vietnam, with especially rapid changes observed in the western north and the southernmost regions, including the Vietnamese Mekong Delta. Quantitatively, the study documented a marked decline in forested areas (approximately 19940 km^2) and wetlands (around 1914 km^2), while aquaculture and urban land expanded dramatically, increasing by roughly threefold and tenfold, respectively, over the study period. In terms of changing patterns, rapid urbanization, the uncontrolled expansion of agricultural and aquaculture activities, particularly in the Vietnamese Mekong Delta, and persistent forest loss associated with the conversion to rice paddies, cropland, and barren land were identified as the dominant change processes.

The Vietnamese Mekong Delta is the most important region in southern Vietnam in terms of agricultural and aquacultural production, serving both domestic consumption and export to global markets (General Statistics Office of Vietnam, 2023). Over recent decades, substantial efforts have been made to detect LULCC across the Vietnamese Mekong Delta, either at the delta scale (e.g., Li et al., 2020b; Phan et al., 2021; Vu et al., 2022) or within specific districts (e.g., Tran et al., 2015; Hauser et al., 2017). At the district scale, Tran et al. (2015) conducted a comprehensive analysis of the spatiotemporal dynamics of LULC in the Tran Van Thoi district, located in the southern part of the Vietnamese Mekong Delta, for the period 1973–2011. Their results revealed pronounced increases in aquaculture ponds and built-up areas, accompanied by substantial declines in bare land and mangrove forest coverage. In a further investigation focusing on the Ca Mau Peninsula, Hauser et al. (2017) examined LULCC in Ngoc Hien District, which hosts the largest mangrove forest in Vietnam, over the period 2004–2013. Their analysis revealed an average net annual decline in mangrove forest area of approximately 0.34%, marked by a phase of deforestation between 2004 and 2009, followed by a period of afforestation from 2009 to 2013. Importantly, the study demonstrated that changes in mangrove forest cover were strongly and inversely correlated with the expansion of aquaculture land-use. At the delta scale, Li et al. (2020b) examined land-use dynamics across the Vietnamese Mekong Delta during 1975–2015 using Landsat imagery. Their analysis showed that cropland remained the dominant land-use type throughout the study period, despite a net reduction of approximately 13.4%, with most of the converted area transitioning to aquaculture. Notably, aquaculture emerged as the second-largest land-use category after cropland since 1995, accounting for approximately 19% of the total delta area in 2015. Consistent with these findings, Phan et al. (2021) demonstrated that the rapid and largely uncontrolled expansion of aquaculture, particularly shrimp farming, has been a major driver of LULCC across the Vietnamese Mekong Delta since the early 2000s, with the most pronounced changes occurring in coastal regions.

More recently, Vu et al. (2022) provided a comprehensive assessment of LULCC across the Vietnamese Mekong Delta for the period 2000–2020 using MODIS satellite data. Their results indicate that during this period, rice cultivation remained the dominant land-use type, accounting for approximately 40–46% of the total delta area, while aquaculture systems (including shrimp–rice farming and inland aquaculture) represented roughly 10–20%. Rice cultivation was primarily concentrated in the upper

delta and along main rivers, where the rapid expansion of triple rice cropping between 2000 and 2017 resulted in a substantial increase in cultivated area. In contrast, aquaculture activities were primarily concentrated in the Ca Mau Peninsula, encompassing Kien Giang, Ca Mau, and Bac Lieu provinces, where the aquaculture area increased more gradually, from approximately 619000 hectares in 2001 to about 856000 hectares in 2020. The land-use patterns for the years 2000 and 2020, as presented by Vu et al. (2022) (Fig. 2.3), clearly illustrate the marked expansion of aquaculture across the Ca Mau Peninsula over the past two decades. In particular, large areas previously classified as double-rice cropping land-use type (yellow color) and other land-use types (brown color) were converted to inland aquaculture (blue color), highlighting the profound LULCC in this sub-region of the delta.

Overall, two dominant LULCC trends characterize the Vietnamese Mekong Delta over recent decades: (i) the sustained expansion of aquaculture in the Ca Mau Peninsula, which is largely at the expense of cropland and mangrove ecosystems; and (ii) the rapid intensification of rice cultivation in the upper zone driven by the widespread adoption of triple rice cropping systems. These processes highlight the significant impact of agricultural intensification and aquaculture development on land-use dynamics throughout the Vietnamese Mekong Delta.

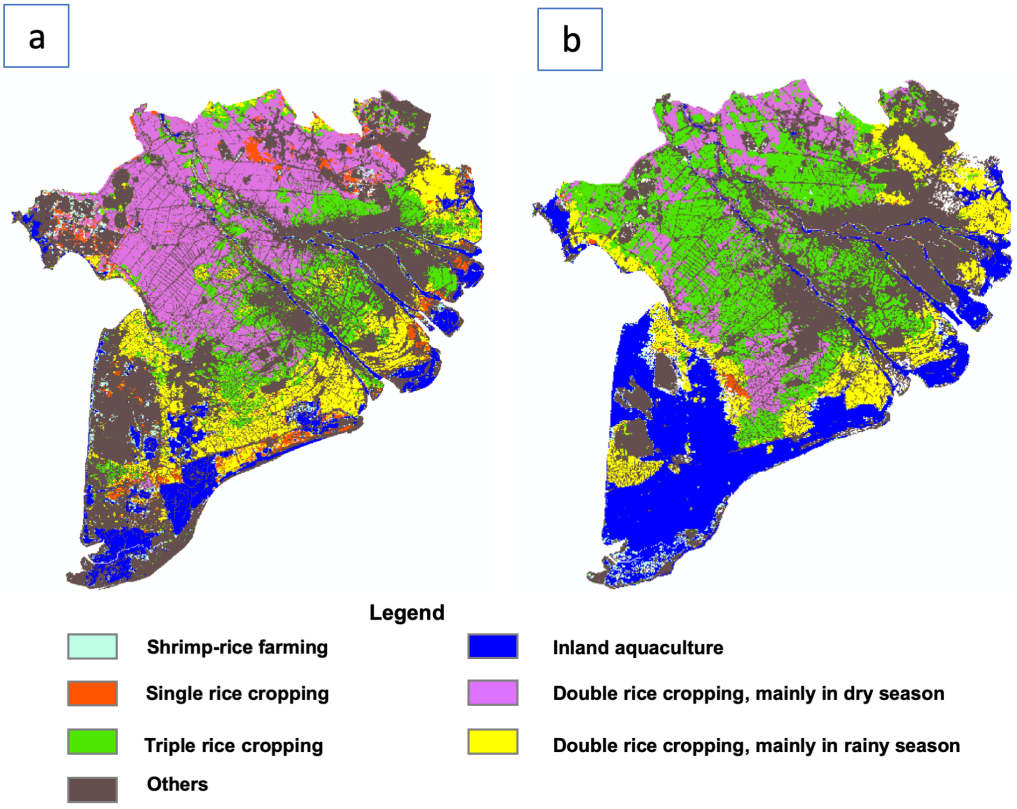

Figure 2.3.: Land-use detection in the Vietnamese Mekong Delta in (a) 2000 and (b) 2020, published by Vu et al. (2022)

2.3. Observed trend in precipitation and evapotranspiration over the Vietnamese Mekong Delta

As the centre hub of agriculture and aquaculture, the Vietnamese Mekong Delta is especially sensitive and prone to the impacts of changing rainfall and evapotranspiration characteristics (Minh et al., 2025). This highlights the urgent need for a robust understanding of rainfall and evapotranspiration trends over recent decades. To date, numerous studies on rainfall trend detection have been published using observational data from in situ stations over different periods. Most of them use the Sen's Slope estimator (Sen, 1968) and Mann-Kendall tests (Kendall, 1975), or modified versions of the Mann-Kendall tests (Hamed and Rao, 1998), to assess the magnitude and statistical significance of observed trends.

In one of the earliest and most comprehensive national-scale assessments, Pham-Thanh et al. (2020) examined long-term trends in annual precipitation and a suite of precipitation extreme indices across Vietnam for the period 1979–2019 (Fig. 2.1b). Their findings indicate that, within the Vietnamese Mekong Delta, statistically significant trends were detected at only two stations: Ca Mau, which exhibited a declining trend of -1.77% per decade, and Bac Lieu, which showed an increasing trend of $+2.19\%$ per decade. In contrast, the majority of stations across the delta displayed weak, statistically insignificant trends. Similar conclusions were reached by Dang et al. (2020b), who analyzed annual precipitation records from 104 rain gauges spanning 1989 to 2017. Their results suggest that no coherent regional-scale trend could be identified, as precipitation trends varied considerably among stations and lacked spatial consistency. More recent evidence reinforces these findings. Using observational data from 14 stations, Dong Phuong et al. (2025) reported that trends in annual rainfall over the Vietnamese Mekong Delta were generally weak and statistically insignificant.

Notably, a consistent declining trend was observed at Ca Mau station across all aforementioned studies. Further investigations by Minh et al. (2024, 2025) provide additional insights into this decline, demonstrating that it occurs in both the wet and dry seasons, with particularly pronounced reductions during specific months, including June and August. These findings highlight Ca Mau as a localized hotspot of rainfall decline within an otherwise heterogeneous regional pattern.

Beyond annual precipitation, several studies have examined trends in extreme rainfall over the Vietnamese Mekong Delta. Lee and Dang (2020) analyzed extreme rainfall characteristics over a 32-year period (1984–2015) using three indices: the number of days with daily rainfall exceeding 20 mm (R20), 50 mm (R50), and 100 mm (R100). Their results indicate that R20 and R50 exhibited declining trends at most stations located in coastal provinces, whereas slight increasing trends were observed at some inland stations. Complementing these findings, Dong Phuong et al. (2025), based on R10 and R20 indices for the period 1978–2022, identified increasing trends during the earlier sub-period (1978–1994), followed by predominantly declining trends during 1995–2022 across nearly all stations. Consistent with results for annual rainfall, Ca Mau station displayed a persistent downward trend in extreme rainfall indices throughout the entire study period, underscoring the robustness of this trend.

In addition to annual rainfall and extreme rainfall, other characteristics of the rainfall regime have also been investigated. Dang et al. (2020b) found that the rainy season starts earlier, ends later, and consequently lasts longer in the western coastal zone of the Mekong Delta. Moreover, ENSO was found to exert a significant influence on rainfall characteristics, particularly the onset, cessation dates, and the length of the rainy season.

While there is a large volume of research available for precipitation, considerably fewer studies have examined long-term trends in evapotranspiration and its related definitions, including AET, PET, and reference evapotranspiration (ET_0) in the Vietnamese Mekong Delta. This research gap is largely attributable to the limited availability of long-term observational data that can serve as reliable references for evapotranspiration analysis.

One of the earliest and most comprehensive investigations was conducted by Luong (2021), who analyzed ET_0 trends across Southern Vietnam using observational data from 40 meteorological stations for the period 1977–2018, while also examining the influence of ENSO on ET_0 variability. The trend analysis indicates a seasonal contrast in the ET_0 trend, with increasing trends observed during the rainy season and decreasing trends during the dry season. Notably, the increasing trend in the rainy season was more distinct and statistically robust than the corresponding changes in the dry season. At the annual scale, ET_0 exhibited an overall upward tendency, with a mean increase of approximately 0.59 ± 0.32 mm yr^{-1}. Regarding ENSO influences, this author demonstrated that ENSO exerts a pronounced impact on ET_0 in the Vietnamese Mekong Delta, particularly during October to May. During these months, the difference in mean daily ET_0 between El Niño and La Niña phases was estimated to be approximately 0.34 mm yr^{-1}.

More recently, Mondal et al. (2022) examined long-term trends in AET over the Vietnamese Mekong Delta using the MODIS MOD16 product for the period 2001–2018. The spatial distribution of monthly AET trends is illustrated in Fig. 2.4. Specifically, decreasing trends were observed during May and July, as well as from September to December. In contrast, a strong increasing trend in AET, exceeding 3 mm yr^{-1}, was observed during the dry periods from December to April. An examination of spatial patterns further shows that AET trends exhibit greater spatial coherence in summer and autumn than in winter and spring. In particular, the months of May and October were characterized by extensive areas experiencing declining AET trends of approximately 2–3 mm yr^{-1}. Conversely, February, March, and April displayed widespread positive trends, with AET increases of nearly 3 mm yr^{-1} across large portions of the Mekong Delta.

Taken together, the literature indicates that long-term annual rainfall trends in the Vietnamese Mekong Delta are generally weak and spatially heterogeneous, with the notable exception of Ca Mau station, which consistently exhibits a declining trend. In parallel, AET exhibits a widespread increasing trend during the late dry-season months, specifically from February to April.

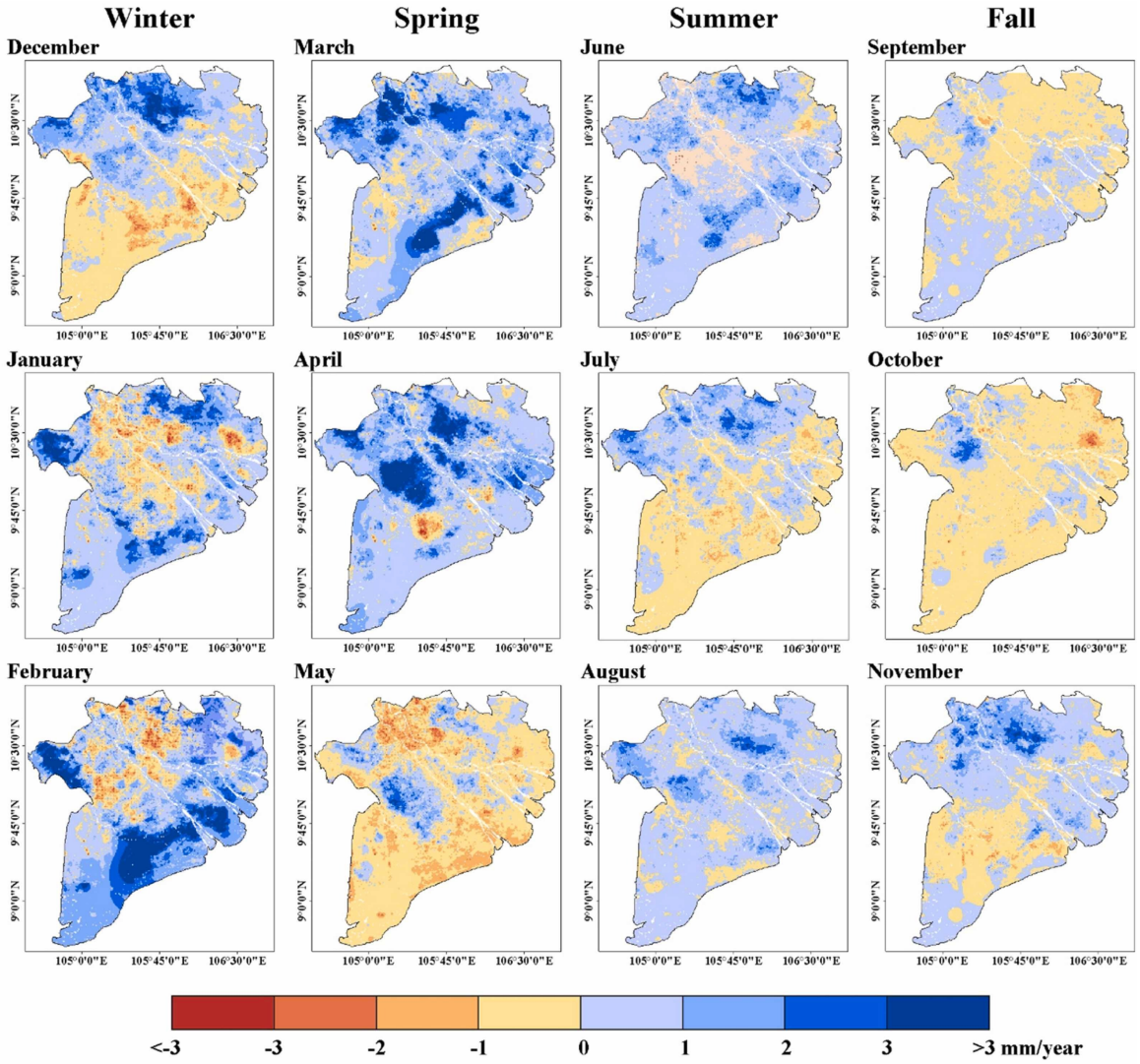

Figure 2.4.: Monthly and seasonal trends in AET based on MODIS products covering 2001–2018, following Mondal et al. (2022). Monthly trend maps are shown in the upper rows, whereas seasonal trend maps are provided in the bottom row. Columns correspond to individual seasons, arranged from winter (left) to fall (right).

2.4. Using regional climate models to simulate the freshwater flux over the Vietnamese Mekong Delta

2.4.1. Impact of the physical parameterization scheme on the freshwater flux simulation at gray-zone resolution

RCMs provide one of the most effective tools for simulating the climate system, in general, and freshwater flux, in particular, at regional scales. Due to their high spatial resolution, RCMs are able to capture land–atmosphere interactions and represent regional forcings, such as large water bodies, surface vegetation, and complex topography, that exert significant influence on local climate (Giorgi, 1990; Xuejie et al., 2001). Available studies using RCMs have been documented to simulate precipitation over Viet-

nam in general (e.g., Phan et al., 2009; Nguyen et al., 2014b), and particularly within the Vietnamese Mekong Delta (e.g., Jiang et al., 2019; Sun et al., 2021a; Hoang-Cong et al., 2022; Fu et al., 2023; Trinh-Tuan et al., 2025).

Nevertheless, significant uncertainties and systematic biases persist in reproducing rainfall patterns in these regions. Phan et al. (2009) applied the RegCM3 model to examine the variations of surface climate variables at seasonal and interannual scales over Vietnam during 1991–2000. Their results indicate that RegCM3 exhibits pronounced dry biases during the rainy season and systematically overestimates annual mean precipitation over southern Vietnam, including the Vietnamese Mekong Delta. Similarly, Nguyen et al. (2014b) employed the Conformal Cubic Atmospheric Model (CCAM) to evaluate mean rainfall patterns and interannual variability for the period 1979–2001. While CCAM satisfactorily reproduces the climatological mean and spatial distribution of rainfall, it performs less well at capturing interannual variability, showing better skill over northern and central Vietnam but with a clear overestimation of rainfall variability in southern Vietnam. More recently, Hoang-Cong et al. (2022) employed the RegCM model version 4.7, driven by boundary conditions from the European Community Earth System Model, to simulate rainfall over parts of Vietnam and the Lower Mekong Basin for the period 1986–2005, using both 25-km and gray-zone 5-km resolutions. Their results show that the model generally captures the large-scale spatial distribution of climatological rainfall, particularly the pronounced east–west contrast during the winter season. However, the convection-permitting 5 km experiment does not exhibit clear improvements in simulating mean or extreme rainfall relative to the coarser 25 km simulation, suggesting that increasing horizontal resolution alone is insufficient to substantially reduce rainfall biases. Figure 2.5, published by Hoang-Cong et al. (2022), presents a comparative analysis of annual and seasonal mean rainfall over a region of Vietnam that includes the Vietnamese Mekong Delta for the period 1986–2005. The comparison includes simulations from a global climate model, an RCM at 25 km resolution, and a convection-permitting RCM at 5 km resolution, alongside observations from the Climate Hazards Group InfraRed Precipitation with Station data (CHIRPS) dataset.

These aforementioned RCMs studies have predominantly employed horizontal resolutions ranging from 20 to 54 km, which are sufficient to resolve large-scale monsoon circulations but inadequate for mesoscale convective systems typical of the delta (Prein et al., 2015; Giorgi et al., 2016). Gray-zone simulations, therefore, have served as an alternative to long-term rainfall modelling, balancing computational efficiency and model performance. Given that precipitation represents a primary component of the freshwater flux, alongside PET, accurate rainfall simulation at gray-zone resolution through the optimization of physical parameterizations is imperative for producing reliable assessments of the freshwater flux over the Vietnamese Mekong Delta.

Among physical parameterizations, planetary boundary layer (PBL) parameterizations play a pivotal role in regulating the exchange of momentum, heat, and moisture between the land surface, ocean, and atmosphere, thereby exerting a decisive influence on the simulation of low-level winds, cloud formation, and thermodynamic profiles (Garratt, 1994). Precipitation exhibits pronounced sensitivity to

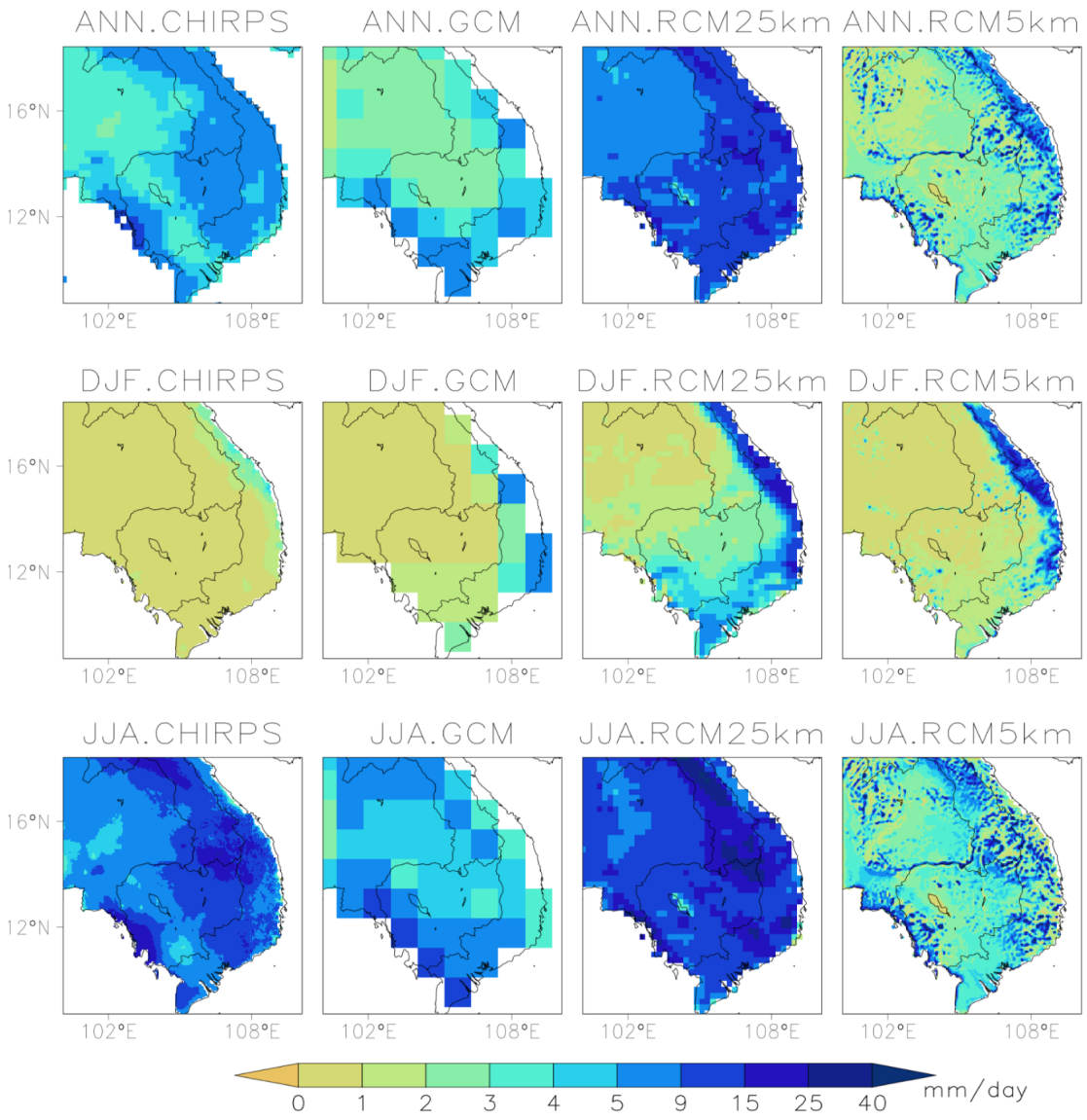

Figure 2.5.: Spatial patterns of mean rainfall over the region of Vietnam, including the Vietnamese Mekong Delta, averaged for the period 1986–2005, as derived from CHIRPS v2.0 and simulated by the global EC-EARTH model as well as RCM configurations at 25-km and 5-km resolution, published by Hoang-Cong et al. (2022). Annual, boreal winter (December-February), and boreal summer (June–August) mean precipitation fields are displayed in the upper, middle, and lower panels, respectively.

the choice of PBL parameterization schemes, both at coarse resolutions (e.g., Laux et al., 2013; Wang et al., 2014; Que et al., 2016) and gray-zone resolution ranges (e.g., Taraphdar and Pauluis, 2021; Taraphdar et al., 2021) across the Asian summer monsoon domain. Wang et al. (2014) used the Weather Research and Forecasting (WRF) model to evaluate the performance of four PBL schemes: Yonsei University (YSU; Hong et al., 2006), Asymmetric Convective Model version 2 (ACM2; Pleim, 2007), Bougeault–Lacarrere (BouLac; Bougeault and Lacarrere, 1989), and Mellor–Yamada–Janjic (MYJ; Janjić, 1994) over the East Asian summer monsoon region during 2000–2009. Their results indicate that simulations using nonlocal PBL schemes (YSU and ACM2) exhibit substantially stronger boundary-layer mixing, thereby enhancing sea-surface latent heat fluxes and convective activity. As a consequence, these configurations tend to overestimate precipitation and induce notable biases in monsoon circulation patterns. Similarly, Que et al. (2016) investigated the sensitivity of WRF-simulated precipitation over the Asian summer monsoon region in 2008 to different physical parameterizations, including two PBL schemes: MYJ and YSU, two microphysics schemes: WRF Single-Moment 3-class and 5-class (Hong et al., 2004), and two cumulus convection schemes: Betts–Miller–Janjic and Tiedtke (Janjić, 1994; Tiedtke, 1989). Their findings demonstrate that precipitation is highly sensitive to the choice of PBL scheme at regional scales, with simulations using the MYJ scheme providing a more realistic representation of the monsoon rain belt distribution, whereas simulations using the YSU scheme substantially overestimate precipitation intensity. At gray-zone resolution, Taraphdar and Pauluis (2021) further examined the sensitivity of monsoon rainfall simulations to PBL and microphysics parameterizations using WRF at 9 km resolution. Their experiments employed two PBL schemes: the Mellor–Yamada–Nakanishi–Niino (MYNN) level 2.5 (MYNN2.5; Nakanishi and Niino, 2006) and ACM2, alongside two microphysics schemes: WRF Double Moment 6-class (WSM6; Lim and Hong, 2010) and the aerosol-aware Thompson–Eidhammer scheme (Thompson et al., 2008). The results reveal that the choice of the PBL scheme exerts a dominant influence on Indian summer monsoon rainfall. Specifically, simulations using ACM2 successfully capture key circulation features and precipitation patterns over India, whereas MYNN-based simulations result in a substantial reduction in seasonal rainfall (approximately 40%) and a pronounced weakening of large-scale atmospheric circulation. In contrast, microphysics schemes exert a relatively minor influence on total rainfall amounts but significantly affect the spatial distribution of precipitation.

Beyond its seasonal variability, the diurnal cycle of precipitation during the rainy season constitutes a distinctive and influential feature of the Asian monsoon system, including Vietnam (Chen, 2020; Lai et al., 2025). The diurnal cycle is particularly important for the Vietnamese Mekong Delta, a major hub of agricultural and aquacultural activities, as shifts in rainfall peak timing may have significant implications for agricultural and regional hydrological processes, as well as disaster risk management (Subrahmanyam et al., 2025). Previous studies have also confirmed that the representation of the diurnal precipitation cycle is highly sensitive to PBL parameterization schemes across Asia (e.g., Koo and Hong, 2010; Zhang et al., 2016; Yang et al., 2018; Mei et al., 2024).

In addition to PBL parameterization schemes, the diurnal variability of SST represents another

critical process influencing rainfall simulations (Senatore et al., 2014; Pilatin et al., 2021). The Ca Mau Peninsula is located within the Tropical Warm Pool, a region globally recognized for its exceptionally high annual mean SST, weak surface winds, intense shortwave radiation under clear-sky conditions, and frequent large-amplitude diurnal SST fluctuations (Zhang et al., 2016). Previous investigations have demonstrated that explicitly accounting for diurnal SST variations improves the representation of air–sea coupling processes, thereby enhancing the performance of coupled climate models (e.g., Wei et al., 2001; Brunke et al., 2008; Clayson and Bogdanoff, 2013). Since version 3.1, the WRF model, one of the most widely used RCMs, has included a prognostic sea surface skin temperature (SSKT) scheme developed by Zeng and Beljaars (2005), through the sst_skin option. The scheme explicitly accounts for the combined influences of sensible and latent heat fluxes, radiative transfer, molecular diffusion, and turbulent mixing, thereby resolving the dominant processes governing diurnal SST variability. Evaluations over the Tropical Warm Pool have confirmed that the scheme successfully reproduces diurnal SST variations under a range of wind and radiation conditions (Zhang et al., 2018).

Unlike precipitation, PET, which constitutes the second major component of the freshwater flux, is not directly simulated by RCMs. Previous studies have attributed variations in PET primarily to sunshine duration or solar radiation (e.g., Xu et al., 2014; Li et al., 2015; Jiang et al., 2016), while other research highlights the dominant role of wind speed at 10-m height (e.g., Yin et al., 2010; Li et al., 2014). Despite its importance, the sensitivity of PET to PBL parameterizations in RCMs remains insufficiently understood. Nonetheless, studies examining the influence of PBL schemes on two key drivers of PET, namely, the wind speed at 10-m height (e.g., Mohan and Bhati, 2011; Xie et al., 2012; Dzebre and Adaramola, 2020; Gholami et al., 2021) and solar radiation (e.g., Hu et al., 2010; Xie et al., 2012), provide strong evidence that PBL scheme selection exerts a significant effect on the simulation of PET.

Overall, the findings of this section underscore that the selection of appropriate physical parameterization schemes is of critical importance for accurately simulating both precipitation and PET at gray-zone resolution, and ultimately for reliable assessments of freshwater fluxes over the Vietnamese Mekong Delta.

2.4.2. Impact of different land-use/land-cover datasets on simulating freshwater flux

LULCC is widely recognized as one of the major drivers of climate change at both regional and global scales (Feddema et al., 2005; Foley et al., 2005), as it modulates the water and energy balance between the land and the atmosphere. The impacts of LULCC tend to be much larger on local and regional scales than on global scales (Mahmood et al., 2014). Since RCMs clearly represent interactions between terrestrial and atmospheric components, they are useful for investigating land-atmosphere feedbacks and assessing the impacts of LULCC at regional scales.

Among the impacts of LULCC patterns, urbanization and deforestation are of great interest to many researchers seeking to understand their effects on regional climate models. The extent of urbaniza-

tion often results in increased surface air temperatures and changes in precipitation intensity and spatial patterns. However, the magnitude of changes depends on various factors such as daytime, season, geographical location, climate regime, circulation feedback, and surrounding land-cover (e.g., Grimmond et al., 2011; Niyogi et al., 2011; Stewart and Oke, 2012; Giannaros et al., 2013). On the other hand, deforestation may lead to a decrease in surface air temperatures in temperate regions but an increase in tropical regions (Costa and Pires, 2010; Dai, 2011). In addition, in some tropical regions, such as Borneo, deforestation creates high-albedo areas, thereby reducing precipitation by reducing evapotranspiration, convection, and horizontal atmospheric moisture inflow (Takahashi et al., 2017).

To date, several RCM studies have been documented to assess the impact of LULCC on both components of the freshwater flux, including precipitation, as well as two concepts of evapotranspiration: AET and PET (e.g., Laux et al., 2017; Lal et al., 2021; Achugbu et al., 2021; Crook et al., 2022; Achugbu et al., 2023). Rather than relying on outdated default LULC datasets embedded in RCMs, most of these studies incorporate updated regional or global LULC datasets or adopt hypothetical LULC scenarios.

Within the framework of the LUCC project over Central Vietnam, Laux et al. (2017) utilized the WRF model to examine the climatic impacts of two hypothetical LULC scenarios. While the deforestation scenario does not yield statistically significant signals in the most crucial surface variables, the urbanization scenario shows a clear temperature rise over converted areas. However, there is no robust precipitation response in either scenario. Lal et al. (2021) also utilized WRF in conjunction with the MODIS Collection 6 Land Cover Type Product (MCD12Q1; Sulla-Menashe and Friedl, 2018) to quantify the impacts of LULCC on precipitation and AET over India from 2002 to 2015. They identified moderate forest cover loss across large parts of northeast India and the Himalayan region, driven by conversion to grassland and agricultural land. These substantial land-cover changes were associated with enhanced AET, which in turn contributed to increased precipitation, particularly in regions previously dominated by forest cover. Further evidence on the climatic impacts of deforestation was provided by Achugbu et al. (2021), who employed WRF simulations driven by the MCD12Q1 LULC dataset alongside multiple hypothetical LULC scenarios, demonstrating that the reduction in precipitation over the Sahel–Sahara interface is due to deforestation. Moreover, this influence is consistent with the general relationship between vegetation cover and moisture availability, with deforestation systematically reducing AET.

More recently, Crook et al. (2022) advanced this line of research by applying a convection-permitting RCM with a horizontal resolution of 4 km, in combination with a regional LULC dataset named Land-Use Harmonization (Hurtt et al., 2011), to examine the impacts of historical deforestation on early monsoon rainfall over West Africa. Their findings indicate that LULCC induces substantial changes in surface energy partitioning, leading to a pronounced spatial redistribution of early monsoon precipitation. Over extensive inland deforested areas located approximately 300 km from the coastline (e.g., western Guinea), deforestation alters surface roughness, resulting in reduced convergence to the

south, enhanced convergence to the north, and locally increased rainfall within the deforested zone. In contrast, coastal deforestation (e.g., in Côte d'Ivoire) strengthens wind-driven sea-breeze circulations, leading to reduced evening rainfall over deforested coastal regions and enhanced precipitation further inland, in agreement with observational evidence. Most recently, Achugbu et al. (2023) conducted a comprehensive set of twelve WRF simulations using six different LULC datasets, including the default model LULC, the MCD12Q1 LULC dataset for 2001 and 2016, and three hypothetical deforestation scenarios, to assess the climatic impacts of LULCC over West Africa. Their findings indicate that all deforestation scenarios result in significant regional warming. Changes in surface albedo associated with LULCC further propagate to other climatic variables, ultimately influencing precipitation patterns. Additionally, deforestation was found to reduce soil moisture from July to September, while increasing it from December to February. Moreover, LULCC alters the atmospheric column by changing the intensities of various atmospheric patterns, such as the African Easterly Jet and the Tropical Easterly Jet. Both thermodynamic variables (e.g., air temperature and dew point) and moisture-related fields (e.g., relative humidity) exhibited marked sensitivity to LULCC.

Overall, the aforementioned studies provide compelling evidence that LULCC patterns, particularly deforestation and urbanization, exert a significant influence on both components of the freshwater flux as simulated by RCMs. However, the impact of converting cropland and mangroves to aquaculture on RCM performance has not been thoroughly examined and remains underexplored. Therefore, the primary objective of this research is to investigate the response of the freshwater flux to LULCC over the Vietnamese Mekong Delta using the WRF model.

3. Objectives and Structure of the Work

The preceding chapter systematically examined long-term trends in climate conditions and LULC over the Vietnamese Mekong Delta during recent decades. It also highlighted the substantial influence of physical parameterizations and LULC scenarios on the simulation of freshwater fluxes using RCMs, with particular emphasis on the WRF model. The study area of this dissertation is the Ca Mau Peninsula, a distinct sub-region of the Vietnamese Mekong Delta comprising the provinces of Ca Mau, Kien Giang, and Bac Lieu. The region is geographically situated between the South China Sea along its eastern margin and the Gulf of Thailand to the west. The Ca Mau Peninsula represents the country's most important aquaculture hub and a major contributor to national rice production (Wilder and Phuong, 2002; Ha et al., 2013), making it highly sensitive to changes in freshwater flux.

In this study, the Advanced Research WRF model version 4.0 (WRF-ARW; Skamarock et al., 2019) is employed at a horizontal resolution of 5 km to simulate freshwater fluxes over the Ca Mau Peninsula. This spatial resolution falls within the so-called gray-zone of atmospheric modelling, typically defined as grid spacings of approximately 4–10 km. It is important to note that these resolutions are inadequate in explicitly resolving individual convective clouds, yet they are too fine to fully rely on convective parameterization (Taraphdar and Pauluis, 2021; Taraphdar et al., 2021). Simulation at gray-zone resolution is regarded as a suitable compromise between computational efficiency and modelling performance for long-term simulations. Given the pronounced seasonality of precipitation in southern Vietnam (Pham et al., 2010; Tuan, 2019), model performance is evaluated separately for the dry and rainy seasons and for the entire year. In addition, the diurnal cycle of precipitation, characterized by a consistent afternoon rainfall maximum during the rainy season, constitutes a key feature of Southern Vietnam's climate (Huang et al., 2025). Accordingly, the capability of WRF-ARW to reproduce the characteristics of the diurnal precipitation cycle over the Ca Mau Peninsula during the rainy season is explicitly assessed. With respect to evapotranspiration, the study examines WRF-ARW's performance in simulating AET and PET, with particular emphasis on PET given the availability of reliable reference estimates for validation. Additionally, land surface models are essential in capturing land–atmosphere interactions by supplying lower boundary conditions to regional climate models (Donaire-Montaño et al., 2025). In this study, the Noah land surface model with multi-parameterization options (Noah-MP; Niu et al., 2011) is coupled with the WRF-ARW model. Within the Noah-MP model, leaf area index (LAI) can be represented either through vegetation-type-dependent parameterizations or prescribed using climatological datasets. Given the central role of vegetation processes in controlling transpiration, a primary component of AET, this study further examines the selection of appropriate vegetation process options within the

Noah-MP model. The overarching objective of this dissertation is to evaluate whether the WRF-ARW can be used as a tool to derive the freshwater flux over the Ca Mau Peninsula, taking LULCC into account. To achieve this objective, the research is structured into three interconnected parts. Firstly, the study identifies an appropriate configuration of WRF-ARW physical parameterizations for simulating freshwater fluxes over the Ca Mau Peninsula. Secondly, the performance of the optimized model configuration is evaluated through long-term simulations spanning 10 years. Thirdly, the impacts of updated, more realistic LULC datasets and hypothetical LULC scenarios on the simulation of freshwater fluxes by the WRF-ARW model are systematically assessed. In the following sections, the proposed research questions are presented and motivated for each of the three parts.

1. RQ 1a Which cumulus convection parameterization, with or without activation of the sst_skin option, provides the most accurate simulation of daily precipitation and its diurnal cycle at 5-km horizontal resolution over the Ca Mau Peninsula?
2. RQ 1b Which is the most appropriate vegetation option in the Noah-MP land surface model to simulate AET over the Ca Mau Peninsula?
3. RQ 1c Among the three commonly used PBL parameterization schemes, including MYJ, MYNN2.5, and ACM2, which scheme is most suitable for simulating both components of the freshwater flux, namely daily precipitation (including its diurnal cycle) and PET, over the Ca Mau Peninsula?
4. RQ 1d What combination of physical parameterization schemes provides the most reliable representation of freshwater fluxes over the Ca Mau Peninsula?

Previous regional climate applications over Vietnam indicate that the WRF-ARW model is capable of representing the essential features of the regional climate system, including large-scale spatial signatures, seasonal cycles, and frequency characteristics of key climate variables (e.g., Chotamonsak et al., 2011; Laux et al., 2013; Hoang-Cong et al., 2022). However, these studies were conducted at relatively coarse spatial resolutions, with the finest resolution limited to 25 km, and concepts related to evapotranspiration were overlooked. To address these limitations, the second part of this dissertation aims to provide a comprehensive assessment of both precipitation and PET over the Ca Mau Peninsula for the period 2007–2016. The results of this analysis will provide a holistic assessment of whether the WRF-ARW model, operated at a 5 km gray-zone resolution, can simulate freshwater fluxes over the Vietnamese Mekong Delta. This part of the study, presented in Chapter 6, addresses the following research questions:

1. RQ 2a Is the WRF-ARW model able to derive the daily precipitation over the Ca Mau Peninsula during the period 2007–2016?
2. RQ 2b Is the WRF-ARW model able to derive all characteristics of the diurnal cycle of precipitation over the Ca Mau Peninsula during the period 2007–2016?

3. RQ 2c Is the WRF-ARW model able to derive the daily PET over the Ca Mau Peninsula during the period 2007–2016?

It is worth noting that the LULC of the Ca Mau Peninsula has undergone substantial changes over the past three decades (1990–2020), primarily driven by the rapid expansion of aquaculture, which has largely replaced cropland and mangrove areas (Phan et al., 2021). As a result, the default LULC dataset embedded in the WRF-ARW model no longer adequately represents current land surface conditions in the region. This raises a critical question regarding whether the integration of updated and more realistic LULC datasets can enhance the performance of the WRF-ARW model in simulating freshwater fluxes over the Ca Mau Peninsula. In addition to incorporating updated LULC datasets, this study further employs a set of hypothetical LULC scenarios to explicitly assess the impacts of converting cropland and mangrove areas to aquaculture areas on the freshwater flux. As the WRF-ARW model does not include a dedicated land-use category for aquaculture, two alternative representations are examined, namely the permanent wetland class and the water body class. To isolate the effects of LULCC, all simulated precipitation and PET from these experiments are evaluated not only against observational datasets but also relative to simulations conducted with the default LULC configuration presented in Chapter 6. The validation strategy and experimental design are described in detail in Chapter 7. The outcomes of this final part of the dissertation provide evidence on whether the WRF-ARW model can realistically represent the current freshwater flux over the Ca Mau Peninsula, accounting for LULCC. Accordingly, the research questions addressed in the final part of this study, presented in Chapter 7, are formulated as follows:

1. RQ 3a What is the response of simulated daily precipitation to updated/more realistic LULC datasets and hypothetical LULC scenarios in the WRF-ARW model?
2. RQ 3b What is the response of the simulated diurnal cycle of precipitation to updated/more realistic LULC datasets and hypothetical LULC scenarios in the WRF-ARW model?
3. RQ 3c What is the response of simulated daily PET to updated/more realistic LULC datasets and hypothetical LULC scenarios in the WRF-ARW model?
4. RQ 3d What is the response of simulated daily AET to updated/more realistic LULC datasets and hypothetical LULC scenarios in the WRF-ARW model?
5. RQ 3e Is the permanent wetland category or the water body category suitable to represent the aquaculture area in the Noah-MP land surface model to simulate AET over the Ca Mau Peninsula?
6. RQ 3f Is the WRF-ARW model able to derive the present freshwater flux over the Ca Mau Peninsula, taking LULCC into account?

Before the analyses are presented, Chapter 4 provides an overview of all types of data and verification methods that are employed in this study.

4. Data and Methods

4.1. Preface

This section is dedicated to the comprehensive description of all data utilized in this dissertation, along with the presentation of all methods employed.

4.2. Data sources and processing

4.2.1. Station data observations

Daily rainfall observations were collected from 24 meteorological stations distributed across the Ca Mau Peninsula (Fig. 4.1). Three of these stations report to the World Meteorological Organization (WMO) at 6-hourly intervals, and one reports real-time at the same frequency to the National Center for Hydro-Meteorological Forecasting (NCHMF) of Vietnam, as listed in Table 4.1. In contrast to rainfall, reliable long-term observational datasets for evapotranspiration over the Ca Mau Peninsula are limited. None of the meteorological stations in the study area is equipped with instruments capable of directly measuring actual evapotranspiration (AET). For potential evapotranspiration (PET), two stations were equipped with the manual evaporimeter GGI-3000, which was formerly used as a standard instrument across the former Soviet Union and measures daily open-water evaporation. In addition, meteorological data, including maximum and minimum temperatures, relative humidity, sunshine duration, and 10-m wind speed from three stations covering the period 2007–2016, were used to compute PET using the Penman–Monteith method (Shuttleworth, 1993) for validation of daily PET. Previous studies suggest that Penman–Monteith PET correlates reasonably with GGI-3000 observations, although it is typically positively biased by approximately ~0.8 mm day^{-1} (Kohut et al., 2014; Iuliana and Neculau, 2015).

4.2.2. Satellite-based observations

Satellite-based datasets, including precipitation, land-use and land-cover (LULC), and leaf area index (LAI), provide an essential source of information for monitoring and analyzing freshwater flux over Vietnam, a region characterized by pronounced climatic variability and frequent extreme weather events. Derived from remote sensing observations, these products offer spatially continuous and temporally consistent representations of rainfall, land surface conditions, and vegetation status across diverse regions

Table 4.1.: Type of station, station name, and locations of the 24 precipitation stations used in this study. Numbers correspond to those used in Fig. 4.1. PR: Public rain gauges; WMO: Stations reporting to the global telecommunication system of the World Meteorological Organization (WMO); LO: Station reporting to the National Centre for Hydro-Meteorological Forecasting (NCHMF) of Vietnam; CM: Ca Mau province; KG: Kien Giang province; BL: Bac Lieu province; CT: Can Tho province.

No	Type of station	Station name	Province	Longitude[^{o}E]	Latitude[^{o}N]
1	PR	Dam Doi	CM	105.200	9.000
2	PR	Song Doc	CM	104.833	9.041
3	PR	Nam Can	CM	105.005	8.763
4	PR	U Minh	CM	104.967	9.417
5	WMO	Ca Mau	CM	105.150	9.183
6	PR	Khanh Hung	CM	104.910	9.137
7	PR	Thoi Binh	CM	105.083	9.350
8	PR	Van Thoi	CM	104.967	9.050
9	PR	Ha Tien	KG	104.483	10.383
10	WMO	Rach Gia	KG	105.083	10.000
11	PR	Xeo Ro	KG	105.100	9.867
12	PR	Hon Dat	KG	104.833	10.267
13	PR	Vinh Hoa Hung	KG	105.383	9.750
14	PR	Tan Hiep	KG	105.233	10.083
15	PR	Giong Rieng	KG	105.317	9.900
16	PR	Kien Luong	KG	104.650	10.283
17	PR	An Bien	KG	105.050	9.983
18	PR	Dong Hai	BL	105.667	9.200
19	LO	Bac Lieu	BL	105.717	9.283
20	PR	Gia Rai	BL	105.467	9.233
21	PR	Ganh Hao	BL	105.422	9.033
22	PR	Ngan Dua	BL	105.467	9.567
23	PR	Phuoc Long	BL	105.450	9.433
24	WMO	Can Tho	CT	105.767	10.033

of the country. Given Vietnam's complex topography and high vulnerability to climate change, satellite-based datasets play a critical role in evaluating and validating the performance of RCMs, such as the WRF-ARW model.

In terms of rainfall data, in this study, two gridded, satellite-based rainfall estimates are used for model validation. These are the 3-hourly Tropical Rainfall Measuring Mission 3B42 V7 at 0.25^o x 0.25^o spatial resolution (TRMM; Huffman and Bolvin, 2013) and the daily Climate Hazard Infrared Precipitation with Stations v2.0 dataset at 0.05^o x 0.05^o spatial resolution (CHIRPS; Funk et al., 2015). The TRMM 3B42 V7 product is part of the TRMM Multi-Satellite Precipitation Analysis (TMPA) framework; hereafter, this dataset is referred to as TMPA. The strength of satellite-based rainfall estimates lies in their good spatial coverage, easy accessibility, and relatively high spatial and temporal resolutions, while their drawbacks have been clearly recognized, comprising a high level of uncertainty, afflicted with the retrieval algorithms, data sources, and gauge adjustment procedures (Ebert et al., 2007; Guo

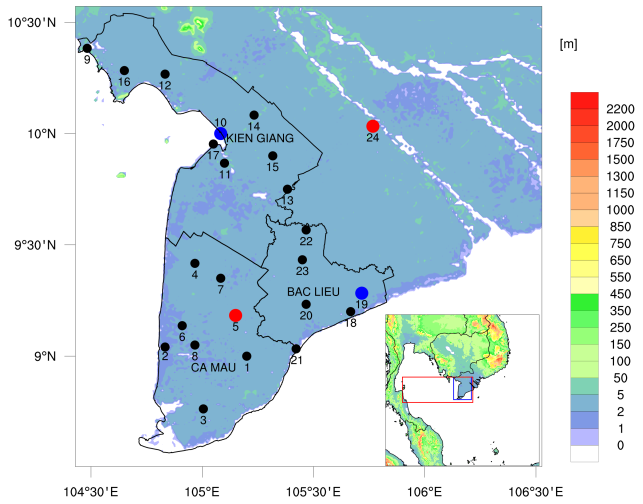

Figure 4.1.: Topography (shading), provinces in the Ca Mau Peninsula, and model domain for WRF-ARW simulations (inset map). Text in capital letters indicates province names. In the inset map, the blue rectangle indicates the study region, while the red rectangle represents the area for analyzing the propagation of rainfall. Black points show rain gauge stations, blue points show stations from which sunshine duration data were used, and red points show stations from which evaporation data were used (see Table 4.1 for station information).

et al., 2015). Therefore, it is necessary to investigate the performance of each satellite-based rainfall estimate in the research area before using it to validate the model's simulated precipitation. To date, CHIRPS v2.0 and TMPA have been evaluated for the Ca Mau Peninsula in several studies (e.g., Guo et al., 2017; Luo et al., 2019; Dinh et al., 2020). The results are consistent, indicating that both TMPA and CHIRPS v2.0 perform well in precipitation estimation, with TMPA exhibiting superior performance. Nevertheless, CHIRPS v2.0, with its higher spatial resolution and reasonable ability to identify and characterize drought events, can be used for validation, especially during the El Niño period and the dry season.

We have provided further evidence that TMPA has good performance over the Ca Mau Peninsula by an analysis of TMPA data at all rain gauges against observations by using the Taylor diagram (Taylor, 2001). Statistics are presented on a Taylor diagram in Fig. 4.2a, which shows the total spatial and temporal variability of daily precipitation from TMPA estimation and its successor: the Integrated Multi-satelliTe Retrievals for Global Precipitation Measurement the latest Version 06 (GPM IMERG; Hou et al., 2014) at all stations in the Ca Mau Peninsula in the rainy season, the dry season and the whole year of the period 2007–2016. Following the successes of TMPA, GPM IMERG has increased its spatial and temporal resolution, from 0.25^o and 3 hours to 0.1^o and half an hour. For the rainy season, TMPA estimates at all stations show a correlation with observations of 0.55; in the dry season, the correlation is lower at 0.46. The normalized standard deviation of space-time variation in daily precipitation in the rainy season is between 0.75 and for the dry season is 0.81. The absolute value of percentage bias is less than 1% in both dry and rainy seasons. These results are in line with previous results in examining the performance of TMPA estimation over the Ca Mau Peninsula (Luo et al., 2019; Dinh et al., 2020). Regarding GPM IMERG, the discrepancies with TMPA in terms of correlation, normalized standard

deviation, and RMSE are considered insignificant; however, the percentage bias is relatively high, especially during the dry season, at approximately 24%. As a result, we choose TMPA instead of GPM IMERG to validate the performance of the model.

Figures 4.3a and 4.3b depict the average daily rainfall in the dry season and rainy season over

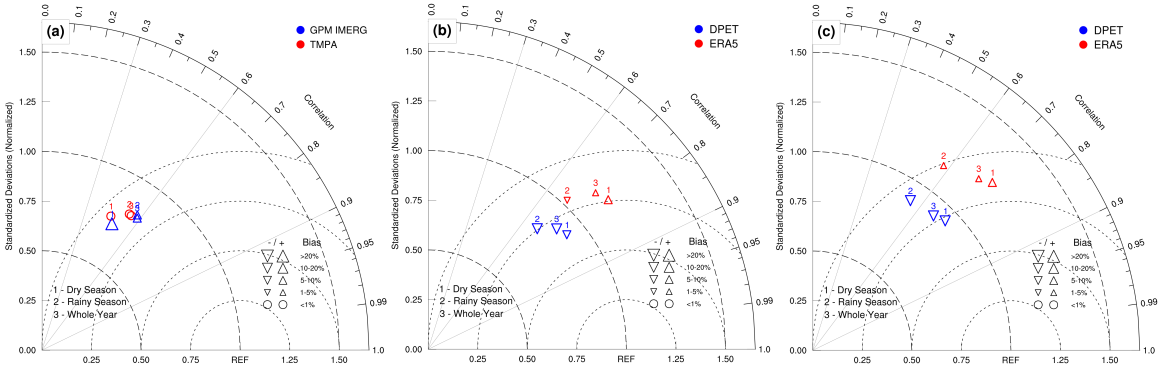

Figure 4.2.: Taylor diagrams of (a) daily TMPA (red symbols), GPM IMERG rainfall (blue symbols) and daily ERA5 PET (red symbols), DPET (blue symbols) evaluated against (b) estimates using the Penman-Monteith equation (red symbols), (c) GGI-3000 measurements for the rainy seasons, dry seasons and whole years over the period from 2008 to 2017.

the Ca Mau Peninsula for the 10-year period 2008–2017 based on TMPA data. Consistent with previous findings based on rain-gauge observations reported by Dang et al. (2020b), a pronounced contrast is evident between the rainfall of the rainy and dry seasons. During the rainy season, significant rainfall is evident across the entire domain, with rates ranging from 6 to 10.5 mm day^{-1}; the regions with the highest rainfall are located on the western coastline of the peninsula. Conversely, during the dry season, rainfall rates across the domain range from 1.5 to 3 mm day^{-1}.

Furthermore, to evaluate the performance of TMPA in estimating the diurnal cycle of precipitation over the Ca Mau Peninsula during the rainy season, 3-hourly precipitation from 14 automatic weather stations was collected for validation in 2019 and 2020. The analysis highlights that the performance of TMPA is very promising in simulating precipitation amount, precipitation frequency, and precipitation intensity (not shown).

With respect to LULC representations, two datasets are commonly available for applications within the WRF-ARW model. The first is the United States Geological Survey (USGS) dataset, derived from Advanced Very High Resolution Radiometer imagery and representing global land-cover conditions during the period from April 1992 to March 1993. This dataset follows the USGS classification scheme comprising 24 land-use categories. The second dataset is produced by the University of Boston based on Moderate Resolution Imaging Spectroradiometer (MODIS) observations and characterizes land-cover conditions for the year 2001. It adopts the International Geosphere–Biosphere Programme (IGBP; Gilliam and Pleim, 2010) classification, which distinguishes 20 discrete land-use categories. A key distinction between the two datasets lies in their treatment of mixed land-cover types. Compared with the MODIS product, the USGS dataset includes more four mixed categories, such as

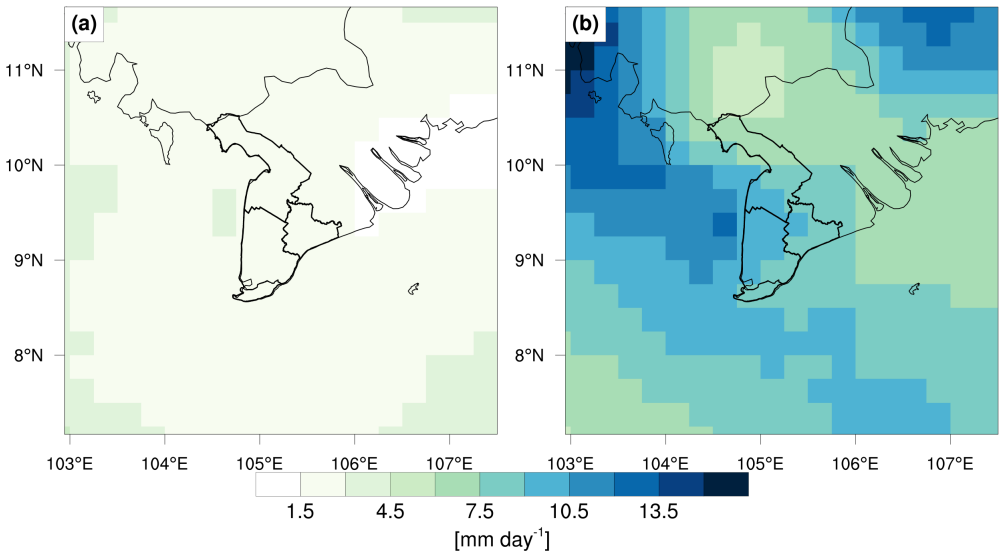

Figure 4.3.: Mean daily TMPA rainfall (a) in the dry seasons and (b) in the rainy seasons over the period from 2008 to 2017.

dryland cropland and pasture, mixed dryland/irrigated cropland and pasture, cropland/woodland mosaic, and herbaceous tundra, that are not commonly representative of land-use conditions within the study domain. Consequently, the MODIS-based dataset is selected as the default land-use representation in the WRF-ARW simulations. Nevertheless, it should be noted that both datasets were generated more than two decades ago, and substantial changes in regional ecosystems and land-use patterns since their production raise concerns regarding their current validity.

In addition to the default land-use data embedded in the WRF-ARW model, this study incorporates two updated and more realistic LULC datasets, including one global-scale product and one regional-scale product. For global land-cover representation, the Climate Change Initiative Land Cover dataset (CCI; Defourny et al., 2012), developed under the European Space Agency framework, is employed and is hereafter referred to as LU1. This dataset is derived from satellite observations acquired by the Medium-Resolution Imaging Spectrometer and provides a consistent and globally harmonized land-cover classification suitable for climate modelling applications. Experience from the GLOBCOVER project indicates that LU1 exhibits a high degree of temporal stability, a property that is particularly critical when land-cover time series are required as model input (Defourny et al., 2012). The LU1 dataset is available at a spatial resolution of 300 m for the period 1992–2015, followed by an enhanced resolution of 100 m for 2016–2019. It distinguishes 22 land-cover categories and is referenced to the World Geodetic System 1984 coordinate. Despite continuous advances in global land-cover mapping, existing global land-cover products generally exhibit overall accuracies ranging from approximately 67% to 81%, with substantial variability across individual land-cover classes (e.g., Mayaux et al., 2006; Friedl et al., 2010; Gong et al., 2013; Tateishi et al., 2014; Chen et al., 2015; Hua et al., 2018). In this context, Achard et al. (2017) reported an overall classification accuracy of 75.4% for LU1 in 2015.

At the regional scale, this study utilizes the LULC dataset from the Regional Land Cover Monitoring System developed for the Greater Mekong region (Saah et al., 2016). This dataset is hereafter denoted as LU2. This product covers five countries, such as Cambodia, the Lao People's Democratic Republic, Myanmar, Thailand, and Vietnam, and was generated for the period 1988–2017 using Landsat archive imagery and supervised classification techniques implemented within the Google Earth Engine platform. LU2 distinguishes 18 land-use categories at a 30m spatial resolution and achieves an overall classification accuracy of approximately 94% when accounting for uncertainty across the full region (Saah et al., 2020). As a regionally tailored product, LU2 demonstrates a clear performance advantage over global land-cover datasets, such as LU1, in the Greater Mekong context. Validation against national forest resources and agricultural productivity statistics for Vietnam indicates an overall accuracy of 89% for LU2 during 1988–2017, with class-specific accuracies ranging from 79% to 99% (Poortinga et al., 2019). At the provincial scale, the highest classification accuracy is reported for Ca Mau Province. Further analysis reveals that Ca Mau experienced rapid expansion of aquaculture ponds, largely driven by the conversion of rice paddies and mangrove areas, consistent with earlier findings by Tran et al. (2015). Beyond land-cover mapping, LU2 has been identified as a valuable dataset for assessing the impacts of policy interventions on food security, ecosystem services, and natural capital across the region (Poortinga et al., 2019).

In terms of LAI products, we employ a global LAI dataset, namely the European Geoland version 2 (GEO; Baret et al., 2013), to examine the performance of the Noah-MP land surface model experiments, coupled with the WRA-ARW model on simulating the LAI.

Among many land-surface types, vegetation significantly impacts Earth's climate (Raupach, 1995; Koster and Walker, 2015; Williams and Torn, 2015). At the global scale, plant transpiration accounts for approximately 80% of terrestrial evapotranspiration (Jasechko et al., 2013; Schlesinger and Jasechko, 2014). Water absorbed by plant roots is subsequently released to the atmosphere through stomatal transpiration at the leaf surface, implying that variations in LAI directly modulate transpiration rates and, consequently, AET. LAI, defined as the one-sided leaf area per unit ground area, therefore represents the effective photosynthetic and transpiring surface of vegetation. Owing to its central role in controlling land–atmosphere exchanges, LAI is a key state variable in land-surface and phenological models governing carbon, energy, and water balances (Cowling and Field, 2003). To support global climate modelling applications, the Global Climate Observing System recommends that LAI products achieve a maximum uncertainty of 15% (GCOS, 2016), while most application communities consider a relative accuracy of approximately 20% to be a minimum requirement.

In this context, the GEO v2.0 LAI product has undergone extensive global validation. Camacho et al. (2018) evaluated GEO v2.0 for the period from October 2013 to October 2014, with subsequent annual assessments of product stability documented by the Copernicus Global Land Service (Copernicus Global Land Service, 2022). Compared with its predecessor (GEO v1.0), the GEO v2.0 product exhibits improved spatial completeness (no gaps) and smoother profiles. Specifically, over evergreen-

deciduous forests, the GEO v2.0 exhibited smooth trajectories with elevated values and minimal seasonality, whereas the GEO v1.0 showed unexpectedly low LAI values, seasonality, and noise attributable to persistent cloud cover. Accuracy assessments based on a limited set of coincident ground observations (fewer than 15 sites) yielded an RMSE of approximately 0.79 for LAI, indicating performance suitable for large-scale climate and land-surface modelling applications.

Lastly, it should be mentioned that this study utilized three categories of satellite-based datasets, which consist of rainfall, LULC, and LAI, to evaluate freshwater flux simulation over the study area, in addition to station-based observational data.

4.2.3. Model-derived gridded evapotranspiration datasets

Given the limited availability of observational data for two evapotranspiration concepts, namely PET and AET, over the Ca Mau Peninsula, additional datasets are required for model evaluation. With respect to PET, only two stations equipped with GGI-3000 evaporimeters and three meteorological stations, where PET can be estimated using the Penman–Monteith formulation (Shuttleworth, 1993), are currently operational in the region. In contrast, no observational station is equipped with instruments capable of directly measuring AET. To address these data limitations, this study employs model-derived gridded evapotranspiration datasets, which provide an independent and spatially continuous reference for assessing the performance of the WRF-ARW model.

Until now, a number of model-derived gridded PET datasets have been developed; these comprise the Global Land Evaporation Amsterdam Methodology v3.5 (GLEAM; Martens et al., 2017), the TerraClimate (Abatzoglou et al., 2018), the ECMWF fifth-generation reanalysis (ERA5; Hersbach et al., 2020), the Japanese 55-year Reanalysis Project (JRA-55; Kobayashi et al., 2015), the Modern-Era Retrospective Analysis for Research and Application 2 (MERRA-2; Gelaro et al., 2017), and the Daily Potential Evapotranspiration (DPET; Singer et al., 2021). The accuracy of the gridded model-derived PET dataset varies significantly across different regions and seasons; however, little research has been conducted to evaluate its ability to mimic the spatial-temporal distribution in the Ca Mau Peninsula. In this study, ERA5 and DPET are selected for PET evaluation.

Our study provides considerable insight into the potential of ERA5 and DPET for estimating PET over the Ca Mau Peninsula. The two datasets have the potential to outperform all previous PET datasets due to the fact that they have a high temporal resolution (hourly), high spatial resolution (0.1 degrees in the case of DPET and 0.25 degrees in the case of ERA5), long available duration, and a small number of missing points over the Ca Mau Peninsula. The Taylor diagrams are used to show the performance of PET estimated from ERA5 and DPET as compared to the estimates using the Penman-Monteith equation at three stations, including Ca Mau, Rach Gia, and Bac Lieu, and GGI-3000 measurements at two stations, consisting of Ca Mau and Bac Lieu (Figs 4.2b,c) for the period from 2008 to 2017. Overall, both the PET estimated from ERA5 and DPET performed better during the dry season than during the

rainy season, and they showed very similar correlation coefficients. Compared with GGI-3000 measurements, the correlation coefficients between the two datasets are relatively high: 0.75 in the dry season and 0.59 in the rainy season. Meanwhile, compared to estimates from the Penman-Monteith equation, the correlation coefficients are higher: 0.80 in the dry season and 0.65 in the rainy season. Regarding the percentage bias, DPET shows negative values relative to both GGI-3000 measurements and estimates from the Penman-Monteith equation, ranging from 10 to 15%. In contrast, most percentage biases from ERA5 are positive values, ranging from 0 to 10%. These positive results suggest that both ERA5 and DPET have a good performance on estimating PET over the Ca Mau Peninsula and will be used for validating the performance of the model on simulating PET.

Figures 4.4a and 4.4b present the spatial distribution of mean daily PET during the dry and rainy

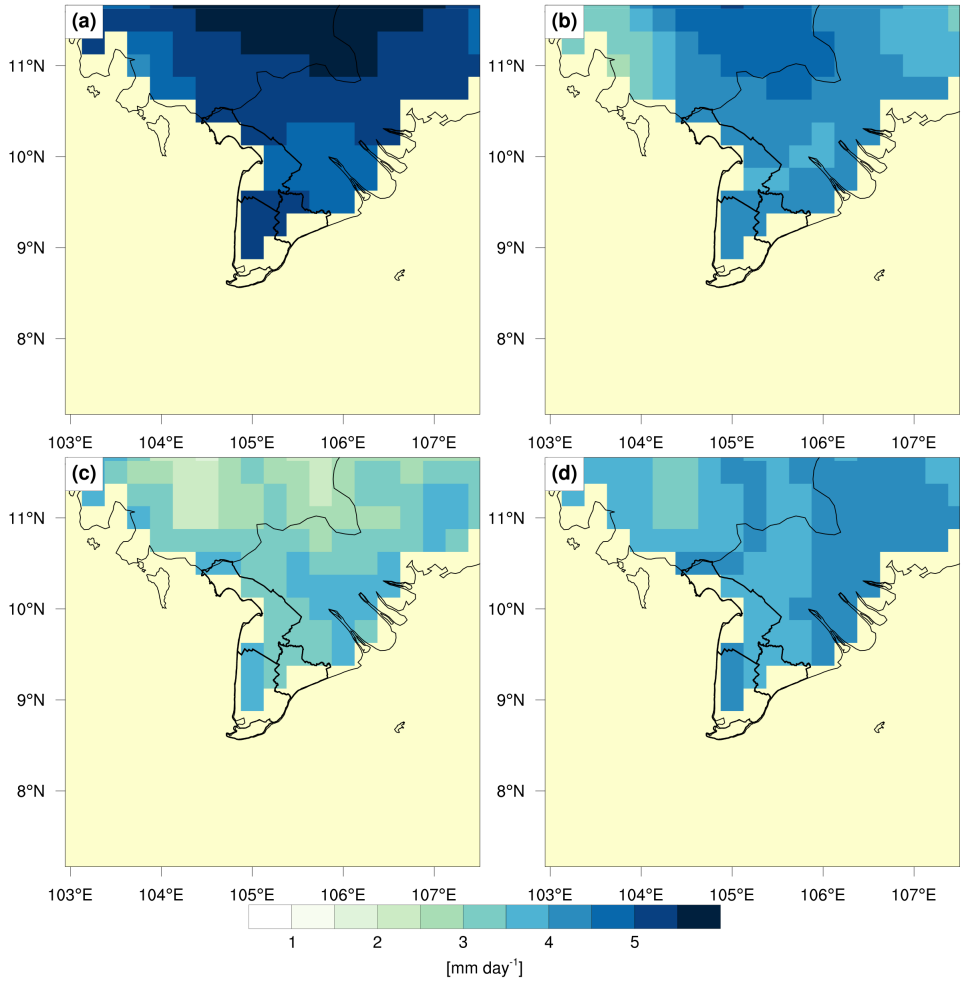

Figure 4.4.: Mean daily ERA5 PET (a) in the dry seasons and (b) in the rainy seasons in the period 2008–2017. (c, d) Same as in (a, b) but for the mean daily ERA5 AET. PET and AET data are only available over the continent; over the ocean, all data points are missing and are marked in yellow.

seasons over the Ca Mau Peninsula for the period 2008–2017, as derived from the ERA5 dataset. Figures 4.5a and 4.5b show the corresponding seasonal PET fields obtained from the DPET dataset. Based on ERA5, the PET across the domain ranges from approximately 4.5 to 5.5 mm day^{-1} in the dry season

and from 3.5 to 4.5 mm day^{-1} in the rainy season, with the highest values consistently observed along the western coastline of the peninsula. PET estimates from DPET exhibit similar spatial patterns but systematically lower magnitudes, with values of approximately 3.5–4.5 mm day^{-1} during the dry season and 3.0–4.0 mm day^{-1} during the rainy season. Overall, in contrast to rainfall, PET displays only a weak seasonal contrast over the Ca Mau Peninsula, and no substantial differences in spatial distribution are observed between ERA5 and DPET.

Figures 4.6a and 4.6b show the daily freshwater flux (TMPA-DPET) in the dry and rainy seasons

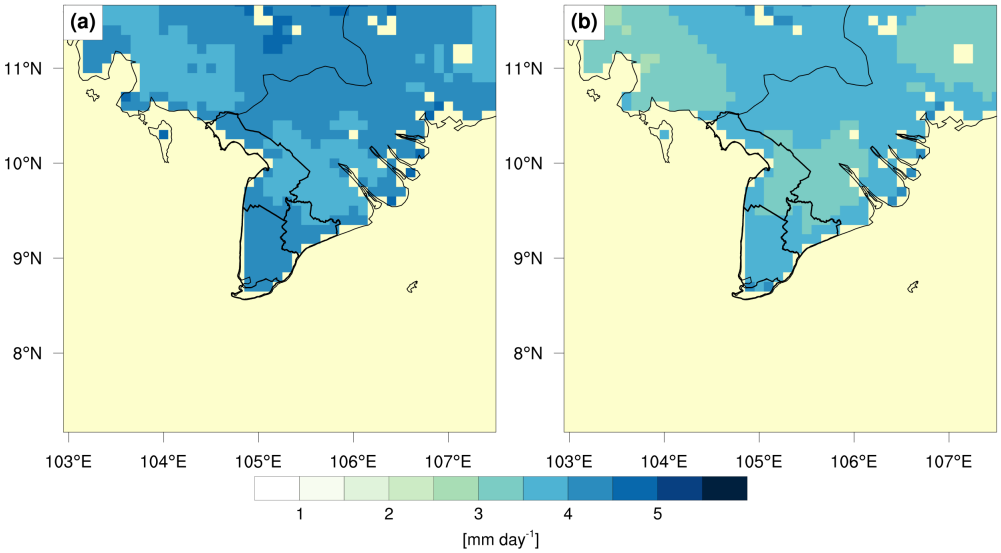

Figure 4.5.: Mean daily DPET PET (a) in the dry seasons and (b) in the rainy seasons over the period from 2008 to 2017. PET data is only available over the continent; over the ocean, all data points are missing and marked in yellow.

across the Ca Mau Peninsula from 2008 to 2017. Freshwater flux over the Ca Mau Peninsula exhibits a marked seasonal contrast. During the dry season, only negative values were detected across the Ca Mau Peninsula, ranging from -1.0 to 3.0 mm day^{-1}. This is the main reason for water scarcity in this region. By contrast, the rainy season is characterized by persistently positive freshwater fluxes exceeding 4 mm day^{-1}, with maximum values concentrated along the western coastline of the peninsula.

Average monthly TMPA rainfall, PET archived from DPET, and the freshwater flux (TMPA-DPET) were presented by the box plots in Fig. 4.7 during the period from 2008–2017. From this figure, it is clear that the monthly rainfall over the Ca Mau Peninsula is lowest in January, February, and March, as these months have values close to zero. In contrast, the maximum value of monthly rainfall occurs in September and October. Regarding the monthly PET value, consistently recorded in March and April, and the PET values in the dry season months are generally higher than those in the rainy season months. In terms of monthly freshwater flux, only negative values were recorded from December to April, while only positive values were found from May to November.

In Vietnam, both daily precipitation and daily PET measured by GGI-3000 evaporimeter from all

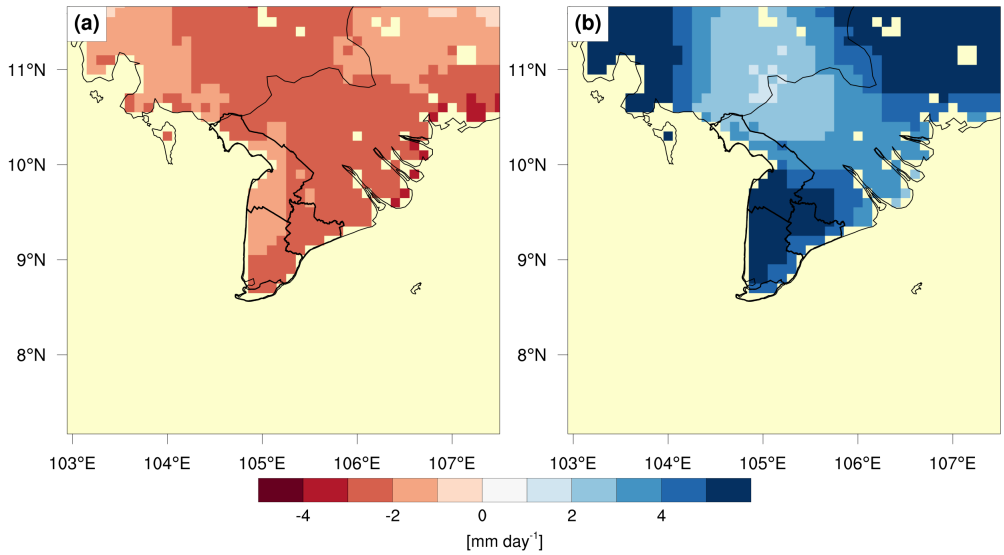

Figure 4.6.: Mean daily freshwater flux (TMPA-DPET) (a) in the dry seasons and (b) in the rainy seasons over the period from 2008 to 2017. The freshwater flux data is only available over the continent; over the ocean, all data points are missing and marked in yellow.

stations were collected and designated as 24h amounts that were accumulated from 12:00 UTC, which corresponds to 19:00 local time (LT), on the previous day to 12:00 UTC on the current day. As a result, the daily-accumulated rainfall from TMPA and the daily PET from ERA5 were calculated for each grid point on a specific date by aggregating 1- or 3-hour data values for the same time period mentioned earlier, before the evaluations were conducted. In terms of CHIRPS v2.0 data, due to the fact that its time resolution is daily, daily precipitation was accumulated over 24h starting at 00:00 UTC (07:00 LT), and all daily precipitation evaluations against this data will be carried out in this time span. Regarding the other gridded PET datasets, due to the different accumulated starting times compared to the observation data (00:00 UTC and 12:00 UTC), we could not provide further evidence for this ability to estimate daily PET over the Ca Mau Peninsula.

For AET estimation, no evidence of the performance of all gridded datasets could be found due to

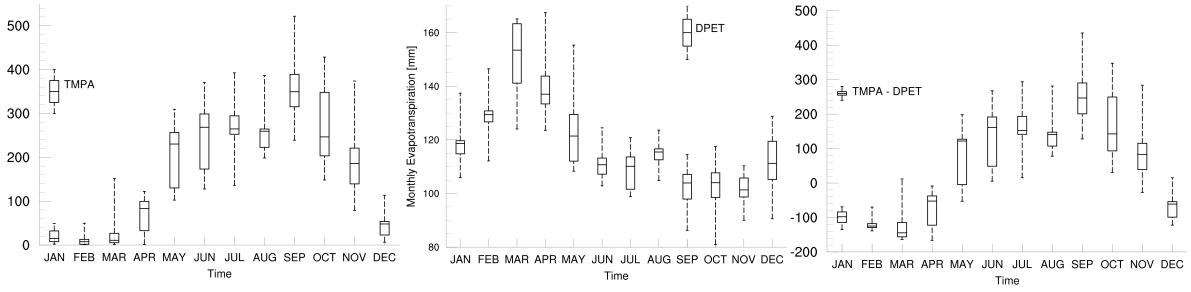

Figure 4.7.: Box plot of (a) mean monthly TMPA rainfall, (b) mean monthly DPET PET, and (c) mean monthly freshwater flux (TMPA-DPET) in all months over the period from 2008 to 2017.

the lack of observation data over the Ca Mau Peninsula. Consequently, it is inevitable for us to manipu-

late all available gridded AET datasets, which include ERA5, GLEAM v3.5, and a merged AET product from three model-based products using the Reliability Ensemble Averaging (REA) method, which minimizes errors (Lu et al., 2021). Figures 4.4c and 4.4d illustrate the spatial distribution of mean daily AET during the dry and rainy seasons over the Ca Mau Peninsula for the period 2008–2017, as derived from ERA5. Overall, the mean daily AET is lower than the PET in both seasons. During the dry season, AET values typically range from 3.5 to 4.5 mm day^{-1}, while higher rates of approximately 4–5 mm day^{-1} are observed in the rainy season. Consistent with the spatial pattern of PET, maximum AET rates are systematically concentrated along the western coastline of the Ca Mau Peninsula.

Notably, in this study, in addition to observations at the station, model-derived datasets were employed to validate the performance of the WRF-ARW on simulating PET and AET. Table 4.2 provides detailed information on all datasets we used in this study.

4.2.4. Conversion of land-use/land-cover datasets to the WRF-ARW model

One of the primary objectives of this study is to replace the outdated default LULC dataset in the WRF-ARW model over the Ca Mau Peninsula. This is achieved by incorporating newly available and updated land-use datasets, as described in Section 4.2.2.

Specifically, two realistic LULC products are employed: (i) an annual global land-cover dataset developed by the European Space Agency (denoted as LU1), and (ii) an annual regional land-cover dataset covering the Greater Mekong region produced within the SERVIR-Mekong framework (denoted as LU2). In addition to these realistic land-cover datasets, two hypothetical extreme LULC scenarios are constructed to explicitly investigate the sensitivity of freshwater fluxes to LULCC over the Ca Mau Peninsula. These scenarios include a Total Permanent Wetland scenario (LU3) and a Total Water Body scenario (LU4). The hypothetical scenarios are generated by systematically modifying the land-use categories within the study domain such that, in LU3, all land-use grid points over the Ca Mau Peninsula are converted to permanent wetlands, whereas in LU4, all grid cells are converted to water bodies. The adoption of such hypothetical extreme LULC scenarios allows for the isolation and amplification of signals, thereby facilitating a clearer assessment of the impacts of LULCC on freshwater fluxes. This approach is particularly justified given the relatively limited area of the Ca Mau Peninsula and the generally weak land–atmosphere coupling in the region, which may otherwise obscure LULCC-induced signals under a more moderate LULC scenario.

All LULC datasets and scenarios implemented in the WRF-ARW domain are illustrated in Fig. 4.8. Table 4.3 summarizes the fractional area coverage of each LULC category, expressed as percentages based on pixel counts, for the control simulation using the default MODIS LULC dataset, as well as for simulations employing the LU1 and LU2 datasets and the two hypothetical scenarios, LU3 and LU4, over the Ca Mau Peninsula in 2007. Each constructed LULC dataset and scenario was subsequently converted into a single binary file compatible with the WRF-ARW model's input requirements. Substan-

Table 4.2.: List of datasets used for validation in this study. RF: Rainfall datasets; PET: Potential evapotranspiration datasets; AET: Actual evapotranspiration datasets; LU: Land-use datasets; LAI: Leaf area index datasets.

No	Type of dataset	Dataset name	Spatial resolution	Temporal resolution	Temporal domain
1	RF	TMPA (https://disc.gsfc.nasa.gov/datasets/TRMM_3B42_7/summary)	0.25^o	3 hours	1998–2020
2	RF	CHIRPS v2.0 (https://data.chc.ucsb.edu/products/CHIRPS-2.0/)	0.05^o	1 day	1981–2022
3	RF	GPM IMERG (https://disc.gsfc.nasa.gov/datasets/GPM_3IMERGHH_06/summary)	0.1^o	0.5 hour	2000–2021
4	PET	ERA5 (https://cds.climate.copernicus.eu/cdsapp#!/dataset/reanalysis-era5-single-levels?tab=overview)	0.25^o	1 hour	1979–2022
5	PET	DPET (https://data.bris.ac.uk/data/dataset/qb8ujazzda0s2aykkv0oq0ctp)	0.1^o	1 hour	1981–2022
6	AET	ERA5 (https://cds.climate.copernicus.eu/cdsapp#!/dataset/reanalysis-era5-single-levels?tab=overview)	0.25^o	1 hour	1979–2022
7	AET	GLEAM v3.5 (https://www.gleam.eu/)	0.25^o	1 day	1980–2020
8	AET	REA (https://zenodo.org/record/4595941#.YkWcKTdBySN)	0.25^o	1 day	1980–2017
9	LU	CCI v1.0(http://maps.elie.ucl.ac.be/CCI/viewer/download.php)	300m	1 year	1992–2015
10	LU	CCI v2.0 (http://maps.elie.ucl.ac.be/CCI/viewer/download.php)	100m	1 year	2016–2019
11	LU	SERVIR-Mekong (https://www.landcovermapping.org/en/landcover/)	30m	1 year	1988–2017
12	LAI	GEO v2.0 (https://land.copernicus.eu/global/products/lai)	1km	10 days	1999–2022
13	LAI	ERA5 (https://cds.climate.copernicus.eu/cdsapp#!/dataset/reanalysis-era5-single-levels?tab=overview)	0.25^o	1 hour	1979–2022

tial differences in land-use distributions are evident among the datasets across the Ca Mau Peninsula. In 2007, croplands accounted for 41.51% of the Ca Mau Peninsula area in the default MODIS dataset, compared to 85.02% in the LU1 dataset and 40.26% in the LU2 dataset (land-use categories follow the classification codes listed in Table 4.4). In LU1, cropland is the dominant land-use category, covering 85.02% of the peninsula, followed by permanent wetlands at 5.25%. In contrast, LU2 is characterized by a predominance of permanent wetlands, which occupy 54.49% of the area, and croplands, which account for 40.26%. The spatial patterns in the LU2 dataset are consistent with previous findings by Phan et al. (2021), reflecting the rapid expansion of agricultural and aquaculture land across the Ca Mau Peninsula since 2000. These results suggest that LU2 offers a more accurate representation of the region's current land-use conditions.

For implementation within the WRF-ARW model, the land-use data derived from both LU1 and

Table 4.3.: Percentage cover of each LULC category in terms of pixel counts for each LULC dataset over the Ca Mau Peninsula in 2007.

LULC variables	**Value**	**Control**	**LU1**	**LU2**	**LU3**	**LU4**
Evergreen Needleleaf Forests	1	18.91	3.18	0.00	0.00	0.00
Evergreen Broadleaf Forests	2	12.92	0.37	0.00	0.00	0.00
Deciduous Needleleaf Forests	3	0.00	0.00	0.00	0.00	0.00
Deciduous Broadleaf Forests	4	0.00	0.00	0.00	0.00	0.00
Mixed Forests	5	13.86	0.00	0.00	0.00	0.00
Closed Shrublands	6	0.19	0.00	0.00	0.00	0.00
Open Shrublands	7	0.56	0.00	0.00	0.00	0.00
Woody Savannas	8	0.00	0.94	0.00	0.00	0.00
Savannas	9	0.00	0.00	0.00	0.00	0.00
Grasslands	10	0.56	0.00	0.00	0.00	0.00
Permanent Wetlands	11	8.24	5.24	54.49	100.00	0.00
Croplands	12	42.51	85.02	40.26	0.00	0.00
Urban and Built-up Lands	13	0.00	0.00	0.00	0.00	0.00
Cropland/Natural Vegetation Mosaics	14	0.00	0.19	0.00	0.00	0.00
Permanent Snow and Ice	15	0.00	0.00	0.00	0.00	0.00
Barren	16	0.75	0.00	0.00	0.00	0.00
Water Bodies	17	1.50	5.06	2.25	0.00	100.00
Wooded Tundra	18	0.00	0.00	0.00	0.00	0.00
Mixed Tundra	19	0.00	0.00	0.00	0.00	0.00
Barren Tundra	20	0.00	0.00	0.00	0.00	0.00

LU2 were reclassified to conform to the MODIS land-use categories. The correspondence between LU1 and LU2 land-use codes and the MODIS categories is summarized in Table 4.4. Each land-use category is characterized by a set of surface properties, including surface albedo (α), emissivity(ε), heat capacity (C), soil moisture availability (M), thermal inertia (λ), and surface roughness length(z_0).

Table 4.4.: Climate Change Initiative (LU1), SERVIR-Mekong (LU2), and Moderate-resolution Imaging Spectroradiometer (MODIS) land-use data code conversion table. x denotes that this category does not exist in this LULC dataset. Parameters from left to right are: surface albedo (α) [%], emissivity (ε) [%], surface roughness length (z_0) [$10^{-2}m$], heat capacity (C) [$10^5\ Jm^{-3}K^{-1}$], thermal inertia (λ) [4.184 x 10^2 J K^{-1} m^{-2} $s^{-1/2}$]

MODIS Categories	**Category name**	α	ε	z_0	C	λ	**LU1 Categories**	**LU2 Categories**
1	Evergreen Needleleaf Forests	12.00	0.95	50	3.33	4	70,71,72	x
2	Evergreen Broadleaf Forests	12.00	0.95	50	1.67	5	50	7,8
3	Deciduous Needleleaf Forests	14.00	0.94	50	2.86	4	80,81,82	x
4	Deciduous Broadleaf Forests	16.00	0.93	50	2.63	4	60,61,62	x
5	Mixed Forests	13.00	0.93	50.	2.11	4	90	9,6
6	Closed Shrublands	22.00	0.93	5	1.56	3	121	x
7	Open Shrublands	20.00	0.95	6	2.14	3	122,120	17
8	Woody Savannas	22.00	0.93	5	1.56	3	100	x
9	Savannas	20.00	0.92	15	2.00	3	110	x
10	Grasslands	19.00	0.96	12	2.37	3	130	16
11	Permanent Wetlands	14.00	0.95	30	1.32	5.5	160,170,180	4,5,15,18
12	Croplands	17.00	0.985	15	2.71	4	10,11,12,20	11,12
13	Urban and Built-up Lands	15.00	0.88	80	1.67	3	190	10
14	Cropland/Natural Vegetation Mosaics	18.00	0.98	14	2.56	4	30,40	
15	Permanent Snow and Ice	55.00	0.95	0.1	0.0	4	220	3
16	Barren	25.00	0.90	1	0.81	2	140,150,151,152, 153,200,201,202	13,14
17	Water Bodies	8.00	0.98	0.01	0	6	210	2
18	Wooded Tundra	15.00	0.93	30	2.67	5	x	x
19	Mixed Tundra	15.00	0.92	15	2.67	5	x	x
20	Barren Tundra	25.00	0.90	10	1.60	2	x	x

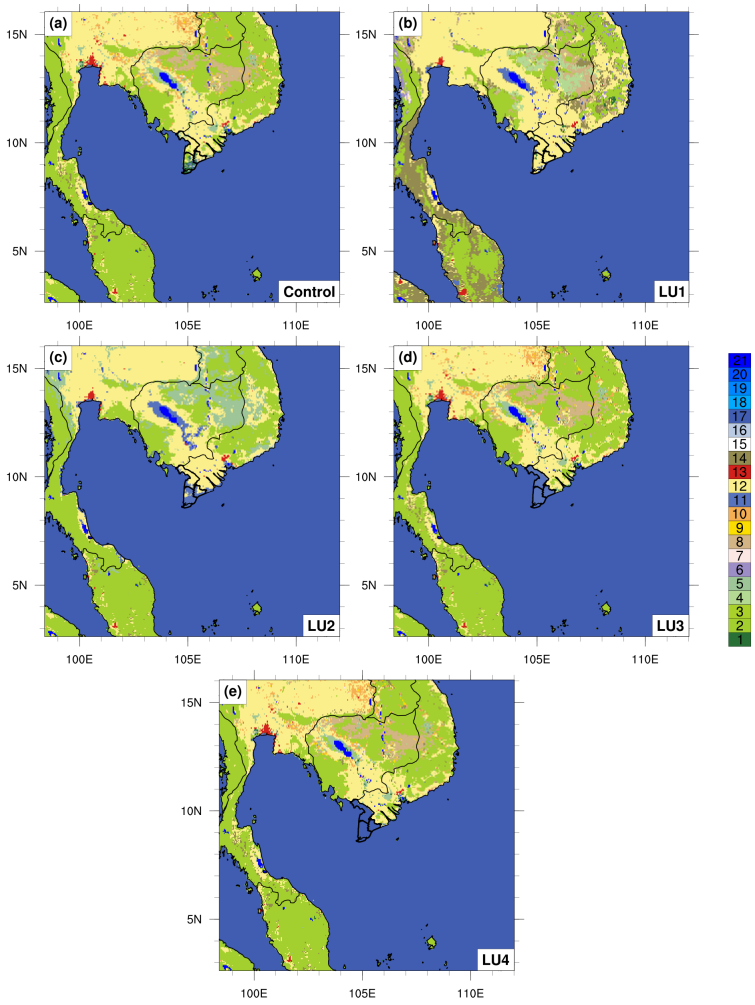

Figure 4.8.: Different LULC datasets used for the simulations over the Ca Mau Peninsula: **a** Control, **b** LU1, **c** LU2, **d** LU3, **e** LU4. The legend value is the same as in Table 4.3.

4.3. Meteorological modelling: the WRF-ARW model

4.3.1. Model description

Simulations of precipitation and PET are conducted using version 4.0 of the WRF-ARW model (Skamarock et al., 2019). The WRF-ARW has been widely employed to study the climate of the Ca Mau Peninsula (e.g., Chotamonsak et al., 2011; Laux et al., 2013; Raghavan et al., 2016; Jiang et al., 2019). In these studies, the main downside of the WRF-ARW model is the inaccurate simulated precipitation over the Ca Mau Peninsula, with overestimation of precipitation during the transition periods between the dry and wet seasons (Jiang et al., 2019) and underestimation in the rainy season (Raghavan et al., 2016).

4.3.2. Model parameterizations and experimental design

The findings presented in Section 2.4.1 highlight that the selection of physical parameterization schemes is critical for accurately simulating freshwater fluxes over the Ca Mau Peninsula. Accordingly, a suite of sensitivity experiments is designed to evaluate the role of key physical parameterizations.

Three planetary boundary layer (PBL) schemes are tested: Mellor-Yamada-Nakanishi-Niino Level 2.5 (MYNN2.5; Nakanishi and Niino, 2006), Mellor–Yamada–Janjic (MYJ; Janjić, 1994), and Asymmetric Convective Model version 2 (ACM2; Pleim, 2007). Based on their representation of vertical turbulent transport, PBL schemes are commonly categorized into local and non-local formulations (Holtslag and Boville, 1993). Local turbulence schemes, such as MYNN2.5 and MYJ, parameterize turbulent mixing using information from only adjacent vertical levels. In contrast, non-local schemes, including ACM2, account for mixing over a deeper vertical extent by incorporating contributions from multiple levels, thereby representing vertically integrated transport processes across the entire PBL (Cohen et al., 2015). It is important to note that both local and non-local PBL schemes rely on simplifying assumptions and may not perform optimally across all climatic regimes. Each scheme is paired with its corresponding surface-layer scheme and further tested with or without the activation of the option proposed by Zeng and Beljaars (2005), resulting in six baseline experiments (Table 4.5a). The sst_skin option accounts for sensible and latent heat fluxes, radiative forcing, and turbulent diffusion, and has been shown to improve representation of diurnal SST variability in tropical oceans.

The model domain covers the Ca Mau Peninsula and adjacent regions, including Central Vietnam,

Table 4.5.: Details of WRF-ARW configurations for (a): different PBL scheme, no Cumulus scheme, corresponding surface layer scheme, sst_skin option (on/off) and (b): MYNN2.5 PBL scheme, different Cumulus scheme, turn on sst_skin option.

Experiment Name	**PBL scheme**	**Cumulus scheme**	**Surface Layer scheme**	**sst_skin**
(a)				
WRF-MYNN2.5	MYNN2.5	NONE	MYNN	ON
WRF-MYJ	MYJ	NONE	ETA	ON
WRF-ACM2	ACM2	NONE	MM5	ON
WRF-MYNN2.5-s	MYNN2.5	NONE	MYNN	OFF
WRF-MYJ-s	MYJ	NONE	ETA	OFF
WRF-ACM2-s	ACM2	NONE	MM5	OFF
(b)				
WRF-MYNN2.5-KF	MYNN2.5	KAIN–FRITSCH	MYNN	ON
WRF-MYNN2.5-BMJ	MYNN2.5	BETTS–MILLER–JANJIC	MYNN	ON
WRF-MYNN2.5-GL	MYNN2.5	GRELL–FREITAS	MYNN	ON
WRF-MYNN2.5-AKW	MYNN2.5	NEW SIMPLIFIED ARAKAWA–SCHUBERT	MYNN	ON
WRF-MYNN2.5-G3D	MYNN2.5	GRELL 3D ENSEMBLE	MYNN	ON

Cambodia, Southern Laos, and Northeastern Thailand (98.4–112^{o}E, 2.6–16^{o}N; Fig. 4.1). The domain resolution is 5 km, with 300 × 300 horizontal grid points, 37 vertical levels, and a model top at 10 hPa. Boundary and initial conditions are provided by the ERA5 reanalysis (Hersbach et al., 2020) at a resolution of ~30 km and a temporal frequency of 3 hours. To assess climate variability, three representative years are selected based on the Niño 3.4 index, from the National Oceanic and Atmospheric Administration (NOAA) Climate Prediction Center (CPC): 2007 (La Niña), 2013 (ENSO-neutral), and 2015 (strong El Niño). Simulations are initialized on 1 December of the preceding year and include a 30-day spin-up to allow the model to be geared toward "climate mode" after 30 days of spin-up time (Zhong et al., 2007).

To address limitations at gray-zone resolutions, additional experiments are conducted for the year 2015, a strong El Niño year, with MYNN2.5 PBL scheme coupled to five cumulus schemes: Kain–Fritsch (Kain, 2004), Betts–Miller–Janjic (Janjić, 1994), Grell–Freitas (Grell and Freitas, 2014), New Simplified Arakawa–Schubert (Kwon and Hong, 2017), and Grell 3D Ensemble (Grell and Dévényi, 2002) to examine the influence of cumulus scheme on simulating precipitation (Table 4.5b). Physics parameterizations unrelated to the PBL are selected following common WRF-ARW practices in Southeast Asia: WSM6 microphysics (Hong and Lim, 2006), Dudhia shortwave radiation (Dudhia, 1989), Rapid Radiative Transfer Model (RRTM) longwave radiation (Mlawer et al., 1997), and the Noah-MP land surface model (Yang et al., 2011; Niu et al., 2011). Together, these simulations allow for a comprehensive assessment of the sensitivity of precipitation and PET to the PBL scheme and the sst_skin option under contrasting ENSO conditions.

4.3.3. Noah-MP Land surface model

Noah-MP represents a next-generation land surface modelling framework that extends the original Noah model by incorporating enhanced physical formulations and multiple parameterization options governing land–atmosphere interactions. These developments enable a more flexible representation of key surface processes, including vegetation dynamics, canopy stomatal resistance, soil moisture controls on transpiration, surface and subsurface runoff, groundwater processes, surface exchange coefficients, canopy radiative transfer, frozen soil hydrology, snow processes, and lower soil boundary conditions. A comprehensive description of the revised physical formulations and underlying theoretical advances is provided by Niu et al. (2011); Yang et al. (2011).

In this study, Noah-MP version 1.6 is employed, and the control configuration for twelve core land-surface processes is adopted following the recommendations of Yang et al. (2011); Ma et al. (2017); Gan et al. (2019) (Table 4.7). Independent evaluations further support the suitability of Noah-MP within the WRF-ARW modelling framework; for example, Achugbu et al. (2024) compared four land surface schemes across multiple regions in West Africa and identified Noah-MP as the most robust option for precipitation simulations.

Most third-generation land surface models represent vegetation state variables such as LAI either through vegetation-type-dependent parameterizations or by prescribing climatological values (Sellers et al., 1997; Pitman, 2003). Given vegetation's central role in controlling AET, particular emphasis is placed here on selecting vegetation process options. Noah-MP version 1.6 provides nine alternative vegetation schemes, which can be broadly grouped into dynamic and non-dynamic configurations (Table 4.6). These options primarily differ in how they treat LAI and vegetation fraction (FVEG). In the dynamic formulations, LAI evolves prognostically through a leaf growth model, whereas in the non-dynamic configurations, LAI is prescribed from monthly lookup tables or derived from external forcing data, such as ERA5.

For the representation of vegetation fraction, Noah-MP offers three alternative approaches: (1) direct specification from atmospheric forcing data, (2) diagnostic estimation as a function of LAI, and (3) assignment of a prescribed maximum vegetation fraction. Monthly LAI values for individual land-use categories are defined within the MPTABLE.TBL file, while maximum FVEG values are specified in the VEGPARM.TBL file. These configurable options allow for systematic sensitivity experiments targeting the role of vegetation processes in land–atmosphere coupling and evapotranspiration dynamics.

The method is employed to calculate the FVEG as a function of the LAI by the following

Table 4.6.: The available options for the vegetation process in Noah-MP version 1.6. The options chosen in this study are in bold.

Options	**Category**	**Method of calculating LAI**	**Method of calculating FVEG**
1	Non-dynamic	Using the monthly value of LAI	Using forcing data (ERA5)
2	Non-dynamic	Using the monthly value of LAI	$LAI = 1 - e^{-0.52 \times LAI}$
3	Non-dynamic	Using the monthly value of LAI	Using the maximum FVEG
4	**Non-dynamic**	**Using the ERA5 forcing data**	**Using forcing data (ERA5)**
5	Non-dynamic	Using the ERA5 forcing data	$LAI = 1 - e^{-0.52 \times LAI}$
6	Non-dynamic	Using the ERA5 forcing data	Using the maximum FVEG
7	**Dynamic**	**Estimated based on the dynamic leaf model**	**Using forcing data (ERA5)**
8	Dynamic	Estimated based on the dynamic leaf model	$LAI = 1 - e^{-0.52 \times LAI}$
9	Dynamic	Estimated based on the dynamic leaf model	Using the maximum FVEG

equation:

$$FVEG = 1 - e^{-0.52 \times LAI} \quad (1)$$

The dynamic vegetation configurations implemented in Noah-MP rely on the Ball–Berry stomatal conductance formulation (Ball et al., 1987) and incorporate a prognostic LAI growth model originally proposed by Dickinson et al. (1998). This vegetation module couples photosynthetic carbon assimilation with vegetation structural dynamics through two interlinked components. The first component, following the framework of Collatz et al. (1991), explicitly represents photosynthesis for both sunlit and shaded leaves and provides the basis for dynamic leaf growth. The second component governs the allocation of assimilated carbon, accounting for respiratory losses and phenological development. To better represent stem-rich plants, Noah-MP further extends this framework by introducing a stem carbon balance equation (Yang and Niu, 2003). Through this formulation, the model explicitly simulates key biochemical and physiological processes, including carbon uptake via photosynthesis, the partitioning of assimilated carbon among multiple reservoirs (leaf, stem, wood, root, and soil), and respiration associated with each carbon pool. The calculation of leaf carbon mass, C_{leaf} (gm^{-2}), follows the formulation given below:

$$\frac{\partial C_{leaf}}{\partial t} = F_{leaf} \times A - (S_{cd} + T_{leaf} + R_{leaf}) \times C_{leaf} \quad (2)$$

where A represents the total carbon uptake rate of both sunny and shaded leaves ($\mathrm{gm}^{-2}\mathrm{s}^{-1}$); F_{leaf} is the proportion of absorbed assimilated carbon designated for the leaf; S_{cd} represents the mortality rate attributable to cold and drought stressors; T_{leaf} is the rate of leaf turnover due to senescence, herbivory, or mechanical loss; and R_{leaf} represents the rate of leaf turnover resulting from senescence, herbivory, or mechanical loss. A simplified representation of the above formulation is given by:

$$C_{leaf} = C_{leaf} + (NPP_{leaf} - T_{leaf} - S_{cd}) \times dt \quad (3)$$

where NPP_{leaf} is the leaf net primary productivity ($\mathrm{gm}^{-2}\mathrm{s}^{-1}$), the LAI ($\mathrm{m}^2\mathrm{m}^{-2}$) is derived from the C_{leaf} via a vegetation-type-dependent statistic known as leaf area per unit mass APU_{leaf} ($\mathrm{m}^2\mathrm{g}^{-1}$).

$$LAI = C_{leaf} \times APU_{leaf} \quad (4)$$

All available options for the vegetation process in Noah-MP version 1.6 are listed in Table 4.6. To identify a suitable vegetation option in the Noah-MP model, we employed two options in this study: option 4 (non-dynamic) and option 7 (dynamic). Since the Noah-MP model simulates LULCC effects within the WRF-ARW model, we conducted two experiments using the MODIS and LU2 LULC datasets to understand how each component of AET responds to these options. The experiments for the comparison of the vegetation process and the LULC datasets are summarized in Table 4.8.

Table 4.7.: Noah-MP Parameterization schemes selected for the experiments

Subprocess	**Options selected**	**Description**
Vegetation process	4, 7	Option 4: It calculates the LAI and FVEG using forcing data. Option 7: It calculates the LAI and FVEG using the growth model proposed by Dickinson et al. (1998).
Canopy stomatal resistance	1	Option 1: It establishes a mechanistic coupling between photosynthesis and transpiration by relating stomatal conductance to CO_2 fluxes through the stomata (Ball et al., 1987).
Plant water stress threshold	1	Option 1: The soil moisture control on stomatal resistance is parameterized as an explicit function of soil water availability (Chen and Dudhia, 2001).
Runoff and groundwater	3	Option 3: Infiltration is parameterized as a function of near-surface soil moisture and soil texture, while surface runoff is diagnosed as the residual of precipitation after infiltration in the model (Schaake et al., 1996).
Surface layer exchange coefficients	2	Option 2: It neglects the zero-displacement height and instead applies distinct roughness length values for heat and momentum (Chen et al., 1997).
Radiation transfer	3	Option 3: It applies a two-stream approximation to the FVEG, while the canopy gap probability is given by 1-FVEG.
Super-cooled liquid water in frozen soil	1	Option 1: It adopts a generalized formulation of the freezing-point depression relationship (Niu and Yang, 2006).
Frozen soil permeability	2	Option 2: It derives hydraulic properties from the liquid water content (Koren et al., 1999).
Snow surface albedo	2	Option 2: It represents snow surface albedo by incorporating the effects of fresh snow and snow age (Verseghy, 1991).
Rain and snow partitioning	1	Option 1: It follows the functional formulation proposed by Jordan (1991).
Surface resistance to evaporation	1	Option 1: It represents the influence of plant litter cover on water vapor exchange and incorporates the effects of under-canopy atmospheric stability on canopy-level turbulent resistance (Sakaguchi and Zeng, 2009).

Table 4.8.: Summary of the WRF-ARW experiments for the intercomparison of the LULC dataset and vegetation process option. For all experiments, the Mellor-Yamada-Nakanishi-Niino Level 2.5 PBL scheme, the MYNN surface layer scheme, the WRF single moment 6-class microphysics scheme, and the explicit convection scheme are used.

Experiment name	Vegetation process	LU dataset
WRF-MYNN2.5-ON	7	MODIS
WRF-MYNN2.5-OFF	4	MODIS
WRF-LU2-ON	7	LU2
WRF-LU2-OFF	4	LU2

4.4. Methods

4.4.1. Potential evapotranspiration and actual evapotranspiration estimation

The presented analyses count on the evaluation of PET using both observation data from stations and model simulations using the WRF-ARW model. In both cases, the Penman-Monteith equation (Shuttleworth, 1993) is used for calculating PET:

$$PET = \frac{\triangle}{\triangle+\gamma} \times (R_n + A_h) + \frac{\gamma}{\triangle+\gamma} \times \frac{6.43 \times (1+0.536 \times U_2) \times D}{\lambda} \quad (5)$$

where PET is the daily PET in mm day $^{-1}$, $\triangle$ is the slope of the saturation vapor pressure curve in kPa °C^{-1}, R_n is the surface net radiation in MJ m^{-2} day^{-1}, A_h is the energy advected to the water body, which is ignored in this study, U_2 is the near-surface wind speed at 2-m height in m s^{-1}, D is the vapor pressure deficit in kPa, γ is the psychrometric coefficient in kPa °C^{-1} and λ is the latent heat of water vaporization in MJ kg^{-1}. Since U_2 is not directly available, it is determined from wind speed at 10-m height as follows:

$$U_2 = \frac{4.87}{\ln(67.8 \times 10 - 5.42)} \times U_{10} \quad (6)$$

where U_{10} is the wind speed at 10-m height in m s^{-1}.

The approach to determine R_n differs between station and model data. For station data, R_n is determined as:

$$R_n = 0.77 \times R_s - 0.5 \times \sigma \times (T_{max,k}^4 + T_{min,k}^4) \times (0.34 - 0.14 \times \sqrt{e_a}) \times (1.35 \times \frac{R_s}{R_{s0}} - 0.35) \quad (7)$$

$$R_s = R_a \times (a + b \times \frac{n}{N}) \quad (8)$$

$$R_{s0} = R_s \times (0.75 + 2 \times 10^{-5} \times z) \quad (9)$$

where R_s is the solar radiation in MJ m^{-2} day^{-1},σ is the Stefan-Boltzmann constant for a day (4.903×10^{-9} MJ K^{-4} m^{-2} day^{-1}), $T_{max,k}$ and $T_{min,k}$ are the maximum and minimum temperature at 2 m height in K, e_a is the actual vapor pressure in kPa, R_{s0} is the clear-sky solar radiation in MJ m^{-2} day^{-1},

R_a is the extraterrestrial radiation in MJ m^{-2} day^{-1}, a and b empirical coefficients (a=0.25 and b=0.5), n is the actual sunshine duration in h, N is the maximum possible sunshine duration in h, and z is the station elevation above the sea in m.

For WRF-ARW simulations, R_n is determined through the accumulated net radiative flux at the surface field from 1200 UTC on the previous day to 1200 UTC on the current day.

$$R_{s0} = \sum_{t=-12}^{t=12} R_{swu} + R_{swd} + R_{lwu} + R_{lwd} \quad (10)$$

where R_{swu} is the upward shortwave radiation, R_{swd} is the downward shortwave, R_{lwu} is the upward longwave radiation, and R_{lwd} is the downward longwave radiation (all at the surface and in MJ m^{-2}).

As Donohue et al. (2010); Dai (2011) previously reported, the Penman-Monteith formula outperforms other formulas for estimating PET.

The AET from the WRF-ARW model was extracted from the Noah-MP model. It is the sum of three components: direct evaporation, evaporation from the canopy, and transpiration.

4.4.2. Evaluation methods

To statistically compare the performance of each WRF-ARW experiment against the gridded products, PET and precipitation fields from the WRF-ARW model output were first remapped to 0.25° spatial resolution to match the TMPA and ERA5 grids and to 0.05° spatial resolution to match the CHIRPS v2.0 grid using conservative remapping (Jones, 1999). After remapping, these data have been evaluated based on three basic statistical indices, the correlation coefficient, Root Mean Square Error (RMSE), and percent bias (PBIAS), which are defined as:

$$CC = \frac{\sum_{i=1}^{n}(O_i - O)(P_i - P)}{\sqrt{\sum_{i=1}^{n}(O_i - O)^2}\sqrt{\sum_{i=1}^{n}(P_i - P)^2}} \quad (11)$$

$$RMSE = \sqrt{\frac{1}{n}\sum_{i=1}^{n}(P_i - O_i)^2} \quad (12)$$

$$PBIAS = \frac{\sum_{i=1}^{n}(P_i - O_i)}{\sum_{i=1}^{n}(O_i)} \times 100 \quad (13)$$

where n is the number of samples, O_i is the observed precipitation or PET, and P_i is the simulated precipitation or PET from WRF-ARW output.

With respect to the statistical evaluation against station data, the simulated precipitation, PET, and AET were interpolated with values at the closest four grid points to the station locations. Instead of evaluating by three separate indices, all indices are represented in a Taylor diagram (Taylor, 2001), which combines these three values into a single point. To simplify comparisons across variables with differ-

ent units, the RMSE and standard deviation have been normalized by each variable's observed standard deviation before plotting (Taylor, 2001). The correlation coefficient values indicate the temporal and spatial similarity between the observations at the station and the simulated precipitation or PET from the WRF-ARW model. In the diagram, the azimuthal angle corresponds to the correlation coefficient. The dashed line, denoted as "REF", represents the normalized standard deviation of the observations, while the dotted semicircles emanating from the intersection between the observational standard deviation and the horizontal axis correspond to contours of normalized RMSE. Experiments with the smallest RMSE are highlighted with a color-filled background of the number indicating the station location. Locations with negative correlations or standard deviations greater than 1.65 are shown as text at the bottom of each Taylor diagram

In southern Vietnam, precipitation exhibits strong seasonality (Phan et al., 2009; Tuan, 2019). For this reason, the performance of each WRF-ARW experiment in simulating daily precipitation is evaluated for the dry season, the rainy season, and the whole year. In addition, intraseasonal oscillations play a vital role in modulating rainfall in Vietnam, with two dominant modes of oscillation: 10–20 days and 20–60 days (Van der Linden et al., 2016; Truong and Tuan, 2018, 2019). Consequently, the performance of each experiment on simulating 5 and 10 days of accumulated precipitation is also evaluated.

Following previous studies of Takahashi et al. (2010); Jin et al. (2016); Li et al. (2020a), to describe the characteristics of the diurnal cycle of precipitation over the Ca Mau Peninsula, three parameters were calculated from both model data and the TMPA product at each 3-hour time slot, including rainfall frequency, rainfall amount, and rainfall intensity. The rainfall frequency is defined as the percentage of time during which a measurable amount of rainfall falls during the analysis period, while rainfall intensity is the mean precipitation rate during the precipitating time. The rainfall amount is the product of rainfall intensity and rainfall frequency. The threshold for measurable rainfall rate used in this study is 0.2 mm h^{-1}. We calculated the parameters at each point during the rainy season (May–October), which is the period during which the diurnal cycle of precipitation is most pronounced in the study region.

5. Impact of physical parameterization on simulating freshwater flux over the Ca Mau Peninsula

This section investigates the influence of physical parameterization schemes, particularly PBL parameterizations, on the simulation of daily precipitation (including its diurnal cycle) and daily PET over the Ca Mau Peninsula. The primary objective is to determine the optimal physical configuration for the WRF-ARW model to simulate the freshwater flux over this region. In addition, sensitivity experiments are conducted to evaluate the impacts of other key physical parameterizations, including the activation of the sst_skin option, the choice of cumulus convection scheme, and the dynamic vegetation option within the Noah-MP land surface model.

5.1. Role of the sst_skin option on simulated daily precipitation

The section discusses the impact of the sst_skin option on simulated daily precipitation. The difference in PBIAS and RMSE against TMPA between daily precipitation for simulation WRF-MYNN2.5-s (not activating the sst_skin option) and simulation WRF-MYNN2.5 (activating the sst_skin option) is shown in Figure 5.1. Whereas the discrepancies in RMSE between the two experiments over the Ca Mau Peninsula are insignificant, with values less than 2 mm day^{-1} in both seasons, those in PBIAS are evident, ranging from 10% to 40%, especially during the rainy season. In addition, it is critical to note that, over the surrounding oceans of the Ca Mau Peninsula, the differences also reach 10–40% in the PBIAS of daily precipitation between the WRF-MYNN2.5-s and WRF-MYNN2.5 simulations in the rainy season. This suggests that improvements in rainfall simulation are not limited to land areas but also extend to adjacent ocean regions, where diurnal SST variability has a more direct influence on surface heat and moisture fluxes. These findings underscore the importance of accurately representing SST diurnal variations for simulating precipitation over coastal and peninsular areas.

5.2. Role of the cumulus scheme on simulated daily precipitation

This section evaluates the sensitivity of simulated precipitation using the WRF-ARW model to the choice of cumulus convection parameterization. The selection of microphysics and cumulus schemes is widely recognized as a critical factor governing the accuracy of precipitation simulations (Li et al., 2017).

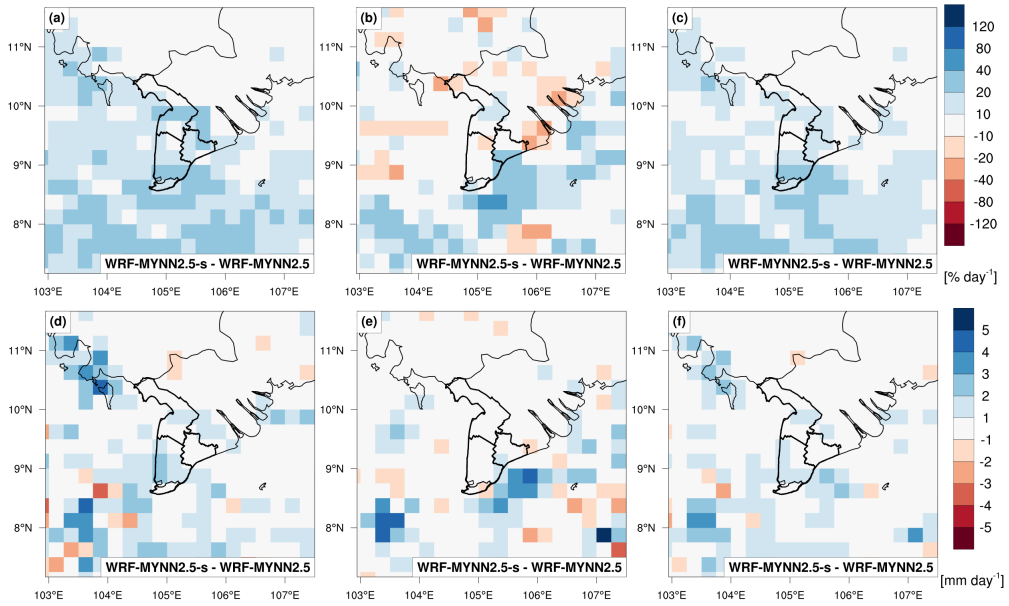

Figure 5.1.: The difference in PBIAS against TMPA between simulated daily rainfall of WRF-MYNN2.5-s and WRF-MYNN2.5 in (a) rainy seasons, (b) dry seasons, and (c) whole years in 2007, 2013, and 2015. (d-f) Same as in (a-c) but for RMSE against TMPA.

Table 5.1 compares the RMSE and PBIAS of simulated daily precipitation of the WRF experiments with different cumulus schemes over the Ca Mau Peninsula in 2015. During the rainy season and for the annual period, the experiment using explicit convection (WRF-MYNN2.5) exhibits the lowest RMSE values, at 17.62 and 13.54 mm day^{-1}, respectively. In contrast, during the dry season, the experiment using the new simplified Arakawa–Schubert scheme (WRF-MYNN2.5-AKW) achieves the smallest RMSE, at 6.52 mm day^{-1}.

Additional insight into model performance is provided through Taylor diagram analysis (Fig.

Table 5.1.: PBIAS and RMSE of simulated daily rainfall for one experiment explicitly simulating convection (without using the cumulus scheme) and five experiments using different cumulus parameterization schemes compared to measurements at 24 stations in the three southern provinces in 2015. Bold numbers indicate the experiment with the lowest RMSE values.

Experiment	**WRF-MYNN2.5**	**WRF-MYNN2.5-KF**	**WRF-MYNN2.5-BMJ**	**WRF-MYNN2.5-GL**	**WRF-MYNN2.5-AKW**	**WRF-MYNN2.5-G3D**
PBIAS(%)						
Rainy season	-20.22	113.45	-21.40	-17.21	23.08	50.49
Dry season	-41.73	51.19	25.76	-33.77	32.68	22.72
Year	-23.64	103.55	-22.09	-19.85	24.61	46.07
RMSE(mm)						
Rainy season	**17.62**	25.21	20.13	18.23	30.72	18.91
Dry season	7.44	7.57	6.81	7.97	**6.52**	7.35
Year	**13.54**	18.63	15.05	13.82	22.23	14.36

A.1). Figure A.1 illustrates Taylor diagrams for (a) daily, (b) 5-day accumulated, and (c) 10-day accumulated precipitation across the different experiments. The results indicate that WRF-MYNN2.5 consistently attains the highest correlation coefficients and the lowest RMSE values for daily, 5-day, and 10-day precipitation, outperforming the other experiments.

Taken together, the results suggest that the WRF-MYNN2.5 configuration provides the most robust performance among the tested experiments over the Ca Mau Peninsula. Accordingly, the explicit convection scheme is adopted in the subsequent analyses.

5.3. Role of the dynamic vegetation option on simulated actual evapotranspiration

A major advancement of the Noah-MP land surface model is the integration of a dynamic vegetation scheme that allows for prognostic representation of plant phenology, LAI, and canopy stomatal resistance. This section evaluates the sensitivity of simulated AET to the activation of the dynamic vegetation option in Noah-MP.

Figure 5.2 illustrates the monthly evolution of LAI in 2007 derived from four WRF-ARW exper-

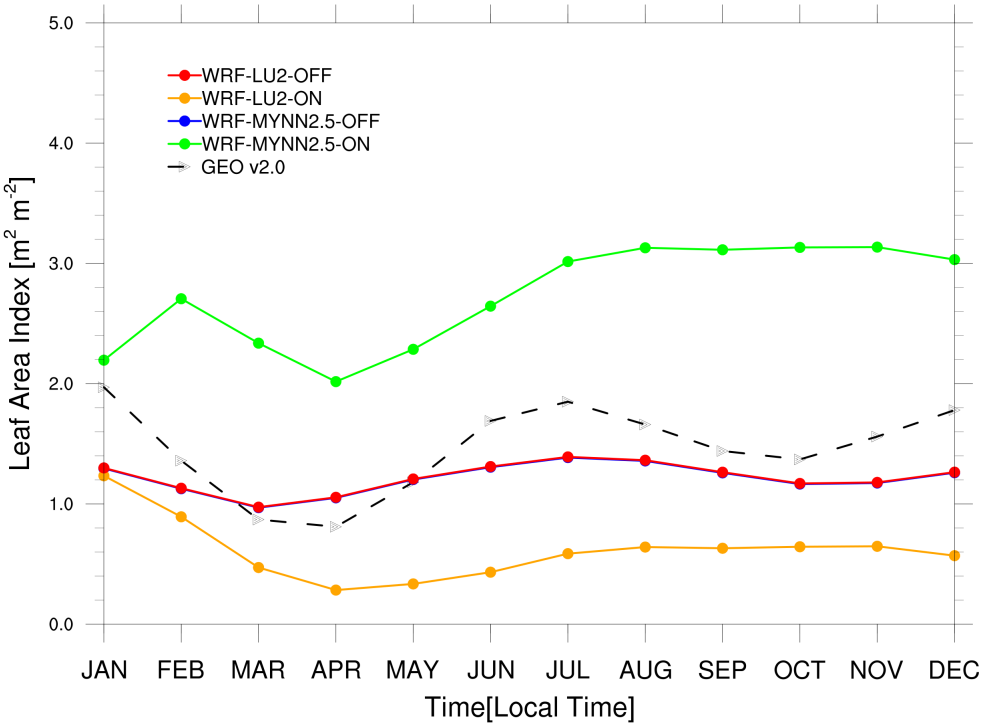

Figure 5.2.: Time series of monthly LAI for GEO v2.0 (black dashed line), experiments WRF-MYNN2.5-ON (yellow line), WRF-MYNN2.5-OFF (blue line), WRF-LU2-ON (green line) and WRF-LU2-OFF (red line) in 2007.

iments listed in Table 4.8 and from the GEO v2.0 dataset over the Ca Mau Peninsula. In general, all simulations can reasonably mimic the 12-month evolution of LAI over the Ca Mau Peninsula. They can

capture the suppressed LAI in March, but only the WRF-LU2-ON experiment can reproduce the timing of the LAI peak in January. Evidently, the simulated LAI values from two experiments, including WRF-MYNN2.5-OFF and WRF-LU2-OFF, which used different LULC datasets but the same non-dynamic option for the vegetation process, were similar to each other (the blue line and the red line in Fig. 5.2). This finding suggests that updating LULC information alone does not significantly impact LAI simulations when the non-dynamic vegetation option is employed.

Taken together, these results indicate that the dynamic vegetation option is crucial for accurately simulating LAI and leading to AET over the Ca Mau Peninsula, particularly when updated LULC datasets are used.

Figure 5.3 presents the monthly variations of individual AET components, consisting of canopy

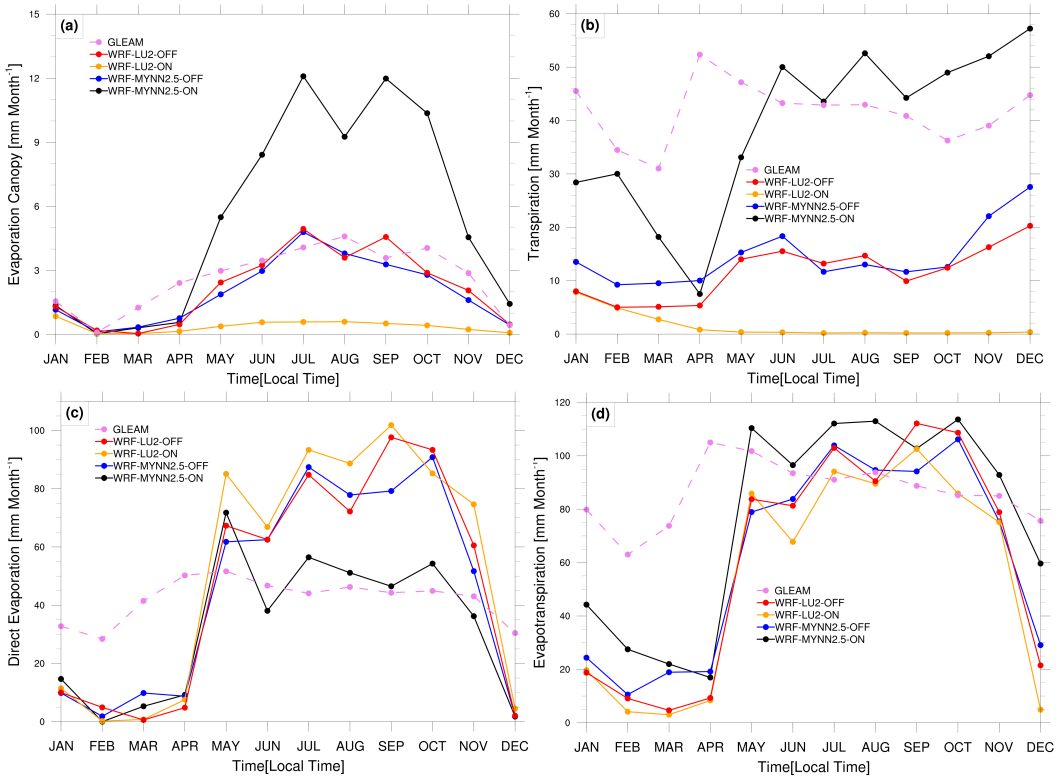

Figure 5.3.: Time series of monthly (a) evaporation canopy, (b) transpiration, (c) direct evaporation, and (d) AET for experiments WRF-MYNN2.5-ON (black line), WRF-MYNN2.5-OFF (blue line), WRF-LU2-ON (green line), WRF-LU2-OFF (red line), and GLEAM (violet dashed line) in 2007.

evaporation, (b) transpiration, (c) direct soil evaporation, and (d) total AET from the four WRF-ARW experiments and the GLEAM v3.5 dataset over the Ca Mau Peninsula in 2007. In general, canopy evaporation contributes the smallest share to total AET, whereas direct evaporation accounts for the largest share. Consistent with the LAI results, the WRF-MYNN2.5-OFF and WRF-LU2-OFF experiments exhibit similar magnitudes across all AET components. In contrast, the largest discrepancies between all experiments arise in the transpiration component, particularly between the WRF-MYNN2.5-ON and WRF-LU2-ON experiments. This highlights that when dynamic vegetation is enabled, the choice of

LULC dataset substantially influences transpiration and, consequently, total AET. The discrepancies between model simulations and the GLEAM v3.5 dataset are most pronounced during the dry season, especially from December to January.

5.4. Role of the planetary boundary layer parameterization schemes on simulated daily precipitation

The section illustrates the impact of the PBL parameterization schemes on simulated daily precipitation over the Ca Mau Peninsula. The three PBL parameterization schemes to be considered are ACM2, MYNN2.5, and MYJ.

Figures 5.4 and 5.5 present the PBIAS and RMSE of daily precipitation for simulation WRF-

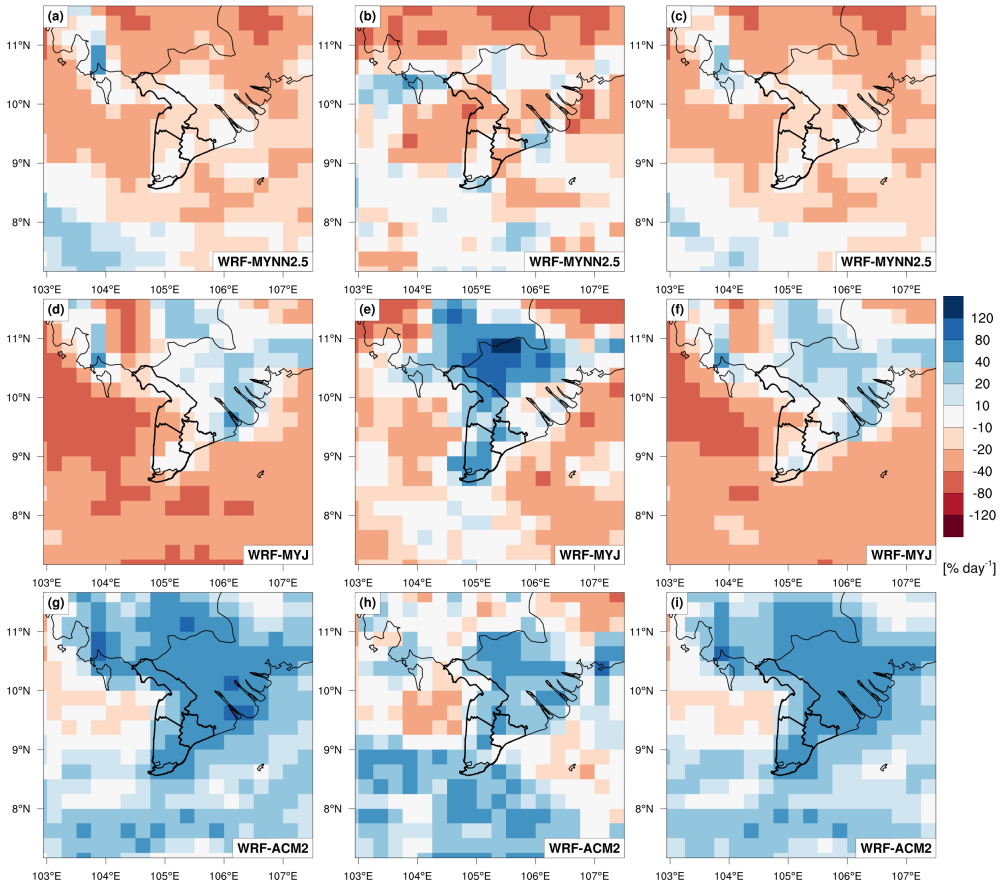

Figure 5.4.: The performance of WRF-ARW experiments using different PBL parameterization schemes is illustrated by the PBIAS of daily rainfall relative to TMPA for the rainy (first column), dry (second column), and annual (third column) periods, in average for the years 2007, 2013, and 2015. Panels (a–c), (d–f), and (g–i) correspond to results from the WRF-MYNN2.5, WRF-MYJ, and WRF-ACM2 experiments, respectively.

MYNN2.5, WRF-MYJ, and WRF-ACM2 for the period 2007–2013–2015 against TMPA. Particularly, our WRF-ACM2 experiments with the non-local PBL parameterization scheme ACM2 produce much

more precipitation over the Ca Mau Peninsula and the surrounding ocean in both the dry and rainy seasons, with PBIAS ranging from 10% to 40% over the ocean region and 40% to 80% over the Ca Mau Peninsula. These results are consistent with the findings of Wang et al. (2014) and can be attributed to enhanced low-level southwesterly flow associated with the East Asian summer monsoon.

For the two experiments employing local PBL parameterization schemes (WRF-MYJ and WRF-

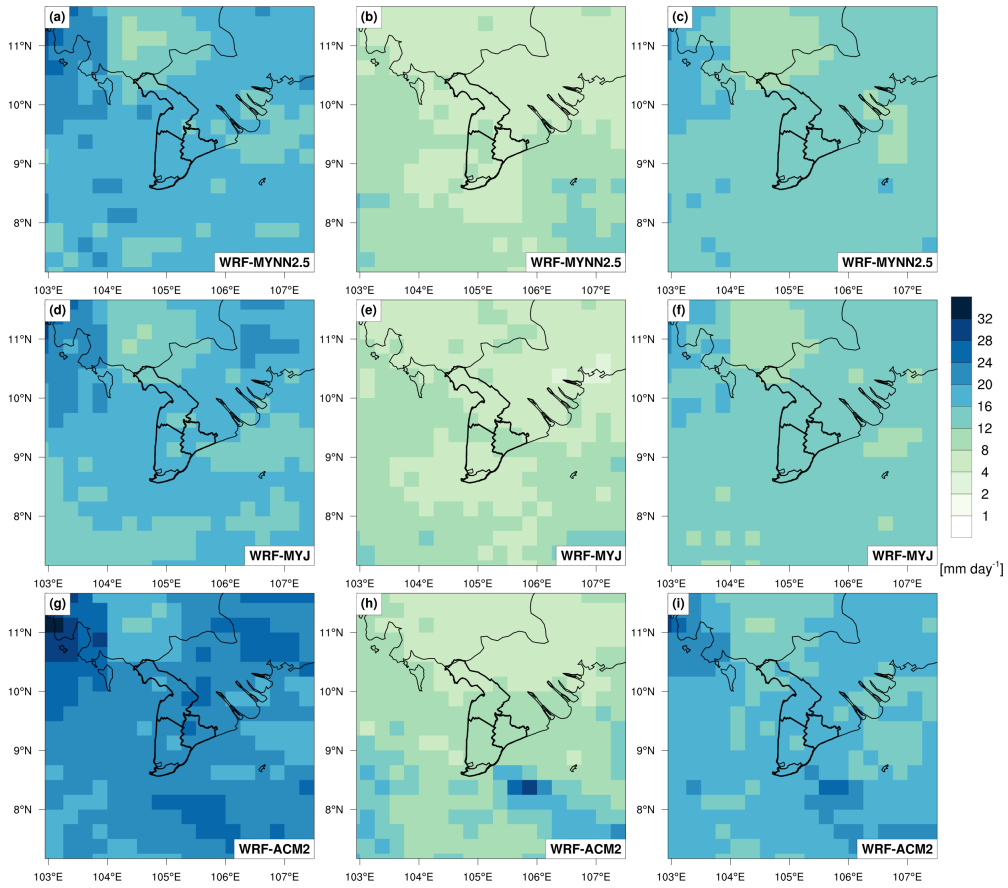

Figure 5.5.: Same as in Figure 5.4 but for RMSE of simulated daily rainfall.

MYNN2.5), contrasting PBIAS in simulated rainfall is evident over the Ca Mau Peninsula. WRF-MYNN2.5 systematically underestimates precipitation in both the dry and rainy seasons, with negative PBIAS values ranging from approximately -10% to -20%. In contrast, WRF-MYJ exhibits a pronounced seasonal dependence, with daily rainfall being substantially overestimated during the dry season, resulting in PBIAS values ranging from 20% to 80%. Conversely, an underestimation is observed during the rainy season, with PBIAS ranging from -20% to 10%. As shown in Fig. 5.5, the differences in RMSE against TMPA between WRF-MYJ and WRF-MYNN2.5 are minor in both seasons. RMSE values for both experiments range from approximately 16–20 mm day^{-1} during the rainy season and 4–8 mm day^{-1} during the dry season. By contrast, WRF-ACM2 underperforms, exhibiting larger errors with RMSE values of about 20–24 mm day^{-1} in the rainy season and 8–12 mm day^{-1} in the dry season.

Figures A.2 and A.3 report the PBIAS and RMSE of daily precipitation for the WRF-MYNN2.5, WRF-MYJ, and WRF-ACM2 simulations for the period 2007–2013–2015 against CHIRPS v2.0. The CHIRPS v2.0 dataset benefits from a high spatial resolution of 0.05^o, which enhances its ability to realistically represent precipitation characteristics (Tuo et al., 2016). Furthermore, Guo et al. (2017) demonstrated that CHIRPS v2.0 has a reasonable ability to identify and characterize drought events; thus, CHIRPS v2.0 is a reliable dataset, especially during the dry season. It is important to note that the daily rainfall in this case was accumulated over 24 hours, starting at 00:00 UTC (07:00 LT). There are no significant differences in PBIAS and RMSE between WRF experiments and the TMPA and CHIRPS v2.0 datasets, despite the CHIRPS v2.0 resolution being finer than TMPA's. The simulated rainfall from WRF-ACM2 performs poorly in both the dry and rainy seasons, with the highest RMSE and positive PBIAS values over the Ca Mau Peninsula. WRF-MYNN2.5 underestimates rainfall in both the rainy and dry seasons, while WRF-MYJ underestimates rainfall in the rainy season but overestimates in the dry season.

To quantitatively assess the performance of each WRF experiment, the PBIAS and RMSE of simulated daily rainfall compared to measurements at 24 stations, CHIRPS v2.0, and TMPA products over the Ca Mau Peninsula are listed in Table 5.2. For the dry season, the WRF-MYNN2.5 experiment provides the smallest RMSE; conversely, the WRF-MYJ experiment reproduces the smallest RMSE in the rainy season. Over the entire year, the WRF-MYJ experiment shows the smallest RMSE; however, the differences in RMSE between the WRF-MYJ and WRF-MYNN2.5 experiments are negligible. In general, WRF-MYJ and WRF-MYNN2.5 experiments have comparable performance in simulating daily precipitation; the WRF-ACM2 experiment performs the worst.

Table 5.2.: PBIAS and RMSE of simulated daily rainfall compared to measurements at 24 stations, CHIRPS v2.0, and TMPA over the Ca Mau Peninsula in 2007, 2013, and 2015. Bold numbers indicate the experiments with the lowest RMSE values for each time period.

	PBIAS(%)			RMSE(mm)		
Experiment	**WRF-MYNN2.5**	**WRF-MYJ**	**WRF-ACM2**	**WRF-MYNN2.5**	**WRF-MYJ**	**WRF-ACM2**
Stations						
Rainy season	-16.14	-16.42	35.22	20.25	**19.84**	26.42
Dry season	-22.24	20.33	9.35	**9.70**	10.45	11.37
Year	-17.02	-17.02	30.73	15.89	**15.87**	20.36
CHIRPS v2.0						
Rainy season	-7.02	-10.00	47.72	16.92	**16.34**	24.30
Dry season	-29.20	11.70	0.70	**7.49**	8.63	9.66
Year	-11.32	-5.77	38.57	13.12	**13.10**	18.55
TMPA						
Rainy season	-8.12	-12.72	44.59	17.37	**17.13**	22.55
Dry season	-6.13	37.54	28.49	**7.47**	7.82	8.97
Year	-4.91	-3.85	43.79	13.37	**13.35**	17.23

Figure 5.6 presents the Taylor diagrams of daily, 5-day accumulated precipitation, and 10-day accumulated precipitation at 24 stations over the Ca Mau Peninsula in the dry season, rainy season, and the whole year for the period 2007–2013–2015. As shown in this figure, the correlation coefficients for daily precipitation in both the dry and rainy seasons across the three WRF experiments are relatively weak, at approximately 0.30. The normalized standard deviation of WRF-ACM2 is consistently the highest, ranging from 1.1 to 1.4. Based on the color-filled background, which indicates the experiment with the lowest RMSE, the experiment with the MYJ scheme outperforms the simulation of daily precipitation in both the rainy season and throughout the year. Regarding the 5-day accumulated precipitation, the correlation coefficients from the three experiments increase substantially, ranging from approximately 0.4 to 0.6. The standard deviation of WRF-ACM2 still has the highest values, ranging from 1.1 to 1.4, and experiment WRF-MYNN2.5 performs better than the other two experiments in both the dry season and throughout the year. For 10-day accumulated precipitation, the correlation coefficients across the three experiments range from 0.4 to 0.65, with WRF-MYJ performing best in both the rainy season and throughout the year. Taken together, these results suggest that WRF-MYNN2.5 has better skills compared to the others in the dry season, while WRF-MYJ outperforms in the rainy season.

For a detailed view of the performance of each experiment in simulating daily precipitation over

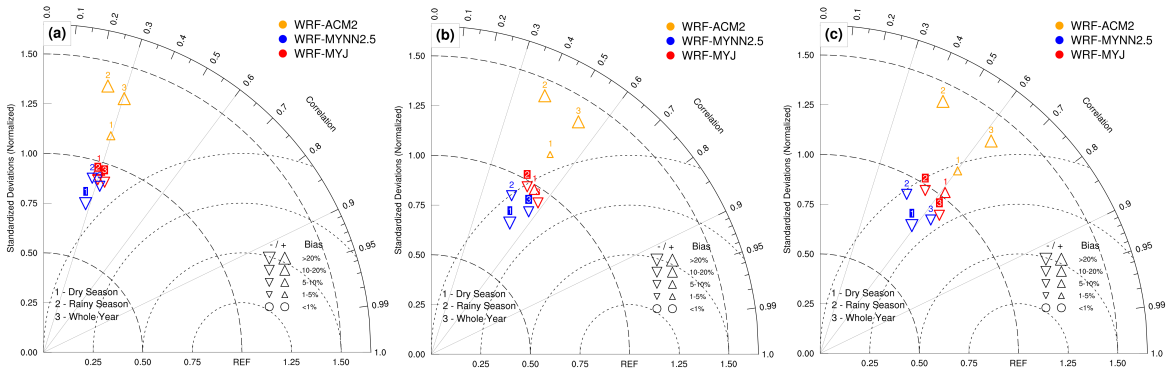

Figure 5.6.: The performance of WRF experiments employing different PBL parameterization schemes is assessed using Taylor diagrams for (a) daily, (b) 5-day, and (c) 10-day accumulated rainfall at 24 stations over the Ca Mau Peninsula. Results are shown for the WRF-MYJ (red symbols), WRF-MYNN2.5 (blue symbols), and WRF-ACM2 (orange symbols) experiments across the dry season, rainy season, and whole year for 2007, 2013, and 2015. Experiments with the smallest RMSE are highlighted with a color-filled background of the numbers indicating the reference period.

the Ca Mau Peninsula, Figure A.4 presents the Taylor diagram of daily precipitation for the separate years 2007, 2013, and 2015. Taken as a whole, all experiments show the best performance in 2015 (the year with strong El Niño conditions), with the highest correlation coefficient (ranging from 0.33 to 0.40) and the smallest normalized RMSE. In all three years, WRF-ACM2 has the worst performance, with the highest normalized standard deviation (ranging from 1.29 to 1.35) and the lowest correlation coefficient (ranging from 0.28 to 0.33). It is worth noting that in 2015 (a year with strong El Niño conditions) and 2007 (a year with strong La Niña conditions), WRF-MYNN2.5 performs well compared to the other

experiments. In contrast, in 2013 (a year with neutral conditions), WRF-MYJ has the best skill in simulating daily precipitation.

5.5. Role of the planetary boundary layer parameterization schemes and sst_skin option on simulated diurnal cycle of precipitation

In the current section, we next evaluate the diurnal cycle of precipitation simulated by all WRF-ARW experiments against the TMPA dataset, to explore the role of the PBL schemes and the sst_skin option on the simulated diurnal cycle of precipitation during rainy seasons over the Ca Mau Peninsula. For clarity, all analyses are presented in local time (LT; UTC+7), facilitating direct comparison of daytime and nighttime precipitation characteristics. Model-simulated rainfall was composited into 3-hourly intervals beginning at 00:00 LT, consistent with TMPA.

Firstly, the role of PBL parameterization schemes in simulating the diurnal cycle of precipitation during rainy seasons is investigated. Figure 5.7 displays the diurnal variations in rainfall frequency and rainfall amount averaged over the Ca Mau Peninsula during the rainy seasons of 2007, 2013, and 2015 from the WRF-ARW experiment with different PBL parameterization schemes and the sst_skin option activated. According to TMPA, rainfall frequency and intensity exhibit a pronounced afternoon maximum between 13:00 and 16:00 LT, in agreement with the findings of Takahashi et al. (2010), who identified an early-afternoon peak over coastal Indochina. The WRF-ARW simulations can reasonably mimic the 24-h evolution of rainfall, in terms of frequency and amount, although the rainfall frequency is generally underestimated. They can also capture the timing of the early afternoon peak in rainfall frequency and intensity, as well as the suppressed rainfall amount at night (22:00–01:00 LT), but fail to reproduce the suppressed rainfall frequency in the early morning (04:00–07:00 LT). Overall, all conducted gray-zone experiments show good performance in reproducing the diurnal cycle of precipitation. These

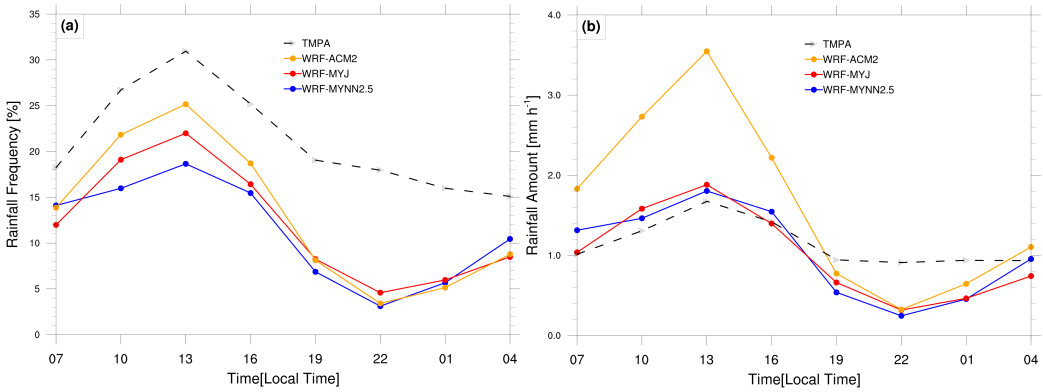

Figure 5.7.: Diurnal cycle of domain-averaged (a) rainfall frequency, and (b) rainfall amount over the Ca Mau Peninsula from TMPA (dashed black lines), WRF-ACM2 (orange lines), WRF-MYJ (red lines), and WRF-MYNN2.5 (blue lines) during the rainy seasons of 2007, 2013, and 2015.

results are consistent with recent findings by Lai et al. (2025), who demonstrated that high-resolution WRF simulations more accurately capture the diurnal cycle of summer rainfall over Mainland Southeast Asia, particularly along coastal and mountainous zones, than coarser reanalysis products.

It is found that the difference in the magnitude of diurnal rainfall between all experiments and

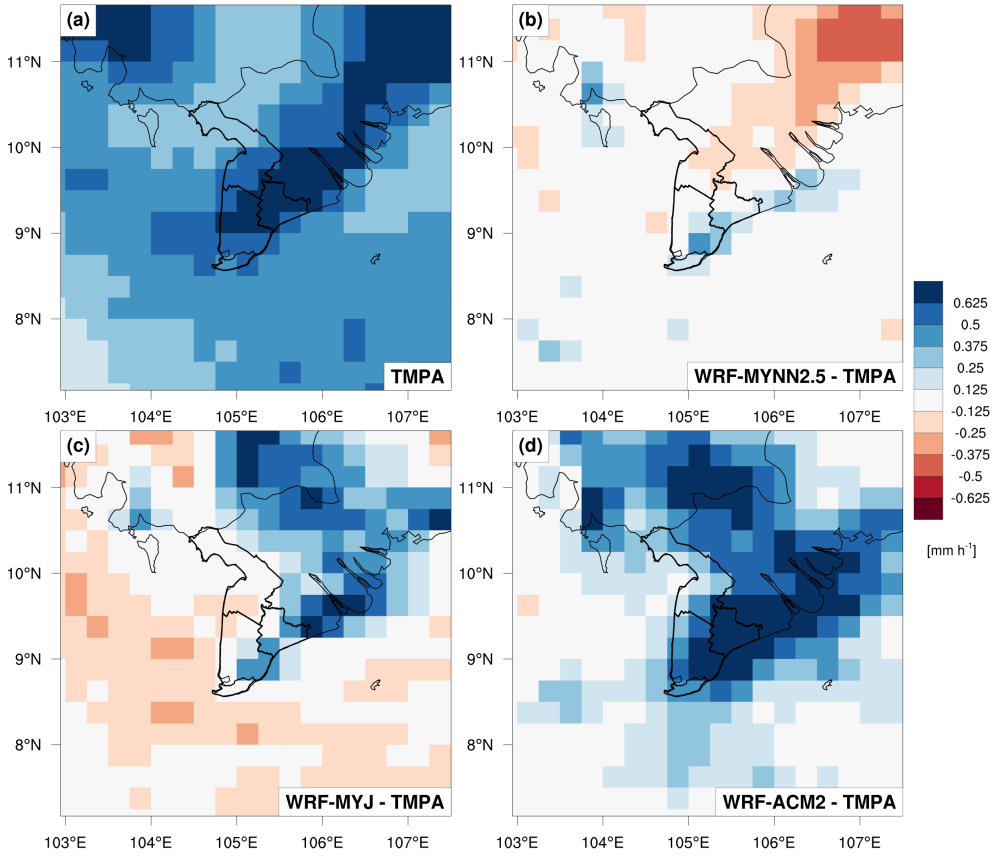

Figure 5.8.: (a) Mean 3-hourly TMPA rainfall intensity during the peak of the diurnal cycle (i.e, 13:00–16:00 LT) over the Ca Mau Peninsula during the rainy seasons of 2007, 2013, and 2015. Difference between the mean 3-hourly rainfall intensity in the same period from (b) WRF-MYNN2.5, (c) WRF-MYJ, and (d) WRF-ACM2 experiments and the TMPA average shown in (a).

TMPA is mainly attributed to the difference in nighttime (19:00–07:00 LT). No appreciable differences in simulated rainfall frequency are found among the three experiments. Conversely, simulated rainfall intensity from WRF-ACM2 is highly overestimated compared to TMPA and other experiments. Similar to the performance in simulating the seasonal variation of daily precipitation, the two experiments, WRF-MYNN2.5 and WRF-MYJ, can reproduce the diurnal cycle of rainfall more closely to the observed values over the Ca Mau Peninsula. Figure 5.8 details the 3-hour mean in 13:00–16:00 LT (peak of the diurnal cycle) of rainfall intensity for the rainy season from TMPA observation, and the difference with three experiments. The results reveal that, compared to other experiments, WRF-MYNN2.5 appears to reproduce rainfall intensity more realistically, with the smallest bias, especially over the western coastline of the Ca Mau Peninsula. This result suggests that WRF-MYNN2.5 is more likely to accurately

reproduce the convective systems that develop over the surrounding seas of the Ca Mau Peninsula and propagate to the western coastline.

To illustrate the tendency of diurnal rainfall cycle migration over the Ca Mau Peninsula during the rainy season, we use a Hovmöller diagram to capture the propagation along with its temporal evolution. The red box in Figure 4.1, whose long sides are roughly perpendicular to the western coastline of the Ca Mau Peninsula, was defined for the purpose of analyzing this propagation.

Figure 5.9 shows the Hovmöller diagram for the time-coastal distance cross-sections averaged

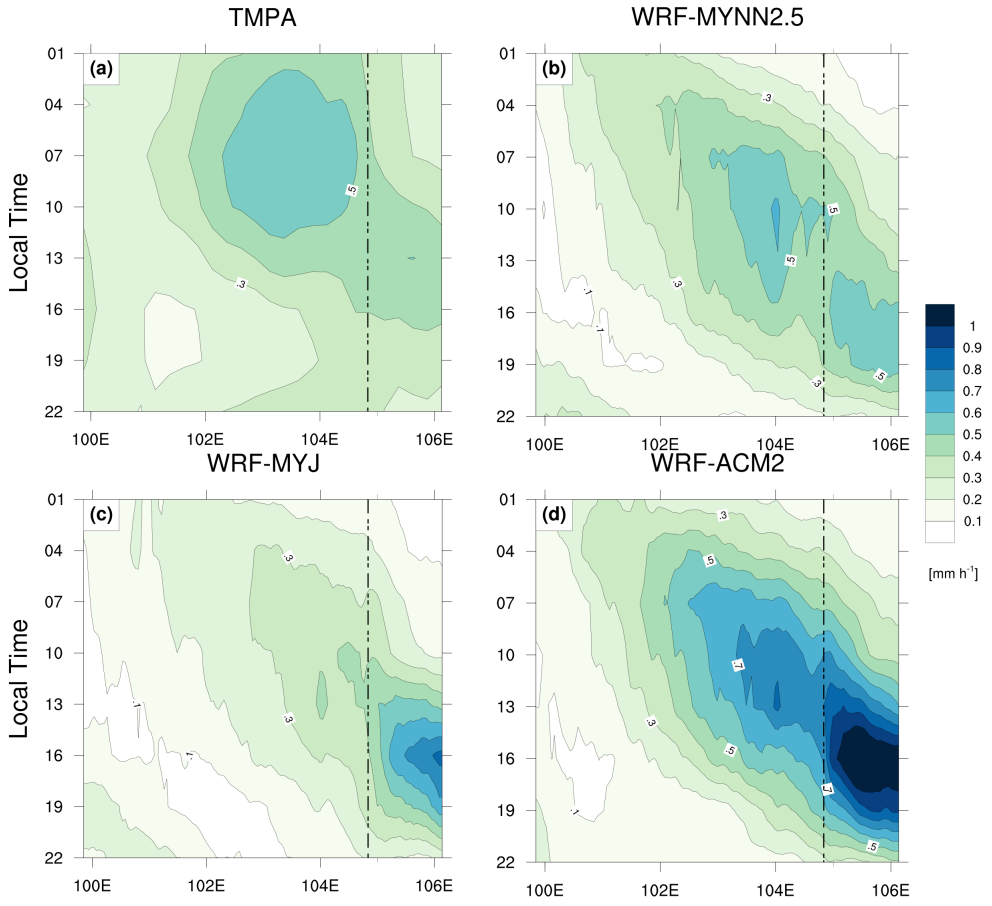

Figure 5.9.: Hovmöller diagrams of the mean diurnal cycles latitudinally averaged over 8.25–10.5°N, 99.875–106.125°E (Red rectangle in Figure 4.1) during the rainy seasons in 2007, 2013, and 2015 from (a) TMPA, and from (b) WRF-MYNN2.5, (c) WRF-MYJ, and (d) WRF-ACM2 experiments. Vertical dashed lines show the approximate location of the western coastline of the Ca Mau Peninsula.

along the coastal direction, based on TMPA as well as all WRF-ARW simulations for the aforementioned box. According to TMPA, it is possible to confirm an early morning peak over the eastern Gulf of Thailand, approximately 200 km from the western coastline of the Ca Mau Peninsula. This peak then migrates eastward along the coastline and into the inland area, resulting in a maximum by early afternoon. This early morning peak fits with the previous finding of Takahashi et al. (2010), who identified three early morning peaks over the Indochina peninsula area, including the eastern Bay of Bengal, the eastern Khorat Plateau, and the eastern Gulf of Thailand. It is found that WRF-MYNN2.5 produces a

rainfall peak over the eastern Gulf of Thailand at about 10:00–13:00 LT, which is three hours later than that in TMPA. The rainfall peak over the western coastline of the Ca Mau Peninsula between 13:00 and 16:00 LT corresponds well with TMPA, and the inland propagation afterwards is reasonably captured. The overall magnitude of the diurnal cycle in WRF-MYNN2.5 is also close to the observed. On the other hand, both WRF-MYJ and WRF-ACM2 fail to capture the above-mentioned diurnal features. In particular, WRF-MYJ produces the early morning peak that is too weak over the eastern Gulf of Thailand (with the underestimation of about 0.2 mm h^{-1} compared to TMPA; Fig. 5.9c) and the early afternoon peak that is too strong overland (with the overestimation of about 0.2 mm h^{-1} compared to TMPA). Whereas, WRF-ACM2 produces a morning peak which is three hours earlier and stronger over the eastern Gulf of Thailand (with the overestimation of about 0.1 mm h^{-1} compared to TMPA; Fig. 5.9d), and the early afternoon peak is much stronger overland (with the overestimation of about 0.5 mm h^{-1} compared to TMPA). Compared to other experiments, it is obvious that WRF-MYNN2.5 outperforms the other simulations in capturing the diurnal rainfall over the Ca Mau Peninsula.

Additionally, we inspect the performance of all WRF-ARW experiments without using the sst_skin option for simulating diurnal cycle migration over the Ca Mau Peninsula during the rainy season (Fig. A.5). Again, compared with experiments without using the sst_skin option, those using the sst_skin option simulate a more realistic magnitude of both the diurnal peak over the eastern Gulf of Thailand and overland. For instance, WRF-MYNN2.5-s produces an afternoon peak over the western coastline of the Ca Mau Peninsula, which is too early (10:00–13:00 LT; Fig. A.5b), whereas WRF-MYNN2.5 is able to accurately capture this one (Fig. 5.9b). Likewise, WRF-ACM2-s (Fig. A.5d) overestimates both the morning peak over the Gulf of Thailand by about 0.4 mm h^{-1} and the early afternoon peak overland by about 0.5 mm h^{-1}, while WRF-ACM2 overestimates the morning peak by about 0.1 mm h^{-1} (Fig. 5.9d).

Overall, the above results demonstrate the superior performance of the WRF-MYNN2.5 experiment in simulating daily precipitation and its diurnal cycle over the Ca Mau Peninsula. The MYNN2.5 PBL scheme, and activating the sst_skin option, will be used in all subsequent experiments.

5.6. Role of the planetary boundary layer parameterization schemes and sst_skin option on simulated daily potential evapotranspiration

This section attempts to attribute the differential performance between WRF-ARW simulations using different PBL parameterization schemes in simulating daily PET over the Ca Mau Peninsula.

Figures 5.10 and 5.11 show the PBIAS and RMSE of daily PET for simulations WRF-MYNN2.5, WRF-MYJ, and WRF-ACM2 for the period 2007-2013-2015 compared to ERA5. Yellow shading denotes ocean grid points for which PET values are not available. While the WRF-MYNN2.5 experiment has a negative bias in both dry and rainy seasons, the other two experiments tend to produce a positive bias in the rainy season and a negative bias in the dry season over the Ca Mau Peninsula. The RMSE of

daily PET over the Ca Mau Peninsula in the dry season is greater than in the rainy season by all three experiments (Table 5.3). Based on the RMSE, all three experiments exhibit comparable performances when compared with ERA5; the discrepancies are insignificant, with a maximum RMSE value of 1.33 mm day^{-1} and a minimum value of 1.29 mm day^{-1} (Table 5.3).

Our study provides further evidence of the performance of individual experiments in simulating

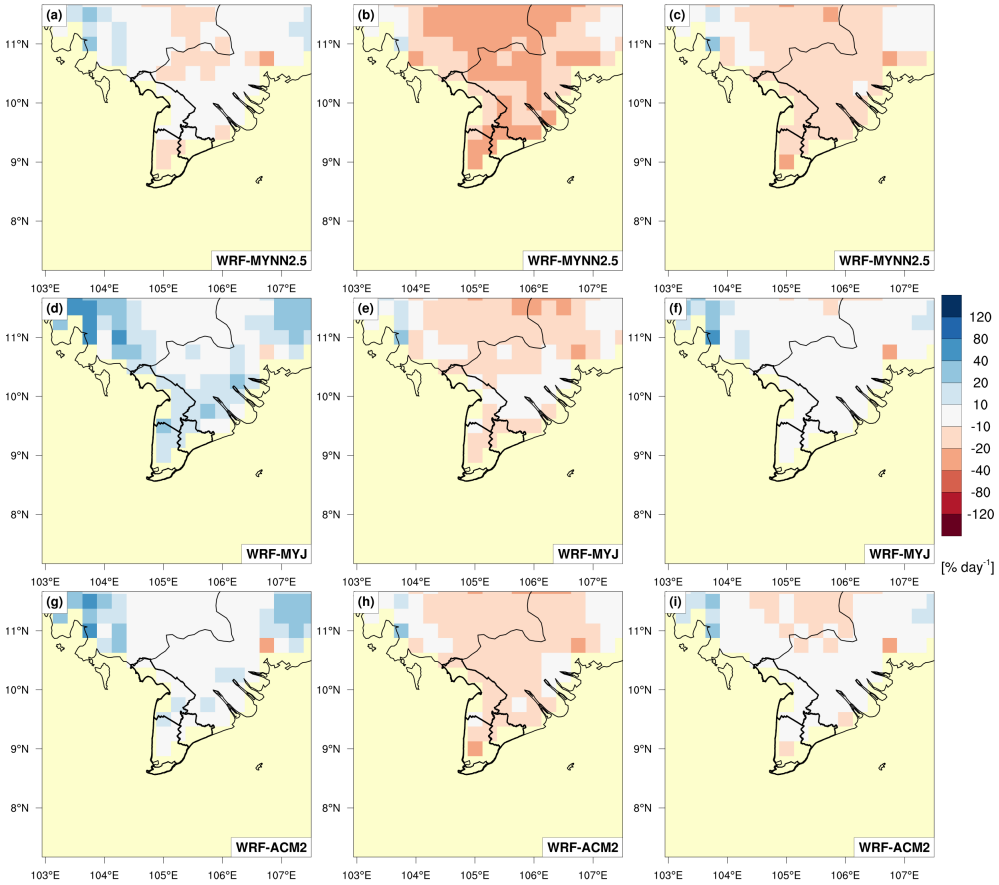

Figure 5.10.: Same as is in Figure 5.4 but for daily PET from the experiments compared to ERA5.

PET through validation with the DPET product. The key advantage of DPET products is their high spatial resolution, which enables them to capture PET spatial patterns more accurately across the Ca Mau Peninsula. Figures A.6 and A.7 present the PBIAS and RMSE of daily PET for each experiment relative to DPET. Generally, both experiments tend to produce a positive bias (overestimation) in the dry and rainy seasons; only the WRF-MYNN2.5 experiment produces a small negative bias in the dry season. In contrast to the comparison with ERA5, the RMSE of the daily PET over the Ca Mau Peninsula is larger in the rainy season than in the dry season in both experiments (see Table 5.3). The WRF-MYNN2.5 experiment achieves the smallest RMSE in dry and rainy seasons: 0.94 mm day^{-1} in the rainy season and 0.81 mm day^{-1} in the dry season.

Figure 5.12 presents the Taylor diagram of daily PET at three stations over the Ca Mau Peninsula for simulations WRF-MYNN2.5, WRF-MYJ, and WRF-ACM2 for the period 2007–2013–2015, com-

pared to PET calculated from the Penman-Monteith equation. Overall, all three experiments show better performance in the dry season than in the rainy season and exhibit negative biases (underestimation) in both seasons. The WRF-MYNN2.5 experiment exhibits the highest correlation coefficient value in both the dry season (about 0.65) and the rainy season (about 0.45). In addition, the WRF-MYNN2.5 experiment yields the smallest RMSE in both dry and rainy seasons, with values of approximately 1.25 mm day^{-1} in the rainy season and 1.15 mm day^{-1} in the dry season (see Table 5.3).

Wind speed at 10-m height and net radiation are the main variables that affect PET, and WRF-

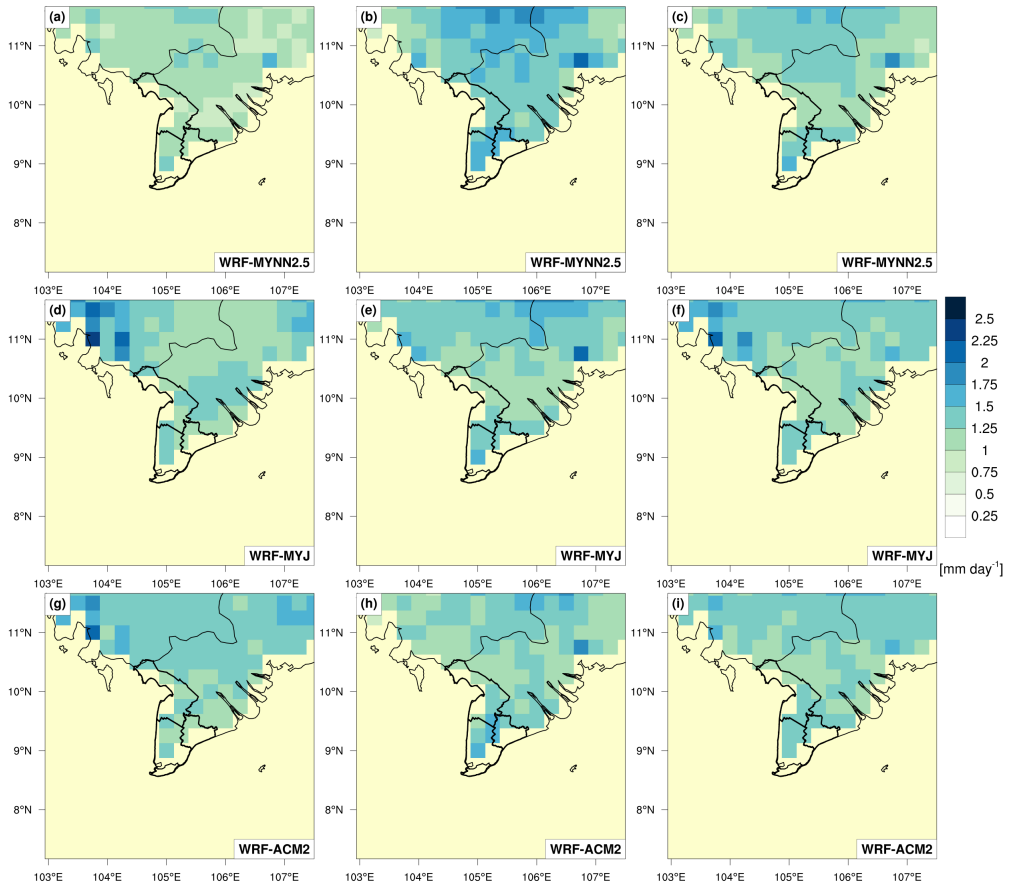

Figure 5.11.: Same as is in Figure 5.5 but for daily PET from the experiments compared to ERA5.

MYNN2.5 tends to simulate these values more accurately than WRF-MYJ and WRF-ACM2 (Table 5.4). The WRF-MYNN.2.5 experiment exhibits the smallest RMSE by 1.54 m s^{-1} on simulating wind speed at 10-m height, and 3.33 MJ m^{-2} on simulating net radiation. Generally, in both the rainy and dry seasons, net radiation is well simulated by all experiments, with the PBIAS ranging from -19% to 1%, and RMSE ranging from 3.27 to 3.97 MJ m^{-2}. However, all experiments have comparatively poor performance in simulating wind speed at 10-m height over the years, with PBIAS ranging from 51% to 66% during the rainy season and 73% to 87% during the dry season.

The high positive bias in wind speed at 10-m height, especially during the dry season, appears to be a major contributor to the bias in PET. We advocate the assumption that this bias is primarily driven

by land-use data that is not properly accounted for in our WRF model setup. In line with Xu et al. (2017); Bughici et al. (2019), our results demonstrate that wind speed at 10-m height bias plays a crucial role in driving biases in simulated PET.

Table 5.3 also presents the PBIAS and RMSE of simulated PET from all experiments compared

Table 5.3.: PBIAS and RMSE of simulated daily PET compared to station data (Penman-Monteith and GGI-3000), ERA5, and DPET over the Ca Mau Peninsula in 2007, 2013, and 2015. Bold numbers indicate the experiments with the lowest RMSE values for each time period.

	PBIAS(%)			RMSE(mm)		
Experiment	**WRF-MYNN2.5**	**WRF-MYJ**	**WRF-ACM2**	**WRF-MYNN2.5**	**WRF-MYJ**	**WRF-ACM2**
Stations (Penman-Monteith)						
Rainy season	-14.13	-8.79	-4.15	**1.26**	1.42	1.31
Dry season	-14.47	-16.25	-8.65	**1.15**	1.41	1.17
Year	-14.30	-12.64	-6.47	**1.21**	1.42	1.24
Stations (GGI-3000)						
Rainy season	-7.90	15.00	5.89	**1.08**	1.32	1.35
Dry season	-15.21	-4.62	-7.70	1.11	**1.01**	1.15
Year	-11.79	4.55	-1.35	**1.09**	1.17	1.25
ERA5						
Rainy season	-7.85	14.57	5.23	**1.09**	1.27	1.26
Dry season	-21.33	-11.41	-15.19	1.50	**1.31**	1.40
Year	-15.31	0.20	-6.06	1.31	**1.29**	1.33
DPET						
Rainy season	5.42	32.45	21.42	**0.94**	1.54	1.42
Dry season	-3.11	10.56	5.26	**0.81**	1.06	1.03
Year	0.85	20.76	12.79	**0.88**	1.32	1.24

to GGI-3000 data at the two stations, Ca Mau and Can Tho.

In the rainy season, the WRF-MYNN2.5 experiment generates the smallest RMSE (about 1.08

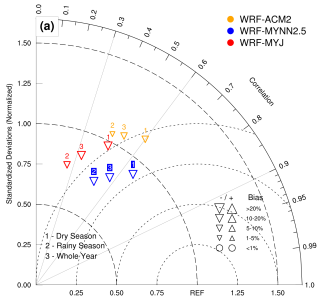

Figure 5.12.: Taylor diagram of daily PET for experiments WRF-MYJ (red symbols), WRF-MYNN2.5 (blue symbols), and WRF-ACM2 (orange symbols) at three stations over the Ca Mau Peninsula during the dry seasons, rainy seasons, and whole years in 2007, 2013, and 2015. Experiments with the smallest RMSE are highlighted with a color-filled background of the numbers indicating the reference period.

mm day^{-1}); meanwhile, in the dry season, the WRF-MYJ experiment exhibits the smallest RMSE (1.01 mm day^{-1}). Over the entire year, the WRF-MYNN2.5 experiment exhibits the best performance in sim-

ulating PET, with the smallest RMSE of 1.09 mm day^{-1}. In general, these results suggest that, similar to what is presented for precipitation, the WRF-MYNN2.5 experiment outperforms in capturing the PET over the Ca Mau Peninsula.

Synthesizing the results presented in Sections 5.1–5.6, this study identifies an optimal configu-

Table 5.4.: PBIAS and RMSE of simulated daily 10-m wind speed and net radiation compared to station data over the Ca Mau Peninsula in 2007, 2013, and 2015. Bold numbers indicate the experiments with the lowest RMSE values for each time period.

	PBIAS(%)			RMSE(mm)		
Experiment	**WRF-MYNN2.5**	**WRF-MYJ**	**WRF-ACM2**	**WRF-MYNN2.5**	**WRF-MYJ**	**WRF-ACM2**
10-m Wind speed						
Rainy season	51.1	66.44	56.04	**1.48**	1.84	1.64
Dry season	73.89	87.70	82.51	**1.59**	1.87	1.74
Year	61.48	76.12	68.09	**1.54**	1.85	1.69
Daily net radiation						
Rainy season	-10.87	-2.87	1.0	**3.27**	3.79	3.63
Dry season	-19.01	-15.71	-11.63	**3.39**	3.97	3.40
Year	-15.04	-9.45	-5.45	**3.33**	3.87	3.52

ration of physical parameterizations for simulating the freshwater flux over the Ca Mau Peninsula using the WRF-ARW model. The most suitable setup comprises the MYNN2.5 PBL scheme, the use of an explicit cumulus scheme, activation of the sst_skin option, and the dynamic vegetation option within the Noah-MP land surface model.

6. Evaluation of the WRF-ARW model performance in simulating the freshwater flux over the Ca Mau Peninsula

6.1. Preface

This section evaluates the performance of the WRF-ARW model, configured with the optimal set of physical parameterizations identified in the preceding section, in simulating precipitation and PET over the Ca Mau Peninsula for the period 2007–2016. Model results are assessed against available observational datasets. For precipitation, the validation is conducted with respect to both daily and the characteristics of the diurnal cycle. In addition, the two primary drivers of PET, including wind speed at 10-m height and net radiation, are also examined.

6.2. WRF-ARW model performance in simulating daily precipitation over the Ca Mau Peninsula

This section presents a validation of the daily precipitation simulated from the WRF-MYNN2.5 experiment against observational data over the Ca Mau Peninsula for the period 2007–2016. Figure 6.1 presents a comparison of the spatial distribution of mean daily precipitation during the rainy season, dry season, and for the annual mean over the period 2007–2016, as derived from the CHIRPS v2.0 dataset and simulated by the WRF-MYNN2.5 experiment.

Overall, the WRF-MYNN2.5 experiment successfully reproduces the dominant spatial characteristics of precipitation over the Ca Mau Peninsula. During the rainy season, the model captures both the spatial pattern and the magnitude of precipitation reasonably well when compared with CHIRPS v2.0. In particular, zones of enhanced rainfall along the western and southwestern coastlines are well represented, suggesting that the model adequately simulates the combined effects of the southwest monsoon circulation and land–sea interactions on rainfall generation. Nevertheless, a slight underestimation of precipitation is evident in several coastal and inland areas. In the dry season, both CHIRPS v2.0 and WRF-MYNN2.5 consistently indicate low precipitation across the entire Ca Mau Peninsula. For the annual mean, the WRF-MYNN2.5 simulation reproduces the overall spatial structure of precipitation, with regions of relatively higher and lower rainfall broadly consistent with CHIRPS v2.0. Despite some localized discrepancies, these results demonstrate the model's ability to realistically represent the regional-scale distribution of annual precipitation.

Figure 6.2 further illustrates the spatial patterns of PBIAS and RMSE for daily precipitation from

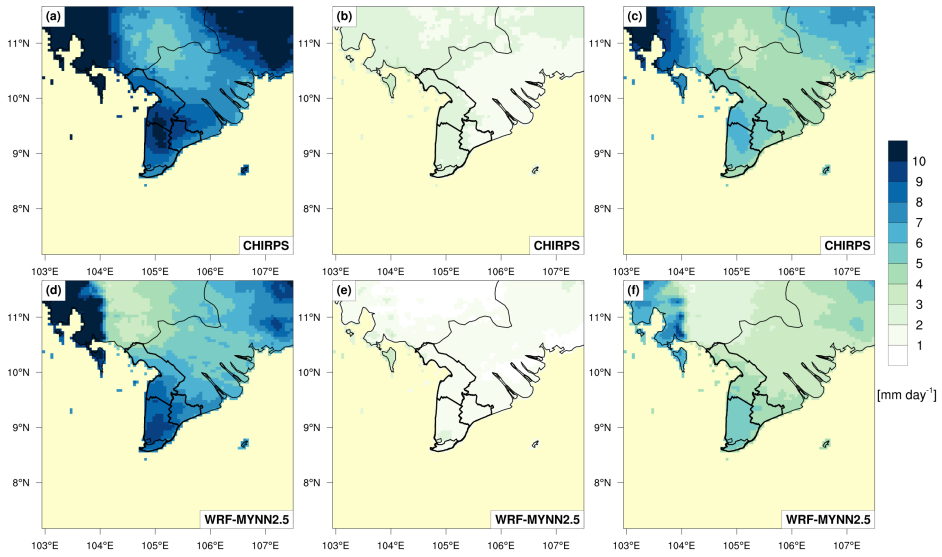

Figure 6.1.: Spatial distribution of mean daily precipitation for the period 2007–2016 over the Ca Mau Peninsula derived from CHIRPS v2.0 and simulated by the WRF-MYNN2.5 experiment, shown for the rainy season (first column), dry season (second column), and annual mean (third column).

the WRF-MYNN2.5 simulation relative to CHIRPS v2.0 over the 2007–2016 period. Negative PBIAS values, indicating an overall underestimation, dominate most of the Ca Mau Peninsula, whereas positive PBIAS values are confined to limited areas in southern Ca Mau Province and along the coastal zone of Bac Lieu Province during the rainy season. In terms of RMSE, values range from approximately 16 to 20 mm day^{-1} during the rainy season and from 4 to 8 mm day^{-1} during the dry season. Figure A.8 presents the corresponding spatial patterns of PBIAS and RMSE for daily precipitation from the WRF-MYNN2.5 simulation evaluated against TMPA over the same period. Consistent with the earlier assessment for the 2007–2009–2015 period, no substantial differences are identified in either the magnitude or spatial distribution of PBIAS and RMSE when comparing validations against CHIRPS v2.0 and TMPA, across both dry and rainy seasons.

Additional evidence of model performance is provided in Table 6.1, which compares WRF-

Table 6.1.: PBIAS and RMSE of simulated daily rainfall for experiment WRF-MYNN2.5 compared to measurements at 24 stations, CHIRPS v2.0, and TMPA over the Ca Mau Peninsula from 2007–2016.

	PBIAS(%)		
Validation Datasets	**Stations**	**CHIRPS 2.0**	**TMPA**
Rainy season	-16.57	-10.55	-11.11
Dry season	-29.66	-31.27	-27.47
Year	-19.17	-14.66	-13.97
	RMSE(mm)		
Rainy season	20.61	17.06	17.39
Dry season	11.13	7.68	8.00
Year	16.57	13.26	13.69

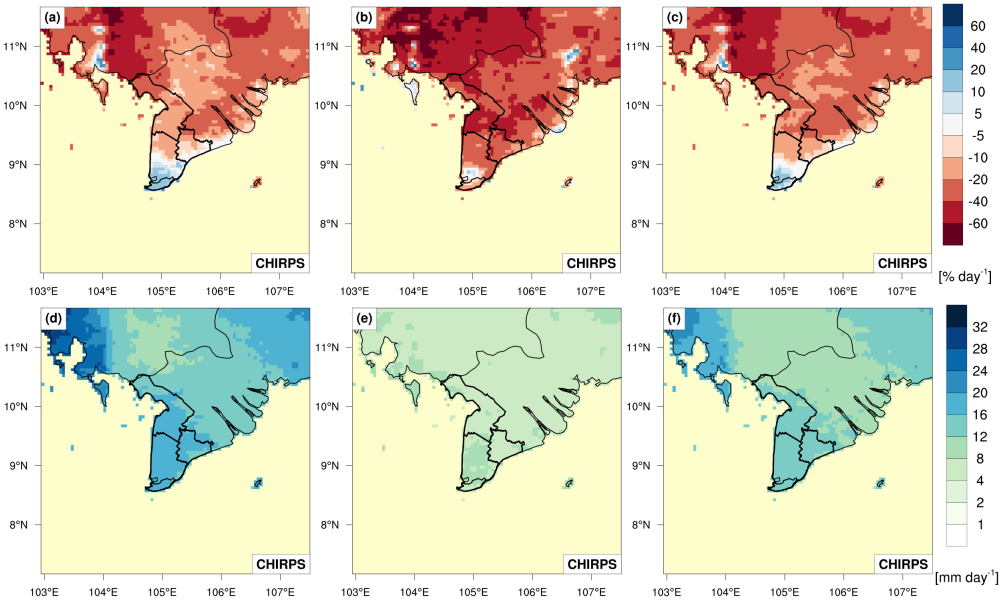

Figure 6.2.: The performance of the WRF-MYNN2.5 experiment is illustrated by the PBIAS and RMSE of daily rainfall relative to CHIRPS v2.0 for the rainy season (first column), dry season (second column), and annual (third column) periods, averaged over the period from 2007 to 2016. Panels (a–c) and (d–f) correspond to the PBIAS and RMSE, respectively.

MYNN2.5 precipitation against observations from 24 rain-gauge stations, as well as against TMPA and CHIRPS v2.0 datasets. When validated against station observations, the model exhibits the largest errors, with RMSE values of 20.61 mm day^{-1} in the rainy season and 11.13 mm day^{-1} in the dry season. In contrast, the errors relative to TMPA and CHIRPS 2.0 are notably smaller, amounting to 17.39 and 17.06 mm day^{-1} in the rainy season, and 7.68 and 8.00 mm day^{-1} in the dry season, respectively. These error magnitudes are consistent with those obtained for the 2007–2013–2015 period discussed in Section 5.4, indicating stable model performance across different evaluation periods.

Figure 6.3 presents Taylor diagrams summarizing the performance of WRF-MYNN2.5 for daily precipitation, 5-day accumulated precipitation, and 10-day accumulated precipitation at 24 stations over the Ca Mau Peninsula for the dry season, rainy season, and the whole year. For daily precipitation, correlation coefficients remain relatively low, around 0.30, reflecting the difficulty of capturing day-to-day rainfall variability at local scales. However, when precipitation is aggregated over longer timescales, model performance improves markedly. Correlation coefficients increase to approximately 0.35 to 0.55 for 5-day accumulated precipitation and further to about 0.40 to 0.60 for 10-day accumulated precipitation. Differences in normalized standard deviation and PBIAS among daily, 5-day, and 10-day accumulations are relatively small, with normalized standard deviation values ranging from 0.6 to 0.9 and PBIAS generally remaining above -20%.

The performance of the WRF-MYNN2.5 simulation is consistent with findings from previous studies over the Vietnamese Mekong Delta. Raghavan et al. (2016) reported a pronounced dry bias over the Vietnamese Mekong Delta when applying the WRF-ARW model at a coarse resolution of 25 km.

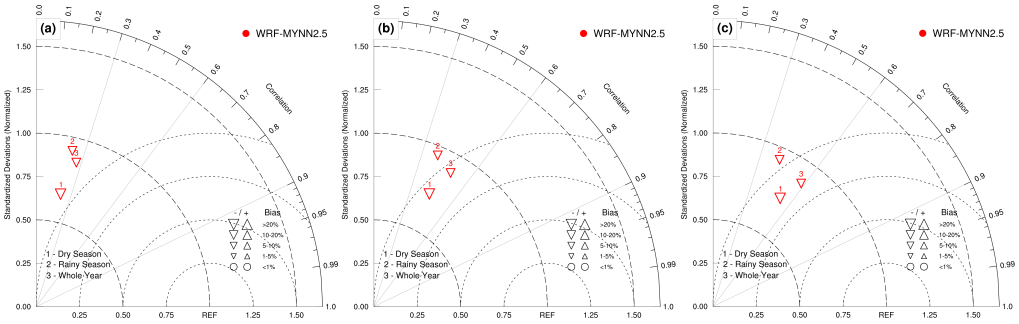

Figure 6.3.: The performance of the WRF-MYNN2.5 experiment is assessed using Taylor diagrams for (a) daily, (b) 5-day, and (c) 10-day accumulated rainfall at 24 stations over the Ca Mau Peninsula. Results are shown for experiment WRF-MYNN2.5 experiment (red symbols) across the dry season, rainy season, and the whole year over the period 2007–2016.

Similarly, Hoang-Cong et al. (2022) showed that while a 25 km RegCM4.7 simulation tends to overestimate precipitation in both dry and rainy seasons, a convection-permitting simulation at 5 km resolution exhibits a systematic underestimation over the Vietnamese Mekong Delta. The underestimation identified in the present study is therefore in line with earlier regional modelling efforts and appears to be a common characteristic of high-resolution regional climate simulations in this region.

Taken together, these results demonstrate that the WRF-MYNN2.5 experiment provides a robust representation of the spatial patterns and seasonal variability of precipitation over the Ca Mau Peninsula. Although systematic biases persist, their magnitude is acceptable for a regional climate model operating at a gray-zone resolution (5 km) and does not substantially limit the model's applicability for subsequent freshwater flux analyses.

6.3. WRF-ARW model performance in simulating the diurnal cycle of precipitation over the Ca Mau Peninsula

We further investigate the WRF-MYNN2.5 experiment's performance in simulating the diurnal cycle of precipitation versus the TMPA product.

Figure 6.4 presents the diurnal cycle of rainfall frequency and rainfall intensity over the Ca Mau Peninsula derived from the TMPA product and simulated by the WRF-MYNN2.5 experiment during the rainy season over the period 2007–2016. It should be noted that each time label on the horizontal axis represents rainfall accumulated over a 3-hour interval (e.g., the value at 13 corresponds to precipitation occurring between 13:00 and 16:00 local time). In general, the WRF-MYNN2.5 experiment successfully captures the main features of the observed diurnal precipitation cycle, particularly the timing of the afternoon maximum and the contrast between daytime and nighttime rainfall. In particular, the model accurately captures the timing of the early-afternoon peak in rainfall frequency and intensity from 13:00 to 16:00 LT, as well as the nocturnal minimum in rainfall amount that occurs between 22:00 and 01:00 LT.

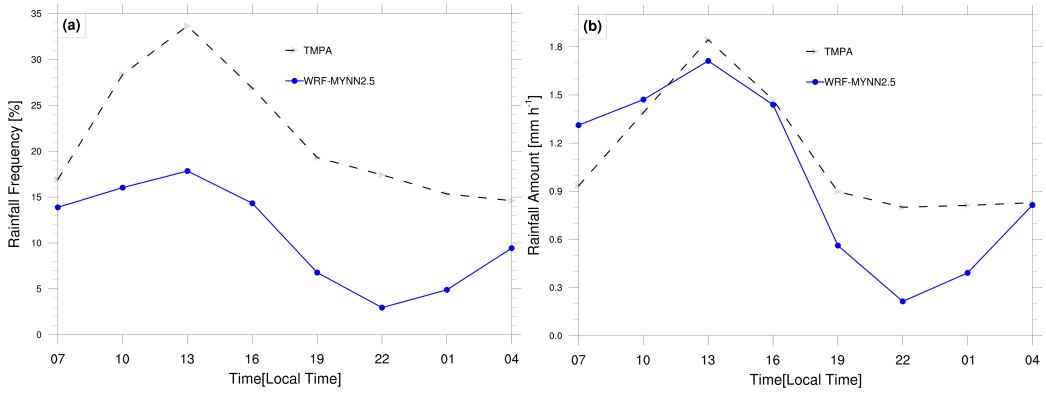

Figure 6.4.: Diurnal cycle of domain-averaged (a) rainfall frequency, and (b) rainfall amount over the Ca Mau Peninsula from TMPA (dashed black lines) and WRF-MYNN2.5 (blue lines) during the rainy seasons of the period 2007–2016.

Nevertheless, the WRF-MYNN2.5 configuration systematically underestimates rainfall frequency relative to TMPA throughout the diurnal cycle and fails to reproduce the pronounced suppression of rainfall frequency during the early-morning period (04:00–07:00 LT). Moreover, discrepancies during the nighttime interval (19:00–07:00 LT) account for a substantial portion of the differences in the magnitude of the simulated diurnal rainfall cycle between the WRF-MYNN2.5 experiment and TMPA.

Figure 6.5 illustrates the spatial distribution of mean 3-hourly rainfall intensity during the peak

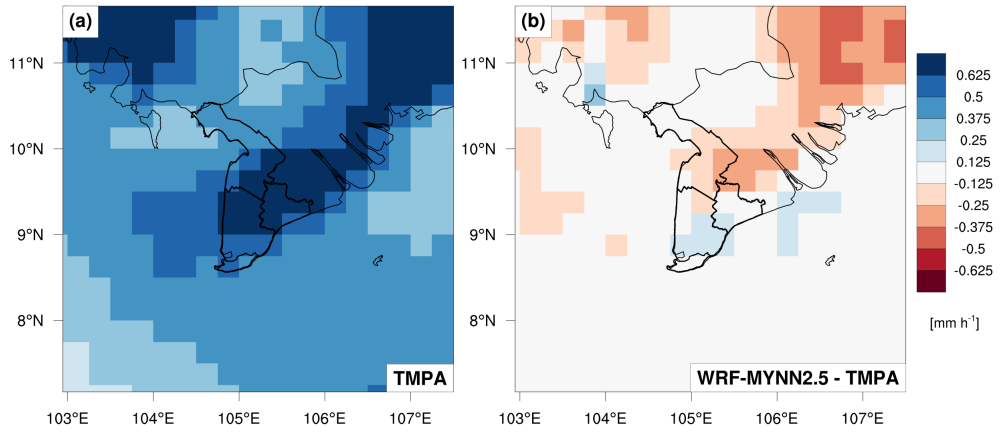

Figure 6.5.: (a) Mean 3-hourly TMPA rainfall intensity during the peak of the diurnal cycle (i.e., 13:00–16:00 LT) over the Ca Mau Peninsula in the rainy season of the period 2007–2016. Difference between the mean 3-hourly rainfall intensity in the same period from (b) WRF-MYNN2.5 and the TMPA average shown in (a).

phase of the diurnal cycle (13:00–16:00 LT) in the rainy season over the period 2007–2016, as derived from TMPA, together with the corresponding difference between the WRF-MYNN2.5 simulation and TMPA. The TMPA product (Fig. 6.5a) indicates pronounced afternoon rainfall intensities across most of the Ca Mau Peninsula, with relatively higher values over inland and western coastal areas. The difference map (Fig. 6.5b) reveals that the WRF-MYNN2.5 experiment generally underestimates rainfall intensity during the afternoon peak relative to TMPA over large portions of the peninsula. The underesti-

mation is most evident over the eastern and northeastern parts of the domain. Overall, the spatial pattern of differences suggests that, although the WRF-MYNN2.5 configuration captures the timing and broad spatial structure of the afternoon rainfall maximum, it tends to underestimate the magnitude of convective rainfall intensity during the peak phase of the diurnal cycle. This behavior indicates limitations in representing local convection intensity at gray-zone resolution over the Ca Mau Peninsula.

To examine the propagation characteristics of the diurnal precipitation cycle over the Ca Mau

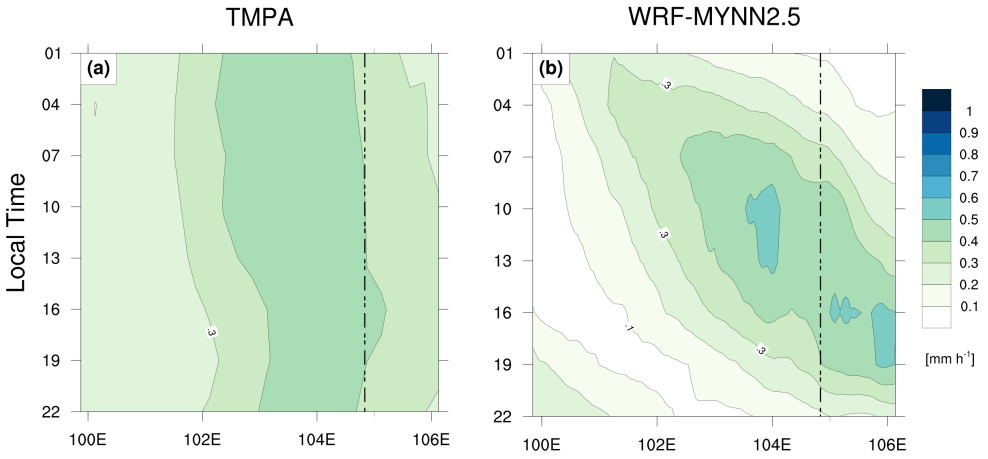

Figure 6.6.: Hovmöller diagrams of the mean diurnal cycles latitudinally averaged over the red rectangle in Fig. 4.1 (8.25–10.5°N, 99.875–106.125°E) for the rainy season of the period 2007–2016 from (a) TMPA and from (b) WRF-MYNN2.5 experiment. Vertical dashed lines show the approximate location of the western coastline of the Ca Mau Peninsula.

Peninsula during the rainy season, the Hovmöller diagram is employed to depict the spatiotemporal migration of rainfall. Figure 6.6 presents time-coastal distance cross-sections averaged along the coastal direction, derived from TMPA observations and the WRF-MYNN2.5 simulation for the rainy seasons from 2007 to 2016. In contrast to the analysis for the period 2007–2013–2015 discussed in Section 5.5, the TMPA product does not indicate a distinct early-morning rainfall maximum over the eastern Gulf of Thailand. Instead, only a pronounced rainfall peak along the western coastline of the Ca Mau Peninsula is evident between 13:00 and 16:00 LT, corresponding to the dominant afternoon convective maximum. By comparison, the WRF-MYNN2.5 simulation exhibits a diurnal evolution similar to that identified in the earlier period, including a rainfall maximum over the eastern Gulf of Thailand during the late morning to early afternoon (approximately 10:00–13:00 LT), followed by a well-defined peak along the western coastline of the Ca Mau Peninsula between 13:00 and 16:00 LT. The latter feature is in close agreement with the TMPA observations.

When considered as a whole, the WRF-MYNN2.5 experiment displays a robust capability in capturing the phase and overall structure of the diurnal precipitation cycle over the Ca Mau Peninsula, which is essential for freshwater flux assessments at gray-zone resolution.

6.4. WRF-ARW model performance in simulating daily potential evapotranspiration over the Ca Mau Peninsula

In this section, the performance of the WRF-MYNN2.5 experiment in simulating daily PET over the Ca Mau Peninsula during the period 2007–2016 is evaluated. The simulated daily PET is assessed against multiple reference datasets, including the ERA5 and DPET products, in situ PET observations derived from GGI-3000 measurements at two stations, and PET estimates calculated using the Penman-Monteith at three meteorological stations.

Figure 6.7 presents the spatial distribution of mean daily PET during the dry season, rainy season,

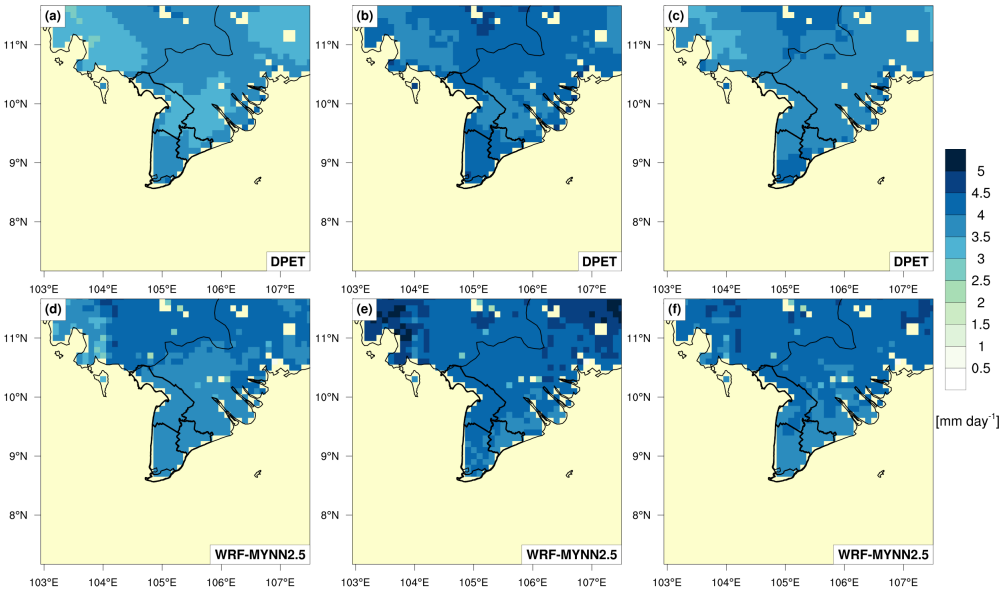

Figure 6.7.: Spatial distribution of mean daily PET for the period 2007–2016 over the Ca Mau Peninsula derived from DPET and simulated by the WRF-MYNN2.5 experiment, shown for the rainy season (first column), dry season (second column), and annual mean (third column).

and for the annual mean, as derived from the DPET dataset and simulated by the WRF-MYNN2.5 experiment over the period 2007–2016. Overall, the WRF-MYNN2.5 configuration successfully reproduces the primary spatial characteristics of PET over the Ca Mau Peninsula, including its relatively homogeneous distribution. During the dry season, both DPET and WRF-MYNN2.5 indicate elevated PET values across the region, reflecting enhanced atmospheric evaporative demand under warmer and drier conditions. The model realistically captures the spatial structure, with higher PET values along the western and southwestern coastal zones. Nevertheless, WRF-MYNN2.5 tends to slightly overestimate PET relative to DPET in some inland areas. During the rainy season, PET values decrease in both datasets compared to the dry season. WRF-MYNN2.5 accurately reproduces this seasonal reduction and maintains good agreement with DPET in terms of spatial patterns, with generally smaller discrepancies than those observed in the dry season. Minor differences persist along coastal areas, likely associated with land–sea interactions and contrasts in surface roughness that influence surface energy fluxes. For the annual mean,

the spatial distribution and magnitude of PET simulated by WRF-MYNN2.5 are broadly consistent with DPET across most of the Ca Mau Peninsula. Importantly, unlike precipitation, PET exhibits only a weak seasonal contrast, a feature that is well captured by the WRF-MYNN2.5 experiment.

Figure 6.8 illustrates the spatial distributions of PBIAS and RMSE for PET simulated by WRF-

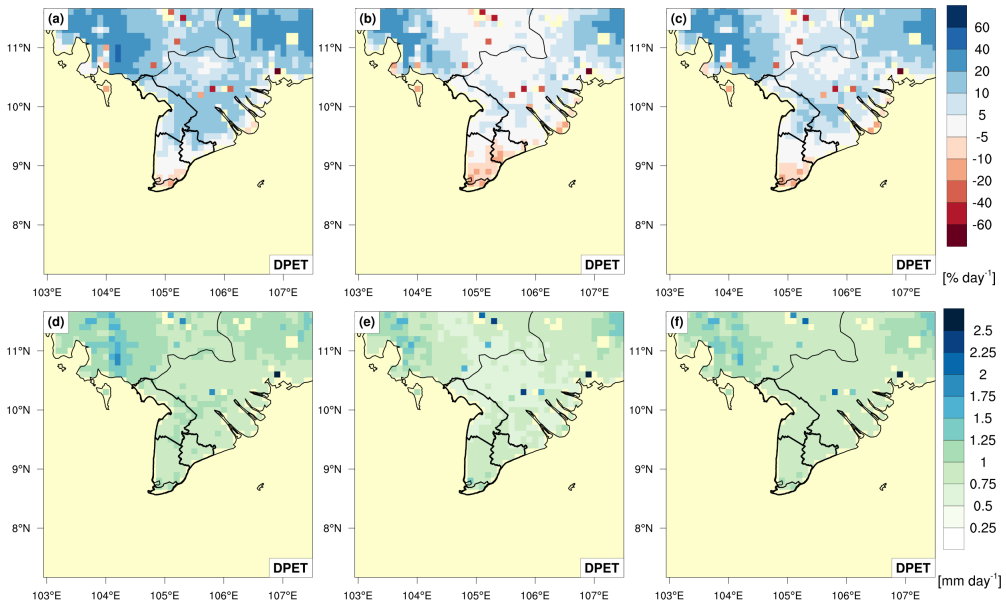

Figure 6.8.: The performance of the WRF-MYNN2.5 experiment is illustrated by the PBIAS and RMSE of daily PET relative to DPET for the rainy season (first column), dry season (second column), and annual (third column) periods, averaged over the period from 2007 to 2016. Panels (a–c) and (d–f) correspond to the PBIAS and RMSE, respectively.

MYNN2.5 relative to DPET. Across both dry and rainy seasons, PBIAS values generally range from -20% to 10%, indicating modest biases over most of the domain. A consistent negative bias is evident over southern Ca Mau Province in both seasons. The RMSE values are relatively low, typically between 0.5 and 1.0 mm day^{-1} across the Ca Mau Peninsula, demonstrating good agreement with DPET. In contrast, when evaluated against ERA5 (Fig. A.9), the WRF-MYNN2.5 experiment exhibits a systematic negative bias over the entire study area in both seasons, with PBIAS values ranging from approximately -5% to -20%. The corresponding RMSE values are higher than those obtained against DPET, varying from 1.0 to 1.75 mm day^{-1}. Domain-averaged RMSE values (Table 6.2) further confirm that the discrepancies relative to ERA5 are larger than those relative to DPET in both the rainy and dry seasons, with RMSE values of 1.11 and 1.45 mm day^{-1} for ERA5, compared to 0.96 and 0.81 mm day^{-1} for DPET, respectively.

To further assess model performance, the Taylor diagram comparing daily PET simulated by WRF-MYNN2.5 at three stations with Penman–Monteith-based estimates is shown in Fig. 6.9a. The model exhibits moderate to high correlations, with coefficients of 0.61 during the dry season and 0.42 during the rainy season. Consistent with the spatial evaluation, WRF-MYNN2.5 underestimates PET at these stations, with PBIAS values of -14.11% in the dry season and -13.42% in the rainy season.

The ability of WRF-MYNN2.5 to reproduce key drivers of PET, namely net radiation and wind

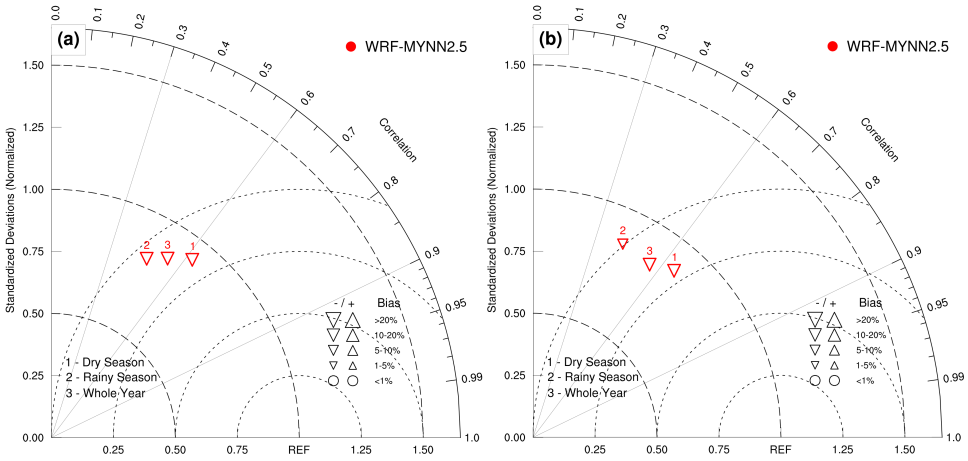

Figure 6.9.: Taylor diagrams of daily PET for experiment WRF-MYNN2.5 (red symbols) against (a) estimates using the Penman-Monteith equation and (b) GGI-3000 measurements in the dry season (number one), rainy season (number two), and whole year (number three) for the period 2007–2016.

speed at 10-m height, is also examined. As summarized in Table 6.3, net radiation is reasonably well simulated in both seasons, with PBIAS values of -9.83% in the rainy season and -17.95% in the dry season, and RMSE values of approximately 3.4–3.5 MJ m^{-2}. In contrast, the model exhibits substantial positive biases in simulating wind speed at 10-m height, with PBIAS values of 44% in the rainy season and 62.9% in the dry season. This pronounced overestimation of wind speed, particularly during the dry season, is identified as a major contributor to the bias in simulated PET. These findings are consistent with previous studies (Du Duc et al., 2016), which reported that wind speed at 10-m height is among the most challenging surface variables to simulate accurately using the WRF-ARW model.

Finally, the WRF-MYNN2.5 experiment is evaluated against PET observations from the GGI-

Table 6.2.: PBIAS and RMSE of simulated daily PET for experiment WRF-MYNN2.5 compared to station data (Penman-Monteith and GGI-3000), ERA5, and DPET over the Ca Mau Peninsula in 2007–2016.

	PBIAS(%)			
Validation Datasets	**Stations (Penman-Monteith)**	**Stations (GGI-3000)**	**ERA5**	**DPET**
Rainy season	-13.42	-7.93	-7.66	5.59
Dry season	-14.11	-14.85	-20.09	-1.93
Year	-13.78	-11.65	-14.51	1.59
	RMSE(mm)			
Rainy season	1.36	1.10	1.11	0.96
Dry season	1.18	1.14	1.45	0.81
Year	1.27	1.12	1.29	0.8

3000 device at two stations (Ca Mau and Can Tho). The Taylor diagram shown in Figure 6.9b indicates relatively strong correlations in both seasons, with values of 0.63 in the dry season and 0.40 in the rainy

season. The model again exhibits a negative bias, underestimating PET by -14.85% in the dry season and -7.93% in the rainy season. RMSE values are 1.45 mm day^{-1} in the dry season and 1.10 mm day^{-1} in the rainy season (Table 6.3), indicating satisfactory agreement given the inherent uncertainties in PET observations.

Due to the limited availability of in situ PET measurements over the Ca Mau Peninsula and across

Table 6.3.: PBIAS and RMSE of simulated daily 10-m wind speed and net radiation compared to station data over the Ca Mau Peninsula for the period 2007–2016.

Variable	10-m Wind speed		Daily net radiation	
	PBIAS(%)	RMSE(ms^{-1})	PBIAS(%)	RMSE(MJ m^{-2})
Rainy season	44.4	1.40	-9.83	3.51
Dry season	62.9	1.60	-17.95	3.40
Year	51.7	1.50	-13.93	3.46

Vietnam, the use of alternative PET sources, including satellite-based and model-derived datasets, is unavoidable. Recent studies have demonstrated the superior performance of DPET at both basin (Faseyiku et al., 2024) and global scales (Singer et al., 2021). The results presented here further confirm that DPET represents a robust and reliable reference for PET evaluation, providing a valuable foundation for subsequent freshwater flux analyses in this study.

Overall, the WRF-MYNN2.5 experiment demonstrates a robust capability in simulating the key components of the freshwater flux over the Ca Mau Peninsula. The experiment successfully reproduces the dominant spatial patterns and seasonal contrasts in precipitation, including enhanced rainfall along the western coastline during the rainy season and suppressed rainfall during the dry season, while also capturing essential characteristics of the diurnal rainfall cycle. Although systematic biases remain, particularly a tendency toward rainfall underestimation and reduced nighttime precipitation, the magnitude of these errors is comparable to those reported in previous RCM studies over southern Vietnam and acceptable for a gray-zone resolution (5 km) simulation. For PET, WRF-MYNN2.5 effectively captures the spatial homogeneity and weak seasonal variability characteristic of the region, with good agreement relative to both model-derived datasets and station-based observations. Despite a consistent underestimation of PET, largely attributable to biases in near-surface wind speed, the model reproduces the primary controls on PET, including net radiation, with satisfactory accuracy. Taken together, these results demonstrate that the WRF-MYNN2.5 configuration, operating at gray-zone resolution (5 km), provides a robust tool for simulating precipitation and PET, and consequently for representing the freshwater flux over the Ca Mau Peninsula.

7. Response of simulated freshwater flux to land-use and land-cover change over the Ca Mau Peninsula

7.1. Preface

In this section, the impacts of LULCC, with particular emphasis on aquaculture expansion, on precipitation and evapotranspiration over the Ca Mau Peninsula are examined. Two concepts related to evapotranspiration, namely PET and AET, are considered in order to comprehensively assess the response of freshwater fluxes to LULCC. To investigate the effects of observed LULCC, two updated LULC datasets (LU1 and LU2) are employed to evaluate their influence on precipitation, at both daily and diurnal-cycle scales, as well as on AET and PET. In addition, two extreme hypothetical LULC scenarios associated with aquaculture expansion (LU3 and LU4) are introduced to quantitatively assess the maximum potential impact of LULCC on freshwater flux components. Differences in precipitation, AET, and PET among the four LULC scenarios (two observation-based and two hypothetical) are systematically analyzed using a 10-year simulation conducted with the WRF-ARW model, configured with the optimal set of physical parameterizations identified in Section 5. The WRF-MYNN2.5 experiment, which employs the default MODIS LULC dataset and has its performance rigorously evaluated in Section 6, serves as the control simulation against which all LULC experiments are compared.

7.2. Response of simulated daily precipitation to land-use and land-cover change over the Ca Mau Peninsula

The objective of this section is to evaluate the performance of the WRF-ARW model in simulating daily precipitation over the Ca Mau Peninsula under different LULC scenarios. Figure 7.1 and Figure A.10 display the spatial distributions of PBIAS of the daily precipitation for the control simulation and the WRF-ARW simulations with LU1, LU2, LU3, and LU4 scenarios against CHIRPS v2.0 and TMPA over the period 2007–2016.

As illustrated in Figure 7.1, the PBIAS of all simulations relative to CHIRPS v2.0 spans a wide range, from -60% to 20%. Positive biases are restricted to the southernmost part of Ca Mau Province and are mainly evident in the control simulation, whereas negative biases dominate nearly the entire domain across all experiments. This indicates a systematic underestimation of daily precipitation by the WRF-ARW model. A comparable spatial pattern emerges when the simulations are evaluated against TMPA (Fig. A.10).

In this case, PBIAS values range from −60% to approximately 5%, with positive biases again

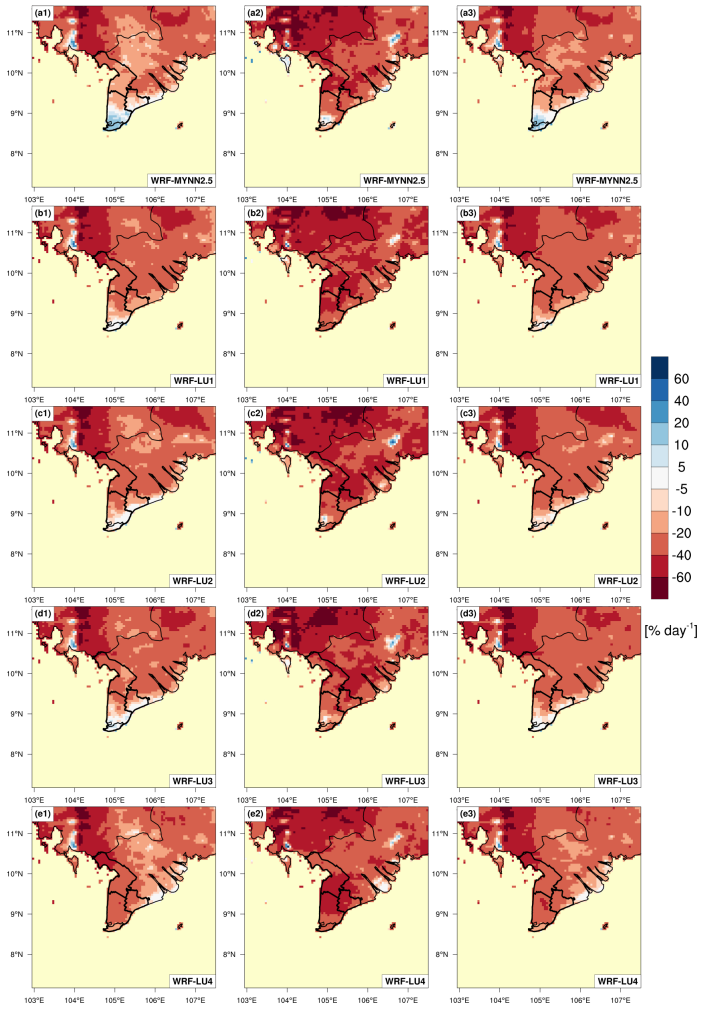

Figure 7.1.: The performance of WRF-ARW experiments using different LULC datasets is illustrated by the PBIAS of daily rainfall relative to CHIRPS v2.0 for the rainy season (first column), dry season (second column), and annual (third column) periods, averaged over the period 2007–2016. Panels (a1–a3), (b1–b3), (c1–c3), (d1–d3), and (e1–e3) correspond to results from the WRF-MYNN2.5, WRF-LU1, WRF-LU2, WRF-LU3, and WRF-LU4 experiments, respectively.

limited to the southern tip of Ca Mau Province in the control simulation. Strong negative biases are observed across most of the peninsula, particularly during the dry season, where the maximum underestimation reaches about −60% in Kien Giang Province. The consistency between the CHIRPS v2.0 and TMPA-based evaluations confirms that all WRF-ARW simulations underestimate daily precipitation in both dry and rainy seasons. Moreover, simulations incorporating alternative LULC scenarios generally exhibit a stronger dry bias than the control run, with the WRF-LU4 experiment showing the most pronounced deviation in PBIAS.

Figures 7.2 and A.11 illustrate the spatial distributions of RMSE of daily precipitation for the control and LULC-based simulations, compared to CHIRPS v2.0 and TMPA. Overall, the RMSE patterns are broadly similar among the experiments, indicating limited sensitivity of RMSE to LULCC. An ex-

ception is observed for the WRF-LU4 simulation, which consistently yields the smallest RMSE in both seasons. Across all experiments, as expected, model performance is clearly superior in the dry season, with RMSE values ranging from 4 to 8 mm day^{-1}, compared to 12 to 20 mm day^{-1} during the rainy season.

Additional quantitative assessment is provided in Table 7.1, which summarizes the RMSE of

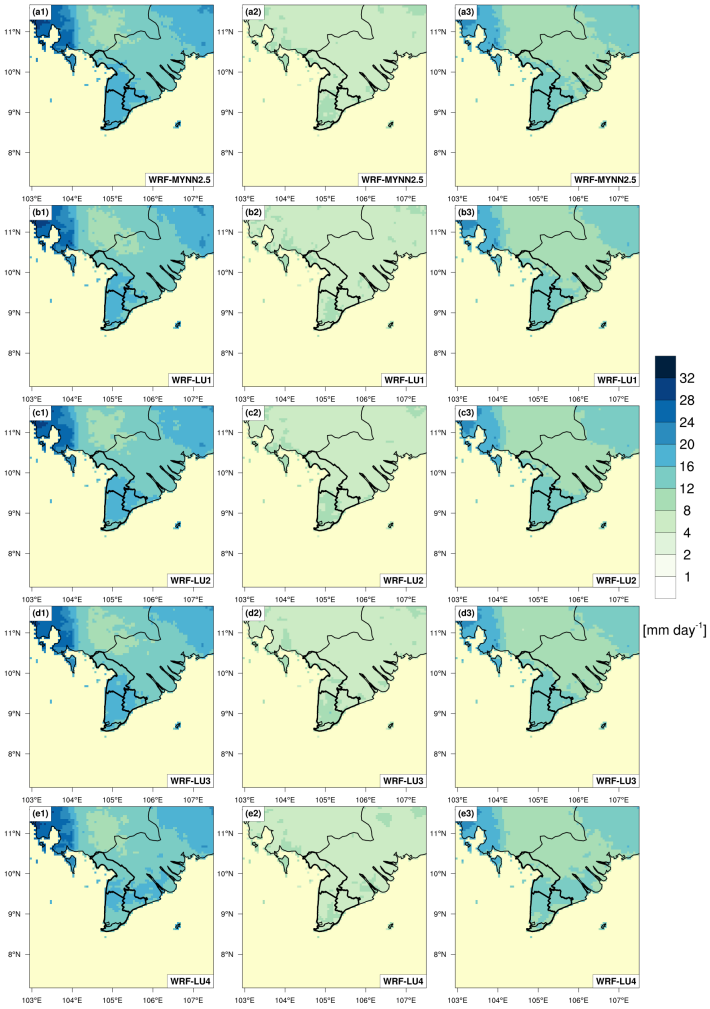

Figure 7.2.: The performance of WRF-ARW experiments using different LULC datasets is illustrated by the RMSE of daily rainfall relative to CHIRPS v2.0 for the rainy season (first column), dry season (second column), and annual (third column) periods, averaged over the period 2007–2016. Panels (a1–a3), (b1–b3), (c1–c3), (d1–d3), and (e1–e3) correspond to results from the WRF-MYNN2.5, WRF-LU1, WRF-LU2, WRF-LU3, and WRF-LU4 experiments, respectively.

daily precipitation relative to observations from 24 rain gauge stations, as well as CHIRPS v2.0 and TMPA. All simulations exhibit larger errors relative to station observations than to satellite-based gridded products, while the RMSE values relative to CHIRPS and TMPA remain comparable. Among the experiments, the control simulation shows the largest RMSE in both seasons. In contrast, simulations using observed LULC datasets (WRF-LU1 and WRF-LU2) demonstrate improved performance, characterized by smaller RMSE values and a similar magnitude of accuracy. The hypothetical LULC ex-

periments (WRF-LU3 and WRF-LU4) outperform the control simulation even further, with WRF-LU4 yielding the lowest RMSE across all reference datasets.

Figure 7.3 further summarizes model performance using Taylor diagrams. For daily precipi-

Table 7.1.: PBIAS and RMSE of simulated daily rainfall compared to measurements at 24 stations, CHIRPS v2.0, and TMPA over the Ca Mau Peninsula for the period from 2007 to 2016. Bold numbers indicate the experiments with the lowest RMSE values for each time period.

	PBIAS(%)				
Experiment	**WRF-MYNN2.5**	**WRF-LU1**	**WRF-LU2**	**WRF-LU3**	**WRF-LU4**
Stations					
Rainy season	-16.57	-26.75	-25.32	-22.46	-33.68
Dry season	-29.66	-36.16	-36.19	-30.06	-42.68
Year	-19.17	-28.57	-27.42	-23.92	-35.41
CHIRPS v2.0					
Rainy season	-10.55	-21.51	-20.22	-17.08	-30.08
Dry season	-31.27	-38.41	-36.05	-31.76	-42.50
Year	-14.66	-24.85	-23.36	-19.99	-32.54
TMPA					
Rainy season	-11.11	-22.07	-21.42	-18.25	-30.32
Dry season	-27.47	-35.78	-32.08	-27.98	-39.58
Year	-13.97	-24.45	-23.22	-19.87	-31.90
	RMSE(mm)				
Stations					
Rainy season	20.61	20.10	20.22	20.29	**19.88**
Dry season	11.13	11.21	11.11	11.42	**10.99**
Year	16.57	16.28	16.33	16.47	**16.07**
CHIRPS v2.0					
Rainy season	17.06	16.11	16.13	16.30	**15.41**
Dry season	7.68	7.49	7.63	7.87	**7.22**
Year	13.26	12.60	12.65	12.83	**12.06**
TMPA					
Rainy season	17.39	16.79	16.88	16.90	**16.66**
Dry season	8.00	7.87	7.88	7.98	**7.73**
Year	13.69	13.17	13.22	13.27	**13.03**

tation (Fig. 7.3a), all simulations exhibit modest correlation coefficients, ranging from approximately 0.25 to 0.30, accompanied by negative PBIAS values exceeding -20%. The violet points are closer to the reference (REF) value, indicating that the WRF-LU4 experiment achieves the lowest RMSE for daily precipitation. When precipitation is aggregated over longer temporal scales (Figs. 7.3b–c), model performance improves substantially. Correlation coefficients increase to approximately 0.35–0.50 for 5-day accumulated precipitation and to 0.35–0.60 for 10-day accumulated precipitation. Nevertheless, all simulations retain negative PBIAS values below -20%. For the whole year, the WRF-LU4 simulation performs best for 5-day accumulated precipitation, whereas the WRF-LU1 simulation yields the lowest

RMSE for 10-day accumulated precipitation.

Overall, the results indicate that incorporating different LULC scenarios leads to modest but con-

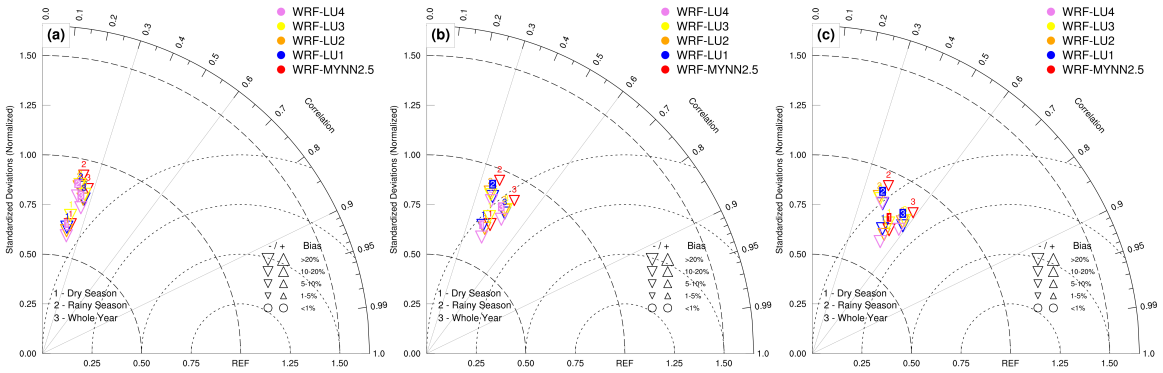

Figure 7.3.: The performance of WRF-ARW experiments employing different LULC datasets is assessed using Taylor diagrams for (a) daily, (b) 5-day, and (c) 10-day accumulated rainfall at 24 stations over the Ca Mau Peninsula. Results are shown for the WRF-MYNN2.5 (red symbols), WRF-LU1 (blue symbols), WRF-LU2 (orange symbols), WRF-LU3 (yellow symbols), and WRF-LU4 (violet symbols) experiments across the dry season, rainy season, and the entire year over the period 2007–2016. Experiments with the smallest RMSE are highlighted with a color-filled background of the numbers indicating the reference period.

sistent improvements in the performance of the WRF-ARW model. All simulations exhibit a persistent dry bias in daily precipitation relative to the control run in both seasons. Simulations based on observed LULC datasets (WRF-LU1 and WRF-LU2) show comparable and improved performance compared to the control simulation. In contrast, the hypothetical LULC scenarios induce more pronounced changes: WRF-LU4, in particular, introduces a stronger dry bias but simultaneously achieves the lowest RMSE for daily and 5-day accumulated precipitation, while WRF-LU3 exhibits performance similar to that of the observed LULC-based simulations.

7.3. Response of simulated diurnal cycle of precipitation to land-use and land-cover change over the Ca Mau Peninsula

This section evaluates the performance of the WRF-ARW simulations under different LULC scenarios in reproducing the diurnal cycle of precipitation over the Ca Mau Peninsula, with reference to the TMPA product.

Figure 7.4 illustrates the diurnal variations of rainfall frequency and rainfall amount averaged over the Ca Mau Peninsula during the rainy season for the period 2007–2016. As indicated by TMPA, the diurnal evolution of rainfall intensity resembles that of rainfall frequency, characterized by a pronounced afternoon maximum between 13:00 and 16:00 LT. With the exception of the WRF-LU4 experiment, all WRF-ARW simulations are able to reasonably capture the overall 24-hour evolution of rainfall in terms of both frequency and intensity. Nevertheless, these simulations systematically underestimate rainfall frequency relative to TMPA. Despite this bias, the WRF-ARW simulations successfully reproduce the

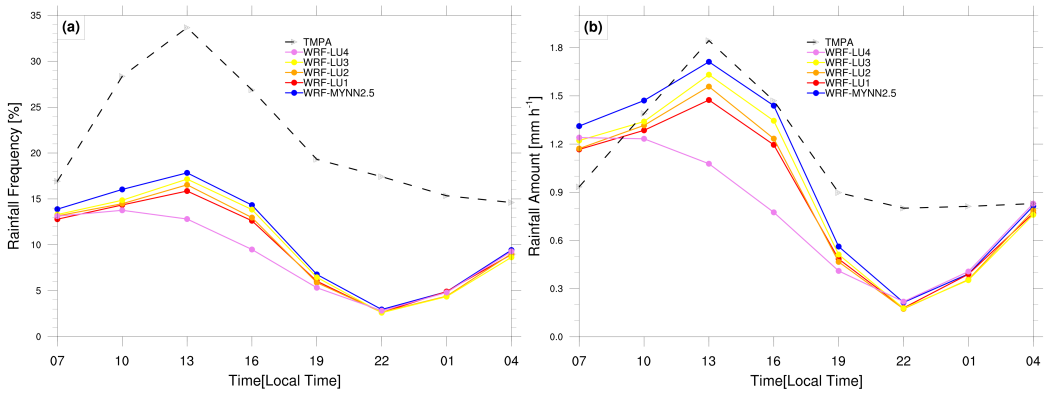

Figure 7.4.: Diurnal cycle of domain-averaged (a) rainfall frequency, and (b) rainfall amount over the Ca Mau Peninsula from TMPA (dashed black lines), WRF-LU4(violet lines), WRF-LU3 (yellow lines), WRF-LU2 (orange lines), WRF-LU1 (red lines), and WRF-MYNN2.5 experiment (blue lines) during the rainy season for the period 2007–2016.

timing of the early afternoon peak in rainfall frequency and intensity, as well as the suppressed rainfall amount during the nighttime period (22:00–01:00 LT). However, none of the simulations adequately capture the suppressed rainfall frequency observed in the early morning hours (04:00–07:00 LT). The discrepancies during the nighttime period (19:00–07:00 LT) account for the majority of the differences in daily precipitation between the WRF-ARW simulations and the TMPA product. Relative to the control simulation, all simulations incorporating alternative LULC scenarios exhibit reduced rainfall frequency and intensity throughout the diurnal cycle.

A distinct behavior is observed for the WRF-LU4 simulation. As shown in Figure 7.4, the diurnal cycle of rainfall intensity in WRF-LU4 closely resembles that of rainfall frequency but displays an early morning peak between 07:00 and 10:00 LT, in contrast to the early afternoon peak observed in TMPA and other simulations. This shift can be physically explained by the hypothetical LU4 scenario, in which the entire Ca Mau Peninsula is converted into water bodies and effectively behaves as part of the East Vietnam Sea. Over this oceanic region, precipitation maxima are commonly observed during the early morning hours (Wei et al., 2020). Consequently, the simulated transition of the diurnal rainfall peak from early afternoon to early morning in WRF-LU4 is physically plausible.

Figure 7.5 presents the mean 3-hourly rainfall intensity during the peak period of the diurnal cycle (13:00–16:00 LT) from TMPA and the corresponding biases of all WRF-ARW simulations for the rainy season over 2007–2016. Except for WRF-LU4, the differences between the WRF-ARW simulations and TMPA are relatively small, with biases ranging from -0.375 to 0.25 mm h^{-1}. Positive biases are primarily concentrated in Ca Mau Province, whereas negative biases dominate Kien Giang Province. In contrast, the WRF-LU4 simulation exhibits a consistent negative bias across the entire peninsula, with values ranging from -0.375 to -0.125 mm h^{-1} (Fig. 7.5f).

To further investigate the propagation characteristics of the diurnal rainfall cycle during the rainy season, Hovmöller diagrams of time–coastal distance cross-sections averaged along the coastline were

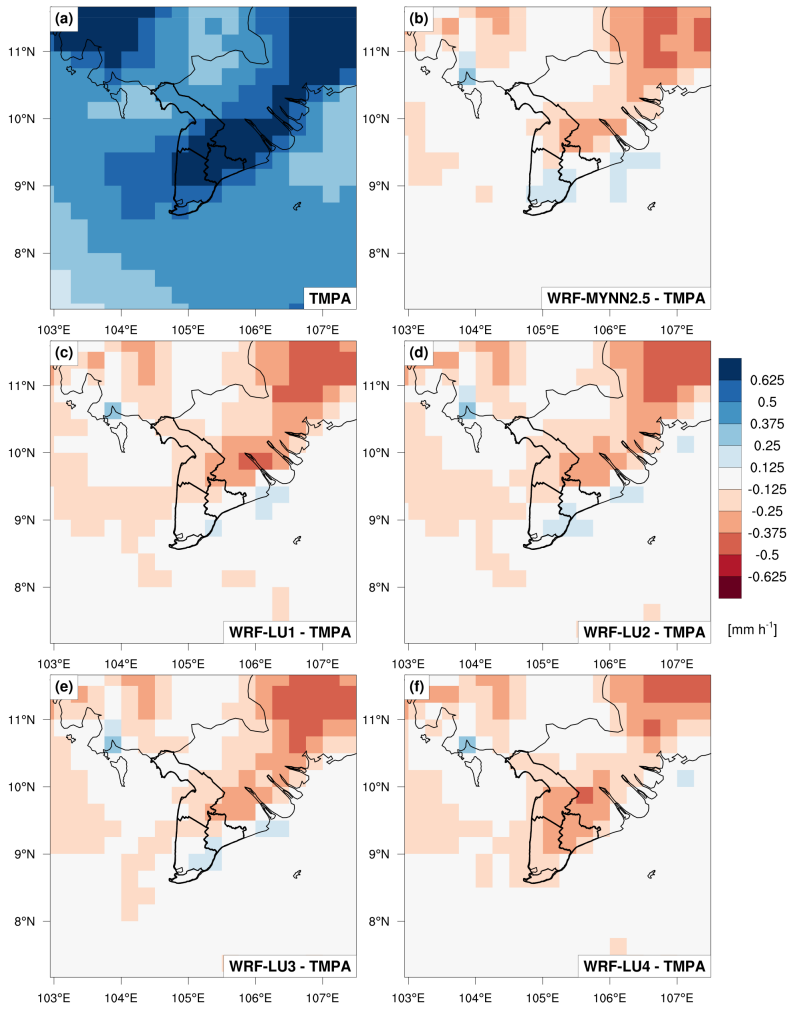

Figure 7.5.: (a) Mean 3-hourly TMPA rainfall intensity during the peak of the diurnal cycle (i.e., 13:00–16:00 LT) during the rainy season for the period 2007–2016. Difference between the mean 3-hourly rainfall intensity in the same period from (b) WRF-MYNN2.5, (c) WRF-LU1, (d) WRF-LU2, (e) WRF-LU3, and (f) WRF-LU4 experiments and the TMPA average shown in (a).

constructed (Fig. 7.6). Based on TMPA, no early-morning rainfall peak is detected over the eastern Gulf of Thailand; instead, a single rainfall maximum is identified along the western coastline of the Ca Mau Peninsula between 13:00 and 16:00 LT. The control simulation reproduces two rainfall maxima: one over the eastern Gulf of Thailand between approximately 10:00 and 13:00 LT, and another over the western coastline between 13:00 and 16:00 LT. In contrast, most WRF-ARW simulations incorporating alternative LULC scenarios fail to reproduce these propagating features, except for WRF-LU4, which simulates a rainfall peak over the western coastline during the early morning period (07:00–10:00 LT).

Overall, the results indicate that LULCC has a generally weak influence on simulating the diurnal precipitation cycle over the Ca Mau Peninsula during the rainy season, except under the extreme hypothetical LU4 scenario. All simulations tend to reduce both rainfall frequency and intensity throughout the diurnal cycle relative to the control simulation. The impact of simulations using observed LULC datasets (WRF-LU1 and WRF-LU2) is negligible, while the hypothetical LULC scenarios exhibit contrasting ef-

fects. Specifically, WRF-LU3 induces only minor changes, whereas WRF-LU4 produces a substantial modification of the diurnal precipitation structure by shifting the rainfall peak from early afternoon to early morning.

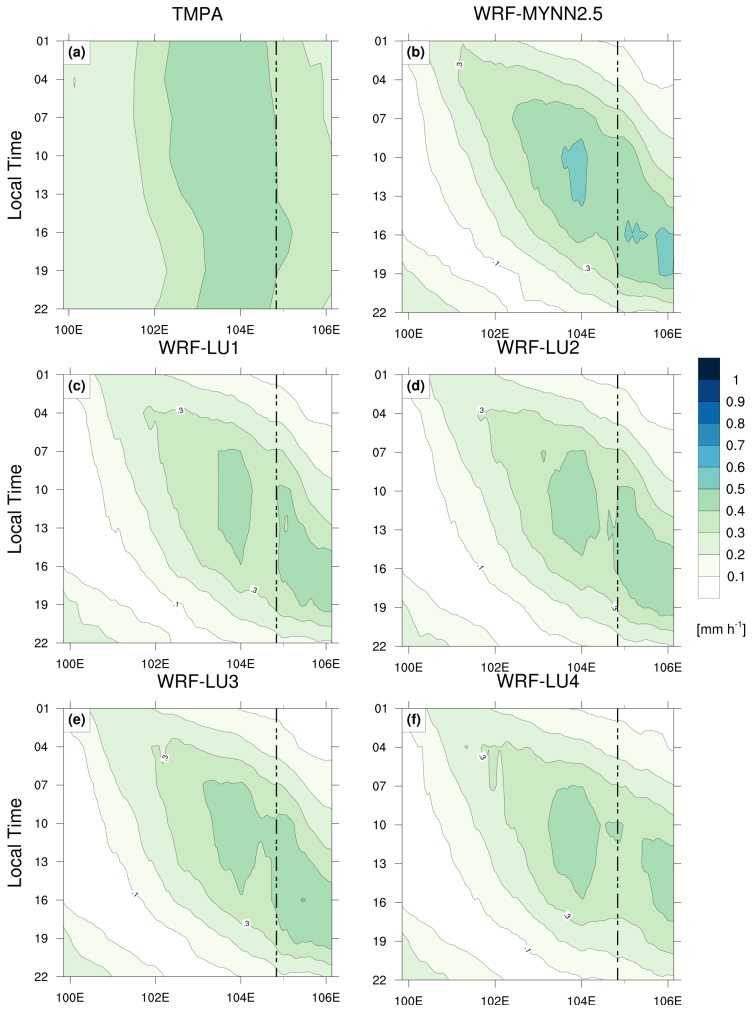

Figure 7.6.: Hovmöller diagrams of the mean diurnal cycles latitudinally averaged over the red rectangle in Fig. 4.1 (8.25–10.5°N, 99.875–106.125°E) for the rainy season over the period 2007–2016 from (a) TMPA, and from (b) WRF-MYNN2.5, (c) WRF-LU1, (d) WRF-LU2, (e) WRF-LU3 and (f) WRF-LU4 experiments. Vertical dashed lines show the approximate location of the western coastline of the Ca Mau Peninsula.

7.4. Response of simulated daily potential evapotranspiration to land-use and land-cover change over the Ca Mau Peninsula

This section investigates the influence of different LULC scenarios on the simulation of PET over the Ca Mau Peninsula.

Figures 7.7 and A.12 present the spatial distributions of PBIAS for daily PET from the control simulation and the WRF-ARW experiments employing the LU1, LU2, LU3, and LU4 scenarios, eval-

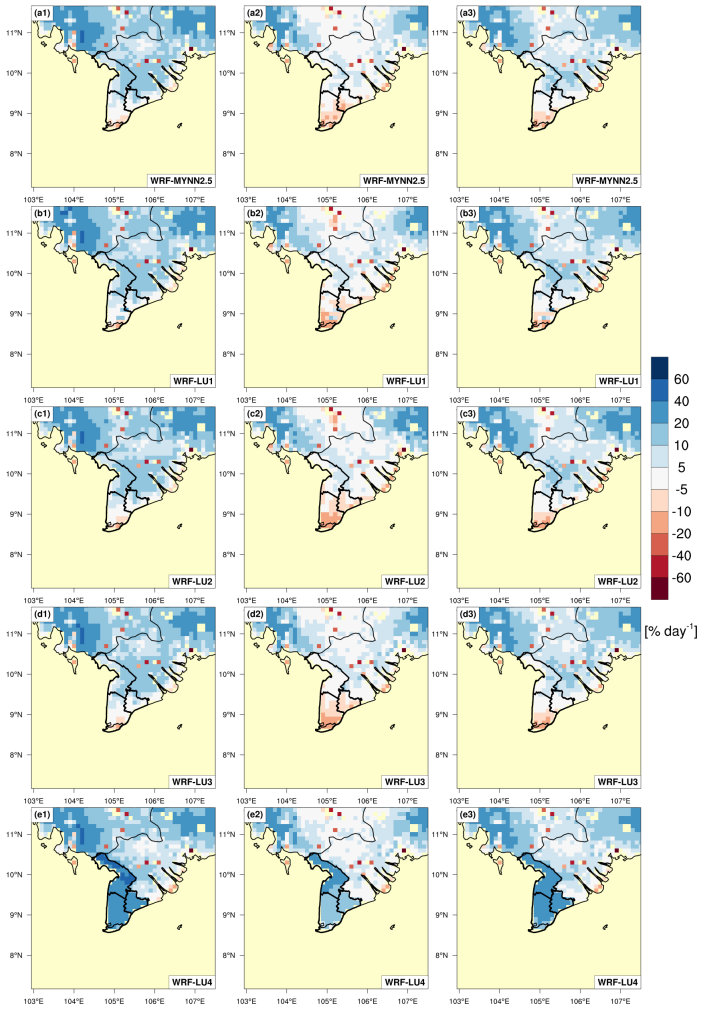

Figure 7.7.: The performance of WRF-ARW experiments using different LULC datasets is illustrated by the PBIAS of daily PET relative to DPET for the rainy season (first column), dry season (second column), and annual (third column) periods, averaged over the period 2007–2016. Panels (a1–a3), (b1–b3), (c1–c3), (d1–d3), and (e1–e3) correspond to results from the WRF-MYNN2.5, WRF-LU1, WRF-LU2, WRF-LU3, and WRF-LU4 experiments, respectively.

uated against the DPET and ERA5 dataset for the period 2007–2016. As shown in Fig. 7.7, with the exception of the WRF-LU4 experiment, all simulations exhibit predominantly positive biases over the Ca Mau Peninsula during the rainy season, while negative biases emerge over southern Ca Mau and Bac Lieu provinces during the dry season when compared with DPET. A similar spatial pattern is evident in Fig. A.12 for the comparison with ERA5, where all simulations except WRF-LU4 display negative biases across most of the domain in both seasons. Notably, for both reference datasets, the magnitude and spatial distribution of PBIAS among the control, WRF-LU1, WRF-LU2, and WRF-LU3 simulations are broadly comparable, whereas the WRF-LU4 experiment exhibits markedly different behavior. Specifically, the PBIAS of WRF-LU4 ranges from 10% to 60% relative to DPET and from -10% to 40% relative to ERA5, in contrast to the narrower ranges of -20% to 20% (DPET) and -40% to 5% (ERA5) observed in the other experiments.

The spatial distributions of RMSE for daily PET are shown in Fig. 7.8 and Fig. A.13 for

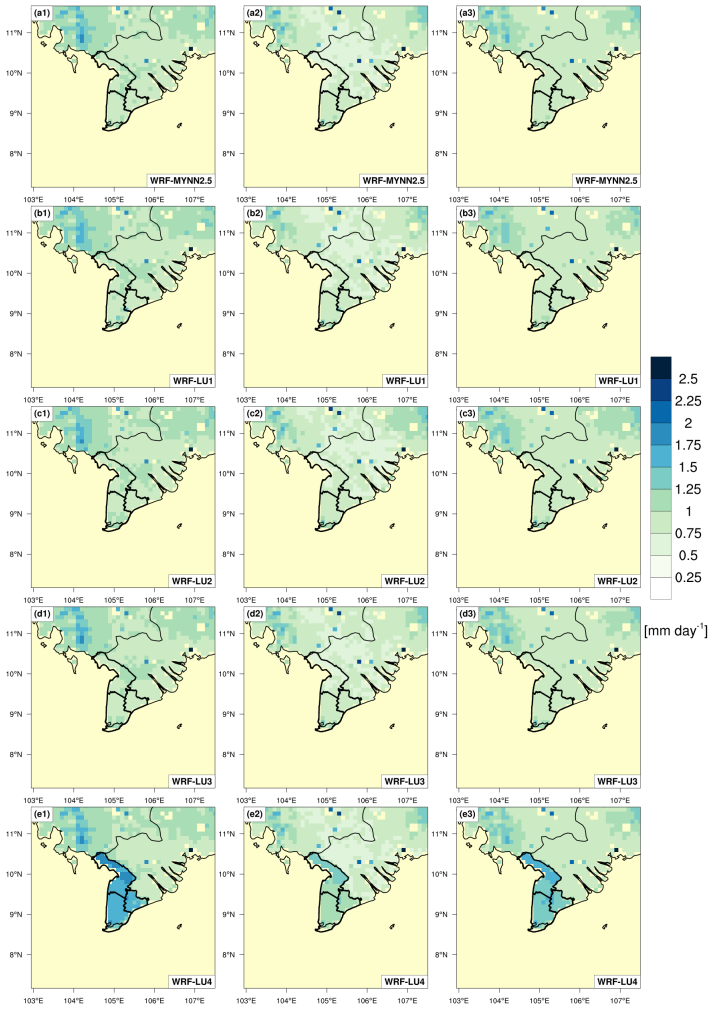

Figure 7.8.: The performance of WRF-ARW experiments using different LULC datasets is illustrated by RMSE of daily PET relative to DPET for the rainy season (first column), dry season (second column), and annual (third column) periods, averaged over the period 2007–2016. Panels (a1–a3), (b1–b3), (c1–c3), (d1–d3), and (e1–e3) correspond to results from the WRF-MYNN2.5, WRF-LU1, WRF-LU2, WRF-LU3, and WRF-LU4 experiments, respectively.

comparisons against DPET and ERA5, respectively. A pronounced distinction is observed between the WRF-LU4 simulation and the remaining experiments. When evaluated against DPET, the WRF-LU4 simulation yields the largest RMSE values in both seasons, ranging from 1.0 to 1.5 mm day^{-1} in the dry season and increasing to 1.5 to 2.0 mm day^{-1} in the rainy season. In contrast, the RMSE values of the other simulations remain within 0.5 to 1.25 mm day^{-1} across both seasons. Overall, all WRF-ARW simulations demonstrate better performance during the dry season than during the rainy season. Except for WRF-LU4, differences in RMSE among the remaining simulations are minor, with the control experiment exhibiting the lowest RMSE in both seasons (see Table 7.2). Similar conclusions are drawn from the comparison with ERA5 (Fig. A.13), where WRF-LU4 again shows the largest RMSE during the rainy season and the smallest during the dry season.

Table 7.2.: PBIAS and RMSE of simulated daily PET compared to station data (Penman-Monteith and GGI-3000), ERA5, and DPET over the Ca Mau Peninsula for the period 2007–2016. Bold numbers indicate the experiments with the lowest RMSE values for each time period.

	PBIAS(%)				
Experiment	**WRF-MYNN2.5**	**WRF-LU1**	**WRF-LU2**	**WRF-LU3**	**WRF-LU4**
Stations (Penman-Monteith)					
Rainy season	-13.42	-11.58	-11.75	-13.46	14.25
Dry season	-14.11	-11.32	-11.49	-14.88	12.22
Year	-13.78	-11.49	-11.62	-14.19	13.31
Stations (GGI-3000)					
Rainy season	-7.93	-7.94	-5.13	-6.66	10.86
Dry season	-14.85	-17.27	-12.18	-13.82	1.18
Year	-11.65	-12.95	-8.92	-10.51	5.66
ERA5					
Rainy season	-7.66	-7.63	-7.34	-7.74	15.69
Dry season	-20.09	-19.67	-20.37	-21.61	-4.56
Year	-14.51	-14.26	-14.52	-15.37	4.54
DPET					
Rainy season	5.59	6.74	5.61	5.12	34.32
Dry season	-1.93	-1.27	-3.27	-4.33	18.92
Year	1.59	2.47	0.88	0.85	26.12
	RMSE(mm)				
Stations (Penman-Monteith)					
Rainy season	1.36	**1.34**	1.36	1.38	1.51
Dry season	1.18	**1.13**	1.15	1.21	1.16
Year	1.27	**1.24**	1.26	1.30	1.35
Stations (GGI-3000)					
Rainy season	1.10	1.23	**1.05**	1.09	1.62
Dry season	1.14	1.31	**1.06**	1.11	1.23
Year	1.12	1.27	**1.06**	1.10	1.44
ERA5					
Rainy season	**1.11**	1.12	1.13	1.14	1.36
Dry season	1.45	1.44	1.49	1.53	**1.16**
Year	1.29	1.29	1.32	1.35	**1.27**
DPET					
Rainy season	**0.96**	0.99	0.98	0.98	1.67
Dry season	**0.81**	0.82	0.84	0.83	1.20
Year	**0.89**	0.91	0.91	0.91	1.46

To further quantify model performance, Taylor diagrams based on PET estimated from the Penman–Monteith equation at three stations are presented in Fig. 7.9a. All simulations exhibit relatively high correlation coefficients, ranging from 0.60 to 0.65 in the dry season and 0.40 to 0.45 in the rainy season. With the exception of WRF-LU4, all experiments display negative PBIAS values between -10% and -20% in both seasons, indicating a systematic underestimation of PET. In contrast, WRF-LU4 shows positive PBIAS values of 10–20%, reflecting an overestimation of PET. In terms of RMSE, the WRF-LU1 experiment achieves the lowest values in both seasons.

The influence of LULC scenarios on the two primary drivers of PET, namely, 10-m wind speed

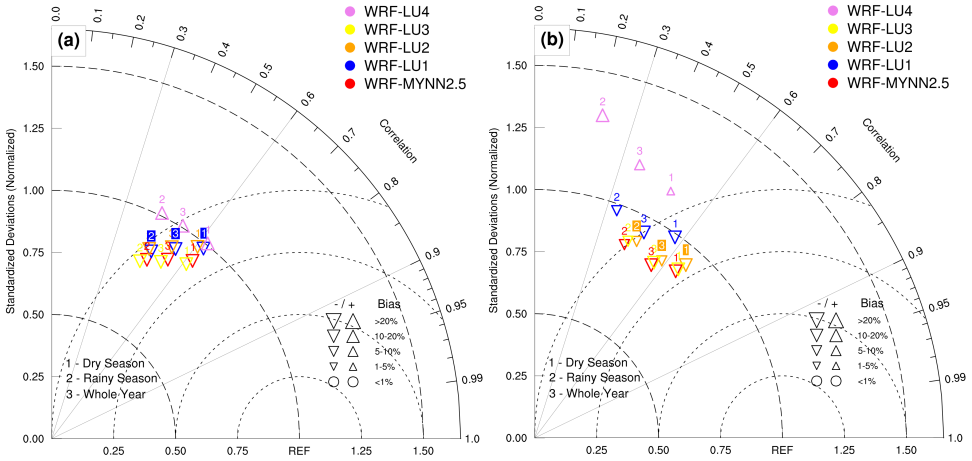

Figure 7.9.: The performance of WRF-ARW experiments employing different LULC datasets is assessed using Taylor diagrams for daily PET against (a) estimates using the Penman Monteith equation and (b) GGI-3000 measurements. Results are shown for the WRF-MYNN2.5 (red symbols), WRF-LU1 (blue symbols), WRF-LU2 (orange symbols), WRF-LU3 (yellow symbols), and WRF-LU4 (violet symbols) experiments across the dry season, rainy season, and the entire year over the period 2007–2016. Experiments with the smallest RMSE are highlighted with a color-filled background of the numbers indicating the reference period.

and net radiation, is summarized in Tables 7.3 and 7.4. For the 10-m wind speed, all LULC scenarios induce an increase in PBIAS relative to the control simulation, with the LU4 scenario producing a particularly large enhancement ($+123.04\%$). Correspondingly, LU4 results in a substantial increase in RMSE ($+2.71$ mm day^{-1}), whereas LU1, LU2, and LU3 cause only modest increases. All simulations perform better in the dry season than in the rainy season. For net radiation, LU4 again induces a pronounced positive shift in PBIAS ($+25.9\%$), whereas the other scenarios result in relatively small changes. RMSE values for net radiation are generally lower during the dry season, and, except for LU4, most LULC scenarios result in a slight reduction in net radiation.

Figure 7.9b further illustrates the Taylor diagrams for PET observed by GGI-3000 devices at two stations. All simulations exhibit higher correlation coefficients during the dry season (0.5–0.65) than during the rainy season (0.3–0.4). The WRF-LU4 experiment consistently shows the lowest correlation coefficients and positive PBIAS values, confirming its tendency to overestimate PET, while the remaining simulations underestimate PET. Among them, WRF-LU2 yields the lowest RMSE in both seasons

(see Table 7.2).

Overall, these results indicate that LULC changes exert only a limited influence on PET simulation over the Ca Mau Peninsula, except under the extreme LU4 scenario. Simulations using observed LULC datasets (WRF-LU1 and WRF-LU2) reveal negligible impacts compared to the control experiment. In contrast, the hypothetical LU4 scenario results in substantial increases in PET, primarily driven by enhanced 10-m wind speed and altered net radiation, whereas the LU3 scenario induces only minor changes.

Table 7.3.: PBIAS and RMSE of simulated daily 10-m wind speed from WRF-ARW experiments compared to station data over the Ca Mau Peninsula for the period 2007–2016. Bold numbers indicate the experiments with the lowest RMSE values for each time period.

	PBIAS (%)				
Experiment	**WRF-MYNN2.5**	**WRF-LU1**	**WRF-LU2**	**WRF-LU3**	**WRF-LU4**
Stations (Penman-Monteith)					
Rainy season	44.4	66.65	66.82	48.9	160.67
Dry season	62.9	84.79	84.75	68.33	191.99
Year	51.7	74.33	75.94	57.7	174.74
	RMSE (ms^{-1})				
Stations (Penman-Monteith)					
Rainy season	**1.40**	1.85	1.87	1.50	4.27
Dry season	**1.60**	1.97	1.95	1.63	4.14
Year	**1.50**	1.91	1.91	1.57	4.21

Table 7.4.: PBIAS and RMSE of simulated net radiation from WRF-ARW experiments compared to station data over the Ca Mau Peninsula for the period 2007–2016. Bold numbers indicate the experiments with the lowest RMSE values for each time period.

	PBIAS (%)				
Experiment	**WRF-MYNN2.5**	**WRF-LU1**	**WRF-LU2**	**WRF-LU3**	**WRF-LU4**
Stations (Penman-Monteith)					
Rainy season	-9.83	-12.4	-13.98	-13.70	12.61
Dry season	-17.95	-18.4	-21.19	-24.91	11.28
Year	-13.93	-15.44	-17.61	-19.34	11.97
	RMSE (MJ m^{-2})				
Stations (Penman-Monteith)					
Rainy season	**3.51**	3.66	3.75	3.78	4.06
Dry season	**3.40**	3.40	3.61	3.97	3.04
Year	**3.46**	3.53	3.68	3.87	3.59

7.5. Response of simulated daily actual evapotranspiration to land-use and land-cover change over the Ca Mau Peninsula

This section evaluates the role of the LULC scenario in the AET simulation. As the entire area of the Ca Mau Peninsula was covered by water in the LU4 scenario, the Noah-MP land surface model was unable to operate and generate all the actual evapotranspiration components. Therefore, in addition to the control simulation, the performance of the WRF-ARW simulations with three scenarios, including LU1, LU2, and LU3, is examined in this section. One of the main issues in our knowledge of AET over the Ca Mau Peninsula is the lack of observational data; no instrument is currently capable of measuring AET in this area. As a result, this study rely only on the model-derived datasets consisting of ERA5, REA, and GLEAM v3.5 products to evaluate the performance of all the WRF-ARW simulations.

Figure 7.10, Figure A.14, and Figure A.16 show the spatial distributions of PBIAS of the daily

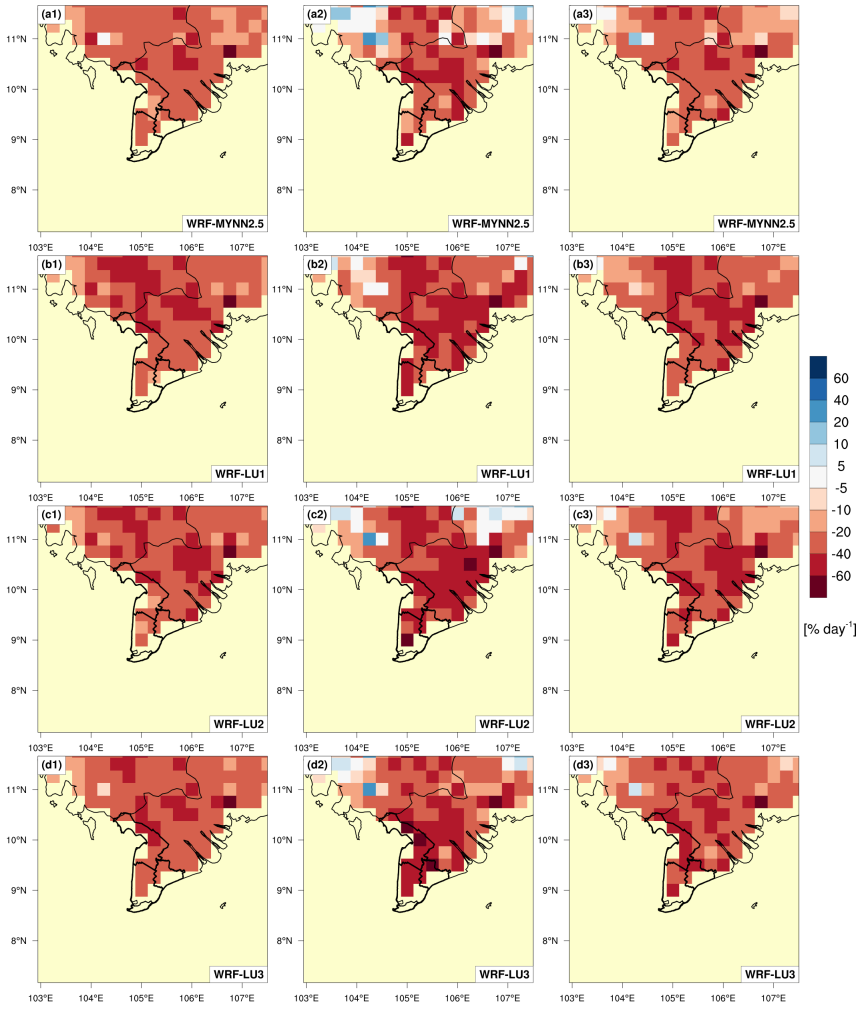

Figure 7.10.: The performance of WRF-ARW experiments using different LULC datasets is illustrated by the PBIAS of daily AET relative to ERA5 for the rainy season (first column), dry season (second column), and annual period (third column), averaged over the period 2007–2016. Panels (a1–a3), (b1–b3), (c1–c3), and (d1–d3) correspond to results from the WRF-MYNN2.5, WRF-LU1, WRF-LU2, WRF-LU3 experiments, respectively.

AET for the control simulation and the WRF-ARW simulations with LU1, LU2, and LU3 scenarios against ERA5, REA, and GLEAM v3.5 product for the period 2007–2016. As detailed in Fig. 7.10 and Fig. A.14, the value of PBIAS of all simulations over the Ca Mau Peninsula against ERA5 and REA are negative in both seasons, ranging from -5% to -60%. On the other hand, Figure A.16 shows both negative and positive values for the PBIAS of all simulations in the two seasons, with the value of PBIAS ranging from -60% to 60%. As shown in the three figures above, compared to the control simulation, simulations with different LULCC scenarios tend to decrease AET and exhibit smaller PBIAS.

Figure 7.11, Figure A.15, and Figure A.17 show the spatial distributions of RMSE of the daily

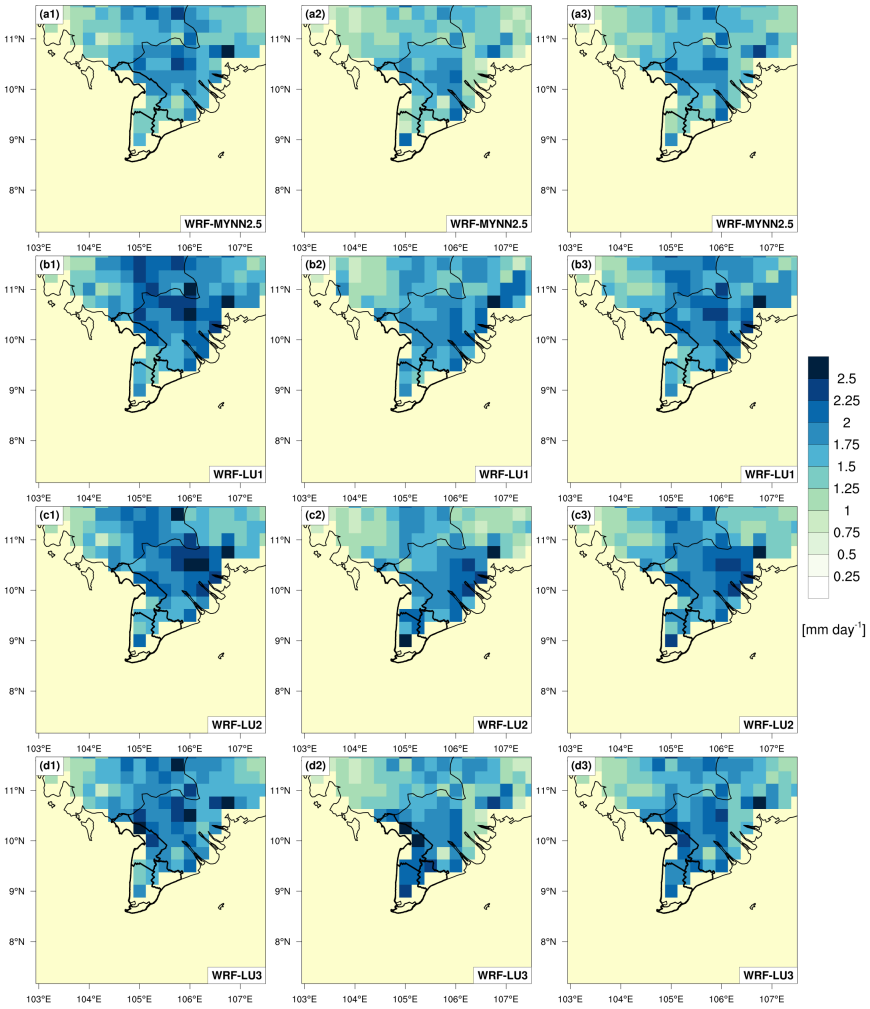

Figure 7.11.: The performance of WRF-ARW experiments using different LULC datasets is illustrated by RMSE of daily AET relative to ERA5 for the rainy season (first column), dry season (second column), and annual period (third column), averaged over the period 2007–2016. Panels (a1–a3), (b1–b3), (c1–c3), and (d1–d3) correspond to results from the WRF-MYNN2.5, WRF-LU1, WRF-LU2, WRF-LU3 experiments, respectively.

AET for the control simulation and the WRF-ARW simulations with LU1, LU2, and LU3 scenarios against ERA5, REA, and GLEAM v3.5 product for the period 2007–2016. In contrast to the PET results described in the previous section, notable differences were observed between the RMSE of the control simulation and those of the other simulations across the three products in both seasons. Notably, the

control simulation consistently yields the smallest RMSE against the three products mentioned above, with values of 1.49 day^{-1} against ERA5, 1.62 day^{-1} against REA, and 1.13 day^{-1} against REA (see Table 7.5). This is followed by WRF-LU1, WRF-LU2 and WRF-LU3.

The results provide robust evidence that LULCC exerts a substantial influence on AET simulations over the Ca Mau Peninsula. Simulations incorporating the observed LULC dataset, as represented by the WRF-LU1 and WRF-LU2 experiments, consistently indicate a notable reduction in daily AET across seasons. Likewise, simulations based on the hypothetical LULC scenarios exhibit an even stronger response, resulting in a more pronounced decline in daily AET, with the most considerable magnitude of change observed under this scenario.

AET is composed of three primary components: canopy evaporation, direct evaporation from the

Table 7.5.: PBIAS and RMSE of simulated daily AET compared to ERA5, REA, and GLEAM v3.5 over the Ca Mau Peninsula for the period 2007–2016. Bold numbers indicate the experiments with the lowest RMSE values for each time period.

	PBIAS(%)			
Experiment	**WRF-MYNN2.5**	**WRF-LU1**	**WRF-LU2**	**WRF-LU3**
ERA5				
Rainy season	-24.98	-29.62	-28.92	-31.79
Dry season	-30.04	-37.75	-45.15	-58.09
Year	-27.30	-33.33	-36.33	-43.76
REA				
Rainy season	-30.23	-33.47	-34.5	-36.65
Dry season	-36.98	-42.29	-53.78	-63.46
Year	-33.28	-37.46	-43.22	-48.77
GLEAM V3.5				
Rainy season	9.17	4.10	2.48	-0.87
Dry season	4.48	-4.33	-23.38	-39.41
Year	7.12	0.41	-8.84	-17.75
	RMSE(mm)			
ERA5				
Rainy season	**1.50**	1.71	1.75	1.88
Dry season	**1.49**	1.70	1.96	2.28
Year	**1.49**	1.70	1.85	2.08
REA				
Rainy season	**1.61**	1.88	1.95	2.06
Dry season	**1.63**	1.85	2.20	2.47
Year	**1.62**	1.87	2.07	2.27
GLEAM v3.5				
Rainy season	**1.11**	1.37	1.40	1.45
Dry season	**1.14**	1.19	1.27	1.46
Year	**1.13**	1.28	1.33	1.45

soil surface, and plant transpiration. By coupling the WRF-ARW model with the Noah-MP land surface scheme, this study provides detailed insights into how LULCC influences the simulation of individual

AET components over the Ca Mau Peninsula.

Table 7.6 summarizes the mean annual contributions of each component to total AET for the period 2007–2016. Understanding the partitioning of AET is essential for interpreting land–atmosphere interactions and their links to hydrological and ecological processes (Wei et al., 2017). In the control and WRF-LU1 simulations, transpiration is the dominant contributor to annual AET, accounting for 52.72% and 50.45%, respectively. In contrast, direct evaporation becomes the dominant component in the WRF-LU2 and WRF-LU3 simulations, contributing 61.46% and 77.35% of annual AET, respectively. Across all simulations, canopy evaporation remains the smallest component, contributing between 1.88% and 6.11%. For the default land-use configuration and LU1, where the Ca Mau Peninsula is primarily covered by vegetated surfaces such as forest and cropland, the ratio of transpiration to total AET (T/AET) exceeds 50% in both the control and WRF-LU1 simulations. Conversely, under the LU2 and LU3 scenarios, which are characterized by extensive wetland coverage, the T/AET ratio decreases markedly to below 35.5% in the WRF-LU3 simulation. These findings are consistent with those of Wei et al. (2017), who demonstrated that transpiration generally dominates AET across most vegetation classes, accounting for approximately 55.0% to 66.0% of total AET. In contrast, in a wetland class, lower LAI results in a substantially reduced transpiration contribution of around 33.0%. Overall, the results indicate that the Noah-MP model is capable of realistically simulating the relative contributions of AET components over the Ca Mau Peninsula.

The seasonal evolution of AET and its components was further examined using monthly mean

Table 7.6.: Annual contribution of each component to AET over the Ca Mau Peninsula for the period 2007–2016. Bold numbers indicate experiments with the highest contribution for each component.

	Annual contribution to AET(%)			
Experiment	**WRF-MYNN2.5**	**WRF-LU1**	**WRF-LU2**	**WRF-LU3**
Transpiration	**52.72**	50.45	35.46	20.77
Direct evaporation	41.17	44.81	61.46	**77.35**
Canopy evaporation	**6.11**	4.74	3.08	1.88

values for all simulations (Figs. 7.12a–d). As shown in Fig. 7.12d, AET exhibits a pronounced seasonal cycle, with higher values during the rainy season and lower values during the dry season across all experiments. The control and WRF-LU1 simulations peak in August, whereas the maximum AET occurs later in the year for WRF-LU2 (September) and WRF-LU3 (October). Throughout the year, the control simulation consistently produces the highest monthly AET, followed by WRF-LU1, WRF-LU2, and WRF-LU3, with differences being more pronounced during the dry season. Monthly AET values range approximately from 20 to 100 mm month^{-1}.

The seasonal patterns of canopy evaporation and direct evaporation (Figs. 7.12a and 7.12c) broadly follow those of total AET, with enhanced values during the rainy season. Canopy evaporation peaks in September for all simulations, while direct evaporation peaks earlier (July) in the control

and WRF-LU1 simulations and later (September) in WRF-LU2 and WRF-LU3. The control simulation consistently yields the highest canopy evaporation (up to 11 mm month^{-1}), whereas it produces the lowest direct evaporation compared to the other experiments. Differences among simulations are again more evident during the dry season, with direct evaporation ranging from approximately 5 to 80 mm month^{-1}. In contrast to total AET, transpiration exhibits an inverse seasonal pattern (Fig. 7.12b), with higher values during the dry season and reduced values during the rainy season. Maximum transpiration occurs in January and February, followed by a gradual decline to a minimum in April and May, and a subsequent increase toward the end of the year. This seasonal behavior closely resembles the observed LAI cycle derived from the GEO v2.0 dataset (Fig. 5.2) and reflects the influence of dynamic vegetation processes represented in the Noah-MP model. Across all months, the control simulation produces the highest transpiration, followed by WRF-LU1, WRF-LU2, and WRF-LU3, with monthly values ranging from approximately 5 to 55 mm month^{-1}. These results indicate that differences in simulated AET among the experiments are primarily driven by variations in transpiration.

The markedly reduced transpiration in the WRF-LU2 and WRF-LU3 simulations is associated

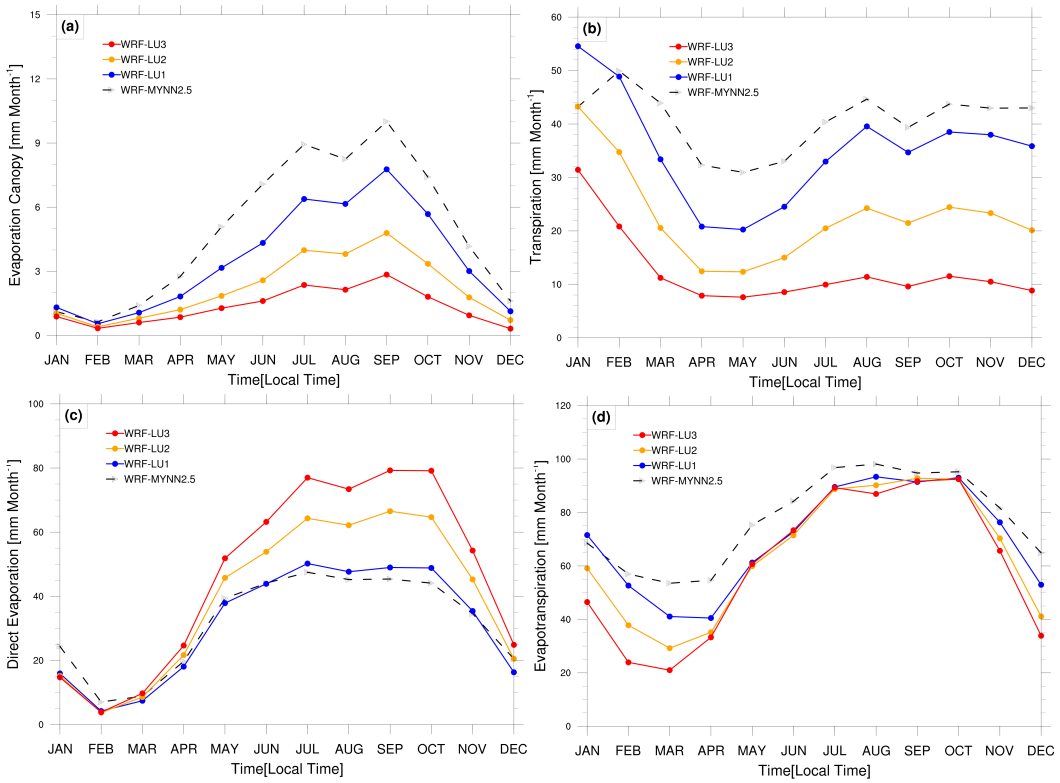

Figure 7.12.: Time series of monthly domain-averaged (a) canopy evaporation, (b) transpiration, (c) direct evaporation, and (d) AET simulated by the WRF-MYNN2.5 (black dashed line), WRF-LU1 (blue line), WRF-LU2 (orange line), and WRF-LU3 (yellow line) experiments over the Ca Mau Peninsula for the period 2007–2016.

with the dominance of wetlands in these scenarios (55.0% coverage in LU2 and 100.0% in LU3). This reduction reflects limitations in the current representation of wetland processes in the Noah-MP model, which employs relatively simplified wetland parameterizations (Zhang et al., 2022).

The aforementioned results demonstrate that LULCC exerts a considerable influence on the simulation of all components of AET in several ways. Primarily, it affects the proportion of each component contributing to annual AET. Secondly, it notably substantially modulates the monthly transpiration, which represents the most dominant component. Synthesizing the findings from Sections 7.2 to 7.5, it can be concluded that when freshwater flux is defined as precipitation minus PET, the influence of LULCC on it over the Ca Mau Peninsula is negligible. However, when freshwater flux is defined as precipitation minus AET, LULCC plays a critical role by significantly modifying transpiration and, ultimately, the overall freshwater flux.

7.6. The freshwater flux over the Ca Mau Peninsula

This section analyzes the freshwater flux over the Ca Mau Peninsula during the period 2007–2016 based on the WRF-LU2 simulation. The LU2 experiment is adopted as the reference scenario because it represents the most realistic observed LULC for the study region. In this analysis, freshwater flux is defined as the difference between precipitation and PET.

Figures 7.13a1–a12 illustrate the spatial distribution of monthly mean daily freshwater flux across the Ca Mau Peninsula as simulated by the WRF-LU2 experiment. A clear seasonal contrast is observed. From December to April, freshwater flux values are uniformly negative over the entire peninsula, indicating that PET exceeds precipitation during the dry season. In contrast, from June to October, freshwater flux values are consistently positive, reflecting a surplus of precipitation during the rainy season. Transitional conditions occur in May and November, with negative freshwater flux observed over Kien Giang province, whereas positive values prevail over Ca Mau and Bac Lieu provinces. The maximum freshwater flux is attained in September, coinciding with the peak of the rainy season, while the minimum occurs in February. These spatial–temporal patterns are consistent with the monthly freshwater flux derived from the TMPA and DPET datasets (Fig. 4.7c). Notably, Kien Giang province consistently exhibits the lowest freshwater flux among the three provinces throughout the year.

Figure 7.14 presents the domain-averaged monthly freshwater flux simulated by the WRF-LU2 experiment. The results reveal a pronounced annual cycle. Freshwater flux remains negative during the first quarter of the year, reaching its minimum in February and March, indicating that atmospheric evaporative demand exceeds precipitation during the late dry season. From April onward, freshwater flux increases rapidly and becomes positive in May. The maximum freshwater flux is recorded in September, when precipitation substantially exceeds PET. Subsequently, freshwater flux declines sharply after September, approaching neutral conditions in November, and then turns negative again in December as rainfall decreases and PET regains dominance. Overall, the simulated seasonal evolution of freshwater flux is physically consistent with the monsoon climate of the Ca Mau Peninsula, characterized by water deficits during the dry season and substantial freshwater surpluses during the rainy season.

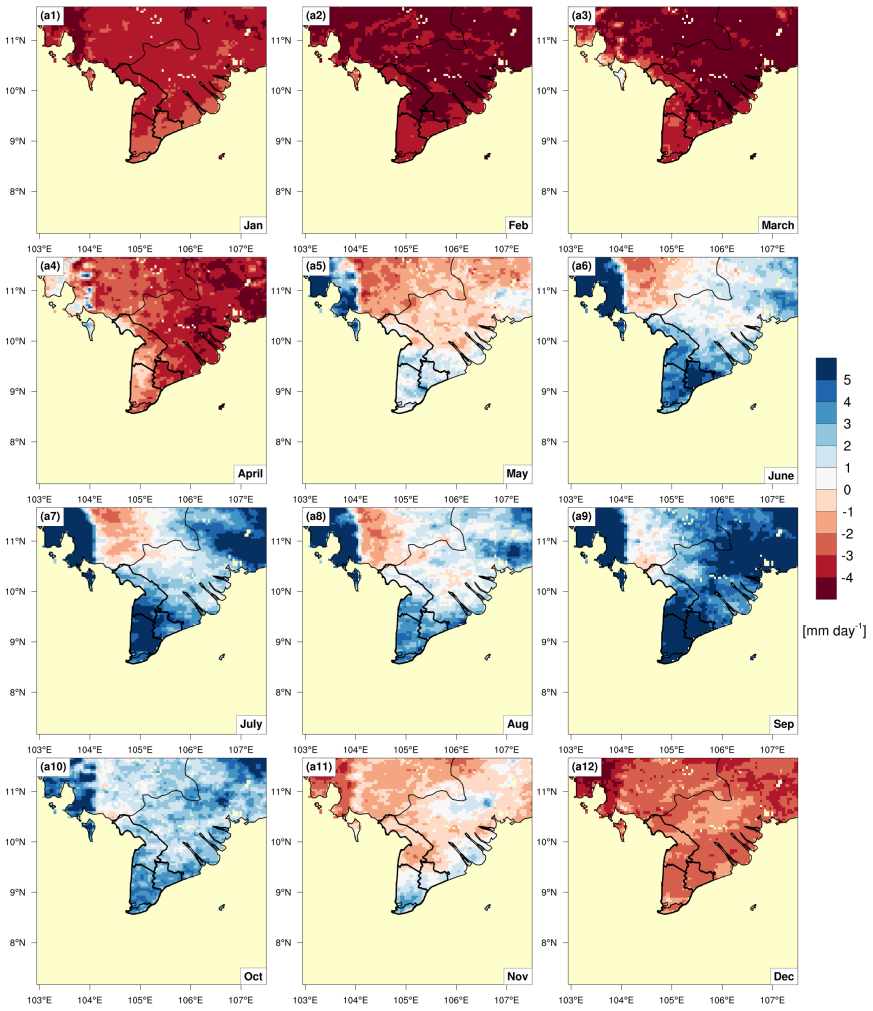

Figure 7.13.: The daily mean freshwater flux of experiment WRF-LU2 in (a1) January, (a2) February, (a3) March, (a4) April, (a5) May, (a6) June, (a7) July, (a8) August, (a9) September, (a10) October, (a11) November and (a12) December over the Ca Mau Peninsula for the period 2007–2016.

Figures 7.15a and 7.15b further depict the spatial distribution of daily freshwater flux during the dry and rainy seasons, respectively. A marked seasonal contrast is evident. During the dry season, freshwater flux is uniformly negative across the peninsula, ranging from -2.0 to -3.0 mm day^{-1} over Kien Giang and Bac Lieu provinces, and from -1.0 to -2.0 mm day^{-1} over Ca Mau Province. In contrast, during the rainy season, freshwater flux values are entirely positive, ranging from 0 to 6.0 mm day^{-1} across the peninsula. Ca Mau province exhibits the highest freshwater flux during this period, with values of approximately 4–5 mm day^{-1}. These results closely agree with freshwater flux estimates derived from the TMPA and DPET datasets (Fig. 4.6), further confirming the robustness of the WRF-LU2 simulation in capturing the seasonal characteristics of freshwater flux over the Ca Mau Peninsula.

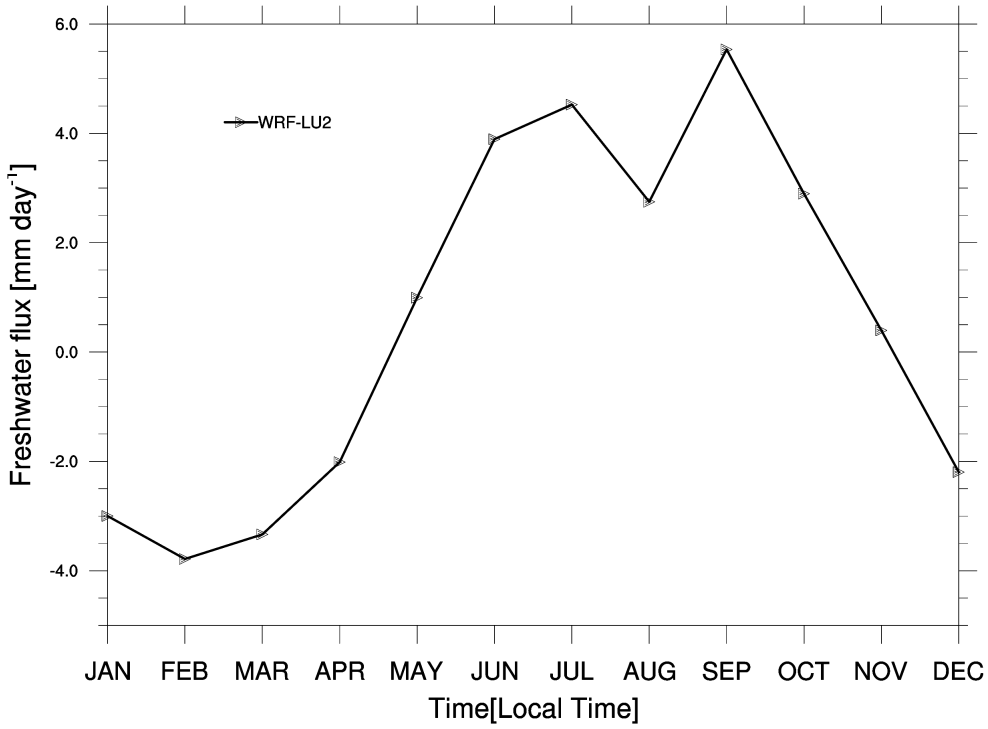

Figure 7.14.: Time series of monthly domain-averaged freshwater flux of experiment WRF-LU2 over the Ca Mau Peninsula for the period 2007–2016.

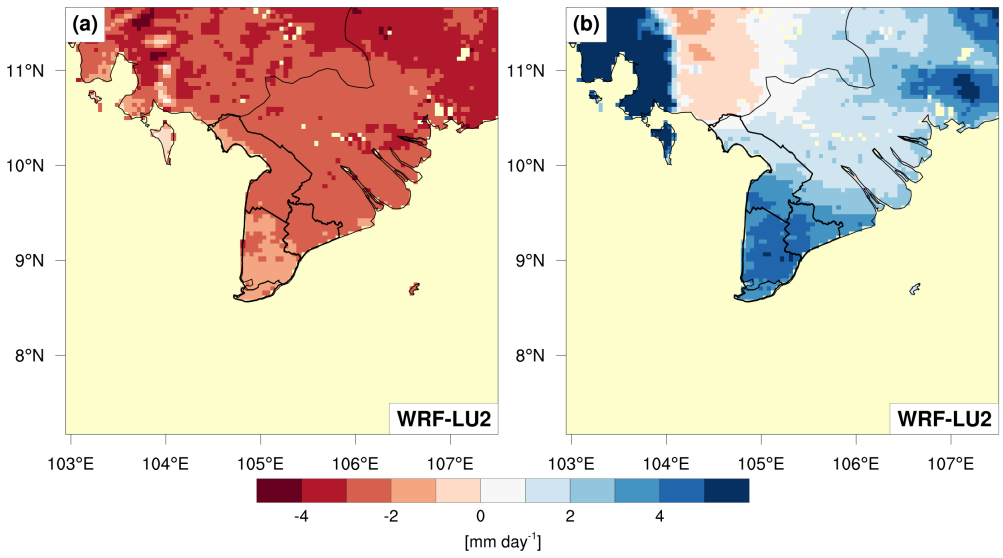

Figure 7.15.: The daily mean freshwater flux of experiment WRF-LU2 in (a) the dry seasons and (b) the rainy seasons over the Ca Mau Peninsula for the period 2007–2016.

8. Conclusions and Outlook

The Ca Mau Peninsula, a sub-region of the Vietnamese Mekong Delta, constitutes the country's most important aquaculture center and a major contributor to national rice production. The freshwater flux in this region plays a crucial role in sustaining food production systems, preserving ecosystem integrity, and supporting the livelihoods of communities that rely on agriculture and aquaculture. Accurate quantification of freshwater flux is therefore critical importance for effective water resource management and climate adaptation planning in this region. Over the past decades, the Vietnamese Mekong Delta has experienced profound LULCC, driven primarily by the rapid, largely uncontrolled expansion of agricultural and aquaculture systems. These changes have substantially modified surface characteristics, evapotranspiration processes, and hydrological responses, thereby introducing additional uncertainty into freshwater flux simulations. Against this background, this dissertation aims to improve the simulation and understanding of freshwater flux over the Ca Mau Peninsula by employing the WRF-ARW model at gray-zone resolution (5 km) for the period 2007–2016, taking into account observed and hypothetical LULC scenarios. Particular emphasis is placed on a comprehensive evaluation of the freshwater flux components, including precipitation and evapotranspiration, using both PET and AET concepts. The primary strength of this study lies in the extensive use of relatively dense in-situ station observations, which serve as robust references for model evaluation. The following section summarizes the main findings of this study and outlines directions for future research.

8.1. Conclusion

The first aim of this work was to identify an appropriate configuration of WRF-ARW physical parameterizations for simulating freshwater fluxes over the Ca Mau Peninsula. Four research questions were asked to address this aim. These questions are answered in chapter five and are summarized as follows:

1. **RQ 1a Which cumulus convection parameterization, with or without activation of the sst_skin option, provides the most accurate simulation of daily precipitation and its diurnal cycle at 5-km horizontal resolution over the Ca Mau Peninsula?**
   At the 5-km "gray-zone" resolution, the most skillful model configuration is obtained by explicitly resolving deep convection (i.e., without employing a cumulus parameterization) in combination with activation of the sst_skin option. The explicit-convection experiment (WRF-MYNN2.5) consistently demonstrates superior performance across daily, 5-day, and 10-day precipitation accumu-

lations, exhibiting the highest correlation coefficients and the lowest RMSE relative to simulations employing alternative cumulus schemes, when evaluated against station observations. Furthermore, enabling the sst_skin option substantially reduces precipitation biases, with improvements of approximately 10–40%, particularly during the rainy season. This configuration also enhances the representation of the diurnal cycle of precipitation, yielding more realistic amplitudes and timing of coastal and oceanic precipitation maxima.

Similar findings have been reported by Senatore et al. (2014); Pilatin et al. (2021), who demonstrated that activating the sst_skin option, by explicitly resolving the thin skin layer at the air-sea interface and its modulation by atmospheric conditions, significantly improves the accuracy of precipitation simulations. Their results indicate that this approach reduces modelling uncertainties in mesoscale atmospheric simulations, particularly over coastal regions and areas characterized by complex topography.

The choice of cumulus parameterization for rainfall simulations at gray-zone resolution over Asia remains a subject of ongoing debate. While several studies advocate disabling cumulus schemes in WRF simulations at convective gray-zone resolutions for long-term rainfall simulation (e.g., Zhou et al., 2023; Sun et al., 2021b; Ou et al., 2020), others emphasize the continued use of scale-aware cumulus parameterizations, such as the Grell–Freitas or multi-scale Kain–Fritsch schemes (e.g., Kwon and Hong, 2017; Park et al., 2022; Qian et al., 2024), to facilitate a gradual transition toward explicitly resolved convection while preserving large-scale moisture convergence and climatological stability. In this context, the present study contributes additional evidence indicating that, for the Ca Mau Peninsula in southern Vietnam, switching off the cumulus parameterization at gray-zone resolutions yields a more accurate representation of long-term rainfall characteristics.

2. **RQ 1b Which is the most appropriate vegetation option in the Noah-MP land surface model to simulate AET over the Ca Mau Peninsula?**

   The dynamic vegetation option emerges as the most appropriate modelling choice. When dynamic vegetation is activated, the model more accurately reproduces the seasonal evolution of the LAI, including the timing of its annual maximum. More importantly, differences in AET among experiments become physically interpretable, as they are primarily driven by variations in transpiration associated with vegetation dynamics. The results further indicate that updating LULC alone exerts only a marginal influence when dynamic vegetation is deactivated. In contrast, dynamic vegetation is indispensable for achieving realistic LAI simulations and, consequently, for a consistent representation of AET, particularly when combined with updated LULC datasets.

   These results are in line with previous evidence demonstrating the capability of the dynamic vegetation option in Noah-MP to reproduce interannual variations in LAI when integrated with parameter optimization and data assimilation frameworks. Specifically, Shu et al. (2022) showed

that such a coupled modelling approach yields realistic representations of LAI variability over the Loess Plateau in China during the 2011–2017 period, exhibiting close agreement with GEO v2.0 observational datasets.

3. **RQ 1c Among the three commonly used PBL parameterization schemes, including MYJ, MYNN2.5, and ACM2, which scheme is most suitable for simulating both components of the freshwater flux, namely daily precipitation (including its diurnal cycle) and PET, over the Ca Mau Peninsula?**

   When both components of the freshwater flux, namely precipitation and PET, are considered, the MYNN2.5 PBL parameterization is found to be the most suitable overall scheme for simulations over the Ca Mau Peninsula at gray-zone resolution.

   For daily precipitation, the results indicate that local-closure PBL schemes, including MYJ and MYNN2.5, exhibit comparable performance and consistently outperform the non-local closure ACM2 scheme. Both local-closure schemes reproduce the observed spatial patterns of precipitation more realistically, particularly during the dry season. In the rainy season, MYJ and MYNN2.5 tend to produce widespread dry biases over the Ca Mau Peninsula and adjacent marine areas, whereas ACM2 systematically generates wet biases across the peninsula. Although the non-local ACM2 scheme has been reported to outperform local-closure schemes in several regions (e.g., Meroni et al., 2021; Huang et al., 2023; Sharma et al., 2024), its application in the Ca Mau Peninsula proves inadequate, as it persistently overestimates rainfall in both seasons. This behavior is consistent with the findings of Wang et al. (2014), who attributed excessive precipitation under the ACM2 scheme to enhanced sea-surface latent heat fluxes and stronger convective activity, leading to deviation in monsoon circulation over East Asia.

   Regarding the diurnal cycle of precipitation, gray-zone WRF-ARW simulations are generally capable of reproducing the key characteristics observed over the Ca Mau Peninsula. Nevertheless, all experiments underestimate both rainfall frequency and intensity during nighttime hours (19:00–04:00 LT). Among the tested schemes, WRF-MYNN2.5 most successfully captures the observed coastal rainfall maximum, located approximately 200 km inland from the western coastline, in both timing and magnitude, and realistically represents the inland early-afternoon precipitation peak. In contrast, WRF-MYJ and WRF-ACM2 tend to produce an unrealistically early coastal rainfall peak in the morning and an overly strong inland afternoon maximum. These results are in agreement with recent findings by Lai et al. (2025), who demonstrated that high-resolution WRF-ARW simulations substantially improve the representation of the diurnal cycle of summer rainfall over Mainland Southeast Asia, especially in coastal and topographically complex regions.

   In terms of PET, performance metrics consistently identify WRF-MYNN2.5 as the best-performing PBL scheme. Although PET RMSE values may appear similar across schemes when evaluated

against ERA5, MYNN2.5 exhibits superior overall skill, characterized by higher correlation coefficients and the lowest RMSE when validated against multiple reference datasets, including DPET. Furthermore, MYNN2.5 more accurately represents the key drivers of PET, particularly 10-m wind speed and net radiation. In line with Xu et al. (2017); Bughici et al. (2019), these results confirm that biases in 10-m wind speed play a dominant role in controlling uncertainties in simulated PET

4. **RQ 1d What combination of physical parameterization schemes provides the most reliable representation of freshwater fluxes over the Ca Mau Peninsula?**
   As emphasized by Taraphdar et al. (2021), gray-zone simulations can achieve performance comparable to convection-permitting configurations when appropriate physical parameterizations are employed to adequately represent synoptic-scale and mesoscale processes. Consistent with this perspective, the present study identifies the most reliable overall configuration for simulating the freshwater flux over the Ca Mau Peninsula at 5-km horizontal resolution as the combination of the MYNN2.5 PBL parameterization scheme, activation of the sst_skin option, explicit convection scheme (i.e., without a cumulus parameterization), and the use of the dynamic vegetation option within the Noah-MP land surface model.

From the above answers, an optimal combination of physical parameterization schemes for the WRF-ARW model has been clearly identified to simulate all major components of freshwater flux over the Ca Mau Peninsula at a 5-km gray-zone resolution. This configuration comprises the MYNN2.5 PBL parameterization scheme, activation of the sst_skin option, an explicit convection scheme (i.e., without a cumulus parameterization), and the dynamic vegetation option within the Noah-MP land surface model. Building upon this configuration, the subsequent step was to provide a comprehensive assessment of whether the WRF-ARW model, operated at 5-km resolution with the selected physical parameterization, is capable of reliably simulating freshwater flux over the Vietnamese Mekong Delta for the long-term period 2007–2016. In chapter six, results answering questions aimed at achieving the second aim of this work were presented. The findings are:

1. **RQ 2a Is the WRF-ARW model able to derive the daily precipitation over the Ca Mau Peninsula during the period 2007–2016?**
   The results demonstrate that the WRF-ARW model, configured at a 5-km gray-zone resolution, is able to realistically reproduce the large-scale spatial patterns and seasonal contrasts of daily precipitation over the Ca Mau Peninsula for the period 2007–2016. In particular, the model captures the pronounced enhancement of rainfall during the rainy season, the substantial reduction during the dry season, and the dominant coastal–inland rainfall gradients. Nevertheless, the simulations exhibit a systematic dry bias, reflected by predominantly negative PBIAS values relative to both

CHIRPS and TMPA products. While domain-averaged RMSE values remain moderate when evaluated against satellite-based datasets, larger discrepancies emerge when compared with rain-gauge observations, underscoring the persistent challenges associated with representing convective precipitation processes at gray-zone resolutions. Overall, the WRF-ARW model provides a physically consistent yet conservative estimate of daily precipitation over the Ca Mau Peninsula.

These findings are broadly consistent with previous studies over the Mekong Delta region. Raghavan et al. (2016) reported a pronounced dry bias in WRF-ARW simulation at 25-km resolution across the Vietnamese Mekong Delta on both seasonal and annual scales. Similarly, Hoang-Cong et al. (2022), using the RegCM4.7 model, showed that while both 25-km and 5-km downscaling experiments capture the spatial distribution of climatological rainfall, higher resolution does not necessarily translate into improved performance. Specifically, their 5-km simulation tends to underestimate precipitation over the Mekong Delta, whereas the 25-km simulation exhibits wet biases in both dry and rainy seasons. These results support the notion that increased horizontal resolution alone cannot compensate for deficiencies in model physics. Instead, at gray-zone scales, the enhancement of local convective activities may alter fine-scale rainfall patterns and amplify biases (Navale and Singh, 2020), emphasizing the critical importance of appropriate physical parameterizations over the resolution-based improvements.

2. **RQ 2b Is the WRF-ARW model able to derive all characteristics of the diurnal cycle of precipitation over the Ca Mau Peninsula during the period 2007–2016?**

   The results show that the WRF-ARW model is able to reproduce the key temporal characteristics of the diurnal cycle of precipitation over the Ca Mau Peninsula, most notably the dominant early-afternoon peak occurring between 13:00 and 16:00 LT, which represents a defining feature in the TMPA observations. The simulations also capture the nocturnal minimum in rainfall amount. However, the model systematically underestimates rainfall frequency throughout the diurnal cycle and does not fully represent the observed suppression of rainfall frequency during the early morning hours. The largest discrepancies between simulations and satellite observations occur during nighttime and early morning periods. Despite these shortcomings, WRF-ARW successfully reproduces the phase, timing, and overall structure of the diurnal rainfall cycle, which is a critical prerequisite for a reliable assessment of freshwater fluxes.

   These findings are consistent with those reported by Lai et al. (2025) for mainland Southeast Asia. Using the WRF model driven by ERA5 at convection-permitting (3-km) and gray-zone (9-km) resolutions for the period 2002–2025, they demonstrated that WRF simulations capture the diurnal cycle of precipitation more realistically than ERA5 reanalysis. In particular, both configurations reproduce the characteristic afternoon rainfall peak over the Ca Mau Peninsula, while substantially

underestimating rainfall frequency relative to GPM IMERG observations.

3. **RQ 2c Is the WRF-ARW model able to derive the daily PET over the Ca Mau Peninsula during the period 2007–2016?**
   The WRF-ARW model exhibits strong capability in simulating daily PET over the Ca Mau Peninsula during the 2007–2016 period. The simulated PET shows good agreement with DPET, ERA5, and station-based reference datasets, with RMSE values remaining within an acceptable range for regional-scale meteorological applications. A systematic negative bias is evident relative to in-situ observations, indicating a general underestimation of PET in both the dry and rainy seasons. Further analysis indicates that PET performance is highly sensitive to the representation of driving variables, particularly 10-m wind speed and net radiation, with biases in 10-m wind speed contributing most substantially to the overall uncertainty in PET.
   Despite these biases, the WRF-ARW simulations successfully reproduce the seasonal evolution and spatial coherence of PET across the Ca Mau Peninsula, thereby providing a physically consistent basis for estimating freshwater flux. These findings are consistent with those of Du Duc et al. (2016), who reported that among surface meteorological variables simulated by WRF-ARW over Vietnam, 10-m wind speed exhibits the largest RMSE.
   Given the scarcity of long-term in situ PET observations over the Ca Mau Peninsula and Vietnam more broadly, reliance on a model-derived PET dataset is unavoidable. In this context, the present results further confirm the suitability of DPET as a reliable benchmark for PET evaluation, consistent with recent studies demonstrating its superior performance at both basin (Faseyiku et al., 2024) and global scales (Singer et al., 2021). Overall, these findings suggest that, when properly configured, WRF-ARW remains a reliable tool for PET analyses.

In summary, the WRF-ARW model, operating at gray-zone resolution, demonstrates a solid capability to simulate daily precipitation, its diurnal variability, and daily PET over the Ca Mau Peninsula, despite the presence of systematic biases. Although precipitation is generally underestimated and certain aspects of the diurnal cycle are not fully resolved, the model consistently reproduces the essential physical characteristics necessary for assessing regional-scale freshwater flux. Given that the LULC of the Ca Mau Peninsula has undergone pronounced transformations over the past three decades, an important question arises as to whether incorporating updated and more realistic LULC datasets can further improve the model's ability to simulate freshwater fluxes. This issue forms the core of the third objective of this study. The corresponding research questions were addressed in Chapter 7, and the main findings are summarized below:

1. **RQ 3a What is the response of simulated daily precipitation to updated/more realistic LULC datasets and hypothetical LULC scenarios in the WRF-ARW model?**
   Overall, integrating alternative LULC scenarios produces limited changes in domain-scale daily rainfall for the realistic (observed) datasets, while the extreme hypothetical scenarios exert a much stronger influence on daily rainfall. Specifically, the impact of the observed LULC updates (LU1–LU2) is described as negligible, whereas LU3 induces only minor changes and LU4 generates the most substantial modification. Across all experiments, daily precipitation remains systematically lower than in the control simulation, indicating a persistent dry bias in both dry and rainy seasons.
   To support the conclusion that, compared to the control simulation, all other simulations yield a slight decrease in precipitation, this study suggests an explanation. In the WRF-LU1 experiment, relative to the control simulation, a substantial proportion of the forested area, approximately 46% of the Ca Mau Peninsula, was converted to cropland. A precipitation analysis comparing the control and WRF-LU1 simulations indicates that this forest-to-cropland transition is associated with a modest reduction in precipitation. This response is consistent with previous studies, which have demonstrated that forestation tends to enhance atmospheric moisture transport, thereby increasing rainfall (Staal et al., 2024). For example, Li et al. (2021) reported that reforestation of cropland resulted in increased summer rainfall and more frequent extreme precipitation events in the Yangtze River basin. Conversely, Mortey et al. (2024) demonstrated that cropland expansion and associated deforestation led to a reduction of approximately 5% in precipitation and 3% in AET over the Sissili–Kulpawn Basin. Collectively, these results indicate that the conversion of forest to other LULC types tends to suppress precipitation, thereby accounting for the systematically drier conditions simulated under the modified LULC scenarios.

2. **RQ 3b What is the response of the simulated diurnal cycle of precipitation to updated/more realistic LULC datasets and hypothetical LULC scenarios in the WRF-ARW model?**
   Regarding the diurnal cycle of precipitation during the rainy season, the influence of LULCC remains weak across LU1–LU3, but becomes pronounced under the extreme hypothetical scenario (LU4). In the LU4 experiment, both rainfall frequency and intensity exhibit a marked shift from the typical early-afternoon maximum to an early-morning peak (07:00–10:00 LT), reflecting a transition toward an ocean-like diurnal cycle of precipitation behavior following the conversion of LULC to water bodies. Consistent with the response observed for daily precipitation, all LULCC experiments systematically reduce rainfall frequency and intensity throughout the diurnal cycle relative to the control simulation.
   This behavior is consistent with the findings of Takahashi et al. (2017) over the Maritime Continent, who used the WRF model to investigate the effects of deforestation on the diurnal cycle of

precipitation and reported a general weakening of all diurnal rainfall characteristics under deforested scenarios.

3. **RQ 3c What is the response of simulated daily PET to updated/more realistic LULC datasets and hypothetical LULC scenarios in the WRF-ARW model?**
   The results demonstrate that LULCC exerts only a limited influence on the simulation of PET over the Ca Mau Peninsula, except under the extreme hypothetical LU4 scenario. Simulations using observed LULC datasets (WRF-LU1 and WRF-LU2), as well as the hypothetical LU3 scenario, reveal negligible differences in PET compared to the control experiment. In contrast, the LU4 scenario induces a pronounced increase in PET, primarily attributable to substantially enhanced 10-m wind speed and altered net radiation.
   To the best of our knowledge, studies explicitly examining the impact of LULCC on PET over the Ca Mau Peninsula, and more broadly across Vietnam, remain scarce. In this context, the present findings provide a valuable foundation for applying RCMs to investigate LULC-PET interactions and offer a first quantitative assessment of the sensitivity of PET to LULC transformations in this region.

4. **RQ 3d What is the response of simulated daily AET to updated/more realistic LULC datasets and hypothetical LULC scenarios in the WRF-ARW model?**
   In contrast to PET, the results of this study indicate that LULCC exerts a substantial influence on the simulation of AET over the Ca Mau Peninsula. Simulations incorporating observed LULC datasets (LU1 and LU2) show a pronounced reduction in daily AET relative to the control experiment in both dry and rainy seasons. The effect is even more pronounced under the hypothetical LU3 scenario, which produces the largest decrease in daily AET across seasons. Nevertheless, when model performance is evaluated using RMSE against multiple AET reference products, the control experiment consistently achieves the lowest RMSE (e.g., annual RMSE of approximately 1.49 mm day^{-1} against ERA5 and 1.62 mm day^{-1} against REA), followed by LU1, LU2, and LU3.
   From a mechanistic perspective, differences in AET among LULC scenarios are primarily attributable to changes in transpiration. LULCC alters both the relative contribution of individual components to annual AET and the seasonal evolution of transpiration, which remains the dominant component of total AET. Variations in transpiration therefore largely explain the inter-scenario differences in simulated AET.
   The systematic reduction in AET relative to the control simulation can be physically explained by LULC transitions. In the WRF-LU1 experiment, approximately 46% of the Ca Mau Peninsula area is converted from forest to cropland. A comparison between the control and WRF-LU1

simulations reveals that this forest-to-cropland conversion results in a significant decrease in AET. This finding is consistent with previous studies. For example, Mortey et al. (2024) reported that deforestation associated with cropland expansion resulted in a 3% reduction in AET in the Sissili–Kulpawn Basin, while López-Espinoza et al. (2020) showed that forest conversion to cropland or bare land reduces vegetation cover, leading to lower AET and diminished latent heat fluxes. Collectively, these results reinforce the conclusion that reductions in vegetation density associated with LULCC suppress transpiration and, consequently, total AET.

5. **RQ 3e Is the permanent wetland category or the water body category suitable to represent the aquaculture area in the Noah-MP model to simulate over the Ca Mau Peninsula?**
   The results indicate that representing aquaculture areas as permanent wetlands constitutes a more physically defensible modelling choice than treating them as water bodies. Under the permanent wetland–dominated scenarios (LU2-LU3), transpiration is substantially reduced, which is consistent with lower LAI and a markedly decreased T/AET ratio. In particular, in the LU3 scenario, where the Ca Mau Peninsula is entirely represented as a permanent wetland, the T/AET ratio falls below 35.5%.
   These findings are consistent with those reported by Wei et al. (2017), who demonstrated that transpiration typically dominates AET across most vegetated land-cover types, accounting for approximately 55–66% of total AET. In contrast, wetland ecosystems exhibit substantially lower transpiration contributions (around 33%) due to their reduced LAI. At the same time, it should be acknowledged that the representation of wetland processes in the Noah-MP land surface model remains relatively simplified, which may limit the realism of wetland evapotranspiration dynamics (Zhang et al., 2022).
   In contrast, the LU4 "all water-body" scenario fundamentally shifts the land-atmosphere system toward an ocean-like regime. This transition alters the atmospheric response, including a shift of the diurnal precipitation peak from early afternoon to early morning. Such behavior indicates that the LU4 configuration does not realistically represent aquaculture landscapes.

6. **RQ 3f Is the WRF-ARW model able to derive the present freshwater flux over the Ca Mau Peninsula, taking LULCC into account?**
   The results demonstrate that the WRF-ARW model is capable of reliably deriving the present freshwater flux over the Ca Mau Peninsula when LULCC is explicitly accounted for. Using the LU2 configuration as the most realistic observed LULC scenario, the model reproduces a physically consistent seasonal cycle of freshwater flux defined as precipitation minus PET. During the dry season (December–April), the freshwater flux is dominated by negative values. In May, the flux becomes positive, reaches a maximum in September, and returns to negative values by De-

cember, in close agreement with the regional monsoon climatology.

Both the seasonal evolution and spatial patterns of simulated freshwater flux closely match independent estimates derived from the TMPA and DPET datasets, confirming the robustness of the WRF-LU2 simulation. Spatially, freshwater flux is uniformly negative during the dry season (-2 to -3 mm day^{-1} over Kien Giang and Bac Lieu, and -1 to -2 mm day^{-1} over Ca Mau), while rainy-season values are consistently positive (0–6 mm day^{-1}), with maxima over Ca Mau Province (4–5 mm day^{-1}).

Importantly, when freshwater flux is defined as precipitation minus PET, the influence of LULC scenarios is negligible at the peninsula scale. In contrast, when freshwater flux is defined as precipitation minus AET, LULCC becomes a critical controlling factor, as it substantially modifies transpiration, the dominant component of AET. This distinction underscores the importance of explicitly considering vegetation processes when evaluating freshwater flux under LULCC.

8.2. Outlook

This thesis provides a comprehensive assessment of the freshwater flux over the Ca Mau Peninsula, southern Vietnam, using the WRF-ARW model at a 5-km gray-zone resolution. Additionally, the study explores how the performance of the WRF-ARW in simulating freshwater flux varies when taking into account the LUCC over the domain. The results provide new insights into the spatial and seasonal characteristics of freshwater flux in this region. Although the assessment was comprehensive, some biases in the simulation of both components of freshwater flux, including precipitation, PET, or AET, could not be analyzed as they were beyond the scope of this study. Therefore, the following are suggested for future work aimed at improving freshwater flux simulation over the Ca Mau Peninsula:

From a precipitation perspective, the WRF-ARW model's performance remains less robust during the rainy season, as reflected by high values of RMSE when simulating daily rainfall and its diurnal cycle over the Ca Mau Peninsula. This suggests that further refinement of the physical parameterization choices remains necessary. Future work should therefore revisit alternative physics parameterization combinations. Additionally, downscaling experiments at convection-permitting resolutions (3 km or finer) are strongly recommended. Such configurations would enable the explicit representation of deep convection, thereby reducing uncertainties associated with cumulus parameterization and enhancing the simulation of rainfall intensity and timing (Kendon et al., 2021). With the continuing increase in computational capacity, long-term convection-permitting simulations using WRF-ARW are expected to become increasingly feasible.

Regarding PET, despite incorporating updated and more realistic LULC datasets, substantial biases in simulated 10-m wind speed persist and remain the dominant source of PET uncertainty. Future studies should therefore explore the application of post-processing and bias-correction techniques to en-

hance the robustness of PET estimates.

For AET, the accurate representation of LAI through the dynamic vegetation option in the Noah-MP land surface model plays a critical role, particularly in constraining the transpiration component, which dominates total AET. Nevertheless, dynamic vegetation modelling remains subject to considerable uncertainty due to the complexity of land–atmosphere interactions. Recent studies have demonstrated that parameter optimization and data assimilation approaches can substantially improve dynamic vegetation performance; therefore, these methods should be systematically explored in future work (Shu et al., 2022). Moreover, despite recent advances, the wetland category in Noah-MP remains highly simplified. Wetlands are currently treated as a static land-cover class, lacking explicit representation of water storage or subgrid hydrological dynamics, which leads to unrealistic instantaneous runoff (Zhang et al., 2022). In reality, wetland depressions retain surface water and interact dynamically with the atmosphere. Developing and implementing a dynamic wetland scheme that explicitly accounts for subgrid water and energy balance processes is therefore essential for improving AET simulations and for more realistically representing land–atmosphere feedbacks in wetland-dominated regions such as the Ca Mau Peninsula.

A. Appendix: Figures

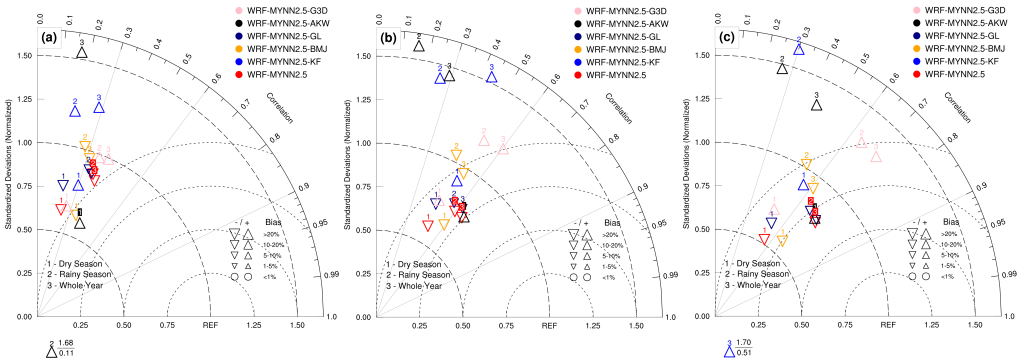

Figure A.1.: The performance of WRF-ARW experiments employing different PBL schemes is assessed using Taylor diagrams for (a) daily, (b) 5-day, and (c) 10-day accumulated rainfall at 24 stations over the Ca Mau Peninsula. Results are shown for the WRF-MYNN2.5 (red symbols), WRF-MYNN2.5-KF (blue symbols), WRF-MYNN2.5-BMJ (orange symbols), WRF-MYNN2.5-GL (navy symbols), WRF-MYNN2.5-AKW (black symbols), and WRF-MYNN2.5-G3D (pink symbols) experiments across the dry season, rainy season, and full year for 2015. Experiments with the smallest RMSE are highlighted with a color-filled background of the numbers indicating the reference period.

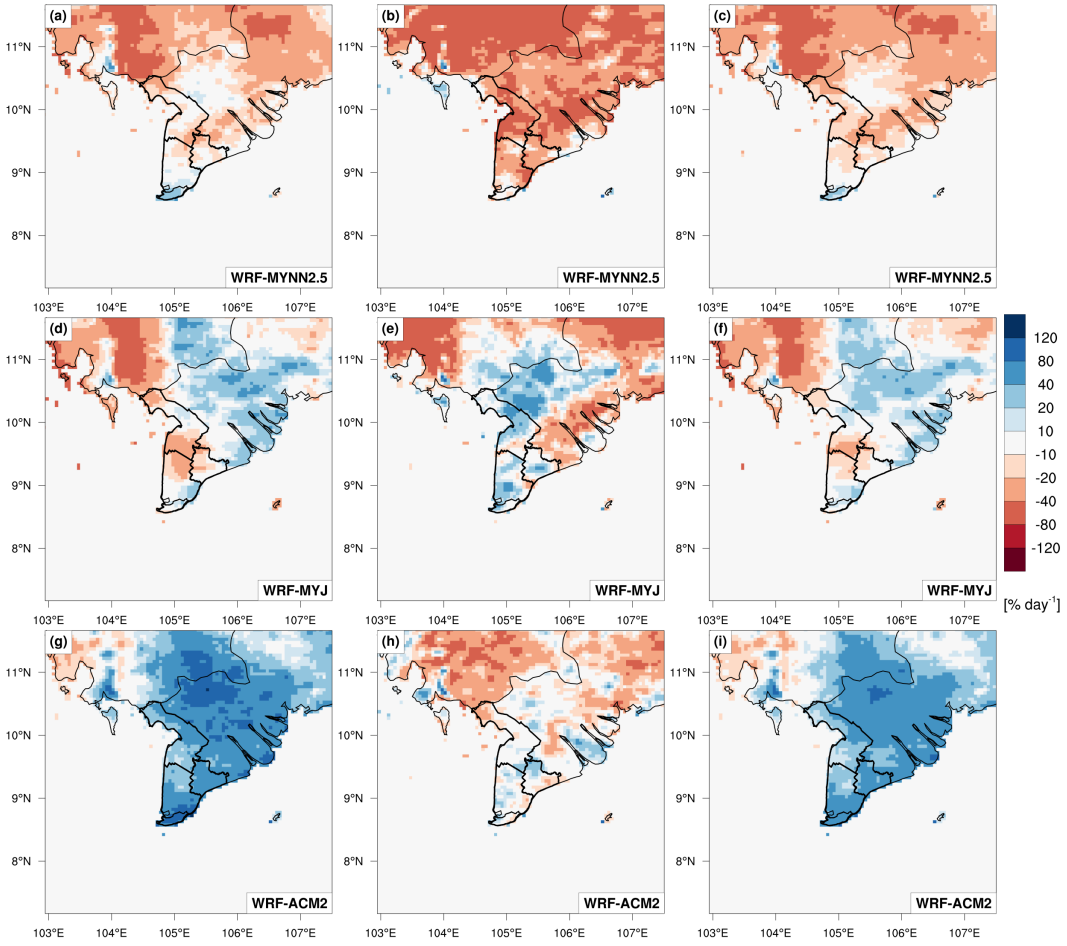

Figure A.2.: The performance of WRF-ARW experiments using different PBL parameterization schemes is illustrated by the PBIAS of daily rainfall relative to CHIRPS v2.0 for the rainy season (first column), dry season (second column), and annual (third column) periods, averaged over the years 2007, 2013, and 2015. Panels (a-c), (d–f), and (g–i) correspond to results from the WRF-MYNN2.5, WRF-MYJ, and WRF-ACM2 experiments, respectively.

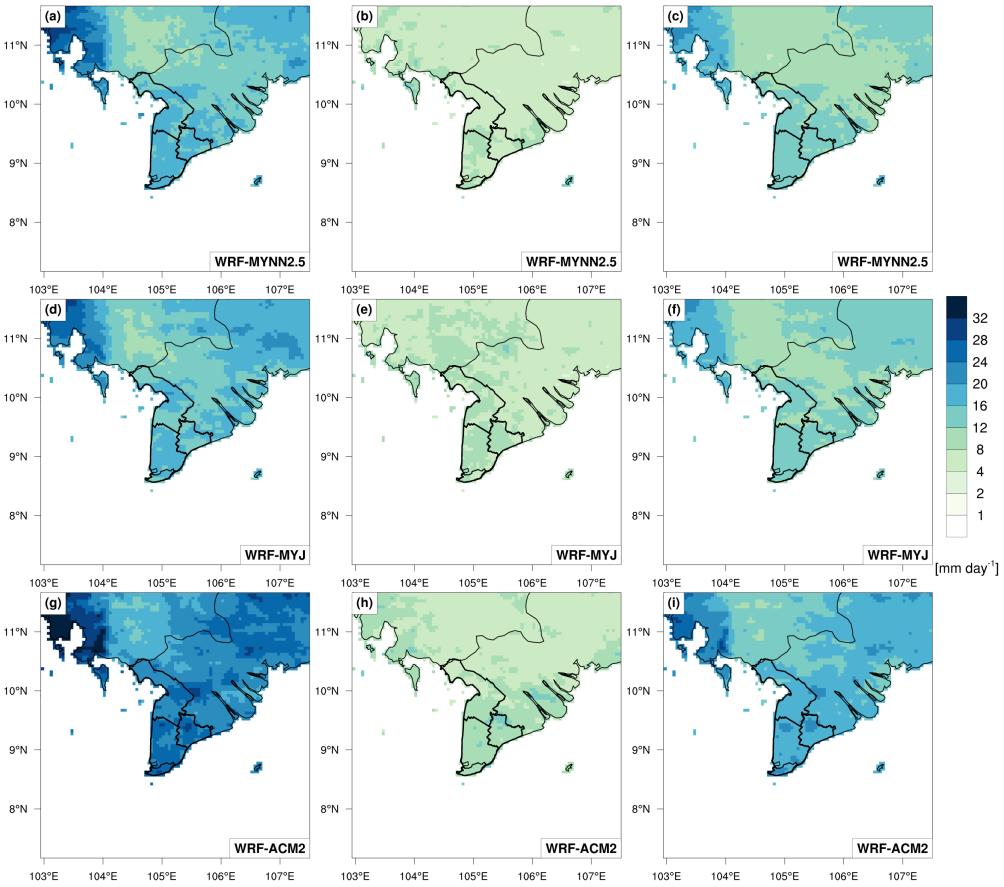

Figure A.3.: Same as in Figure A.2 but for RMSE of simulated daily rainfall.

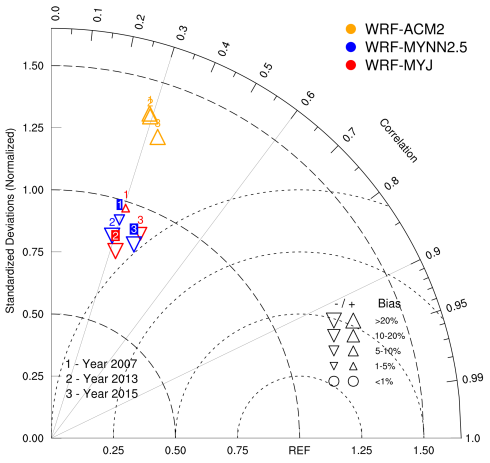

Figure A.4.: The performance of WRF-ARW experiments employing different PBL schemes is assessed using Taylor diagrams for daily rainfall at 24 stations over the Ca Mau Peninsula. Results are shown for the WRF-MYJ (red symbols), WRF-MYNN2.5 (blue symbols), and WRF-ACM2 (orange symbols) experiments in the whole year of 2007 (number one), 2013 (number two), and 2015 (number three). Experiments with the smallest RMSE are highlighted with a color-filled background of the numbers indicating the reference period.

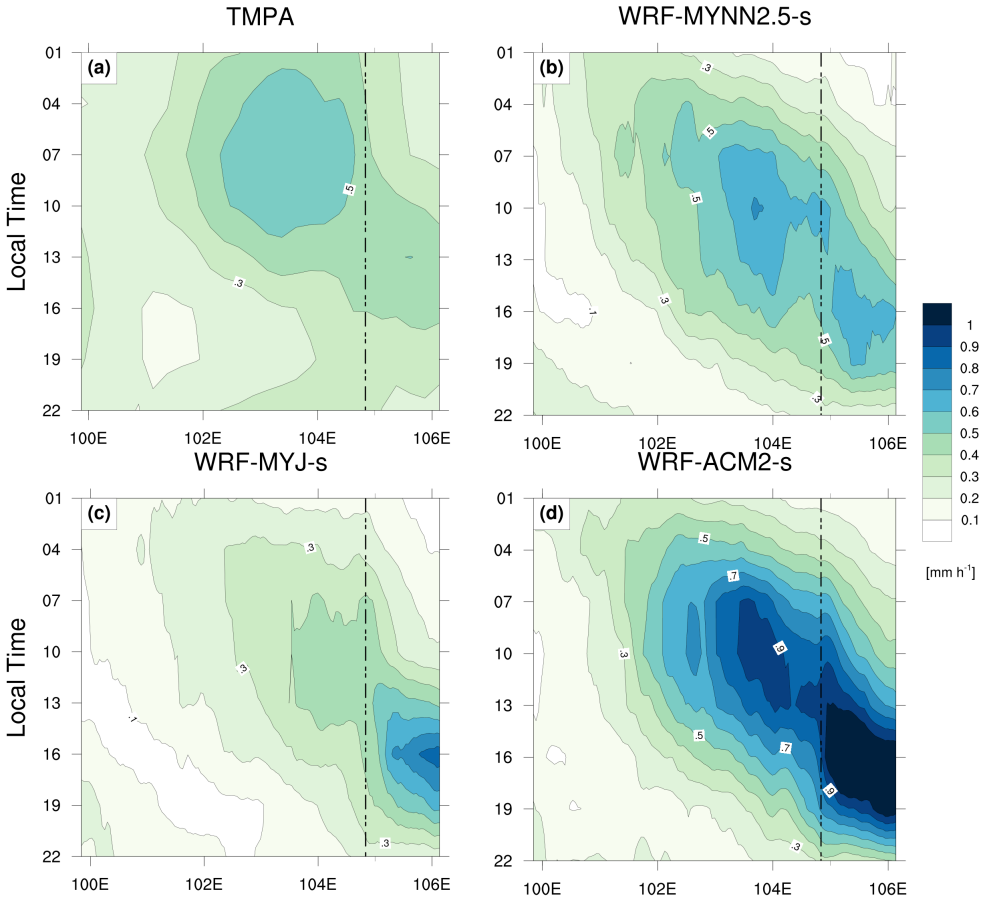

Figure A.5.: The Hovmöller diagrams of the mean diurnal cycles latitudinally averaged over 8.25–10.5°N, 99.875–106.125°E for the rainy seasons in 2007, 2013, and 2015 from (a) TMPA, and from (b) WRF-MYNN2.5-s, (c) WRF-MYJ-s, and (d) WRF-ACM2-s experiments. Vertical dashed lines show the approximate location of the western coastline of the Ca Mau Peninsula.

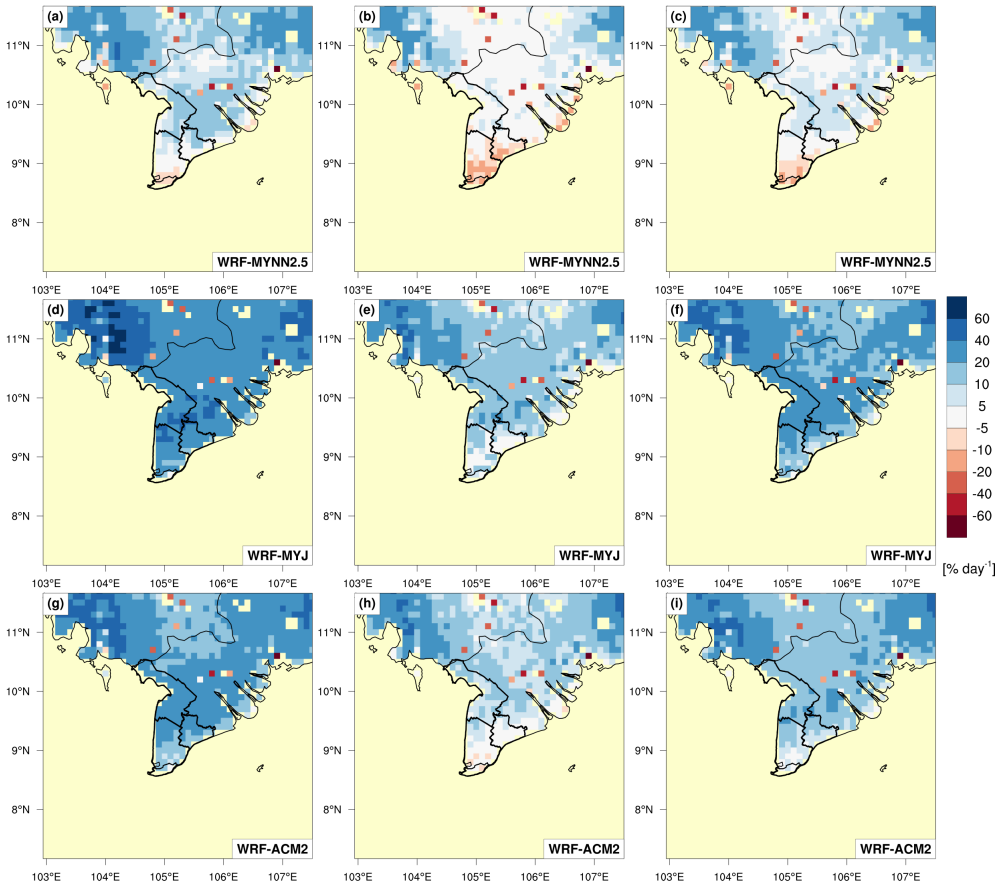

Figure A.6.: The performance of WRF-ARW experiments using different PBL parameterization schemes is illustrated by the PBIAS of daily PET relative to DPET for the rainy season (first column), dry season (second column), and annual (third column) periods, averaged over the years 2007, 2013, and 2015. Panels (a–c), (d–f), and (g–i) correspond to results from the WRF-MYNN2.5, WRF-MYJ, and WRF-ACM2 experiments, respectively.

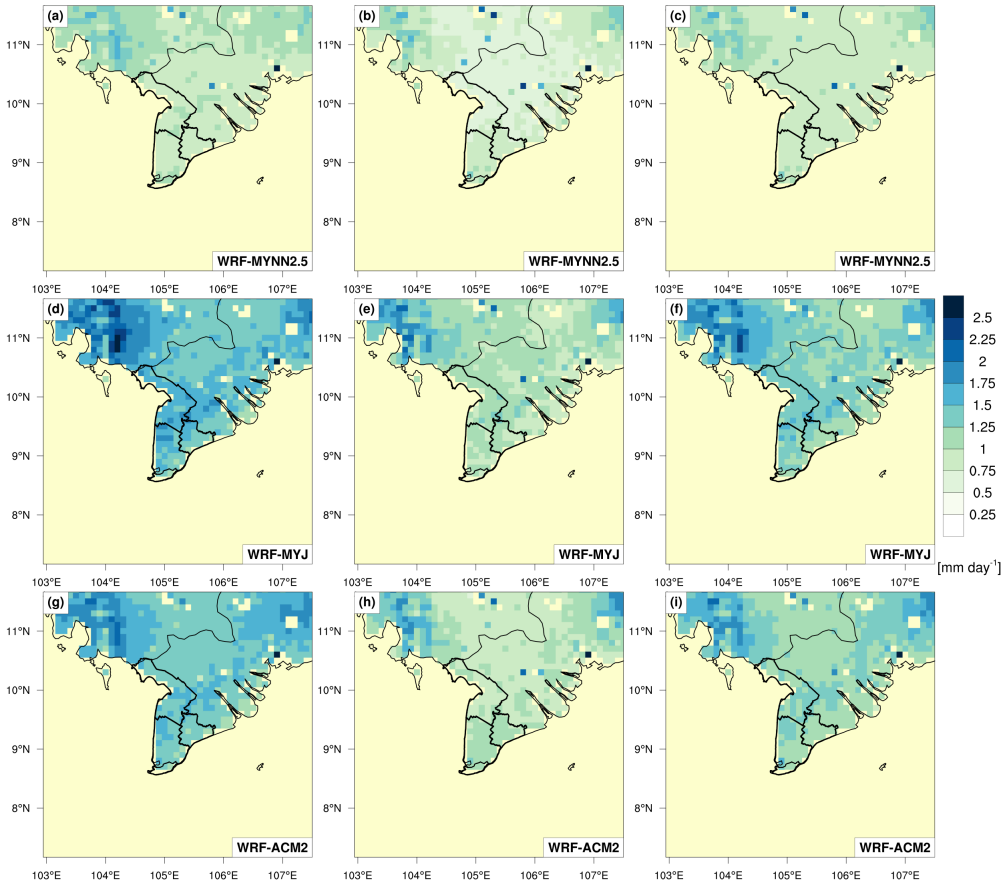

Figure A.7.: Same as in Figure A.2 but for RMSE of simulated daily PET.

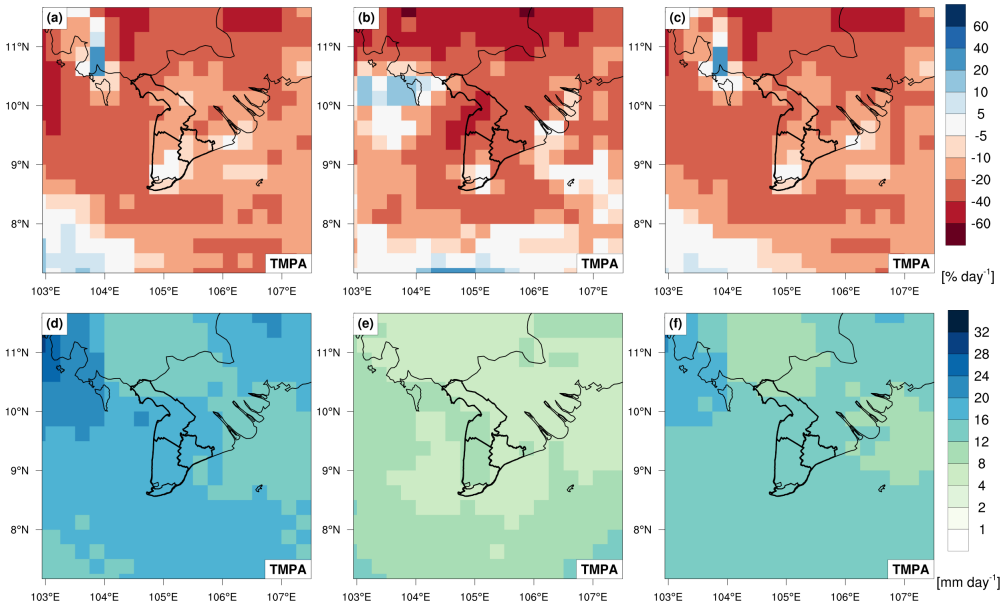

Figure A.8.: The performance of the WRF-MYNN2.5 experiment is illustrated by the PBIAS and RMSE of daily rainfall relative to TMPA for the rainy season (first column), dry season (second column), and annual (third column) periods, averaged over the period from 2007 to 2016. Panels (a–c) and (d–f) correspond to the PBIAS and RMSE, respectively.

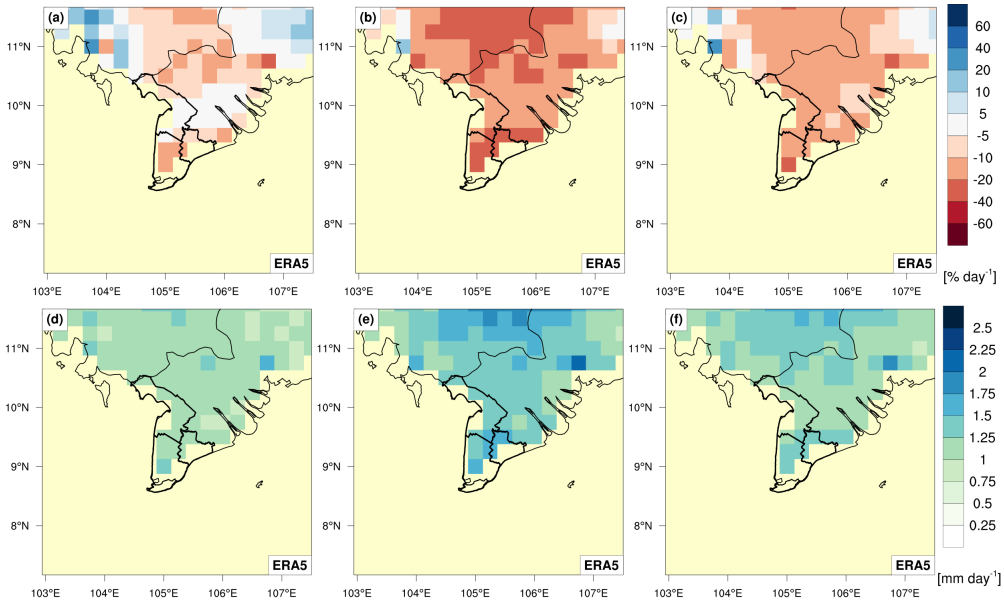

Figure A.9.: The performance of the WRF-MYNN2.5 experiment is illustrated by the PBIAS and RMSE of daily PET relative to ERA5 for the rainy season (first column), dry season (second column), and annual (third column) periods, averaged over the period from 2007 to 2016. Panels (a–c) and (d–f) correspond to the PBIAS and RMSE, respectively.

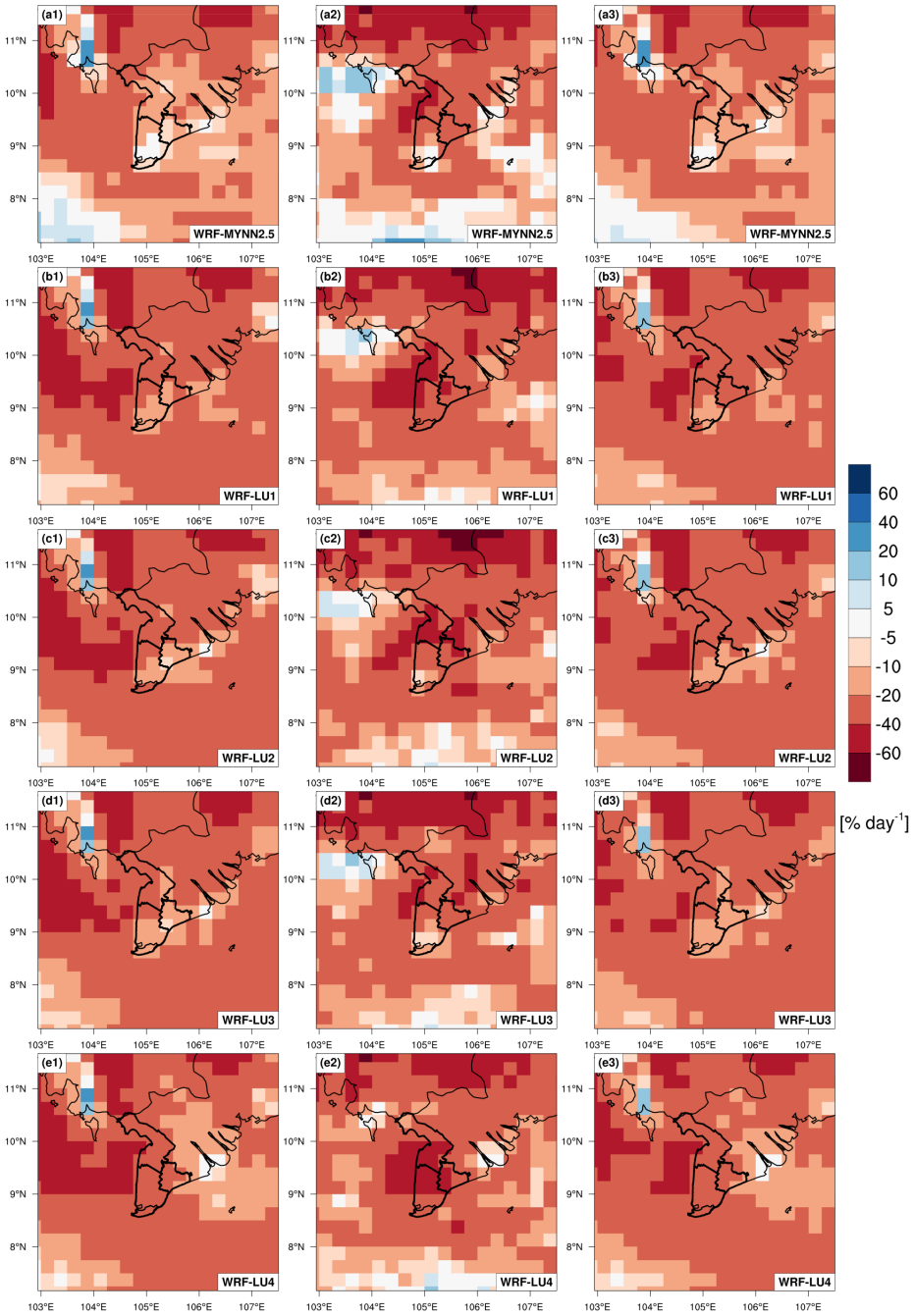

Figure A.10.: The performance of WRF-ARW experiments using different LULC datasets is illustrated by the PBIAS of daily rainfall relative to TMPA for the rainy season (first column), dry season (second column), and annual (third column) periods, averaged over the period 2007–2016. Panels (a1–a3), (b1–b3), (c1–c3), (d1–d3), and (e1–e3) correspond to results from the WRF-MYNN2.5, WRF-LU1, WRF-LU2, WRF-LU3, and WRF-LU4 experiments, respectively.

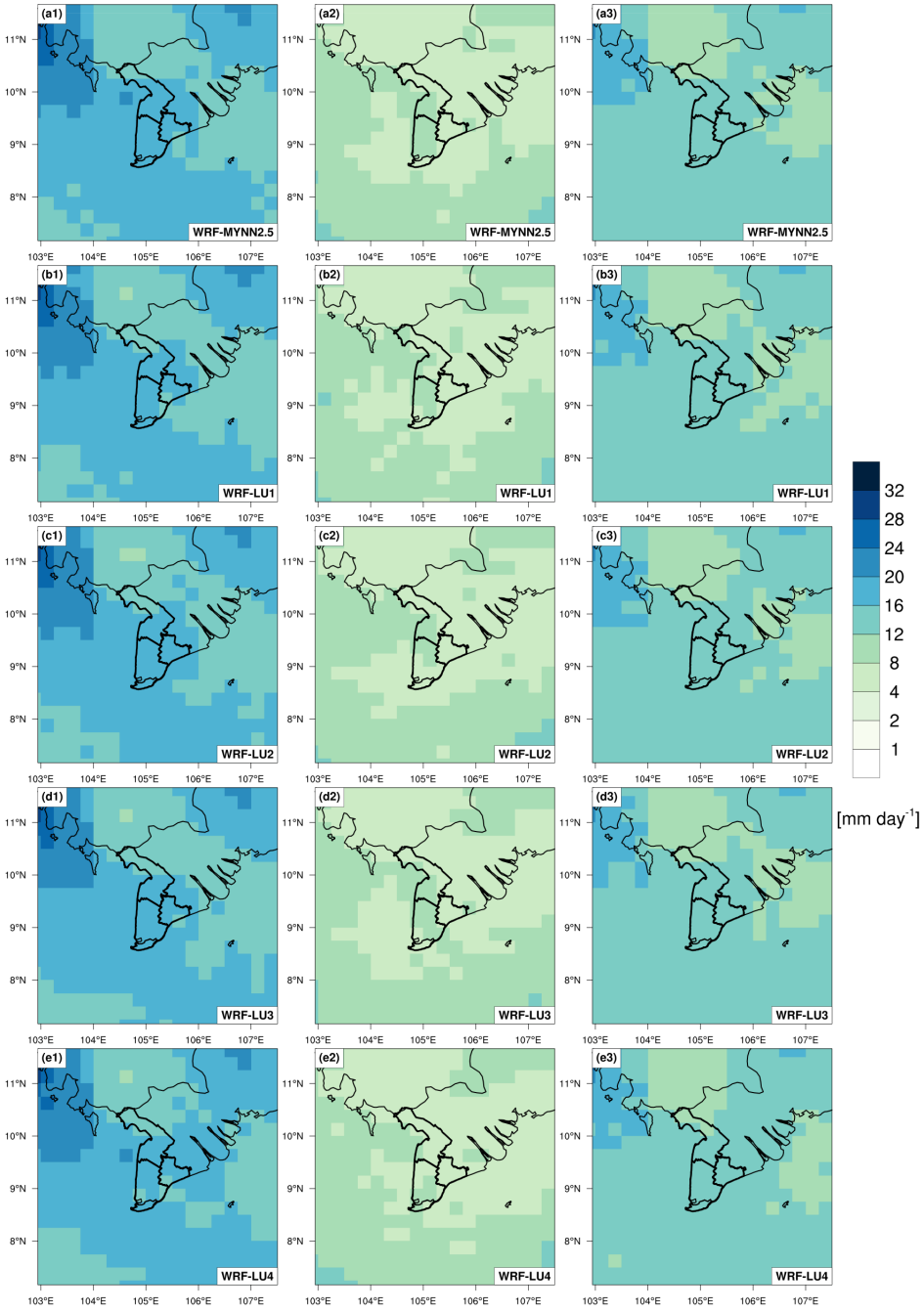

Figure A.11.: Same as in Figure A.10 but for RMSE of simulated daily rainfall.

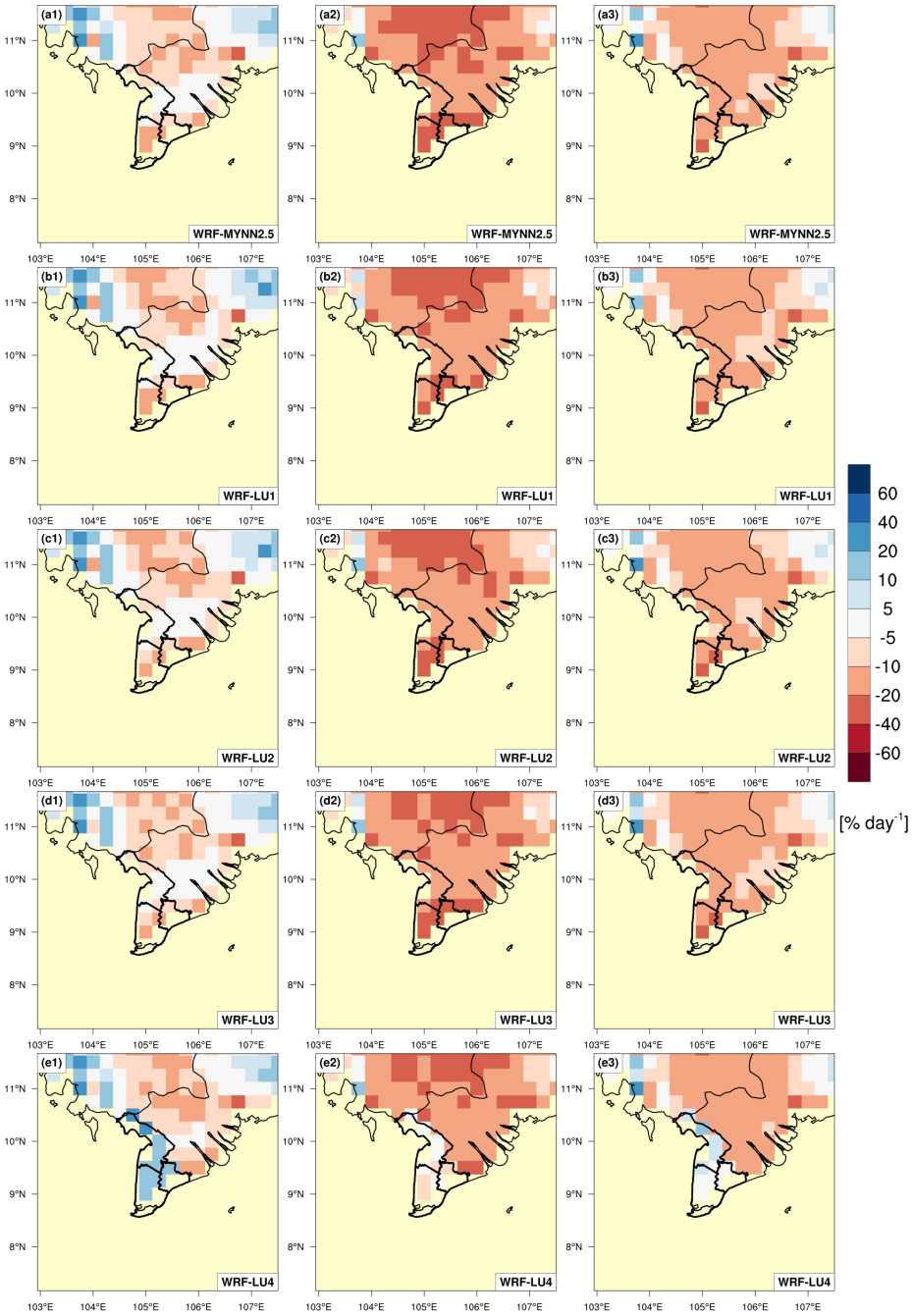

Figure A.12.: The performance of WRF-ARW experiments using different LULC datasets is illustrated by the PBIAS of daily PET relative to ERA5 for the rainy season (first column), dry season (second column), and annual (third column) periods, averaged over the period 2007–2016. Panels (a1–a3), (b1–b3), (c1–c3), (d1–d3), and (e1–e3) correspond to results from the WRF-MYNN2.5, WRF-LU1, WRF-LU2, WRF-LU3, and WRF-LU4 experiments, respectively.

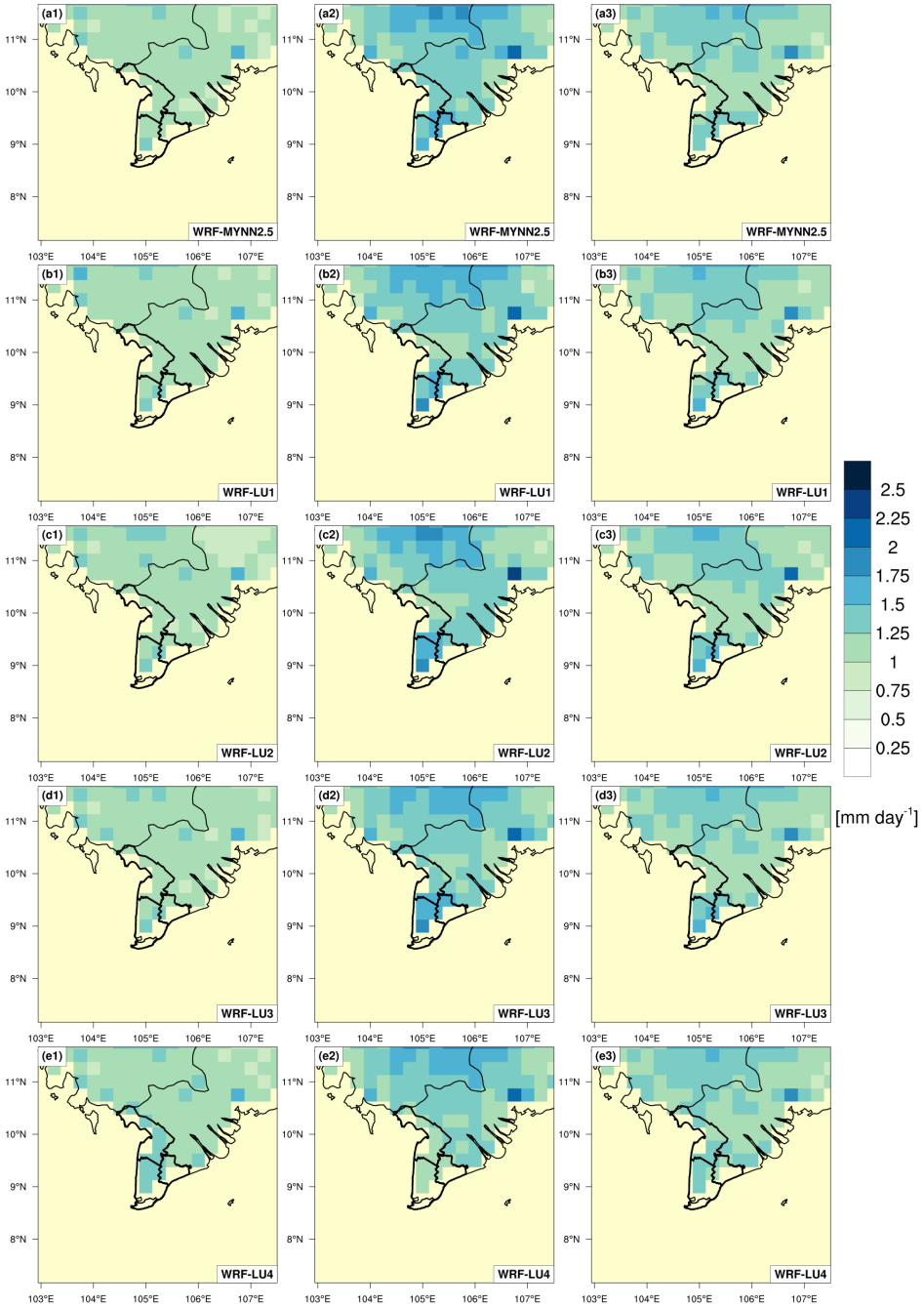

Figure A.13.: Same as in Figure A.12 but for RMSE of simulated daily PET.

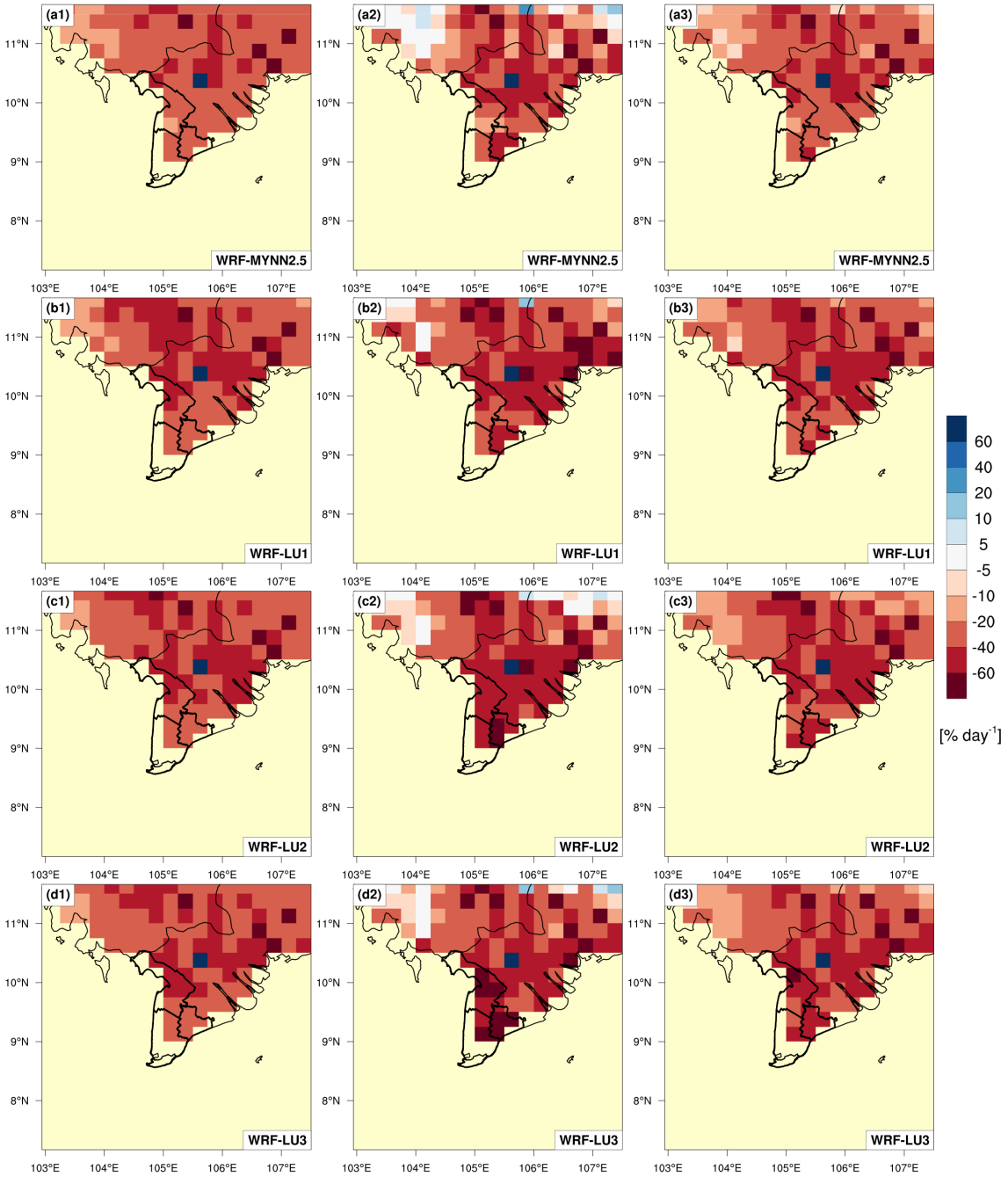

Figure A.14.: The performance of WRF-ARW experiments using different LULC datasets is illustrated by the PBIAS of daily AET relative to REA for the rainy season (first column), dry season (second column), and annual (third column) periods, averaged over the period 2007–2016. Panels (a1–a3), (b1–b3), (c1–c3), and (d1–d3) correspond to results from the WRF-MYNN2.5, WRF-LU1, WRF-LU2, and WRF-LU3 experiments, respectively.

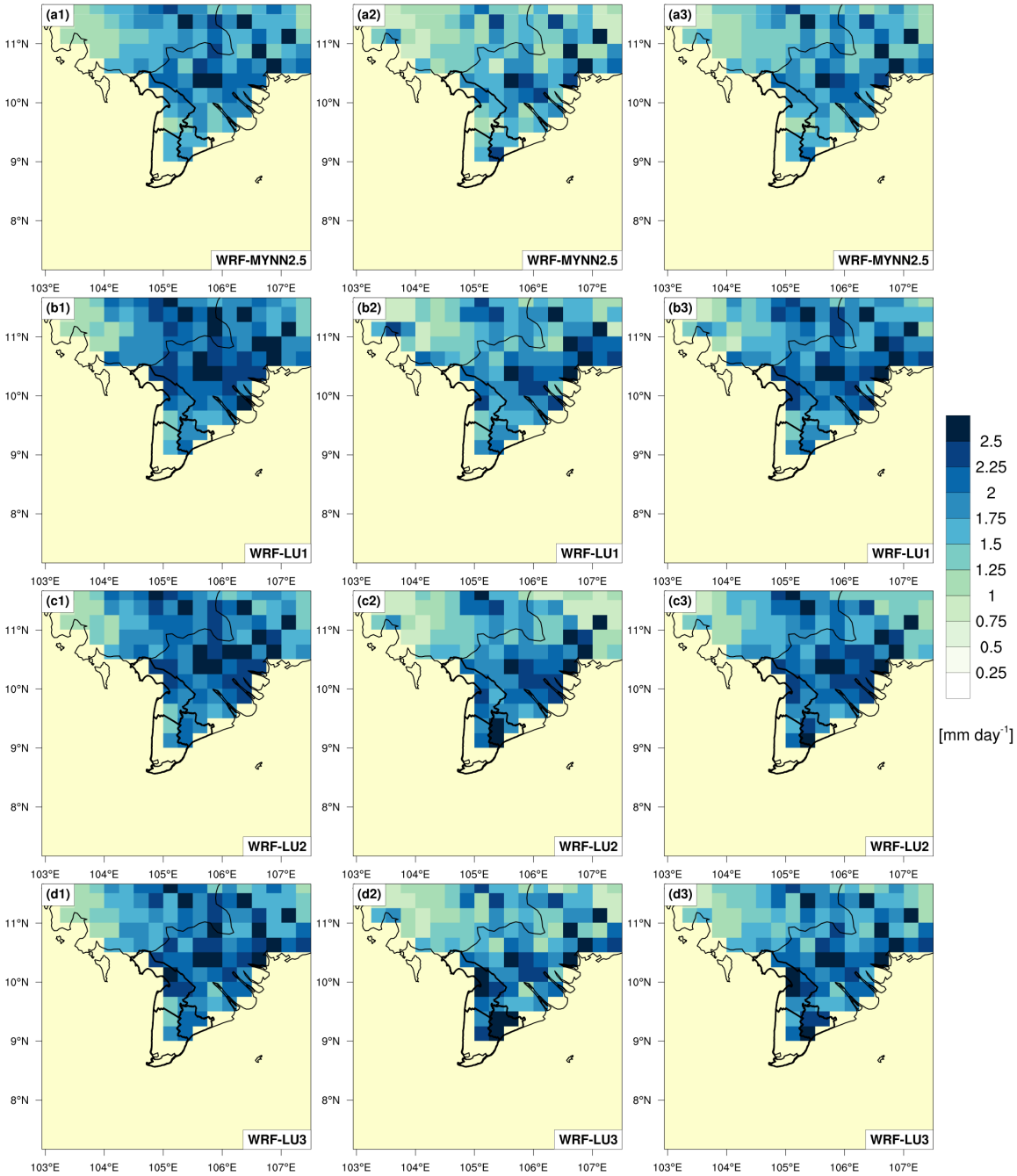

Figure A.15.: Same as in Figure A.14 but for RMSE of simulated daily AET.

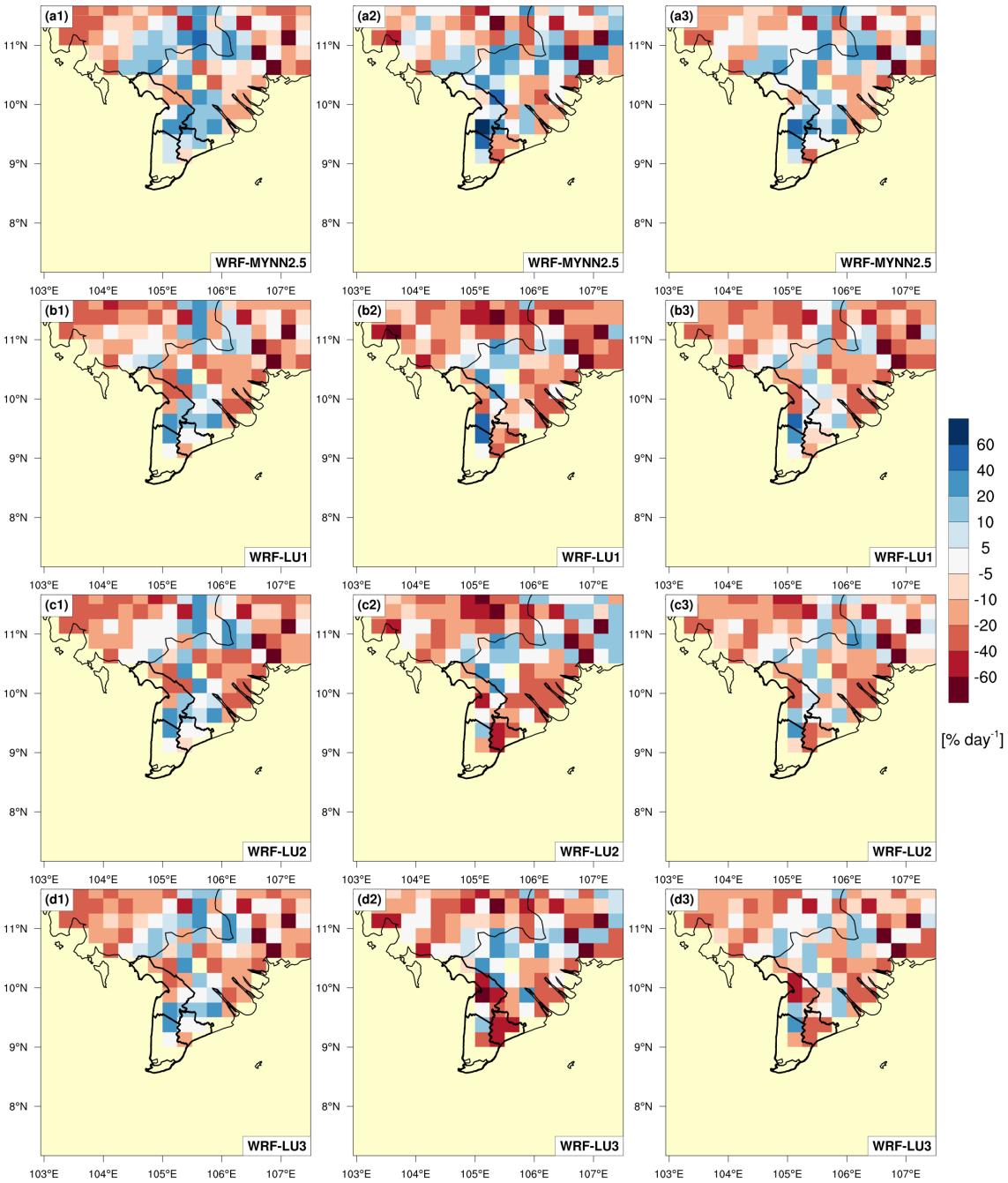

Figure A.16.: The performance of WRF-ARW experiments using different LULC datasets is illustrated by the PBIAS of daily AET relative to GLEAM v3.5 for the rainy season (first column), dry season (second column), and annual (third column) periods, averaged over the period 2007–2016. Panels (a1–a3), (b1–b3), (c1–c3), and (d1–d3) correspond to results from the WRF-MYNN2.5, WRF-LU1, WRF-LU2, and WRF-LU3 experiments, respectively.

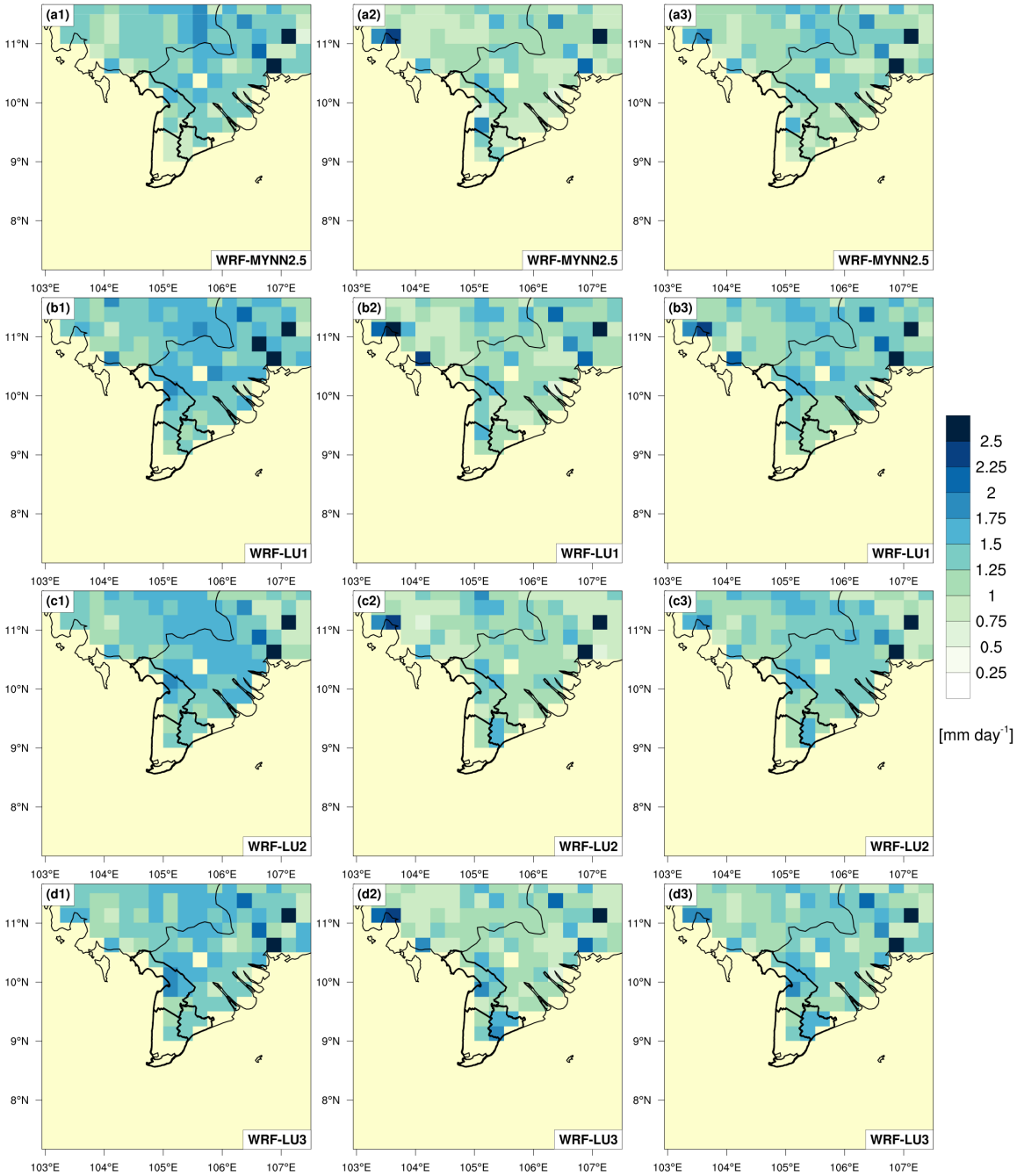

Figure A.17.: Same as in Figure A.16 but for RMSE of simulated daily AET.

B. Bibliography

Abatzoglou, J. T., S. Z. Dobrowski, S. A. Parks, and K. C. Hegewisch, 2018: Terraclimate, a high-resolution global dataset of monthly climate and climatic water balance from 1958–2015. *Scientific data*, **5 (1)**, 1–12.

Achard, F., S. Bontemps, C. Lamarche, T. Da Maet, P. Mayaux, E. Van Bogaert, and P. Defourny, 2017: Quality assessment of the cci land cover maps. *Proceedings of the First CCI Land Cover User Workshop, Frascati, Italy*, Vol. 31.

Achugbu, I. C., P. Laux, L. Chen, J. Dudhia, I. A. Balogun, J. Arnault, Z. D. Adeyewa, O. A. Akintola, and H. Kunstmann, 2024: Performance evaluation of a high-resolution regional climate model in west africa: sensitivity to land surface schemes. *Theoretical and Applied Climatology*, **155 (4)**, 3099–3118.

Achugbu, I. C., P. Laux, A. A. Olufayo, I. A. Balogun, J. Dudhia, J. Arnault, I. E. Gbode, E. Naabil, and H. Kunstmann, 2023: The impacts of land use and land cover change on biophysical processes in west africa using a regional climate model experimental approach. *International Journal of Climatology*, **43 (4)**, 1731–1755.

Achugbu, I. C., A. A. Olufayo, I. A. Balogun, E. A. Adefisan, J. Dudhia, and E. Naabil, 2021: Modeling the spatiotemporal response of dew point temperature, air temperature and rainfall to land use land cover change over west africa. *Modeling Earth Systems and Environment*, 1–26.

Allen, R., M. Smith, L. Pereira, and A. Perrier, 1994: An update for the calculation of reference evapotranspiration. *ICID bulletin*, **43 (2)**, 35–92.

Allen, R. G., L. S. Pereira, D. Raes, M. Smith, et al., 1998: Crop evapotranspiration-guidelines for computing crop water requirements-fao irrigation and drainage paper 56. *Fao, Rome*, **300 (9)**, D05 109.

Ball, J. T., I. E. Woodrow, and J. A. Berry, 1987: A model predicting stomatal conductance and its contribution to the control of photosynthesis under different environmental conditions. *Progress in photosynthesis research*, Springer, 221–224.

Baret, F., M. Weiss, R. Lacaze, F. Camacho, H. Makhmara, P. Pacholcyzk, and B. Smets, 2013: Geov1: Lai and fapar essential climate variables and fcover global time series capitalizing over existing products. part1: Principles of development and production. *Remote sensing of environment*, **137**, 299–309.

Bougeault, P. and P. Lacarrere, 1989: Parameterization of orography-induced turbulence in a mesobeta–scale model. *Monthly weather review*, **117 (8)**, 1872–1890.

Brunke, M. A., X. Zeng, V. Misra, and A. Beljaars, 2008: Integration of a prognostic sea surface skin temperature scheme into weather and climate models. *Journal of Geophysical Research: Atmospheres*, **113 (D21)**.

Bughici, T., N. Lazarovitch, E. Fredj, and E. Tas, 2019: Evaluation and bias correction in wrf model forecasting of precipitation and potential evapotranspiration. *Journal of Hydrometeorology*, **20 (5)**, 965–983.

Camacho, F., J. Sánchez-Zapero, and B. Fuster, 2018: Quality assessment report: Lai, fapar, fcover from proba-v collection 1km, version 2, issue i1. 20.

Chen, F. and J. Dudhia, 2001: Coupling an advanced land surface–hydrology model with the penn state–ncar mm5 modeling system. part i: Model implementation and sensitivity. *Monthly weather review*, **129 (4)**, 569–585.

Chen, F., Z. Janjić, and K. Mitchell, 1997: Impact of atmospheric surface-layer parameterizations in the new land-surface scheme of the ncep mesoscale eta model. *Boundary-Layer Meteorology*, **85 (3)**, 391–421.

Chen, G., 2020: Diurnal cycle of the asian summer monsoon: Air pump of the second kind. *Journal of Climate*, **33 (5)**, 1747–1775.

Chen, H., P. Gnanamoorthy, Y. Chen, L. R. Mansaray, Q. Song, K. Liao, A. Shi, G. Feng, and C. Sun, 2022: Assessment and inter-comparison of multi-source high spatial resolution evapotranspiration products over lancang–mekong river basin, southeast asia. *Remote Sensing*, **14 (3)**, 479.

Chen, H., H. Liu, X. Chen, and Y. Qiao, 2020: Analysis on impacts of hydro-climatic changes and human activities on available water changes in central asia. *Science of the Total Environment*, **737**, 139 779.

Chen, J., J. Chen, A. Liao, X. Cao, L. Chen, X. Chen, C. He, G. Han, S. Peng, M. Lu, et al., 2015: Global land cover mapping at 30 m resolution: A pok-based operational approach. *ISPRS Journal of Photogrammetry and Remote Sensing*, **103**, 7–27.

Chen, X., O. M. Pauluis, and F. Zhang, 2018: Regional simulation of indian summer monsoon intraseasonal oscillations at gray-zone resolution. *Atmospheric Chemistry and Physics*, **18 (2)**, 1003–1022.

Chotamonsak, C., E. P. Salathé Jr, J. Kreasuwan, S. Chantara, and K. Siriwitayakorn, 2011: Projected climate change over southeast asia simulated using a wrf regional climate model. *Atmospheric Science Letters*, **12 (2)**, 213–219.

Clayson, C. A. and A. S. Bogdanoff, 2013: The effect of diurnal sea surface temperature warming on climatological air–sea fluxes. *Journal of Climate*, **26 (8)**, 2546–2556.

Cohen, A. E., S. M. Cavallo, M. C. Coniglio, and H. E. Brooks, 2015: A review of planetary boundary layer parameterization schemes and their sensitivity in simulating southeastern us cold season severe weather environments. *Weather and forecasting*, **30 (3)**, 591–612.

Coleman, J. M., O. K. Huh, and D. Braud, 2003: *Major world deltas: A perspective from space*. Lousiana State University Baton Rouge, LA.

Collatz, G. J., J. T. Ball, C. Grivet, and J. A. Berry, 1991: Physiological and environmental regulation of stomatal conductance, photosynthesis and transpiration: a model that includes a laminar boundary layer. *Agricultural and Forest meteorology*, **54 (2-4)**, 107–136.

Copernicus Global Land Service, 2022: Documents lai characteristics. `https://land.copernicus.eu/global/products/lai`, Last accessed on 2022-01-01.

Costa, M. H. and G. F. Pires, 2010: Effects of amazon and central brazil deforestation scenarios on the duration of the dry season in the arc of deforestation. *International Journal of Climatology*, **30 (13)**, 1970–1979.

Cowling, S. A. and C. B. Field, 2003: Environmental control of leaf area production: implications for vegetation and land-surface modeling. *Global Biogeochemical Cycles*, **17 (1)**, 7–1.

Crook, J., C. Klein, S. Folwell, C. M. Taylor, D. J. Parker, A. Bamba, and K. Kouadio, 2022: Effects on early monsoon rainfall in west africa due to recent deforestation in a convection-permitting ensemble. *Weather and Climate Dynamics Discussions*, **2022**, 1–31.

Dai, A., 2011: Characteristics and trends in various forms of the palmer drought severity index during 1900–2008. *Journal of Geophysical Research: Atmospheres*, **116 (D12)**.

Dang, K. K., T. H. Do, T. H. L. Le, T. T. H. Le, and T. D. Pham, 2020a: Impacts of farmers' adaptation to drought and salinity intrusion on rice yield in vietnam's mekong delta. *Journal of Agribusiness in Developing and Emerging Economies*.

Dang, V. H., D. D. Tran, D. D. Cham, P. T. T. Hang, H. T. Nguyen, H. V. Truong, P. H. Tran, M. B. Duong, N. T. Nguyen, K. V. Le, et al., 2020b: Assessment of rainfall distributions and characteristics in coastal provinces of the vietnamese mekong delta under climate change and enso processes. *Water*, **12 (6)**, 1555.

Das, S., P. Datta, D. Sharma, and K. Goswami, 2022: Trends in temperature, precipitation, potential evapotranspiration, and water availability across the teesta river basin under 1.5 and 2 c temperature rise scenarios of cmip6. *Atmosphere*, **13 (6)**, 941.

Defourny, P., G. Kirches, C. Brockmann, M. Boettcher, M. Peters, S. Bontemps, C. Lamarche, M. Schlerf, and M. Santoro, 2012: Land cover cci. *Product User Guide Version*, **2**, 325.

Dickinson, R. E., M. Shaikh, R. Bryant, and L. Graumlich, 1998: Interactive canopies for a climate model. *Journal of Climate*, **11 (11)**, 2823–2836.

Dinh, K. D., T. N. Anh, N. Y. Nguyen, D. D. Bui, R. Srinivasan, et al., 2020: Evaluation of grid-based rainfall products and water balances over the mekong river basin. *Remote Sensing*, **12 (11)**, 1858.

Donaire-Montaño, D., M. G.-V. Ojeda, N. Tacoronte, J. J. Rosa-Cánovas, Y. Castro-Díez, M. J. Esteban-Parra, and S. R. Gámiz-Fortis, 2025: Finding optimal noah-mp parameterizations for the characterization of surface heat fluxes in the iberian peninsula. *Atmospheric Research*, **323**, 108 143.

Dong Phuong, D., L. Trinh-Tuan, V. Nguyen, and N. K. Loi, 2025: Multi-temporal trend analysis for climate means and extremes in vietnam's mekong delta. *Climate Dynamics*, **63 (2)**, 1–26.

Donohue, R. J., T. R. McVicar, and M. L. Roderick, 2010: Assessing the ability of potential evaporation formulations to capture the dynamics in evaporative demand within a changing climate. *Journal of Hydrology*, **386 (1-4)**, 186–197.

Du Duc, T., L. R. Hole, D. Tran Anh, C. Hoang Duc, and T. Nguyen Ba, 2016: Verification of forecast weather surface variables over vietnam using the national numerical weather prediction system. *Advances in Meteorology*, **2016 (1)**, 8152 413.

Duc, H. N., H. Q. Bang, and N. X. Quang, 2018: Influence of the pacific and indian ocean climate drivers on the rainfall in vietnam. *International Journal of Climatology*, **38 (15)**, 5717–5732.

Dudhia, J., 1989: Numerical study of convection observed during the winter monsoon experiment using a mesoscale two-dimensional model. *Journal of Atmospheric Sciences*, **46 (20)**, 3077–3107.

Dzebre, D. E. and M. S. Adaramola, 2020: A preliminary sensitivity study of planetary boundary layer parameterisation schemes in the weather research and forecasting model to surface winds in coastal ghana. *Renewable Energy*, **146**, 66–86.

Ebert, E. E., J. E. Janowiak, and C. Kidd, 2007: Comparison of near-real-time precipitation estimates from satellite observations and numerical models. *Bulletin of the American Meteorological Society*, **88 (1)**, 47–64.

Erban, L. E., S. M. Gorelick, and H. A. Zebker, 2014: Groundwater extraction, land subsidence, and sea-level rise in the mekong delta, vietnam. *Environmental Research Letters*, **9 (8)**, 084 010.

Faseyiku, O. O., O. A. Obiora-Okeke, A. S. Olowoselu, O. R. Olafusi, and J. R. Adewumi, 2024: Validation of selected gridded potential evapotranspiration datasets with ground-based observations over the ogun-osun river basin, nigeria. *Arabian Journal of Geosciences*, **17 (5)**, 153.

Feddema, J. J., K. W. Oleson, G. B. Bonan, L. O. Mearns, L. E. Buja, G. A. Meehl, and W. M. Washington, 2005: The importance of land-cover change in simulating future climates. *Science*, **310 (5754)**, 1674–1678.

Foley, J. A., R. DeFries, G. P. Asner, C. Barford, G. Bonan, S. R. Carpenter, F. S. Chapin, M. T. Coe, G. C. Daily, H. K. Gibbs, et al., 2005: Global consequences of land use. *science*, **309 (5734)**, 570–574.

Friedl, M. A., D. Sulla-Menashe, B. Tan, A. Schneider, N. Ramankutty, A. Sibley, and X. Huang, 2010: Modis collection 5 global land cover: Algorithm refinements and characterization of new datasets. *Remote sensing of Environment*, **114 (1)**, 168–182.

Fu, Y., X. Gao, Y. Xu, and F. Giorgi, 2023: Climate change projection over mainland southeast asia and the lancang-mekong river basin based on a set of regcm4 simulations. *International Journal of Climatology*, **43 (2)**, 683–701.

Funk, C., P. Peterson, M. Landsfeld, D. Pedreros, J. Verdin, S. Shukla, G. Husak, J. Rowland, L. Harrison, A. Hoell, et al., 2015: The climate hazards infrared precipitation with stations—a new environmental record for monitoring extremes. *Scientific data*, **2 (1)**, 1–21.

Gan, Y., X.-Z. Liang, Q. Duan, F. Chen, J. Li, and Y. Zhang, 2019: Assessment and reduction of the physical parameterization uncertainty for noah-mp land surface model. *Water Resources Research*, **55 (7)**, 5518–5538.

Garratt, J. R., 1994: The atmospheric boundary layer. *Earth-Science Reviews*, **37 (1-2)**, 89–134.

GCOS, 2016: The global observing system for climate: Implementation needs. *World Meteorol. Organ.*, **200**, 316.

Gelaro, R., W. McCarty, M. J. Suárez, R. Todling, A. Molod, L. Takacs, C. A. Randles, A. Darmenov, M. G. Bosilovich, R. Reichle, et al., 2017: The modern-era retrospective analysis for research and applications, version 2 (merra-2). *Journal of climate*, **30 (14)**, 5419–5454.

General Statistics Office of Vietnam, 2023: *Statistics of the Mekong Delta Region*. General Statistics Office of Vietnam, Hanoi, Vietnam.

Gholami, S., S. Ghader, H. Khaleghi-Zavareh, and P. Ghafarian, 2021: Sensitivity of wrf-simulated 10 m wind over the persian gulf to different boundary conditions and pbl parameterization schemes. *Atmospheric Research*, **247**, 105 147.

Giannaros, T. M., D. Melas, I. A. Daglis, I. Keramitsoglou, and K. Kourtidis, 2013: Numerical study of the urban heat island over athens (greece) with the wrf model. *Atmospheric Environment*, **73**, 103–111.

Gilliam, R. C. and J. E. Pleim, 2010: Performance assessment of new land surface and planetary boundary layer physics in the wrf-arw. *Journal of Applied Meteorology and Climatology*, **49 (4)**, 760–774.

Giorgi, F., 1990: Simulation of regional climate using a limited area model nested in a general circulation model. *Journal of climate*, **3 (9)**, 941–963.

Giorgi, F., C. Torma, E. Coppola, N. Ban, C. Schär, and S. Somot, 2016: Enhanced summer convective rainfall at alpine high elevations in response to climate warming. *Nature Geoscience*, **9 (8)**, 584–589.

Giri, C., P. Defourny, and S. Shrestha, 2003: Land cover characterization and mapping of continental southeast asia using multi-resolution satellite sensor data. *International journal of remote Sensing*, **24 (21)**, 4181–4196.

Gobin, A., H. Nguyen, V. Pham, and H. Pham, 2016: Heavy rainfall patterns in vietnam and their relation with enso cycles. *International Journal of Climatology*, **36 (4)**, 1686–1699.

Gong, P., J. Wang, L. Yu, Y. Zhao, Y. Zhao, L. Liang, Z. Niu, X. Huang, H. Fu, S. Liu, et al., 2013: Finer resolution observation and monitoring of global land cover: First mapping results with landsat tm and etm+ data. *International Journal of Remote Sensing*, **34 (7)**, 2607–2654.

Grell, G. A. and D. Dévényi, 2002: A generalized approach to parameterizing convection combining ensemble and data assimilation techniques. *Geophysical Research Letters*, **29 (14)**, 38–1.

Grell, G. A. and S. R. Freitas, 2014: A scale and aerosol aware stochastic convective parameterization for weather and air quality modeling. *Atmospheric Chemistry and Physics*, **14 (10)**, 5233–5250.

Grimmond, C. S. B., M. Blackett, M. J. Best, J.-J. Baik, S. Belcher, J. Beringer, S. Bohnenstengel, I. Calmet, F. Chen, A. Coutts, et al., 2011: Initial results from phase 2 of the international urban energy balance model comparison. *International Journal of Climatology*, **31 (2)**, 244–272.

Guo, H., A. Bao, T. Liu, F. Ndayisaba, D. He, A. Kurban, and P. De Maeyer, 2017: Meteorological drought analysis in the lower mekong basin using satellite-based long-term chirps product. *Sustainability*, **9 (6)**, 901.

Guo, H., S. Chen, A. Bao, J. Hu, A. S. Gebregiorgis, X. Xue, and X. Zhang, 2015: Inter-comparison of high-resolution satellite precipitation products over central asia. *Remote Sensing*, **7 (6)**, 7181–7211.

Ha, T. T. P., H. van Dijk, R. Bosma, and L. X. Sinh, 2013: Livelihood capabilities and pathways of shrimp farmers in the mekong delta, vietnam. *Aquaculture economics & management*, **17 (1)**, 1–30.

Hamed, K. H. and A. R. Rao, 1998: A modified mann-kendall trend test for autocorrelated data. *Journal of hydrology*, **204 (1-4)**, 182–196.

Hauser, L. T., G. N. Vu, B. A. Nguyen, E. Dade, H. M. Nguyen, T. T. Q. Nguyen, T. Q. Le, L. H. Vu, A. T. H. Tong, and H. V. Pham, 2017: Uncovering the spatio-temporal dynamics of land cover change and fragmentation of mangroves in the ca mau peninsula, vietnam using multi-temporal spot satellite imagery (2004–2013). *Applied Geography*, **86**, 197–207.

Hersbach, H., B. Bell, P. Berrisford, S. Hirahara, A. Horányi, J. Muñoz-Sabater, J. Nicolas, C. Peubey, R. Radu, D. Schepers, et al., 2020: The era5 global reanalysis. *Quarterly Journal of the Royal Meteorological Society*, **146 (730)**, 1999–2049.

Hoang-Cong, H., T. Ngo-Duc, T. Nguyen-Thi, L. Trinh-Tuan, C. J. Xiang, F. Tangang, S. Jerasorn, and T. Phan-Van, 2022: A high-resolution climate experiment over part of vietnam and the lower mekong basin: performance evaluation and projection for rainfall. *Vietnam Journal of Earth Sciences*, 92–108.

Holtslag, A. and B. Boville, 1993: Local versus nonlocal boundary-layer diffusion in a global climate model. *Journal of climate*, **6 (10)**, 1825–1842.

Hong, S.-Y., J. Dudhia, and S.-H. Chen, 2004: A revised approach to ice microphysical processes for the bulk parameterization of clouds and precipitation. *Monthly weather review*, **132 (1)**, 103–120.

Hong, S.-Y. and J.-O. J. Lim, 2006: The wrf single-moment 6-class microphysics scheme (wsm6). *Asia-Pacific Journal of Atmospheric Sciences*, **42 (2)**, 129–151.

Hong, S.-Y., Y. Noh, and J. Dudhia, 2006: A new vertical diffusion package with an explicit treatment of entrainment processes. *Monthly weather review*, **134 (9)**, 2318–2341.

Hou, A. Y., R. K. Kakar, S. Neeck, A. A. Azarbarzin, C. D. Kummerow, M. Kojima, R. Oki, K. Nakamura, and T. Iguchi, 2014: The global precipitation measurement mission. *Bulletin of the American Meteorological Society*, **95 (5)**, 701–722.

Hu, S. and X. Mo, 2021: Attribution of long-term evapotranspiration trends in the mekong river basin with a remote sensing-based process model. *Remote Sensing*, **13 (2)**, 303.

Hu, X.-M., J. W. Nielsen-Gammon, and F. Zhang, 2010: Evaluation of three planetary boundary layer schemes in the wrf model. *Journal of Applied Meteorology and Climatology*, **49 (9)**, 1831–1844.

Hua, T., W. Zhao, Y. Liu, S. Wang, and S. Yang, 2018: Spatial consistency assessments for global land-cover datasets: A comparison among glc2000, cci lc, mcd12, globcover and glcnmo. *Remote Sensing*, **10 (11)**, 1846.

Huang, W.-R., H. Bui-Manh, T.-Y. Chiang, and S. B. Koralegedara, 2025: Seasonal variation of diurnal rainfall characteristics over vietnam. *Science of the Total Environment*, **971**, 179 058.

Huang, Y., M. Xue, X.-M. Hu, E. Martin, H. M. Novoa, R. A. McPherson, A. Perez, and I. Y. Morales, 2023: Convection-permitting simulations of precipitation over the peruvian central andes: Strong sensitivity to planetary boundary layer parameterization. *Journal of Hydrometeorology*, **24 (11)**, 1969–1990.

Huffman, G. J. and D. T. Bolvin, 2013: Trmm and other data precipitation data set documentation. *NASA, Greenbelt, USA*, **28 (2.3)**, 1.

Hurtt, G. C., L. P. Chini, S. Frolking, R. Betts, J. Feddema, G. Fischer, J. Fisk, K. Hibbard, R. Houghton, A. Janetos, et al., 2011: Harmonization of land-use scenarios for the period 1500–2100: 600 years of global gridded annual land-use transitions, wood harvest, and resulting secondary lands. *Climatic change*, **109 (1)**, 117.

Iuliana, S. and G. Neculau, 2015: Estimation of reference evapotranspiration from pan evaporation data in romania. *Romanian Journal of Meteorology*, **Volume 12**, 65–73.

Janjić, Z. I., 1994: The step-mountain eta coordinate model: Further developments of the convection, viscous sublayer, and turbulence closure schemes. *Monthly weather review*, **122 (5)**, 927–945.

Jasechko, S., Z. D. Sharp, J. J. Gibson, S. J. Birks, Y. Yi, and P. J. Fawcett, 2013: Terrestrial water fluxes dominated by transpiration. *Nature*, **496 (7445)**, 347–350.

Jiang, C., Z. Nie, X. Mu, F. Wang, and W. Liu, 2016: Potential evapotranspiration change and its attribution in the qinling mountains and surrounding area, china, during 1960–2012. *Journal of Water and Climate Change*, **7 (3)**, 526–541.

Jiang, Z., S. V. Raghavan, J. Hur, Y. Sun, S.-Y. Liong, V. Q. Nguyen, and T. Van Pham Dang, 2019: Future changes in rice yields over the mekong river delta due to climate change—alarming or alerting? *Theoretical and Applied Climatology*, **137 (1)**, 545–555.

Jin, E. K., I.-J. Choi, S.-Y. Kim, and J.-Y. Han, 2016: Impact of model resolution on the simulation of diurnal variations of precipitation over east asia. *Journal of Geophysical Research: Atmospheres*, **121 (4)**, 1652–1670.

Jones, P. W., 1999: First-and second-order conservative remapping schemes for grids in spherical coordinates. *Monthly Weather Review*, **127 (9)**, 2204–2210.

Jordan, R. E., 1991: A one-dimensional temperature model for a snow cover: Technical documentation for sntherm. 89. Tech. rep., COLD REGIONS RESEARCH AND ENGINEERING LAB HANOVER NH.

Kain, J. S., 2004: The kain–fritsch convective parameterization: an update. *Journal of applied meteorology*, **43 (1)**, 170–181.

Kendall, M. G., 1975: *Rank Correlation Methods*. 4th ed., Griffin, London.

Kendon, E., A. Prein, C. Senior, and A. Stirling, 2021: Challenges and outlook for convection-permitting climate modelling. *Philosophical Transactions of the Royal Society A*, **379 (2195)**, 20190 547.

Kobayashi, S., Y. Ota, Y. Harada, A. Ebita, M. Moriya, H. Onoda, K. Onogi, H. Kamahori, C. Kobayashi, H. Endo, et al., 2015: The jra-55 reanalysis: general specifications and basic characteristics. *Journal of the Meteorological Society of Japan. Ser. II*, **93 (1)**, 5–48.

Kohut, M., J. Rožnovskỳ, and G. Knozová, 2014: Comparison of actual evaporation from water surface measured by ggi-3000 evaporimeter with values calculated by the penman equation. *Contributions to Geophysics and Geodesy*, **44 (3)**, 231–240.

Kontgis, C., A. Schneider, M. Ozdogan, C. Kucharik, N. H. Duc, J. Schatz, et al., 2019: Climate change impacts on rice productivity in the mekong river delta. *Applied Geography*, **102**, 71–83.

Koo, M.-S. and S.-Y. Hong, 2010: Diurnal variations of simulated precipitation over east asia in two regional climate models. *Journal of Geophysical Research: Atmospheres*, **115 (D5)**.

Koren, V., J. Schaake, K. Mitchell, Q.-Y. Duan, F. Chen, and J. Baker, 1999: A parameterization of snowpack and frozen ground intended for ncep weather and climate models. *Journal of Geophysical Research: Atmospheres*, **104 (D16)**, 19 569–19 585.

Koster, R. and G. Walker, 2015: Interactive vegetation phenology, soil moisture, and monthly temperature forecasts. *Journal of Hydrometeorology*, **16 (4)**, 1456–1465.

Kwon, Y. C. and S.-Y. Hong, 2017: A mass-flux cumulus parameterization scheme across gray-zone resolutions. *Monthly Weather Review*, **145 (2)**, 583–598.

Lai, H.-W., T. Ou, A. Dai, X. Chen, and A. Chen, 2025: Diurnal cycle of summer precipitation over mainland southeast asia revealed by observations, reanalysis, and dynamic downscaling. *Journal of Geophysical Research: Atmospheres*, **130 (11)**, e2024JD043 020.

Lal, P., A. Shekhar, and A. Kumar, 2021: Quantifying temperature and precipitation change caused by land cover change: A case study of india using the wrf model. *Frontiers in Environmental Science*, 588.

Laux, P., P. N. B. Nguyen, J. Cullmann, and H. Kunstmann, 2017: Impacts of land-use/land-cover change and climate change on the regional climate in the central vietnam. *Land Use and Climate Change Interactions in Central Vietnam*, Springer, 143–151.

Laux, P., V. T. Phan, C. Lorenz, T. Thuc, L. Ribbe, and H. Kunstmann, 2013: Setting up regional climate simulations for southeast asia. *High Performance Computing in Science and Engineering '12*, Springer, 391–406.

Lee, S. K. and T. A. Dang, 2019: Spatio-temporal variations in meteorology drought over the mekong river delta of vietnam in the recent decades. *Paddy and Water Environment*, **17 (1)**, 35–44.

———, 2020: Extreme rainfall trends over the mekong delta under the impacts of climate change. *International Journal of Climate Change Strategies and Management*, **12 (5)**, 639–652.

Li, B., F. Chen, and H. Guo, 2015: Regional complexity in trends of potential evapotranspiration and its driving factors in the upper mekong river basin. *Quaternary International*, **380**, 83–94.

Li, L., D. J. Gochis, S. Sobolowski, and M. D. Mesquita, 2017: Evaluating the present annual water budget of a himalayan headwater river basin using a high-resolution atmosphere-hydrology model. *Journal of Geophysical Research: Atmospheres*, **122 (9)**, 4786–4807.

Li, P., K. Furtado, T. Zhou, H. Chen, J. Li, Z. Guo, and C. Xiao, 2020a: The diurnal cycle of east asian summer monsoon precipitation simulated by the met office unified model at convection-permitting scales. *Climate Dynamics*, **55 (1)**, 131–151.

Li, W., L. Li, J. Chen, Q. Lin, and H. Chen, 2021: Impacts of land use and land cover change and reforestation on summer rainfall in the yangtze river basin. *Hydrology and Earth System Sciences*, **25 (8)**, 4531–4548.

Li, X., D. Chen, Y. Duan, H. Ji, L. Zhang, Q. Chai, X. Hu, et al., 2020b: Understanding land use/land cover dynamics and impacts of human activities in the mekong delta over the last 40 years. *Global Ecology and Conservation*, **22**, e00 991.

Li, Z., Y. Chen, J. Yang, and Y. Wang, 2014: Potential evapotranspiration and its attribution over the past 50 years in the arid region of northwest china. *Hydrological Processes*, **28 (3)**, 1025–1031.

Lim, K.-S. S. and S.-Y. Hong, 2010: Development of an effective double-moment cloud microphysics scheme with prognostic cloud condensation nuclei (ccn) for weather and climate models. *Monthly weather review*, **138 (5)**, 1587–1612.

López-Espinoza, E. D., J. Zavala-Hidalgo, R. Mahmood, and O. Gómez-Ramos, 2020: Assessing the impact of land use and land cover data representation on weather forecast quality: A case study in central mexico. *Atmosphere*, **11 (11)**, 1242.

Lu, J., G. Wang, T. Chen, S. Li, D. F. T. Hagan, G. Kattel, J. Peng, T. Jiang, and B. Su, 2021: A harmonized global land evaporation dataset from model-based products covering 1980–2017. *Earth System Science Data*, **13 (12)**, 5879–5898, URL `https://essd.copernicus.org/articles/13/5879/2021/`.

Luo, X., W. Wu, D. He, Y. Li, and X. Ji, 2019: Hydrological simulation using trmm and chirps precipitation estimates in the lower lancang-mekong river basin. *Chinese Geographical Science*, **29 (1)**, 13–25.

Luong, V. V., 2021: Effects of enso and climate change on reference evapotranspiration in southern vietnam. *Journal of Meteorological Research*, **35 (5)**, 868–881.

Ma, N., G.-Y. Niu, Y. Xia, X. Cai, Y. Zhang, Y. Ma, and Y. Fang, 2017: A systematic evaluation of noah-mp in simulating land-atmosphere energy, water, and carbon exchanges over the continental united states. *Journal of Geophysical Research: Atmospheres*, **122 (22)**, 12–245.

Madden, R. A. and P. R. Julian, 1972: Description of global-scale circulation cells in the tropics with a 40–50 day period. *Journal of Atmospheric Sciences*, **29 (6)**, 1109–1123.

Mahmood, R., R. A. Pielke Sr, K. G. Hubbard, D. Niyogi, P. A. Dirmeyer, C. McAlpine, A. M. Carleton, R. Hale, S. Gameda, A. Beltrán-Przekurat, et al., 2014: Land cover changes and their biogeophysical effects on climate. *International journal of climatology*, **34 (4)**, 929–953.

Martens, B., D. G. Miralles, H. Lievens, R. Van Der Schalie, R. A. De Jeu, D. Fernández-Prieto, H. E. Beck, W. A. Dorigo, and N. E. Verhoest, 2017: Gleam v3: Satellite-based land evaporation and root-zone soil moisture. *Geoscientific Model Development*, **10 (5)**, 1903–1925.

Mayaux, P., H. Eva, J. Gallego, A. H. Strahler, M. Herold, S. Agrawal, S. Naumov, E. E. De Miranda, C. M. Di Bella, C. Ordoyne, et al., 2006: Validation of the global land cover 2000 map. *IEEE Transactions on Geoscience and Remote Sensing*, **44 (7)**, 1728–1739.

Mei, H., X.-Z. Liang, M. Zeng, Y. Yang, C. Sun, and X. Li, 2024: Improving diurnal precipitation forecasts through coherent coupling of cumulus and planetary boundary layer parameterizations. *Journal of Geophysical Research: Atmospheres*, **129 (11)**, e2023JD040 295.

Meroni, A. N., K. A. Oundo, R. Muita, M.-J. Bopape, T. R. Maisha, M. Lagasio, A. Parodi, and G. Venuti, 2021: Sensitivity of some african heavy rainfall events to microphysics and planetary boundary layer schemes: Impacts on localised storms. *Quarterly Journal of the Royal Meteorological Society*, **147 (737)**, 2448–2468.

Minderhoud, P., L. Coumou, L. Erban, H. Middelkoop, E. Stouthamer, and E. Addink, 2018: The relation between land use and subsidence in the vietnamese mekong delta. *Science of the Total Environment*, **634**, 715–726.

Minderhoud, P., L. Coumou, G. Erkens, H. Middelkoop, and E. Stouthamer, 2019: Mekong delta much lower than previously assumed in sea-level rise impact assessments. *Nature communications*, **10 (1)**, 1–13.

Minderhoud, P., G. Erkens, V. Pham, V. T. Bui, L. Erban, H. Kooi, and E. Stouthamer, 2017: Impacts of 25 years of groundwater extraction on subsidence in the mekong delta, vietnam. *Environmental research letters*, **12 (6)**, 064 006.

Minh, D. H. T., L. Van Trung, and T. Le Toan, 2015: Mapping ground subsidence phenomena in ho chi minh city through the radar interferometry technique using alos palsar data. *Remote sensing*, **7 (7)**, 8543–8562.

Minh, H. V. T., B. T. B. Lien, D. T. Hong Ngoc, T. V. Ty, N. V. C. Ngan, N. P. Cong, N. K. Downes, G. Meraj, and P. Kumar, 2024: Understanding rainfall distribution characteristics over the vietnamese mekong delta: a comparison between coastal and inland localities. *Atmosphere*, **15 (2)**, 217.

Minh, H. V. T., G. Meraj, P. Kumar, N. D. G. Nam, B. T. B. Lien, N. V. C. Ngan, L. Van Thinh, and N. K. Downes, 2025: Assessment of long-term rainfall trends and variability in the vietnamese mekong delta: implications for water resources management strategies. *Discover Environment*, **3 (1)**, 1–24.

Mlawer, E. J., S. J. Taubman, P. D. Brown, M. J. Iacono, and S. A. Clough, 1997: Radiative transfer for inhomogeneous atmospheres: Rrtm, a validated correlated-k model for the longwave. *Journal of Geophysical Research: Atmospheres*, **102 (D14)**, 16 663–16 682.

Mohan, M. and S. Bhati, 2011: Analysis of wrf model performance over subtropical region of delhi, india. *Advances in Meteorology*, **2011**.

Mondal, A., M.-H. Le, and V. Lakshmi, 2022: Land use, climate, and water change in the vietnamese mekong delta (vmd) using earth observation and hydrological modeling. *Journal of Hydrology: Regional Studies*, **42**, 101 132.

Mortey, E. M., J. Arnault, M. M. Inoussa, S. Madougou, T. Annor, P. Laux, M. D. B. Dieng, and H. Kunstmann, 2024: Regional climate response to land cover change in tropical west africa: a numerical sensitivity experiment with esa land cover data and advanced wrf-hydro. *Frontiers in Water*, **6**, 1372 333.

Mu, Q., M. Zhao, and S. Running, 2011: Improvements and evaluations of the modis global evapotranspiration algorithm. *Remote Sensing of Environment*, **115 (8)**, 1781–1800.

Nakanishi, M. and H. Niino, 2006: An improved mellor–yamada level-3 model: Its numerical stability and application to a regional prediction of advection fog. *Boundary-Layer Meteorology*, **119 (2)**, 397–407.

Nations, U., 2016: The sustainable development goals 2016. Tech. rep., eSocialSciences.

Navale, A. and C. Singh, 2020: Topographic sensitivity of wrf-simulated rainfall patterns over the north west himalayan region. *Atmospheric research*, **242**, 105 003.

Nguyen, D.-Q., J. Renwick, and J. McGregor, 2014a: Variations of surface temperature and rainfall in vietnam from 1971 to 2010. *International Journal of Climatology*, **34 (1)**, 249–264.

Nguyen, K. C., J. J. Katzfey, and J. L. McGregor, 2014b: Downscaling over vietnam using the stretched-grid ccam: verification of the mean and interannual variability of rainfall. *Climate Dynamics*, **43 (3)**, 861–879.

Nguyen, T., P. Hoang, and T. Dang, 2022: Climate variability induced drought across the coastal fringes of the mekong delta, vietnam. *Mausam*, **73 (3)**, 525–536.

Niu, G.-Y. and Z.-L. Yang, 2006: Effects of frozen soil on snowmelt runoff and soil water storage at a continental scale. *Journal of Hydrometeorology*, **7 (5)**, 937–952.

Niu, G.-Y., Z.-L. Yang, K. E. Mitchell, F. Chen, M. B. Ek, M. Barlage, A. Kumar, K. Manning, D. Niyogi, E. Rosero, et al., 2011: The community noah land surface model with multiparameterization options (noah-mp): 1. model description and evaluation with local-scale measurements. *Journal of Geophysical Research: Atmospheres*, **116 (D12)**.

Niyogi, D., P. Pyle, M. Lei, S. P. Arya, C. M. Kishtawal, M. Shepherd, F. Chen, and B. Wolfe, 2011: Urban modification of thunderstorms: An observational storm climatology and model case study for the indianapolis urban region. *Journal of Applied Meteorology and Climatology*, **50 (5)**, 1129–1144.

Ou, T., D. Chen, X. Chen, C. Lin, K. Yang, H.-W. Lai, and F. Zhang, 2020: Simulation of summer precipitation diurnal cycles over the tibetan plateau at the gray-zone grid spacing for cumulus parameterization. *Climate Dynamics*, **54 (7)**, 3525–3539.

Pal, S. and P. Sharma, 2021: A review of machine learning applications in land surface modeling. *Earth*, **2 (1)**, 174–190.

Pan, X., S. Liu, Y. Yang, C. You, Z. Yang, W. Xie, and T. Li, 2022: Spatio-temporal characteristics of the evapotranspiration in the lower mekong river basin during 2008–2017. *Remote Sensing*, **14 (11)**, 2609.

Park, H., G. Kim, D.-H. Cha, E.-C. Chang, J. Kim, S.-H. Park, and D.-K. Lee, 2022: Effect of a scale-aware convective parameterization scheme on the simulation of convective cells-related heavy rainfall in south korea. *Journal of Advances in Modeling Earth Systems*, **14 (6)**, e2021MS002 696.

Pham, X. T., B. Fontaine, and N. Philippon, 2010: Onset of the summer monsoon over the southern vietnam and its predictability. *Theoretical and applied climatology*, **99 (1)**, 105–113.

Pham-Thanh, H., T. Ngo-Duc, J. Matsumoto, T. Phan-Van, and H. Vo-Van, 2020: Rainfall trends in vietnam and their associations with tropical cyclones during 1979-2019. *Sola*.

Phan, D. C., T. H. Trung, V. T. Truong, T. Sasagawa, T. P. T. Vu, D. T. Bui, M. Hayashi, T. Tadono, and K. N. Nasahara, 2021: First comprehensive quantification of annual land use/cover from 1990 to 2020 across mainland vietnam. *Scientific reports*, **11 (1)**, 1–20.

Phan, V.-T., T. Ngo-Duc, et al., 2009: Seasonal and interannual variations of surface climate elements over vietnam. *Climate Research*, **40 (1)**, 49–60.

Pilatin, H., I. Yucel, E. Duzenli, and M. T. Yilmaz, 2021: Sensitivity of wrf-derived hydrometeorological extremes to sea surface temperatures in regions with complex topography and diverse climate. *Atmospheric Research*, **264**, 105 816.

Pitman, A. J., 2003: The evolution of, and revolution in, land surface schemes designed for climate models. *International Journal of Climatology: A Journal of the Royal Meteorological Society*, **23 (5)**, 479–510.

Pleim, J. E., 2007: A combined local and nonlocal closure model for the atmospheric boundary layer. part i: Model description and testing. *Journal of Applied Meteorology and Climatology*, **46 (9)**, 1383–1395.

Poortinga, A., Q. Nguyen, K. Tenneson, A. Troy, D. Saah, B. Bhandari, W. L. Ellenburg, A. Aekakkararungroj, L. Ha, H. Pham, et al., 2019: Linking earth observations for assessing the food security situation in vietnam: A landscape approach. *Frontiers in Environmental Science*, 186.

Prein, A. F., W. Langhans, G. Fosser, A. Ferrone, N. Ban, K. Goergen, M. Keller, M. Tölle, O. Gutjahr, F. Feser, et al., 2015: A review on regional convection-permitting climate modeling: Demonstrations, prospects, and challenges. *Reviews of geophysics*, **53 (2)**, 323–361.

Qian, Q., Z. Yu, X. Jia, and D. Wang, 2024: Two high-impact extreme precipitation events during the meiyu season: simulations and their sensitivity to a scale-aware convective parameterization scheme. *Environmental Research Communications*, **6 (4)**, 045 002.

Que, L.-J., W.-L. Que, and J.-M. Feng, 2016: Intercomparison of different physics schemes in the wrf model over the asian summer monsoon region. *Atmospheric and Oceanic Science Letters*, **9 (3)**, 169–177.

Raghavan, S., M. Vu, and S. Liong, 2016: Regional climate simulations over vietnam using the wrf model. *Theoretical and Applied Climatology*, **126 (1)**, 161–182.

Raupach, M., 1995: Vegetation-atmosphere interaction and surface conductance at leaf, canopy and regional scales. *Agricultural and Forest Meteorology*, **73 (3-4)**, 151–179.

Saah, D., K. Tenneson, A. Aekakkararungroj, P. Cutter, J. Broadhead, M. Patterson, Q. H. Nguyen, K. Markert, and E. Anderson, 2016: Production and operational framework of the regional land cover monitoring system (rlcms) for the lower mekong basin. Tech. rep., SERVIR-Mekong / Asian Disaster Preparedness Center (ADPC) / NASA Applied Sciences Program, URL `https://www.landcovermapping.org/en/landcover/`, dataset documentation; RLCMS land cover mapping system.

Saah, D., K. Tenneson, A. Poortinga, Q. Nguyen, F. Chishtie, K. San Aung, K. N. Markert, N. Clinton, E. R. Anderson, P. Cutter, et al., 2020: Primitives as building blocks for constructing land cover maps. *International Journal of Applied Earth Observation and Geoinformation*, **85**, 101 979.

Sakaguchi, K. and X. Zeng, 2009: Effects of soil wetness, plant litter, and under-canopy atmospheric stability on ground evaporation in the community land model (clm3. 5). *Journal of Geophysical Research: Atmospheres*, **114 (D1)**.

Schaake, J. C., V. I. Koren, Q.-Y. Duan, K. Mitchell, and F. Chen, 1996: Simple water balance model for estimating runoff at different spatial and temporal scales. *Journal of Geophysical Research: Atmospheres*, **101 (D3)**, 7461–7475.

Schär, C., O. Fuhrer, A. Arteaga, N. Ban, C. Charpilloz, S. Di Girolamo, L. Hentgen, T. Hoefler, X. Lapillonne, D. Leutwyler, et al., 2020: Kilometer-scale climate models: Prospects and challenges. *Bulletin of the American Meteorological Society*, **101 (5)**, E567–E587.

Schlesinger, W. H. and S. Jasechko, 2014: Transpiration in the global water cycle. *Agricultural and Forest Meteorology*, **189**, 115–117.

Sellers, P., R. Dickinson, D. Randall, A. Betts, F. Hall, J. Berry, G. Collatz, A. Denning, H. Mooney, C. Nobre, et al., 1997: Modeling the exchanges of energy, water, and carbon between continents and the atmosphere. *Science*, **275 (5299)**, 502–509.

Sen, P. K., 1968: Estimates of the regression coefficient based on kendall's tau. *Journal of the American Statistical Association*, **63 (324)**, 1379–1389.

Senatore, A., G. Mendicino, H. R. Knoche, and H. Kunstmann, 2014: Sensitivity of modeled precipitation to sea surface temperature in regions with complex topography and coastlines: A case study for the mediterranean. *Journal of Hydrometeorology*, **15 (6)**, 2370–2396.

Sharma, A., D. Sharma, S. Panda, and A. Kumar, 2024: Sensitivity analysis of different parameterization schemes of the weather research and forecasting (wrf) model to simulate heavy rainfall events over the mahi river basin, india. *Agricultural and Forest Meteorology*, **346**, 109 885.

Shu, Z., B. Zhang, L. Tian, and X. Zhao, 2022: Improving dynamic vegetation modeling in noah-mp by parameter optimization and data assimilation over china's loess plateau. *Journal of Geophysical Research: Atmospheres*, **127 (19)**, e2022JD036 703.

Shuttleworth, W. J., 1993: Evaporation. *Handbook of Hydrology*, Maidment, D. R., Ed., McGraw-Hill, New York, 4.1–4.53.

Singer, M. B., D. T. Asfaw, R. Rosolem, M. O. Cuthbert, D. G. Miralles, D. MacLeod, E. A. Quichimbo, and K. Michaelides, 2021: Hourly potential evapotranspiration at 0.1° resolution for the global land surface from 1981-present. *Scientific Data*, **8 (1)**, 1–13.

Skamarock, W. C., J. B. Klemp, J. Dudhia, D. O. Gill, Z. Liu, J. Berner, W. Wang, J. G. Powers, M. G. Duda, D. M. Barker, and X.-Y. Huang, 2019: A description of the advanced research wrf version 4. Tech. Rep. NCAR/TN-556+STR, National Center for Atmospheric Research (NCAR).

Staal, A., J. J. Theeuwen, L. Wang-Erlandsson, N. Wunderling, and S. C. Dekker, 2024: Targeted rainfall enhancement as an objective of forestation. *Global Change Biology*, **30 (1)**, e17 096.

Stewart, I. D. and T. R. Oke, 2012: Local climate zones for urban temperature studies. *Bulletin of the American Meteorological Society*, **93 (12)**, 1879–1900.

Subrahmanyam, K. V., P. Kumar, N. R. Nelli, S. Anoop, M. Ramana, M. Rajeevan, and P. Chauhan, 2025: Regional shift in the peak time of maximum indian summer monsoon rainfall in recent decades. *Geophysical Research Letters*, **52 (6)**, e2024GL112 697.

Sulla-Menashe, D. and M. A. Friedl, 2018: User guide to collection 6 modis land cover (mcd12q1 and mcd12c1) product. URL `https://lpdaac.usgs.gov/documents/101/MCD12_User_Guide_V6.pdf`, dataset DOI: 10.5067/MODIS/MCD12Q1.006.

Sun, C., Z.-N. Xiao, and M. Nguyen, 2021a: Projection on precipitation frequency of different intensities and precipitation amount in the lancang-mekong river basin in the 21st century. *Advances in Climate Change Research*, **12 (2)**, 162–171.

Sun, H., F. Su, Z. He, T. Ou, D. Chen, Z. Li, and Y. Li, 2021b: Hydrological evaluation of high-resolution precipitation estimates from the wrf model in the third pole river basins. *Journal of Hydrometeorology*, **22 (8)**, 2055–2071.

Syvitski, J. P., A. J. Kettner, I. Overeem, E. W. Hutton, M. T. Hannon, G. R. Brakenridge, J. Day, C. Vörösmarty, Y. Saito, L. Giosan, et al., 2009: Sinking deltas due to human activities. *Nature Geoscience*, **2 (10)**, 681–686.

Ta, Z., R. Yu, X. Chen, G. Mu, and Y. Guo, 2018: Analysis of the spatio-temporal patterns of dry and wet conditions in central asia. *Atmosphere*, **9 (1)**, 7.

Takahashi, A., T. Kumagai, H. Kanamori, H. Fujinami, T. Hiyama, and M. Hara, 2017: Impact of tropical deforestation and forest degradation on precipitation over borneo island. *Journal of Hydrometeorology*, **18 (11)**, 2907–2922.

Takahashi, H., H. Fujinami, T. Yasunari, and J. Matsumoto, 2010: Diurnal rainfall pattern observed by tropical rainfall measuring mission precipitation radar (trmm-pr) around the indochina peninsula. *Journal of Geophysical Research: Atmospheres*, **115 (D7)**.

Taraphdar, S. and O. M. Pauluis, 2021: Impact of planetary boundary layer and cloud microphysics on the sensitivity of monsoon precipitation using a gray-zone regional model. *Earth and Space Science*, **8 (5)**, e2020EA001 535.

Taraphdar, S., O. M. Pauluis, L. Xue, C. Liu, R. Rasmussen, R. Ajayamohan, S. Tessendorf, X. Jing, S. Chen, and W. W. Grabowski, 2021: Wrf gray-zone simulations of precipitation over the middle-east and the uae: Impacts of physical parameterizations and resolution. *Journal of Geophysical Research: Atmospheres*, **126 (10)**, e2021JD034 648.

Tateishi, R., N. T. Hoan, T. Kobayashi, B. Alsaaideh, G. Tana, and D. X. Phong, 2014: Production of global land cover data-glcnmo2008. *Journal of Geography and Geology*, **6 (3)**, 99.

Taylor, K. E., 2001: Summarizing multiple aspects of model performance in a single diagram. *Journal of Geophysical Research: Atmospheres*, **106 (D7)**, 7183–7192.

Thompson, G., P. R. Field, R. M. Rasmussen, and W. D. Hall, 2008: Explicit forecasts of winter precipitation using an improved bulk microphysics scheme. part ii: Implementation of a new snow parameterization. *Monthly weather review*, **136 (12)**, 5095–5115.

Tiedtke, M., 1989: A comprehensive mass flux scheme for cumulus parameterization in large-scale models. *Monthly weather review*, **117 (8)**, 1779–1800.

Tran, H., T. Tran, and M. Kervyn, 2015: Dynamics of land cover/land use changes in the mekong delta, 1973–2011: A remote sensing analysis of the tran van thoi district, ca mau province, vietnam. *Remote Sensing*, **7 (3)**, 2899–2925.

Trinh-Tuan, L., T. Ngo-Duc, T. Phan-Van, H. Tran, T. Trinh, N. Pham-Quang, T. Nguyen-Xuan, Q. Tran-Anh, N. Do, and T. Nguyen, 2025: Future rainfall projections for the lower mekong basin using cmip6 dynamical downscaling. *Journal of Water and Climate Change*, **16 (5)**, 1863–1876.

Truong, N. M. and B. M. Tuan, 2018: Large-scale patterns and possible mechanisms of 10–20-day intraseasonal oscillation of the observed rainfall in vietnam. *International Journal of Climatology*, **38 (10)**, 3801–3821.

———, 2019: Structures and mechanisms of 20–60-day intraseasonal oscillation of the observed rainfall in vietnam. *Journal of Climate*, **32 (16)**, 5191–5212.

Tuan, B. M., 2019: Extratropical forcing of submonthly variations of rainfall in vietnam. *Journal of Climate*, **32 (8)**, 2329–2348.

Tuo, Y., Z. Duan, M. Disse, and G. Chiogna, 2016: Evaluation of precipitation input for swat modeling in alpine catchment: A case study in the adige river basin (italy). *Science of the total environment*, **573**, 66–82.

Van der Linden, R., A. H. Fink, J. G. Pinto, T. Phan-Van, and G. N. Kiladis, 2016: Modulation of daily rainfall in southern vietnam by the madden–julian oscillation and convectively coupled equatorial waves. *Journal of Climate*, **29 (16)**, 5801–5820.

Verseghy, D. L., 1991: Class—a canadian land surface scheme for gcms. i. soil model. *International Journal of Climatology*, **11 (2)**, 111–133.

Vu, H. T. D., D. D. Tran, A. Schenk, C. P. Nguyen, H. L. Vu, P. Oberle, F. Nestmann, et al., 2022: Land use change in the vietnamese mekong delta: New evidence from remote sensing. *Science of The Total Environment*, **813**, 151 918.

Wagner, F., V. B. Tran, and F. G. Renaud, 2012: Groundwater resources in the mekong delta: availability, utilization and risks. *The Mekong Delta System*, Springer, 201–220.

Wang, B., 2006: *The asian monsoon*. Springer Science & Business Media.

Wang, Z., A. Duan, and G. Wu, 2014: Impacts of boundary layer parameterization schemes and air-sea coupling on wrf simulation of the east asian summer monsoon. *Science China Earth Sciences*, **57 (7)**, 1480–1493.

Wei, L., Y. Rucong, L. Hailong, and Y. Yongqiang, 2001: Impacts of diurnal cycle of sst on the intraseasonal variation of surface heat flux over the western pacific warm pool. *Advances in Atmospheric Sciences*, **18 (5)**, 793–806.

Wei, Y., Z. Pu, and C. Zhang, 2020: Diurnal cycle of precipitation over the maritime continent under modulation of mjo: Perspectives from cloud-permitting scale simulations. *Journal of Geophysical Research: Atmospheres*, **125 (13)**, e2020JD032 529.

Wei, Z., K. Yoshimura, L. Wang, D. G. Miralles, S. Jasechko, and X. Lee, 2017: Revisiting the contribution of transpiration to global terrestrial evapotranspiration. *Geophysical Research Letters*, **44 (6)**, 2792–2801.

Wilder, M. and N. T. Phuong, 2002: The status of aquaculture in the mekong delta region of vietnam: Sustainable production and combined farming systems. *Fisheries science*, **68 (sup1)**, 847–850.

Williams, I. N. and M. S. Torn, 2015: Vegetation controls on surface heat flux partitioning, and land-atmosphere coupling. *Geophysical Research Letters*, **42 (21)**, 9416–9424.

Xie, B., J. C. Fung, A. Chan, and A. Lau, 2012: Evaluation of nonlocal and local planetary boundary layer schemes in the wrf model. *Journal of Geophysical Research: Atmospheres*, **117 (D12)**.

Xu, L., R. D. Pyles, R. Snyder, E. Monier, M. Falk, S.-H. Chen, et al., 2017: Impact of canopy representations on regional modeling of evapotranspiration using the wrf-acasa coupled model. *Agricultural and Forest Meteorology*, **247**, 79–92.

Xu, Y.-P., S. Pan, G. Fu, Y. Tian, and X. Zhang, 2014: Future potential evapotranspiration changes and contribution analysis in zhejiang province, east china. *Journal of Geophysical Research: Atmospheres*, **119 (5)**, 2174–2192.

Xuejie, G., Z. Zongci, D. Yihui, H. Ronghui, and F. Giorgi, 2001: Climate change due to greenhouse effects in china as simulated by a regional climate model. *Advances in Atmospheric Sciences*, **18 (6)**, 1224–1230.

Yang, B., Y. Zhou, Y. Zhang, A. Huang, Y. Qian, and L. Zhang, 2018: Simulated precipitation diurnal cycles over east asia using different cape-based convective closure schemes in wrf model. *Climate Dynamics*, **50 (5)**, 1639–1658.

Yang, Z.-L. and G.-Y. Niu, 2003: The versatile integrator of surface and atmosphere processes: Part 1. model description. *Global and Planetary Change*, **38 (1-2)**, 175–189.

Yang, Z.-L., G.-Y. Niu, K. E. Mitchell, F. Chen, M. B. Ek, M. Barlage, L. Longuevergne, K. Manning, D. Niyogi, M. Tewari, et al., 2011: The community noah land surface model with multiparameterization options (noah-mp): 2. evaluation over global river basins. *Journal of Geophysical Research: Atmospheres*, **116 (D12)**.

Yin, Y., S. Wu, G. Chen, and E. Dai, 2010: Attribution analyses of potential evapotranspiration changes in china since the 1960s. *Theoretical and applied climatology*, **101 (1)**, 19–28.

Zeng, X. and A. Beljaars, 2005: A prognostic scheme of sea surface skin temperature for modeling and data assimilation. *Geophysical Research Letters*, **32 (14)**.

Zhang, H., H. Beggs, L. Majewski, X. H. Wang, and A. Kiss, 2016: Investigating sea surface temperature diurnal variation over the tropical warm pool using mtsat-1r data. *Remote Sensing of Environment*, **183**, 1–12.

Zhang, H., H. Beggs, C. J. Merchant, X. H. Wang, L. Majewski, A. E. Kiss, J. Rodríguez, L. Thorpe, C. Gentemann, and M. Brunke, 2018: Comparison of sst diurnal variation models over the tropical warm pool region. *Journal of Geophysical Research: Oceans*, **123 (5)**, 3467–3488.

Zhang, Z., F. Chen, M. Barlage, L. Bortolotti, J. Famiglietti, Z. Li, X. Ma, and Y. Li, 2022: Cooling effects revealed by modeling of wetlands and land-atmosphere interactions. *Water Resources Research*, **58 (3)**, e2021WR030 573.

Zhou, P., M. Shao, M. Ma, T. Ou, and J. Tang, 2023: Wrf gray-zone dynamical downscaling over the tibetan plateau during 1999–2019: Model performance and added value. *Climate Dynamics*, **61 (3)**, 1371–1390.

C. List of Figures

D. List of Tables

Acknowledgments

Nearly eight years is a long time, and this doctoral dissertation could not have been completed without the guidance and encouragement of many individuals and organizations, to whom I will always be grateful throughout my life.

First and foremost, I would like to express my deepest gratitude to my main supervisor, Professor Andreas H. Fink, of the Institute of Meteorology and Climate Research at the Karlsruhe Institute of Technology. He is the one who gave me the opportunity to study in Germany starting in 2018. He is a leading professor in meteorology in Germany, with an unwavering passion for the field, and is a truly dedicated and hardworking scientist who has published numerous high-quality papers. Thanks to him, I have the opportunity to pursue work on modelling freshwater fluxes over the Vietnamese Mekong Delta. Furthermore, he always cared for an Asian student like me, and even provided me with a part-time job to supplement my income and support my family. He is a typical German, outwardly reserved, but inwardly warm, who always encouraged me not to give up and to successfully defend my thesis. I would also like to express my sincere gratitude to my co-supervisor, Prof. Harald Kunstmann. Despite holding many important positions, he consistently provided me with helpful advice.

I would like to thank Prof. Phan Van Tan, Dr. Patrick Laux, Dr. Roderick Van der Linden, and Dr. Joël Arnault for their insightful discussions, suggestions, and scientific support over the past years. Their expertise and feedback were instrumental in the successful completion of this dissertation. I also sincerely thank the members of my PhD Examination Commission for their time, support, and valuable comments.

I would like to extend my sincere gratitude to the Catholic Academic Exchange Service (KAAD) for providing financial support during my doctoral studies. I always remember attending the annual congress and seminars organized by KAAD. Thanks to these events, I had the opportunity to visit some of Germany's biggest cities and broaden my understanding of the country. Furthermore, I gratefully acknowledge the German Federal Ministry of Education and Research (BMBF) for funding the project ViWat Mekong - Integrated Solutions for Sustainable Development in the Mekong Delta: Land, Water, Energy and Climate, Sub-project 1 ViWat Engineering (Grant No. 02WCL1474A).

I would also like to acknowledge my colleagues at the Vietnam National Centre for Hydro-Meteorological Forecasting, with special thanks to Du Duc Tien and Mai Khanh Hung for their support and collaboration. My sincere thanks are extended to Maurus Borne, a colleague and close friend, whose encouragement and support were invaluable during the particularly challenging initial phase of my doctoral journey. I deeply appreciated our discussions and shared moments, which greatly contributed to

my motivation and well-being. I am also grateful to all colleagues at the Institute of Meteorology and Climate Research, KIT, for fostering a supportive and stimulating working environment.

I would also like to thank my Vietnamese friends, Vu Huu Long, Trinh Cong Dan, Tran Viet Hoan, Pham Cam Van, Vu Hoang Thai Duong, Tran Diep Anh, and Vu Tuan Dung. They shared their experiences, joys, and sorrows, and helped me overcome gout during my time in Germany. You were like family to me.

Finally, I would like to express my boundless gratitude to my family for their unwavering support and encouragement throughout my studies in Germany. I send my love to my wife, Ngo Thi Thanh Nga, who has always been there to encourage, share, and sacrifice herself to care for the family, allowing me to dedicate more time to my research. I am deeply grateful to my father, Tran Duc Huy, who spent four years studying in Germany and has always been a shining example for me to follow. I also deeply love my mother, Dang Thi Nu, who has cared for me from birth to the present day. I also send my love to my son, Tran Duc Minh, hoping he will follow in the academic footsteps of his father and grandfather, so that one day he can study in Germany. And finally, I would like to express my gratitude to my younger brother, Tran Duc Cuong, who has provided me with financial support, enabling me to focus on my studies without worrying about financial concerns.